PARTICLE-FLUID TWO-PHASE FLOW

The Energy-Minimization Multi-Scale Method

Jinghai Li and Mooson Kwauk

Metallurgical Industry Press
Beijing
1994

PARTICLE-FLUID TWO-PHASE FLOW

The Energy-Minimization Multi-Scale Method

Jinghai Li and Mooson Kwauk

Metallurgical Industry Press
Beijing
1994

PARTICLE-FLUID TWO-PHASE FLOW

The Energy-Minimization Multi-Scale Method

Jinghai Li and Mooson Kwauk

Multi-Phase Reaction Laboratory
Institute of Chemical Metallurgy
Academia Sinica

Metallurgical Industry Press, Beijing
1994

Published and distributed by
Metallurgical Industry Press
39 Songzhuyuan Beixiang, Beiheyan Dajie
Beijing 100009, P. R. China

Printed in the People's Republic of China

ISBN 7-5024-1572-6/TQ.67

PREFACE

This book is devoted to concurrent-up particle-fluid two-phase flow which forms the basis of, among others, fluidization. Depending on operating conditions and the properties of fluid and solids, the two-phase system can be operated in either the so-called particulate or the aggregative pattern. Particulate systems, such as L/S fluidization, can be analyzed relatively easily since particles are discretely distributed in the fluid, while the analysis of aggregative systems is complicated due to the prevailing heterogeneity not only on the local scale but also on the overall scale. To date, there has been no adequate account to either differentiate the particulate from the aggregative pattern, or reconcile the two. Are they really different or are they merely different phenomena of some common mechanism? Why two distinct phases (particle-rich dense and fluid-rich dilute) can coexist in an aggregative system, and why a series of regime transitions, including the so-called choking, can occur? Such questions have engaged the attention of both theorists and practitioners for decades.

The object of this book is to provide a comprehensive understanding of heterogeneous particle-fluid two-phase flow on the basis of two essential concepts—*energy minimization* and *multi-scale* analysis (EMMS). These concepts are applied to the various possible structures of two phase flow, designated under four categories—*phase, regime, pattern and region*—to describe both *local* and *overall* fluid dynamics. Differences in phase structures are subject to the manipulable variables of operating conditions, material properties and boundary conditions. The usual fixed-bed/fluidization/transport notion is further characterized by the corresponding designation PD/PFC/FD (*particle-dominating / particle-fluid-compromising / fluid-dominating).* Such an EMMS approach has enabled the authors to elucidate some of the underlying mechanisms of phenomena besides providing a method for the design and operation of particle-fluid two-phase equipment: chemical reactors, heat and mass

transfer apparatus, pipelines for transporting or moving granular materials.

The book consists of five chapters. The first chapter introduces the essential characteristics of particle-fluid two-phase flow, and proposes the system designation as its primary framework. With these basic concepts necessary for discussing fluid dynamics, Chapter 2 formulates the EMMS model, by first describing the three scales of particle-fluid interaction and the resolution of the energy consumption for particle-fluid systems into what is necessary for suspending and transporting the particles and what is dissipated, and then presenting the PD/PFC/FD characterization. Chapter 3 gives the solution of the model and presents the results of computation dealing, in succession, with local fluid dynamics (phases), dependency of local fluid dynamics on operating conditions (regimes), and on material properties (patterns), and, lastly, overall fluid dynamics, or spatial distribution of regimes (regions). Chapter 4 outlines significant experimental evidence for the EMMS model and other relevant phenomena connected to particle-fluid two-phase flow. Following up, Chapter 5 presents an example of simulating a typical two-phase flow system—a circulating fluidized bed, to demonstrate the calculation procedure for its whole flow field, and shows, as additional examples of application, several new types of reactors designed according to the principle of the EMMS model. This last chapter concludes the book with prospects for further development.

This book mainly focuses on regular aspects of particle-fluid two-phase flow, while the irregular dynamics of such a heterogeneous system, which is related to the dissipation process, has not been dealt with, and will be relegated to future research.

As engineers, the authors have combined theory with empiricism, exploring new methodology and expounding the mechanisms of relevant phenomena, and do not claim mathematical rigor. They therefore stand ready to welcome criticism. In the course of completing their study, they have received encouragement from Academia Sinica in the form of financial assistance and a Natural Science Award. For that and assistance from National Natural Science Foundation of China and China Petrochemical Corporation, the authors wish to express their gratitude.

For their tireless efforts at experiment, computation and processing the manuscript of this book, the authors wish to thank Ms. Aihua Chen, Mr. Guihua Qian, Ms. Yunru Bai, Ms. Zhoulin Yan, Mr. Wenyuan Wu, Mr. Rushan Bie, Ms. Yan Chen, Mr. Guangwen Xu, Mr. Xiaoji Zhang and all colleagues and graduate students engaged in this study. Specially, the authors wish to extend their sincere thanks to Prof. Lothar Reh of Swiss Federal Institute of Technology and Prof. Herbert Weinstein of the City University of New York for their encouragement and cooperation when one of the authors worked in their laboratories, and to Prof. Yuanki Tung for his efforts and cooperation during the earlier stage of this study. Prof. Lothar Reh reviewed the manuscript of this book with critical comments and valuable suggestions. Ms. Aihua Chen helped the authors in preparing the camera-ready manuscript. Their efforts deserve added appreciation.

Contents

Chapter 1

CHARACTERISTICS OF PARTICLE-FLUID TWO-PHASE FLOW

Particle-fluid two-phase flow can be operated in different directions—vertical, horizontal, inclined, etc., while the particles and the fluid can move concurrently or countercurrently with respect to each other. Of these combinations, concurrent-up flow is the most common, and therefore forms the focus of this book.

When a fluid passes upward through a bed of particles at very low velocities, a certain fraction of the weight of solids is supported by the drag of the fluid, and the system is said to operate as a packed or fixed bed. With increasing fluid velocity, the ratio of drag to solid weight increases, and reaches unity at a velocity called minimum fluidization velocity U_{mf}. At this velocity, the particles are buoyed by the upflowing fluid and the bed of particles becomes liquid-like, or fluidized. The simplest case, wherein the solids are fluidized but have no net upward velocity, constitutes one of the most common and widespread applications for particle-fluid two-phase flow in chemical engineering, that is, classical or low expansion fluidization.

At minimum fluidization, the particle-fluid two-phase system is normally **particulate**, that is, "homogeneous", with particles uniformly

distributed in the flowing fluid. Beyond U_{mf}, depending on the properties of the fluid and the solids, the particle-fluid system could either become immediately **aggregative**, that is, showing a two "phase" structure consisting of a dilute phase segregated into rising bubbles in a surrounding dense phase of an emulsion-like particle-fluid mixture, or remain particulate in uniform expansion through some fluid velocity range, until bubbles appear at the so-called minimum bubbling velocity U_{mb}. Although the term "phase" usually refers to the state of aggregation of matter—solid, liquid or gas—in the parlance of particle-fluid two-phase flow, it is also traditionally used to denote the mode of distribution of particles in their surrounding fluid. Thus, a "dilute phase" denotes a particle-fluid mixture in which particles are sparsely distributed in the fluid, and a "dense phase" denotes rather compact particles distribution, more or less in the form of an emulsion. A "two phase structure" refers to the simultaneous presence of a dense phase and a dilute phase, intermixed with each other in certain characteristic configuration. This book adopts such a traditional terminology.

1.1 Particulate System

Liquid/solid (L/S) fluidization is generally considered particulate, because it appears uniform. However, it has been found that L/S fluidization could well be aggregative, as for the lead/water (Wilhelm and Kwauk, 1948) or copper/water (Yu, 1986) system. As a matter of fact, no L/S system ever achieves complete uniformity. Yet its very **appearance** of uniformity has led to the concept of idealized fluidization of complete homogeneity (Kwauk, 1973), analogous to the concept of an ideal gas, for which the gas molecules occupy no volume and do not attract or repel one another. Idealized fluidization, such as is **approached** by most L/S systems, is characterized by smooth or uniform bed expansion as shown in Figure 1-1, as if the particle-fluid mixture were an elastic continuum stretching under the dynamic forces of augmented flow. In idealized or particulate fluidization of monosized particles, the slip velocity U_{slip} between the fluid and the particles is always lower than the terminal velocity U_t of the individual particles, and particles are discretely distributed in the fluid, that is, only one "phase" can exist. The fluid dynamics of such a system, expressed as the variation of

voidage ε with fluid velocity U_g, was first studied by Hancock (1937) and then demonstrated by Wilhelm and Kwauk (1948) to be linear on log-log plots, that is

$$U_g = U_t \varepsilon^n$$

Richardson and Zaki (1954) formulated sectionwise correlations of the exponent n to the terminal Reynolds number $Re_t = d_p U_t / \nu_f$. With increasing fluid velocity, the system expands smoothly as a "single phase" from $\varepsilon = \varepsilon_{mf}$ to $\varepsilon = 1$ as U_g increases from U_{mf} to U_t, as shown in Figure 1-1. This correlation between ε and U_g applies only to spherical particles with a narrow size distribution. For particles with a wide size distribution, the mean particle diameter must be used, as will be discussed in Section 1.4.1.

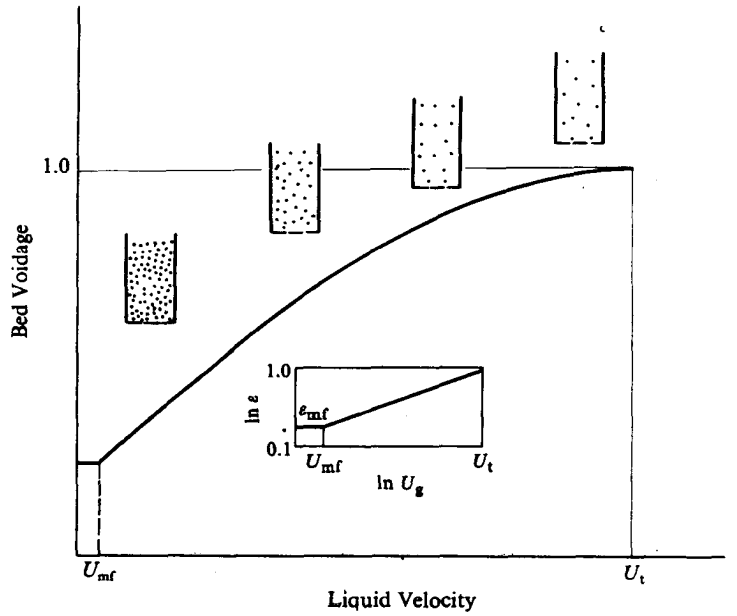

Figure 1-1 Particulate Particle-Fluid Two-Phase Flow

Idealized fluidization is of basic importance in understanding the essential features of the complicated fluid dynamics of particle-fluid system,

which can be resolved into simpler idealized subsystems—dense-phase, dilute-phase and inter-phase, as will be discussed in Chapter 2.

1.2 Aggregative System

In gas/solid (G/S) fluidization, beyond the minimum fluidization velocity U_{mf} for coarse particles, or beyond the minimum bubbling velocity U_{mb} for fine and graded powders, the particle-fluid system acquires a "two phase" structure consisting of a dilute phase of discrete gas-rich bubbles, and a continuous dense phase of solid-rich emulsion. The voidage in the dilute bubble phase is near to unity, while the voidage in the dense phase remains more or less constant and close to the voidage at minimum fluidization ε_{mf}. The preferential aggregation of the majority of the solid particles into the dense emulsion phase led to the designation of such a "two phase" operation as "aggregative."

Fluidization was thus thought to comprise these two distinct species, particulate and aggregative, and criteria were proposed to distinguish particulate from aggregative fluidization, mostly on the basis of the Froude Number (Wilhelm and Kwauk, 1948; Romero and Johanson, 1962).

However, in actuality the demarcation is fuzzy rather than definitive (Kwauk 1957). If the solid particles were made with smoother surfaces and graded in size, especially with the incorporation of fines, G/S fluidization would be less aggregative and more particulate: bubbles would be smaller and more numerous, and at higher gas velocities it would even be possible to alter the shape of the bubbles so much, especially with recycling of solids from the top to the bottom of the fluidized bed, as to produce a new two phase structure with strands or clusters of solids as a discontinuous phase, dispersed in a dilute continuous phase of sparse solid particles population. This new high-velocity phenomenon is called "circulating fluid bed" (Reh, 1971), or "fast fluidization" (Yerushalmi, Turner and Squires, 1976), which is generally characterized by the simultaneous presence of a dilute region at the top and a dense region at the bottom of the retaining vessel (Li and Kwauk, 1980).

Apparently there is a phase inversion from the bubbling mode, where gas aggregates into rising cavities, to the "fast" mode, where solids aggregate into strands or clusters. Thus, the original concept of aggregative fluidization is resolved into gas aggregation at low velocities and solids aggregation at high velocities (Kwauk, 1980). The transition from the one to the other mode, or the "phase inversion" in aggregative fluidization, is diffuse rather than clear cut, accompanied by a high degree of deformation of bubbles with simultaneous dissection of the dense phase sporadically into primordial strands or clusters. This transition corresponds to what is often referred to as "turbulent fluidization" (Lanneau, 1960; Keohe and Davidson, 1971).

With increasing gas velocity, the aggregative system thus encompasses a series of phenomenon—bubbling, turbulent and fast fluidization—to culminate in dilute transport at a velocity U_{pt} corresponding to the so-called saturation carrying capacity K^*, as shown in Figure 1-2. At U_{pt} the two-region fast fluidization consisting of a dilute region at the top coexisting with a dense region at the bottom, as shown in Figure 1-2, terminates all of a sudden with the onset of single-region dilute trans-

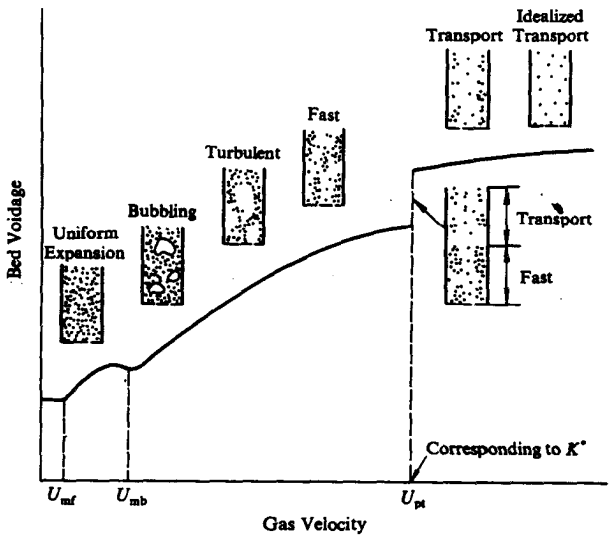

Figure 1-2 Aggregative Particle-Fluid Two-Phase Flow

port. This sudden reversion is characterized by a jump change in voidage and bed structure. In dilute transport, a G/S system demonstrates the pseudo-homogeneous nature of any usual L/S system. At last, at still higher gas velocities, idealized homogeneity becomes evident as particles begin to behave discretely.

The aggregative system is characterized not only by the so-called local heterogeneity—two phase structure, but also by the distribution of the heterogeneous phase structure over both time and space. The time dependency of flow structure appears in the form of phase alternation at a local position, that is, the alternate dissolution and reformation of the two phases. This contributes to the chaotic nature of the system. The space dependency of flow structure prevails in both the axial and radial directions, showing the co-existence of a dilute region at the top and a dense region at the bottom, as well as a dilute region at the center and a dense region near the wall of the retaining vessel. Spatial distribution causes intensive backmixing of both fluid and particles, thus affecting fluid-particle contacting in the system, and therefore, impairing the performance of a reactor. Heterogeneity in aggregative systems gives rise to a feature distinct from particulate systems—much higher mean slip velocity U_s between the fluid and the clustered particles than the terminal velocity U_t.

For any G/S system, as it expands with increasing gas flow, the volume fraction of the dense-phase f decreases while bubbles grow in size and increase in number, though the intraphase structures of the dilute and dense phases remain essentially unchanged. Thus, expansion of the G/S system could be construed as to reside mainly in a change in the volume fraction of the dense-phase f. A phase inversion can therefore be considered to take place in turbulent fluidization when f reaches about $\frac{1}{2}$, that is, half dense and half dilute, making it difficult to identify whether the dense or the dilute phase is continuous (Grace, 1985). Beyond this point of $f = \frac{1}{2}$, the dilute phase gradually becomes the continuous phase as fast fluidization takes over, while the dense phase is now shredded into particle clusters or strands.

Liquid-solid fluidization, on the other hand, is essentially all particulate throughout the fluid velocity range, except for large, heavy particles.

Between the G/S and L/S systems, expectation for provision of experimental evidence for diminishing bubbling and fast regimes, lies in the use of fluids having properties bridging the gap between gases and liquids, e.g., fluids near their critical points (Kwauk, 1957).

It can be seen that a phase structure could be confined locally to fairly small regions in a particle-fluid system, such as a bubble or a cluster, or could be extended through much larger regions in the radial or axial direction of the confining vessel. Local heterogeneity is attributed to the intrinsic instability of a particle-fluid system, while extended or overall heterogeneity results from the boundary conditions of the equipment, e.g., walls, inlet and exit configurations in relation to overall stability, as will be discussed in Section 3.7.

1.3 System Designation

Figure 1-3 shows various possible structures of two-phase flow and their change with operating parameters and material properties. For describing such a complicated phenomenon, the following system of designation is proposed by Kwauk (1990).

The term *meso-heterogeneity* denotes local heterogeneity describing localized coexistence of **PHASES**, the solid-rich *dense phase* and the fluid-rich *dilute phase*, due to the *primary instability* inherent in fluid-particle systems. The configurations of phase combination which depends on *operating* parameters, notably fluid velocity, is described by a spectrum of **REGIMES**: particulate expansion, bubbling fluidization, turbulent fluidization, fast fluidization and dilute transport, as occur in gas fluidization of fine powders. The constitution of the regime spectrum is subject to variations in *material properties*, that is, not all the regimes mentioned above would show up for systems composed of different materials. For instance, particulate expansion regime is seldom detected for large particles fluidized by a gas, and L/S systems always fluidize particulately. Such a material-dependent change of regime spectrum is described as **PATTERNS**.

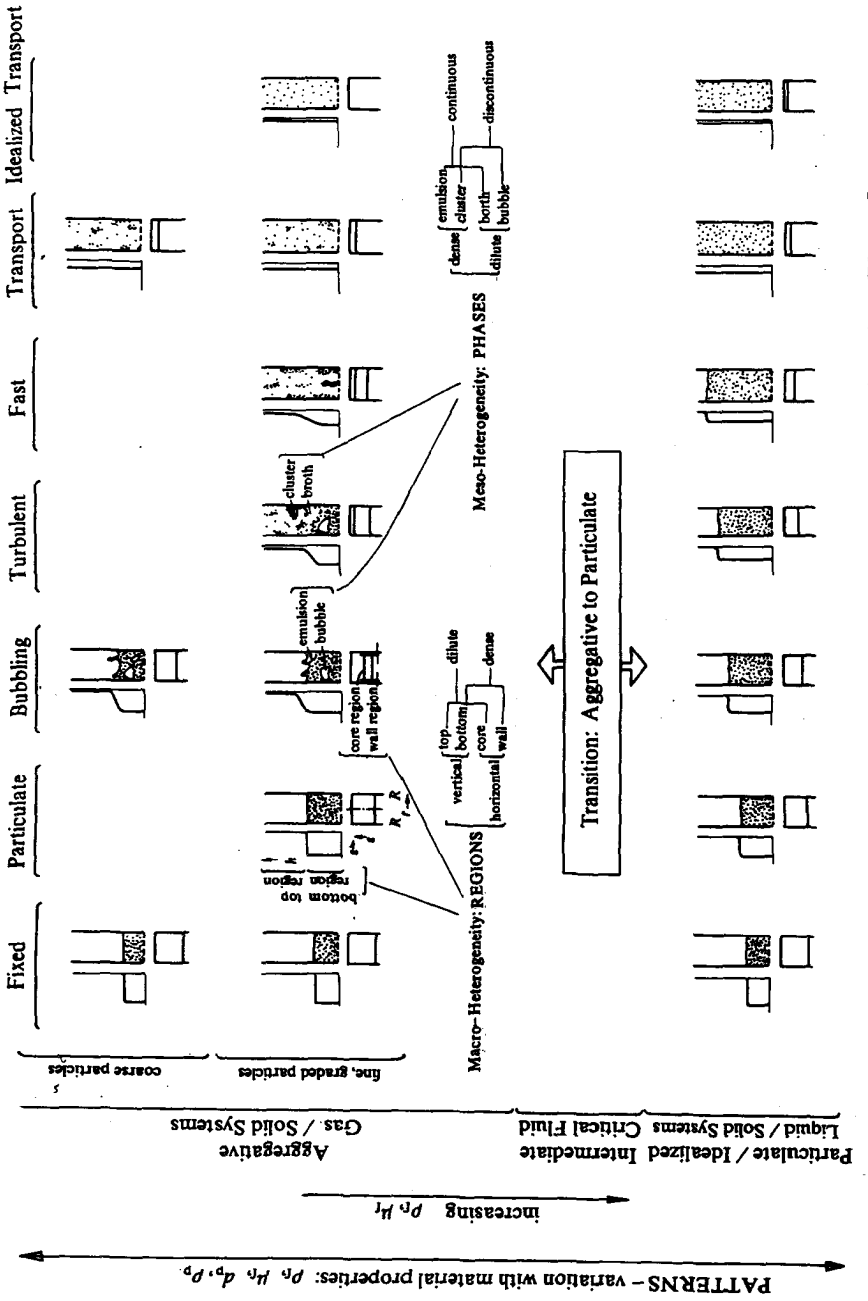

Figure 1-3 System Designation and Regime Diagram for Particle-Fluid Two-Phase flow

The term *macro-heterogeneity* denotes overall heterogeneity describing segregation into dilute and dense **REGIONS** in different *parts* of the equipment due to *secondary instability* of fluid-particle systems caused by *equipment configuration* and other factors. For fast fluidization in a cylindrical vessel, for instance, macro-heterogeneity is resolved in two dimensions:

Axial: *dense region* at the bottom surmounted by a *dilute region* at the top.

Radial: *wall region* of low voidage surrounding a *core region* of high voidage.

In summary, the proposed system of designation comprises the following four categories:

Phase — state of particle aggregation (meso-heterogeneity)

	continuous		discontinuous
dense —	emulsion	or	clusters
dilute —	broth	or	bubbles

Regime — configuration of phase combination dependent on operating parameters: bubbling, turbulent, fast, transport

Pattern — constitution of regime spectrum dependent on material properties:
bubbling/transport for coarse G/S systems;
particulate/bubbling/turbulent/fast/transport for FCC catalyst/air systems;
particulate only for most L/S systems

Region — spatial distribution of phases dependent on boundary conditions (macro-heterogeneity):
top and bottom; core and wall

Figure 1-3 is also a methodological scheme directed toward a compre-

hensive understanding of concurrent-up fluid-particle two-phase flow, indicating the relationships, or interdependencies between the above four categories: *phase*, *regime*, *pattern* and *region* and the three independent factors dominating the system—operating parameters, material properties and boundary conditions. It provides the very framework in which this book is organized. Notations in Figure 1-3 will be further explained in the succeeding chapters.

1.4 Parameters for Particle-Fluid Two-Phase Flow

To describe the complex phase structures in particle-fluid two-phase flow, Figure 1-4 shows a system of parameters which are further defined

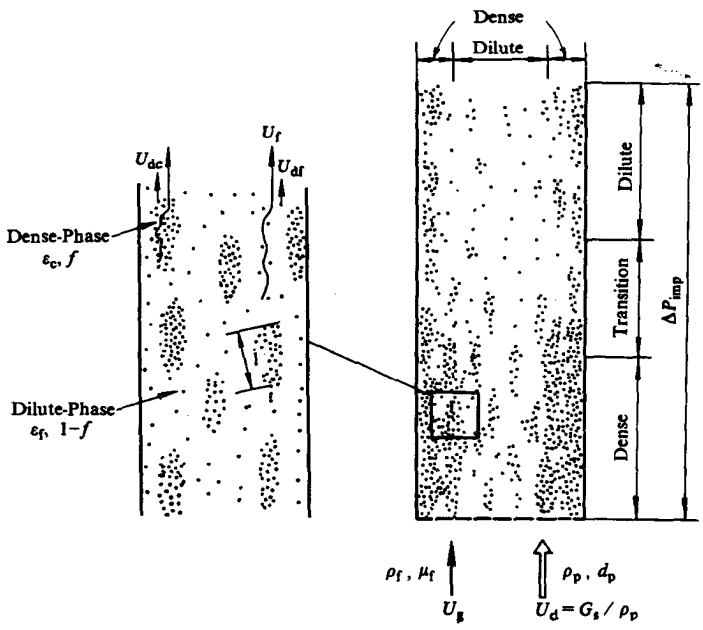

Figure 1-4 Heterogeneous Flow Structure in Particle-Fluid Systems and Related Parameters

in Table 1-1. These parameters can be grouped into three types: independent, dependent and characteristic, as will be described in this section.

1.4.1 Independent Parameters

Independent parameters are those which can be changed at will by design and in operation, and the dynamic states of particle-fluid systems will follow. They usually consist of material properties, operating conditions and boundary conditions.

Material Properties

Material properties include fluid density ρ_f, fluid viscosity μ_f, particle density ρ_p and particle diameter d_p, which are process-independent.

Since most particles handled in engineering are multisized, a characteristic mean diameter has to be defined. The most commonly used mean diameter is the so-called surface-to-volume mean diameter defined as

$$\overline{d}_s = (\sum_{i=1}^{M} x_i/d_i)^{-1}$$

which is dependent only on size distribution without consideration of the interaction between the particles and the fluid, and therefore causes deviation in flow calculations. In order to reasonably represent the fluid dynamic equivalence between multisized particles and monosized particles, the interaction between particles and fluid, in addition to geometry, needs to be considered, and the following fluid dynamic mean diameter $\overline{d}$ is therefore defined for particles in free fall (Li *et al.*, 1991b)

$$g(\rho_p - \rho_f)\frac{\pi \overline{d}^3}{6} = \overline{C}_D \frac{\pi \overline{d}^2}{4}\frac{\rho_f U_g^2}{2}$$

If the diameter on the lefthand side of the equation is summated over all the particle sizes for their gravity effect, and the righthand side, for

Table 1-1 Parameters and Formulas

Parameters	Dense-Phase	Dilute-Phase	Inter-Phase	Global
fluid density	ρ_f	ρ_f	ρ_f	
particle density	ρ_p	ρ_p	$\rho_p(1-\varepsilon_c)$	
solid-phase scale	d_p	d_p	l(cluster)	
voidage	ε_c	ε_f	$1-f$	$\varepsilon=\varepsilon_f(1-f)+\varepsilon_c f$
volume fraction	f	$1-f$		1
superficial velocity: gas	U_c	U_f	$U_f(1-f)$	$U_g=U_f(1-f)+U_c f$
solid	U_{dc}	U_{df}		$U_d=U_{df}(1-f)+U_{dc}f$
slip	$U_{sc}=U_c-\frac{U_{dc}\varepsilon_c}{1-\varepsilon_c}$	$U_{sf}=U_f-\frac{U_{df}\varepsilon_f}{1-\varepsilon_f}$	$U_{si}=\left(U_f-\frac{U_{dc}\varepsilon_f}{1-\varepsilon_c}\right)(1-f)$	$U_s=U_g-\frac{U_d\varepsilon}{1-\varepsilon}$
characteristic Reynolds number	$\mathrm{Re}_c=\left(U_c-\frac{U_{dc}\varepsilon_c}{1-\varepsilon_c}\right)d_p/\nu_f$	$\mathrm{Re}_f=\left(U_f-\frac{U_{df}\varepsilon_f}{1-\varepsilon_f}\right)d_p/\nu_f$	$\mathrm{Re}_i=\frac{U_{si}l}{\nu_f}$	
drag coefficient: single sphere	$C_{D_{sc}}=\frac{24}{Re_c}+\frac{3.6}{Re_c^{0.313}}$	$C_{D_{sf}}=\frac{24}{Re_f}+\frac{3.6}{Re_f^{0.313}}$	$C_{D_{si}}=\frac{24}{Re_i}+\frac{3.6}{Re_i^{0.313}}$	
fluidized spheres	$C_{D_c}=C_{D_{sc}}\varepsilon_c^{-4.7}$	$C_{D_f}=C_{D_{sf}}\varepsilon_f^{-4.7}$	$C_{D_i}=C_{D_{si}}(1-f)^{-4.7}$	
number of particles or clusters in unit volume	$m_c=(1-\varepsilon_c)/\frac{\pi d_p^3}{6}$	$m_f=(1-\varepsilon_f)/\frac{\pi d_p^3}{6}$	$m_i=f/\frac{\pi l^3}{6}$	
force acting on each particle or cluster	$F_{dense}=C_{D_c}\frac{\pi d_p^2}{4}\frac{\rho_f}{2}U_{sc}^2$	$F_{dilute}=C_{D_f}\frac{\pi d_p^2}{4}\frac{\rho_f}{2}U_{sf}^2$	$F_{bulk}=C_{D_i}\frac{\pi l^2}{4}\frac{\rho_f}{2}U_{si}^2$	
total force in unit volume or pressure drop	$\Delta P_{dense}=m_c F_{dense}$	$\Delta P_{dilute}=m_f F_{dilute}$	$\Delta P_{inter}=F_{inter}=m_i F_{bulk}$	
power: in unit volume	$(W_{st})_{dense}=\Delta P_{dense}U_c f$	$(W_{st})_{dilute}=\Delta P_{dilute}U_f(1-f)$	$(W_{st})_{inter}=\Delta P_{inter}U_f(1-f)$	W_{st}
for unit mass of particles	$(N_{st})_{dense}=(W_{st})_{dense}/(1-\varepsilon)\rho_p$	$(N_{st})_{dilute}=(W_{st})_{dilute}/(1-\varepsilon)\rho_p$	$(N_{st})_{inter}=(W_{st})_{inter}/(1-\varepsilon)\rho_p$	N_{st}

their drag forces, then the above equation becomes

$$g(\rho_p - \rho_f)\frac{\pi \bar{d}_g^3}{6} = \overline{C}_D^D \frac{\pi \bar{d}_D^2}{4}\frac{\rho_f U_g^2}{2}$$

where $\bar{d}_g$ is the mean diameter for calculating gravity, while $\bar{d}_D$ is the mean diameter for calculating drag force, for which $\overline{C}_D^D$ is related to $\bar{d}_D$. Combining these two equations, we get

$$\bar{d} = \frac{\overline{C}_D \bar{d}_g^3}{\overline{C}_D^D \bar{d}_D^2}$$

For gravity equivalence, in the case of multisized particles,

$$\frac{\pi \bar{d}_g^3}{6}\rho_p g \sum_{i=1}^{M} n_i = \sum_{i=1}^{M} n_i \rho_p g \frac{\pi d_i^3}{6}$$

from which

$$\bar{d}_g^3 = (\sum_{i=1}^{M} n_i d_i^3) / \sum_{i=1}^{M} n_i$$

and for drag equivalence,

$$\overline{C}_D^D \frac{\pi \bar{d}_D^2}{4}\frac{\rho_f U_g^2}{2}\sum_{i=1}^{M} n_i = \sum_{i=1}^{M} C_{D_i} n_i \frac{\pi d_i^2}{4}\frac{\rho_f U_g^2}{2}$$

from which

$$\bar{d}_D^2 = (\sum_{i=1}^{M} C_{D_i} d_i^2 n_i) / (\overline{C}_D^D \sum_{i=1}^{M} n_i)$$

Substituting $\bar{d}_D^2$ and $\bar{d}_g^3$ into the expression of $\bar{d}$, we get the so-called fluid dynamic mean diameter

$$\bar{d} = \overline{C}_D / \sum_{i=1}^{M} C_{D_i} x_i / d_i$$

Computation of $\overline{d}$ according to the above definition calls for an iteration process. It should be remembered that the value of $\overline{d}$ is subject not only to particle size but also to flow.

It can be shown that $\overline{d}$ takes to a minimum at very low Reynolds number ($Re_p < 2$ for all particles), at which $C_D = 24/Re_p$, that is,

$$\overline{d}_{min} = (\sum_{i=1}^{M} x_i/d_i^2)^{-0.5}$$

With increasing Reynolds number, $\overline{d}$ increases from minimum $\overline{d}_{min}$ to maximum $\overline{d}_{max}$ at high Re_p for which

$$\overline{d}_{max} = (\sum_{i=1}^{M} x_i/d_i)^{-1}$$

This is identical to the surface-to-volume mean diameter $\overline{d}_s$ mentioned at the beginning of this section. The gradual transition from $\overline{d}_{min}$ to $\overline{d}_{max}$ is shown typically in Figure 1-5, computed for the particular system glass/air ($d_1 = 7.255$mm, $d_2 = 4.255$mm, $d_3 = 1.480$mm and $x_1 = 22\%$, $x_2 = 33\%$, $x_3 = 45\%$). It is thus clear that for fluid dynamic equivalence, $\overline{d}_s$ can be applied only to large particles and/or to high fluid velocities corresponding to $Re_p > 2000$.

In addition, Archimedes number Ar is usually used to represent the integrated effect of material properties of both fluid and particles (Reh, 1971), formulated as

$$Ar = \frac{d_p^3 g \rho_f (\rho_p - \rho_f)}{\mu_f^2}$$

Operating Conditions

Configuration of phase combination in particle-fluid two-phase flow depends on operating conditions which include superficial fluid velocity and superficial particle velocity, defined respectively as

$$U_g = \frac{\text{total fluid mass flow rate over the overall cross section}}{(\text{cross-sectional area})(\text{fluid density})}$$

$$U_d = \frac{\text{total solid mass flow rate over the overall cross section}}{(\text{cross-sectional area})(\text{solid density})}$$

As defined above, U_g and U_d are independent of each other, and they differ from their corresponding actual velocities U_g/ε and $U_d/(1-\varepsilon)$ which vary with the dependent parameter ε.

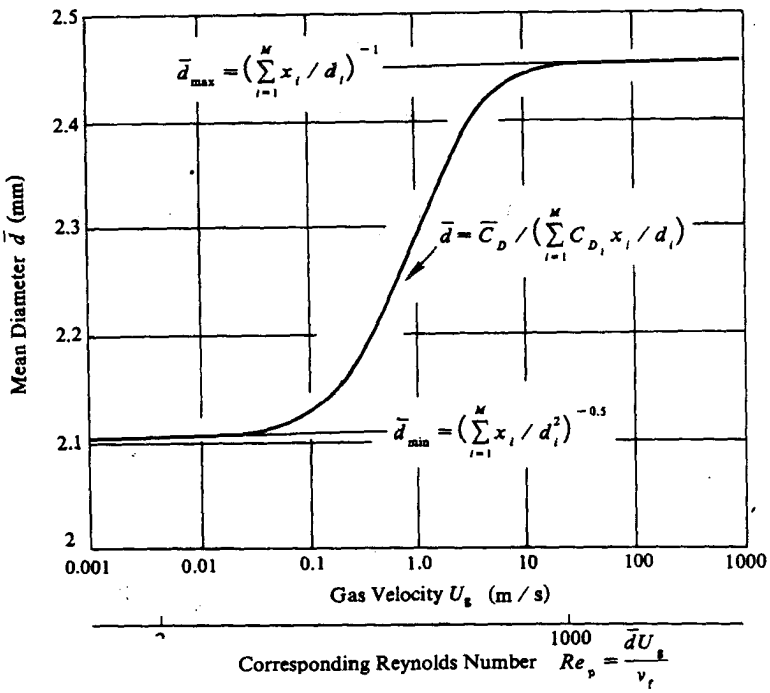

Figure 1-5 Fluid Dynamic mean Diameter of Multisized Particles Increases with Increasing Fluid Velocity (glass beads/air: $d_1 = 7.255$ mm, $d_2 = 4.255$ mm $d_3 = 1.48$ mm; $x_1 : x_2 : x_3 = 2 : 3 : 4$)

Boundary Conditions

Boundary conditions affecting the distribution of regions in space, are equipment-related external constraints, which generally consist of the retaining wall, entrance and exit configurations and the imposed pressure drop ΔP_{imp} over the particle-fluid two-phase system.

Wall effect gives rise to radial heterogeneity. Although boundary conditions were established for various models (Soo, 1989; Ding *et al.*, 1992; Ding and Gidaspow, 1990), it is still considered necessary to measure relevant parameters near the wall, such as fluid velocity, particle velocity, void fraction and so on. Inlet and outlet effects are even more difficult to generalize, and will therefore be discussed only in a qualitative sense.

The imposed pressure drop ΔP_{imp} is a global factor related to the effects of the solids inventory, the resistance of the solids circulation loop and the configuration of the system. It plays an important role in determining axial voidage profiles (Weinstein *et al.*, 1983), which, according to operation, fall into three modes: dilute region only, dense region only and both regions coexisting in a unit. Its effect will be discussed in Chapter 3.

1.4.2 Dependent Parameters

Figure 1-4 shows the eight principal dependent parameters in a generalized concurrent-up particle-fluid two-phase system, the local state of which can be described by some functional relationship between a dependent parameter vector $\mathbf{X}(r)$ in terms of these eight parameters:

$$\mathbf{X}(r) = \{\varepsilon_{\text{f}}(r), \varepsilon_{\text{c}}(r), f(r), U_{\text{f}}(r), U_{\text{c}}(r), l(r), U_{\text{d}_{\text{f}}}(r), U_{\text{d}_{\text{c}}}(r)\}$$

These eight dependent parameters will be described below.

Particle and Fluid Velocity

Various average velocities can be derived as shown in Table 1-1:

- local average fluid velocity:

$$U_g(r) = U_f(r)(1 - f(r)) + U_c(r)f(r)$$

- local average particle velocity:

$$U_d(r) = U_{df}(r)(1 - f(r)) + U_{dc}(r)f(r)$$

from which the corresponding cross-sectional average velocities can be defined:

$$U_g = \frac{2}{R^2}\int_0^R U_g(r)r\mathrm{d}r$$

$$U_d = \frac{2}{R^2}\int_0^R U_d(r)r\mathrm{d}r$$

Although in conventional voidage measurements time-averaged signals normally yield average bed voidages, however, in velocity measurements time-averaged signals are not true responses of $U_g(r)$ or $U_d(r)$, due to disparities of velocities and voidages in the dilute and dense phases, as will be discussed in Chapter 4, and therefore flow structure must be considered in analyzing the signals. This means that simultaneous measurement of velocity and bed density has to be conducted.

Voidage

Voidage represents the degree of expansion of particle-fluid systems, defined as

$$\text{Voidage} = \frac{(\text{total volume}) - (\text{volume occupied by particles})}{\text{total volume}}$$

For heterogeneous particle-fluid systems, a variety of voidages, with respect to phases and regions, is employed for describing their complicated structures. Local voidage in the dense-phase $\varepsilon_c(r)$ and local voidage in the dilute-phase $\varepsilon_f(r)$, are the two basic voidages from which other

voidages are derived:

- local average voidage:

$$\varepsilon(r) = \varepsilon_c(r)f(r) + \varepsilon_f(r)(1 - f(r))$$

- cross-sectional average voidage:

$$\bar{\varepsilon} = \frac{2}{R^2}\int_0^R \varepsilon(r) r \mathrm{d}r$$

- global average voidage:

$$\bar{\bar{\varepsilon}} = \frac{1}{H}\int_0^H \bar{\varepsilon}(h)\mathrm{d}h$$

Usually $\bar{\bar{\varepsilon}}$ and $\bar{\varepsilon}$ are calculated from measured pressure drops, while measurements of $\varepsilon(r), \varepsilon_c(r)$ and $\varepsilon_f(r)$ are much more delicate due to difficulty in calibration as will be discussed in Chapter 4.

Phase Structure

The dependent parameters, $l(r)$, for the dimension of a particle cluster, and $f(r)$, for the volume fraction occupied by the dense phase, are designed to describe the phase structure of particle-fluid systems together with $\varepsilon_c(r)$ and $\varepsilon_f(r)$. Among others (Yerushalmi and Cankurt, 1979; Subbarao, 1986), a correlation for the size of a particle aggregate $l(r)$ was proposed by Li (1987) and Li *et al.*(1988c) with the assumption that $l(r)$ is inversely proportional to the input energy. Details will be introduced in the next chapter.

It should be understood that $l(r)$ is used fictitiously as an equivalent dimension for calculating the interaction between the dense and dilute phases, rather than a parameter to represent the real size of a cluster.

1.4.3 Characteristic Parameters

Characteristic parameters are those which are not related directly to operating and boundary conditions, but depend mainly on material properties.

Drag Coefficient

Due to the heterogeneous structure in particle-fluid two-phase flow, three drag coefficients are needed for calculating multi-scale interactions between particles and fluid, as listed in Table 1-1. Drag coefficient for single particles can be calculated for $Re_p < 1000$ (Flemmer and Banks, 1986) as

$$C_{D_o} = 24/Re_p + 3.6/Re_p^{0.313}$$

and for particles in homogeneous suspensions (Wallis, 1969) as

$$C_D = C_{D_o}\varepsilon^{-4.7}$$

Although particles in two-phase flow are not uniformly distributed, the dense and the dilute phases can be considered, each in its own, as uniform suspensions, and the global system can thus be regarded as to consist of dense clusters dispersed in a broth of sparsely distributed discrete particles, as shown in Figure 1-4. The above correlations will therefore be used respectively in the dilute and the dense phases, for calculating micro-scale fluid-particle interaction, and also for evaluating meso-scale inter-phase interaction between clusters and the broth, as shown in Table 1-1, for C_{D_c}, C_{D_f} and C_{D_i}.

Terminal Velocity

The terminal velocity U_t of a particle is also called its free falling velocity. It is the maximum velocity which a single particle eventually reaches while falling down freely in a still fluid, or the minimum velocity for a flowing fluid to carry this single particle upward. The value of U_t can

be derived from force balance between the gravity of a particle and the drag exerted by the fluid, that is,

$$\frac{\pi d_p^3}{6}(\rho_p - \rho_f)g = C_{D_o}\frac{\pi d_p^2}{4}\frac{\rho_f U_t^2}{2}$$

therefore,

$$U_t = \left(\frac{4gd_p(\rho_p - \rho_f)}{3\rho_f C_{D_o}}\right)^{0.5}$$

Minimum Fluidization Velocity U_{mf} and Minimum Bubbling Velocity U_{mb}

Minimum fluidization velocity is the lowest fluid velocity at which a particle-fluid system starts to fluidize, which can be calculated from (Kunii and Levenspiel, 1969)

$$\frac{1.75}{\phi_s \varepsilon_{mf}^3}\left(\frac{d_p U_{mf}\rho_f}{\mu_f}\right)^2 + \frac{150(1-\varepsilon_{mf})}{\phi_s^2 \varepsilon_{mf}^3}\frac{d_p U_{mf}\rho_f}{\mu_f} = \frac{d_p^3 \rho_f(\rho_p - \rho_f)g}{\mu_f^2}$$

where ε_{mf} is the bed voidage at minimum fluidization which depends on the physical properties of the particles and their mode of packing, and ϕ_s is the shape factor. Without knowing ϕ_s and ε_{mf}, U_{mf} can be approximated as (Kunii and Levenspiel, 1969)

for small particles ($Re_p < 20$)

$$U_{mf} = \frac{d_p^2(\rho_p - \rho_f)g}{1650\mu_f}$$

for large particles ($Re_p > 1000$)

$$U_{mf}^2 = \frac{d_p(\rho_p - \rho_f)g}{24.5\rho_f}$$

A extensive review on U_{mf} was made by Couderc (1985), listing a variety of correlations for U_{mf}.

Minimum bubbling velocity U_{mb} is defined as the fluid velocity at which a particle-fluid system starts to bubble. This velocity is difficult to measure, especially for Class A powders, because of the inherent instability of the system when it bubbles. For large particles, U_{mb} is considered to be equal to U_{mf}. A typical correlation for calculating U_{mb} is (Abrahamsen and Geldart, 1980)

$$\frac{U_{mb}}{U_{mf}} = \frac{2300\rho_f^{0.126}\mu_f^{0.523}\exp(0.716\Omega)}{\bar{d}_s^{0.8} g^{0.954}(\rho_p - \rho_f)^{0.934}}$$

where Ω is the fraction of fine particles smaller than 45 μm. This transition will be further discussed in Chapter 4.

Saturation Carrying Capacity

Saturation carrying capacity K^* is the critical flux of solids flow corresponding to the transition from dense-phase fluidization to dilute-phase transport, at which these two fluid dynamic states coexist. This is often called "choking." Though much attention has been paid to measuring K^*, resulting in a number of correlations (Briens and Bergougnou, 1986; Satija *et al.*, 1985 and Yang, 1983), for example (Knowlton and Bachovchin, 1975),

$$\left(\frac{U_{pt}}{gd_p}\right)^{0.5} = 9.07\left(\frac{\rho_p}{\rho_f}\right)^{0.347}\left(\frac{K^* d_p}{\mu_f}\right)^{0.214}\left(\frac{d_p}{d_B}\right)^{0.246}$$

its underlying mechanism is still not understood, as will be discussed in Chapter 4.

1.4.4 Derived Parameters

Other parameters in Table 1-1, exclusive of those discussed here, can be formulated as functions of the above parameters and are therefore called derived parameters which will be dealt with wherever they arise.

Chapter 2

FORMULATION OF THE ENERGY-MINIMIZATION MULTI-SCALE (EMMS) MODEL

For very dilute particle-fluid systems in which particles are discretely distributed, invoking the conditions for the conservation of mass and momentum normally suffices to define its fluid dynamic states, because, as the traditional theory expects, it always operates in a ***single*** state. The methodology of dealing with dilute systems has been inherited, though regrettably, in studying dense particle-fluid systems which are characterized by structural heterogeneity and regime multiplicity, for which some additional constraints need to be specified.

An appropriate understanding of particle-fluid two-phase flow rests on an adequate analysis of the local fluid dynamics corresponding to the scale of bubbles or clusters, as well as the overall fluid dynamics corresponding to the scale of the retaining vessel. As shown in Figure 1-3, local fluid dynamics, designated as phases, is rooted in the intrinsic characteristics of particle-fluid systems, whereas overall fluid dynamics, designated as regions, depends on geometrical boundary conditions. Any specific local

fluid dynamic state in a system is subject to the constraints of overall fluid dynamics, whereas every point of the overall system has to satisfy the constraints of local fluid dynamics.

As the basic part of this book, this chapter will deal with the *phases* in particle-fluid two-phase flow by developing a mathematical model to quantify local fluid dynamic states. In this analysis, any global particle-fluid two-phase system is considered to be composed of a binary mixture of a gas-rich dilute phase (bubbles or broth), and a solid-rich dense phase (emulsion or cluster) (Kwauk, 1980). These phases, in combination, give rise to structural heterogeneity and regime multiplicity. This analysis will reveal the insufficiency of the conditions for the conservation of mass and momentum alone in determining the fluid dynamic states of heterogeneous particle-fluid systems, and calls for a methodology different from what is used in analyzing dilute uniform flow. For this purpose the concept of *multi-scale interaction* between particles and fluid and the method of *energy minimization* are proposed.

2.1 Methodology for Modeling Particle-Fluid Two-Phase Flow

There are two principal approaches to formulate particle-fluid two-phase flow: the pseudo-fluid model and the two-phase model.

2.1.1 Pseudo-Fluid Approach

The pseudo-fluid approach inherits the methodology for analyzing single-phase fluid flow, and considers a fluid-particle system to consist of k distinct fictitious fluids with interaction between each other. The simplest case is called *the one-fluid model*, that is, $k = 1$, assuming that particles are distributed in the fluid discretely. It was used for modeling voidage distributions in fast fluidized beds (Li and Kwauk, 1980; Zhang *et al.*, 1990).

More popular pseudo-fluid model is the so-called *two-fluid model*, that

is, $k = 2$, in which the particle phase is considered as a fictitious fluid, and separate fluid dynamic equations are established for both the particle phase and the fluid phase (Soo, 1967; Jackson, 1963; Grace and Tuot, 1979; Batchelor, 1988; Gidaspow, 1986; 1989; Arastoopour and Gidaspow, 1979; Yang, 1988; Ding and Gidaspow, 1990; Bai *et al.*, 1991; Militzer, 1986; Zhou, 1991; Yang, 1991; Liu, 1993).

For considering radial heterogeneity in a two-phase system, the pseudo-fluid model is simultaneously applied to the core dilute region and the wall dense region, resulting in the so-called two-channel model (Nakamura and Capes, 1973; Bai *et al.*, 1988; Yang, 1988; Ishii *et al.*, 1989).

Although the pseudo-fluid approach can be strictly formulated, it is hardly capable of describing the flow structure difference between the dilute phase and the dense phase, that is, the scale cannot reach that of individual particles, and regime transitions, related to inflective changes of flow structure, can not be treated.

2.1.2 Two-Phase Approach

The two-phase approach is based on the phenomenological nature of particle-fluid flow which is two-phase in structure. It considers a heterogeneous system to consist of two different phases, a solid-rich dense phase and a gas-rich dilute phase, for each of which mass and momentum conservation is analyzed with consideration of interaction and exchange between the two phases. The two-phase model was proposed for bubbling fluidization (Toomey, 1952; Davidson, 1961; Grace and Clift, 1974) to analyze the bubble phenomenon, and was then used for calculating cluster diameter (Yerushalmi *et al.*, 1978; Subbarao, 1986), and analyzing local flow structure (Hartge, 1988) in fast fluidized beds. To account for the stability of two-phase structure in fast fluidization, Li (1987) and Li *et al.*(1988b; 1990) proposed the energy-minimization multi-scale (EMMS) model, considering that mass and momentum conservation alone is not sufficient for determining the flow structure in fluidization, and that an additional condition is needed.

The two-phase approach can be used to analyze the interaction between

the fluid and individual particles, though it is not convenient for analyzing turbulent and time-dependent behavior of the system. Generally speaking, and in the authors' opinion, the pseudo-fluid approach is more suitable for dilute two-phase flow, while the two-phase approach, for dense fluidization. Combination of the two-phase model with the pseudo-fluid model may even be a more effective approach.

This book is based on the two-phase approach, focusing attention on the specific aspect of the heterogeneous flow structure of particle-fluid two-phase flow.

2.2 Three Scales of Interaction

To account for the intrinsic characteristics of particle-fluid two-phase flow, the particles and the fluid are considered to interact with each other on both a micro-scale and a meso-scale level to produce local or meso-scale heterogeneity (phases), and the overall fluid-particle system interacts with the equipment boundaries on a much larger scale to produce macro-scale heterogeneity (regions).

Micro-Scale

Micro-scale interaction is the smallest scale of interaction between the particles and fluid in the system, corresponding to the size of the constituent particles and prevailing in both the dense phase and the dilute phase. This interaction, expressed as force acting on a single particle, can be written for the dense phase:

$$F_{\text{dense}} = C_{\text{D}_\text{c}} \frac{\pi d_\text{p}^2}{4} \frac{\rho_\text{f} U_\text{sc}^2}{2}$$

and for the dilute phase:

$$F_{\text{dilute}} = C_{\text{D}_\text{f}} \frac{\pi d_\text{p}^2}{4} \frac{\rho_\text{f} U_\text{sf}^2}{2}$$

Meso-Scale

Meso-scale interaction is concerned with the interaction between clusters and the dilute-phase broth surrounding them, or the interaction between bubbles and the emulsion in which they exist. For the former, this interaction is expressed as force acting on a cluster by the broth through the so-called interphase

$$F_{\text{bulk}} = C_{\text{D}_\text{i}} \frac{\pi l^2}{4} \frac{\rho_\text{f} U_{\text{si}}^2}{2}$$

where U_{si} is the superficial relative velocity between the clusters and the dilute-phase broth as defined in Table 1-1. Here, for simplicity, the interaction between the particles in the clusters and the particles in the broth is neglected.

Macro-Scale

Macro-scale interaction occurs between the global particle-fluid system and its boundaries, resulting in macro-heterogeneity. Macro-scale interaction generally extends in both the radial (lateral) and axial directions. Radial macro-scale interaction is caused by wall effect leading to radial distribution of parameters. Axial macro-scale interaction originates primarily from ΔP_{imp} and inlet and outlet effects. The imposed pressure drop ΔP_{imp} also governs the shape of axial profiles. Macro-scale interaction underlies the dependence of meso-scale fluid dynamics on location, and it will be discussed in Chapter 3 in connection with overall fluid dynamics.

In effect, such a multi-scale analysis resolves a macro-scale heterogeneous system into three meso- to micro-scale subsystems—dense-phase, dilute-phase and inter-phase. Thus, modeling a heterogeneous particle-fluid two-phase system is reduced to calculations for the three lower-scale subsystems, making possible the application of the much simpler theory of particulate fluidization to aggregative fluidization and the formulation of energy consumptions with respect to phases (dense, dilute and inter) and processes (transport, suspension and dissipation).

2.3 Energy Analysis and System Resolution

2.3.1 Specific Energy

Per Unit Mass of Particles

The *total* energy associated with a flowing particle-fluid system, expressed as power per *unit mass* of solids, N_T, is considered to consist of the sum of two portions, one used in *suspending and transporting* the particles N_{st}, and one purely *dissipated* in particle collision, circulation, acceleration, etc., N_d. And N_{st} can be further split into that for particles suspension N_s and for transport N_t, and can also be apportioned between the dense cluster phase, the surrounding dilute phase and interaction between the two, that is,

$$\begin{aligned} N_T &= N_{st} + N_d \\ N_{st} &= N_s + N_t \\ &= (N_{st})_{dense} + (N_{st})_{dilute} + (N_{st})_{inter} \end{aligned}$$

In fact, N_s which results from the slip between the fluid and the particles, is also dissipated because it does not contribute to the upward motion of the particles, making the total dissipated energy equal to $N_s + N_d$. However, this portion of dissipated energy is responsible for retaining the potential energy of the particles which are suspended in the system, that is, keeping the system expanded, and is therefore, different from the purely dissipated energy N_d.

The average voidage of the system ε is formulated additively from the dense and dilute phases as

$$\varepsilon = \varepsilon_c f + \varepsilon_f (1 - f)$$

If wall friction is neglected, then

$$N_T = \frac{\Delta P U_g}{(1-\varepsilon)\rho_p} = \frac{(1-\varepsilon)(\rho_p - \rho_f) g U_g}{(1-\varepsilon)\rho_p} = \frac{\rho_p - \rho_f}{\rho_p} U_g g$$

The three components of N_{st} in the three subsystems can thus be calculated as follows:

$$(N_{st})_{dense} = \frac{1}{(1-\varepsilon)\rho_p}\Delta P_{dense} U_c f$$

$$(N_{st})_{dilute} = \frac{1}{(1-\varepsilon)\rho_p}\Delta P_{dilute} U_f (1-f)$$

$$(N_{st})_{inter} = \frac{1}{(1-\varepsilon)\rho_p}\Delta P_{inter} U_f (1-f)$$

Substituting the above and from the expressions for ΔP_{dense}, ΔP_{dilute} and ΔP_{inter} in Table 1-1, we get

$$N_{st} = \frac{1}{(1-\varepsilon)\rho_p}[\Delta P_{dense} U_c f + \Delta P_{dilute} U_f (1-f) + \Delta P_{inter} U_f (1-f)]$$

$$= \frac{3}{4(1-\varepsilon)\rho_p}\left[C_{D_c}\frac{1-\varepsilon_c}{d_p}\rho_f U_{sc}^2 U_c f + C_{D_f}\frac{1-\varepsilon_f}{d_p}\rho_f U_{sf}^2 U_f (1-f)\right.$$

$$\left. + C_{D_i}\frac{f}{l}\rho_f U_{si}^2 U_f (1-f)\right]$$

By difference, the dissipated energy N_d can be deduced from N_{st} and N_T:

$$N_d = N_T - N_{st} = N_T - (N_s + N_t)$$

where N_t, the energy for transporting the particles at a flow rate of G_s through a distance of $\frac{1}{(1-\varepsilon)\rho_p}$ and related to unit mass of particles in unit area, can be written as

$$N_t = \frac{U_d(\rho_p - \rho_f)g}{(1-\varepsilon)\rho_p}$$

and then, again by difference, the energy for suspending the particles can be calculated:

$$N_s = N_{st} - N_t$$

The total energy consumption N_T has thus been resolved into its components according to the constituent processes involved in particle-fluid interaction.

Per Unit Volume of Vessel

By multiplying the above energy terms by $(1-\varepsilon)\rho_p$ which is the total mass of particles in unit volume, they are converted into the corresponding energy consumptions with respect to *unit volume* of the retaining vessel, that is,

$$W_T = N_T(1-\varepsilon)\rho_p$$
$$W_{st} = N_{st}(1-\varepsilon)\rho_p$$
$$W_s = N_s(1-\varepsilon)\rho_p$$
$$W_d = N_d(1-\varepsilon)\rho_p$$
$$W_t = N_t(1-\varepsilon)\rho_p$$

Per Unit Mass of Fluid

Corresponding to N, energy consumption per unit mass of fluid can be calculated by dividing W with $\varepsilon\rho_f$ which is the total mass of fluid in unit volume. For instance, the energy consumption per unit mass of fluid for suspending and transporting particles is

$$\frac{W_{st}}{\varepsilon\rho_f}$$

2.3.2 Characterizations of Energy Consumptions

Obviously, the different energy terms characterize different aspects of particle-fluid two-phase flow, among which, those related to particle suspension and transport are of importance in analyzing fluid-particle interaction, and, in particular, for identifying system stability:

N_{st}: characterizes the intrinsic tendency of particles toward an array of the lowest interaction with the fluid;

W_{st} or $\frac{W_{st}}{\varepsilon \rho_f}$: represents the intrinsic tendency of the fluid to seek flow paths for the lowest resistance to flow

2.3.3 System Resolution

According to the above energy analysis and using the symbols defined in Figure 1-4, Figure 2-1 shows graphically how a particle-fluid two-phase

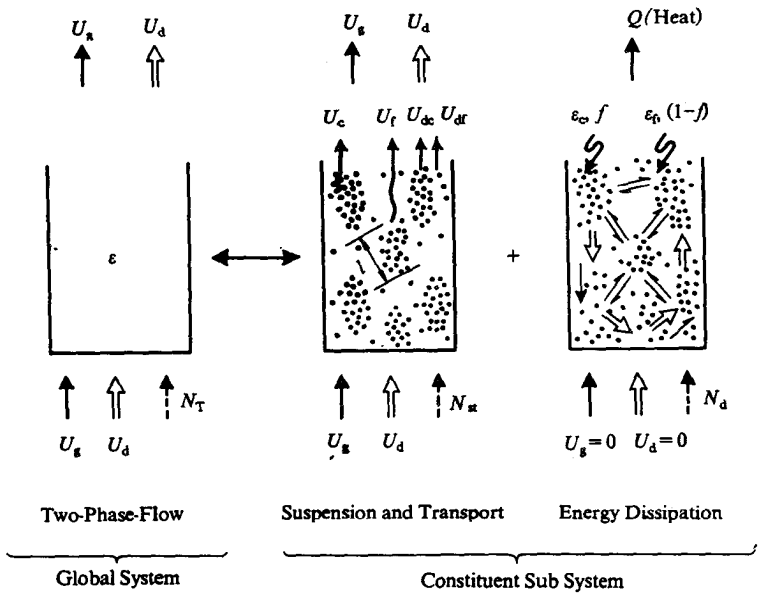

Figure 2-1 System Resolution for Particle-Fluid Systems

system can be resolved into the suspension and transport (ST) subsystem corresponding to N_{st}, and the energy dissipation (ED) subsystem corresponding to N_d.

The beginning of this section has already shown that both N_d and N_{st} are dependent on vector **X**, that is, related to flow structure, while N_T

is only subject to the independent parameter U_g, and therefore independent of flow structure as long as the particles are suspended.

2.4 Momentum and Mass Conservation for the ST Subsystem

Following Figure 2-1, Figure 2-2 shows the two steps used in analyzing the ST subsystem. The first step shows the whole ST subsystem as a combination of the two phases interacting with each other through an

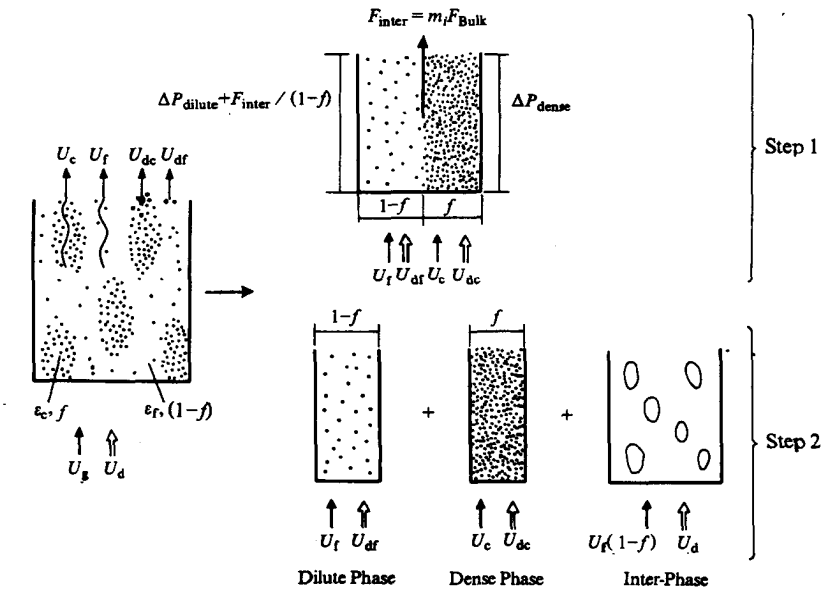

Figure 2-2 Two-Step Resolution for ST Subsystem

interface—a dense phase with voidage ε_c and volume fraction f, and a dilute phase with voidage ε_f and volume fraction $(1-f)$. The overall fluid flow is split into two streams—$U_c f$ through the dense phase and $U_f(1-f)$ through the dilute phase, and the pressure drops due to fluid flow in the two phases should be equal. The second step depicts the interaction between the dense and the dilute phases as to take place through an independent fictitious interphase between the clusters and

the surrounding broth. The energy consumed in the ST subsystem N_{st} is thereby resolved into the three constituent terms given in Section 2.2.

$$N_{st} = (N_{st})_{dense} + (N_{st})_{dilute} + (N_{st})_{inter}$$

This resolution of N_{st} makes possible the formulation of the following six equations on mass and momentum conservation:

1. Force balance for clusters in unit bed volume. The number of clusters in a unit bed volume is m_i, and the number of particles in the dense phase in this volume is $m_c f$. The fluid dynamic forces acting on these clusters can be equated to their weight:

$$m_c f F_{dense} + F_{bulk} m_i = F_g m_i$$

where F_{dense} and F_{bulk} were defined in Section 2.1, and F_g is the effective weight of a single cluster, defined as

$$F_g = \frac{\pi l^3}{6}(1-\varepsilon_c)(\rho_p - \rho_f)g$$

Referring to Table 1-1, we get

$$F_1(\mathbf{X}) = \frac{3}{4}C_{D_c}\frac{1-\varepsilon_c}{d_p}\rho_f U_{sc}^2 f + \frac{3}{4}C_{D_i}\frac{f}{l}\rho_f U_{si}^2 - (1-\varepsilon_c)(\rho_p - \rho_f)gf = 0$$

2. Equal pressure drop. As shown in Step 1 of Figure 2-2, the fluid flowing in the dilute phase has to support the discrete particles it contains as well as the clusters in suspension, and the combined forces result in a pressure drop equal to that of the parallel dense-phase fluid flow:

$$\begin{array}{ccccc} \Delta P_{dilute} & + & F_{inter}/(1-f) & = & \Delta P_{dense} \\ \| & & \| & & \| \\ m_f F_{dilute} & + & F_{bulk} m_i/(1-f) & = & m_c F_{dense} \\ \underbrace{\qquad} & & \underbrace{\qquad\qquad} & & \\ \text{particles} & & \text{clusters} & & \\ \underbrace{\qquad\qquad\qquad\qquad} & & & & \underbrace{\qquad} \\ \text{dilute phase} & & & & \text{dense phase} \end{array}$$

from which,

$$F_2(\mathbf{X}) = C_{\mathrm{D_f}}\frac{1-\varepsilon_\mathrm{f}}{d_\mathrm{p}}\rho_\mathrm{f}U_\mathrm{sf}^2 + \frac{f}{1-f}C_{\mathrm{D_i}}\frac{1}{l}\rho_\mathrm{f}U_\mathrm{si}^2 - C_{\mathrm{D_c}}\frac{1-\varepsilon_\mathrm{c}}{d_\mathrm{p}}\rho_\mathrm{f}U_\mathrm{sc}^2 = 0$$

3. Particle suspension for dilute phase. The weight of particles in the dilute phase is

$$m_\mathrm{f}F_\mathrm{dilute} = (1-\varepsilon_\mathrm{f})(\rho_\mathrm{p}-\rho_\mathrm{f})g$$

from which

$$F_3(\mathbf{X}) = \frac{3}{4}\frac{1-\varepsilon_\mathrm{f}}{d_\mathrm{p}}C_{\mathrm{D_f}}\rho_\mathrm{f}U_\mathrm{sf}^2 - (1-\varepsilon_\mathrm{f})(\rho_\mathrm{p}-\rho_\mathrm{f})g = 0$$

4. Continuity for the fluid.

$$F_4(\mathbf{X}) = U_\mathrm{g} - U_\mathrm{f}(1-f) - U_\mathrm{c}f = 0$$

5. Continuity for the particles.

$$F_5(\mathbf{X}) = U_\mathrm{d} - U_\mathrm{df}(1-f) - U_\mathrm{dc}f = 0$$

6. Cluster diameter. The diameter of a cluster l is assumed to be inversely proportional to the energy input according to Chavan (1984):

$$l = \frac{\mathrm{K}}{\mathrm{energy\ \ input}}$$

where the input energy refers to that which is responsible for breaking up the dense phase into clusters. At minimum fluidization, $l \to \infty$, Therefore, the energy input $(N_\mathrm{st})_\mathrm{mf}$ at minimum fluidization should be subtracted from the total input N_st, thus leading to the expression:

$$l = \frac{\mathrm{K}}{N_\mathrm{st} - (N_\mathrm{st})_\mathrm{mf}}$$

As Matsen (1982) mentioned for very fine particles, when the fluid velocity is high enough for the voidage to reach 0.9997, all particles are discretely distributed in the fluid, that is, clusters disappear, or $l = d_p$. On the other hand, Wu *et al.* (1993) found that any system possesses its own unique maximum voidage ε_{max} beyond which clusters do not exist. When voidage reaches ε_{max}, N_{st} is almost all consumed in transporting particles at a solids flow rate of G_s with hardly any energy dissipated, that is, N_s and N_d can both be neglected. Therefore,

$$N_{st} \approx N_T \approx N_t$$

that is,

$$(N_{st})|_{\varepsilon=\varepsilon_{max}} = \frac{U_d(\rho_p - \rho_f)g}{(1-\varepsilon_{max})\rho_p}$$

Thus, we get

$$d_p = \frac{K}{\frac{U_d g}{1-\varepsilon_{max}} \frac{\rho_p - \rho_f}{\rho_p} - (N_{st})_{mf}}$$

from which

$$l = \frac{d_p(\frac{U_d g}{1-\varepsilon_{max}} \frac{\rho_p - \rho_f}{\rho_p} - (N_{st})_{mf})}{N_{st} - (N_{st})_{mf}}$$

where

$$(N_{st})_{mf} = \frac{\rho_p - \rho_f}{\rho_p}(U_g)_{mf} g = \frac{\rho_p - \rho_f}{\rho_p}(U_{mf} + \frac{U_d \varepsilon_{mf}}{1-\varepsilon_{mf}})g$$

leading to,

$$F_6(\mathbf{X}) = l - \frac{d_p\left(\frac{U_d g}{1-\varepsilon_{max}} - (U_{mf} + \frac{U_d \varepsilon_{mf}}{1-\varepsilon_{mf}})g\right)}{N_{st} \cdot \frac{\rho_p}{\rho_p - \rho_f} - (U_{mf} + \frac{U_d \varepsilon_{mf}}{1-\varepsilon_{mf}})g} = 0$$

The above equation shows that ε_{max} depends not only on operating conditions but also on material properties. For instance, its value for L/S

systems can be much lower than those for G/S systems. Such a dependency will be analyzed in Chapter 3 in combination with pattern change.

The six equations in $F_i(\mathbf{X})$ $(i = 1, 2, ..., 6)$ described above in terms of force balance and continuity, are, however, not sufficient to determine the fluid dynamic state of a heterogeneous particle-fluid system, because with these, multiple solutions would result among which only one is valid to represent the stable state. An additional condition is needed to define this solution.

2.5 Energy Minimization and the PD, PFC and FD regimes

Minimizing the energy consumption for transporting and suspending particles is considered to be this missing condition (Li, 1987; Li *et al.*, 1988b; 1988c; 1990). For steady *single-fluid* flow, Helmholtz proposed the so-called minimum energy dissipation theorem for incompressible Newtonian fluids with constant viscosity and negligible interior and conservative volumetric forces. This theorem states that the integral of the energy dissipation over the whole flow field tends toward a minimum under unchanged boundary conditions (Lamb, 1945). However, it has not been extended to particle-fluid *two-phase* flow.

Azbel and Liapis (1983) analyzed gas/liquid systems with the assumption that the available energy at steady state is at a minimum. Reh (1971) mentioned the concept of the lowest resistance to fluid flow, and in a somewhat alternate way, the so-called minimum pressure drop was used by Nakamura and Capes (1973) in analyzing the annular structure in dilute transport risers. By introducing small disturbances into uniform suspensions (Jackson, 1963; Molerus, 1967; Grace and Tuot, 1979; Batchelor, 1988), it was verified that a uniform suspension is not stable.

It was indicated that there is no single and general variational theorem for nonlinear steady-state dissipative systems (Gage *et al.*, 1966). Therefore, the stability condition for heterogeneous particle-fluid two-phase flow has to be analyzed individually.

In concurrent-up fluid-particle two-phase flow, the fluid tends to choose an upward path with minimal resistance, while the particles tend to array themselves with minimal potential energy. Stability of the two-phase system calls for mutual coordination, as much as possible, between the fluid and the particles in following their respective tendencies. This applies for all the three broad regimes of operation: fixed bed, fluidization and transport. When neither the fluid nor the particles can dominate the system, either has to compromise and yield its intrinsic tendencies to that of the other in order to reach a stable state. However, if the system is fully dominated by either the fluid or the particles, the intrinsic tendency of the dominant one will be satisfied exclusively, with full suppression of that of the other.

If the fluid velocity is lower than U_{mf}, that is, for the fixed bed, the fluid-particle system is totally *dominated* by the particles, inasmuch as the flowing fluid cannot change the geometric state of the system, which is therefore fully particle-dependent, or *particle-dominated* (PD). In fact, this regime belongs to single-fluid flow through a maze of complicated channels composed of particles packed under gravity, and the theory of single-phase flow can be used.

When fluidized, at velocities between U_{mf} and U_{pt}, neither the particles nor the fluid can dominate the other in displaying either's tendency exclusively: they have to compromise each other in such a way that the particles seek as much as possible minimal potential energy and the fluid flows through them as much as possible with minimal resistance. In the lower-velocity end of this range, the particles tend to aggregate into a continuous dense-phase emulsion to admit excess gas to flow in the form of bubbles, and as velocity increases toward the higher velocity end of this range, the particles in the emulsion tend to shred themselves into strands, which are discontinuous and dense-phase, distributed in a broth of sparsely dispersed individual particles. On a macro scale, particles tend to aggregate next to the wall of the retaining vessel leaving a core of dilute solids concentration in the center of the vessel. Such two-phase structures in this velocity range are but irrefutable phenomena of nature. Evidently the particles, made mobile by the flowing fluid, react in turn upon the fluid to affect its flow and velocity distribution. The fluid with

its intrinsic tendency to choose an upward path with minimal resistance, and the particles with their intrinsic tendency to array themselves with minimal potential energy, seem to accommodate each other to form this ***particle-fluid-compromising*** (PFC) regime (Li *et al.*, 1992). This regime is characterized by minimal energy per unit mass of the particles, N_{st}, for which particles aggregate into clusters or emulsion, and also by conditionally minimizing W_{st} and $W_{st}/\varepsilon\rho_f$, for which the fluid flows with relatively low resistance.

At higher velocities, beyond U_{pt}, all particles fed into the system are transported in dilute phase out of the system without prolonged residence, and without being able to aggregate themselves to the same extent as the $U_{mf} \sim U_{pt}$ range. Inasmuch as particle arrangement is suppressed by the high-velocity fluid, this dilute homogeneous regime is ***fluid dominated*** (FD) and is characterized by minimal energy either per unit mass of the fluid, $\frac{W_{st}}{\varepsilon\rho_f}$, or per unit volume W_{st}. Under this condition, the fluid disperses the particles as discretely as possible in order to achieve the lowest resistance to fluid flow. Maximal particles dispersion corresponds to maximal energy expenditure per unit mass of particles, that is, N_{st} =max. Therefore, the stability condition for this regime can be represented by W_{st} =min, $(\frac{W_{st}}{\varepsilon\rho_f})$ =min and N_{st} =max. The condition N_{st} =max represents the ideal case of uniform, or particulate expansion of particles for which $N_{st} = \max = \frac{\rho_p - \rho_f}{\rho_p} U_g g = \text{constant}$.

Other relationships between the extrema of N_{st}, W_{st} and $W_{st}/\varepsilon\rho_f$ will be further discussed in Section 3.4 in connection with computation results.

The choice of the minimal energy to characterize different regimes—N_{st} for fluidization, and W_{st} for dilute-phase transport—may sound *a priori* or hypothetical, but as any hypothesis goes, its justification lies in how well it is subsequently corroborated by fact, as will be demonstrated in the latter parts of Chapter 3.

Transitions between these three regimes are distinct. PD/PFC transition occurs at the minimum fluidization velocity U_{mf} at which the fluid has acquired enough velocity to force the particles to move, thus enabling the particles to compromise with the fluid. Transition from the PFC to the FD regime takes place at a fluid velocity corresponding to its

saturation carrying capacity K^* ("choking"), at which the fluid begins to dominate the particles to realize the lowest resistance to flow. Details about these transitions will be further discussed in Section 3.4.

With the transition from the PFC regime to the FD regime, N_{st}, characterizing the intrinsic tendency of the particles, jumps from a minimum to a maximum, while W_{st} and $W_{st}/\varepsilon\rho_f$, both characterizing the intrinsic tendency of the fluid, changes from a conditional minimum to a absolute minimum, implying that the particles have lost their dominance over the system and have surrendered to the fluid at the choking point.

2.6 The EMMS Model

By considering the set of six equations on mass and momentum conservation on the one hand, and the characteristic energy extrema for stability of the three broad regimes of operation on the other, mathematical modeling for local fluid dynamics of particle-fluid two-phase flow beyond minimum fluidization needs therefore to satisfy the following constraints:

$$\left.\begin{array}{ll} a) & N_{st} = \text{extreme (min for } G_s \geq K^*, \\ & \qquad \text{max for } G_s \leq K^*) \\ b) & F_i(\mathbf{X}) = 0 \quad (i = 1, 2, ..., 6) \\ c) & U_{sc} \geq 0, \quad U_{sf} \geq 0, \quad U_{si} \geq 0 \end{array}\right\} \text{ Model LG (Local–General)}$$

where U_{sc}, U_{sf} and U_{si}, stand for the slip velocities in the dense phase, the dilute phase and the inter phase, respectively:

$$U_{sc} = U_c - \frac{U_{dc}\varepsilon_c}{1-\varepsilon_c}$$

$$U_{sf} = U_f - \frac{U_{df}\varepsilon_f}{1-\varepsilon_f}$$

$$U_{si} = (U_f - \frac{U_{dc}\varepsilon_f}{1-\varepsilon_c})(1-f)$$

This is a nonlinear optimization problem with eight variables and nine constraints, called Energy-Minimization Multi-Scale (EMMS) model, from which the parameter vector $\mathbf{X}$ and various energy consumptions can be calculated without using any adjustable parameters.

For solving the EMMS model, the saturation carrying capacity K^* has to be determined to ascertain whether N_{st} should be minimized or maximized in Model LG (Local General), that is, to identify the transition from the PFC regime to the FD regime. This transition is characterized by the following equality (Li *et al.*, 1992):

$$(W_{st})_{PFC} \equiv (W_{st})_{(N_{st})_{min}} = (W_{st})_{(N_{st})_{max}}|_{\varepsilon_c=\varepsilon_{mf}} \equiv (W_{st})_{FD}$$

The physical implication of this transition will be explained with computation in Section 3.3, and its extension to macro scale will be discussed in Section 3.7.

Chapter 3

SOLUTION OF THE EMMS MODEL

In this chapter the EMMS model developed for analyzing meso-heterogeneity of the ST system will be solved both analytically and numerically, and then extended to both radial and axial overall fluid dynamics, to provide a comprehensive description of phases, regimes, patterns and regions, and of the role of operating conditions, material properties and boundary conditions. Numerical solution of the EMMS model for both local and overall hydrodynamics will be illustrated with the system FCC/air ($\rho_p = 930 \text{kg/m}^3, d_p = 54\mu\text{m}$).

3.1 Identification of Solutions

3.1.1 Analytical Solution

Model LG (Local General) can be transformed into the so-called Lagrange's extreme problem, that is, to find $\mathbf{X}$ which satisfies

$$L(\mathbf{X}) = N_{st} + \lambda_i F_i(\mathbf{X}) = \text{extrema}$$

or, stated alternatively, to solve the following set of equations with respect to $\mathbf{X}$ and λ_i $(i = 1, 2, \cdots, 6)$:

$$\begin{cases} \frac{\partial L(\mathbf{X})}{\partial x_j} = 0 \quad (j = 1, 2, \cdots, 8) \\ F_i(\mathbf{X}) = 0 \quad (i = 1, 2, \cdots, 6) \end{cases}$$

It can be shown that there exist two solutions.

Solution 1, corresponding to $f = 0$ ($f = 1.0$ represents the same solution as $f = 0$), can be expressed analytically as

$$f = 0, \quad U_f = U_c = U_g, \quad U_{dc} = U_{df} = U_d, \quad \varepsilon_f = \varepsilon_c = \varepsilon$$

The above conditions represent obviously the single-phased uniform state of a particle-fluid system characterized by W_{st} =min and ε =max. And the eight parameters in $\mathbf{X}$ degenerate into a form of a single-parameter ε which can be calculated from U_g and U_d by using the simple correlation of particulate fluidization described in Section 1.1. That is, Model LG is reduced to

$$\frac{\pi d_p^3}{6}(\rho_p - \rho_f) \cdot g = C_{Do}\varepsilon^{-4.7}\frac{\pi d_p^2}{4} \cdot \frac{\rho_f U_s^2}{2}$$

where

$$C_{D_o} = 24/Re + 3.6/Re^{0.313}$$

and

$$Re = \frac{d_p U_s}{\nu_f}$$

What Solution 1 represents is an unstable state, unless the momentum of the fluid is sufficient to fully dominate the particles as in the FD regime. In fact, even so, for any actual system operating in the FD regime, a certain degree of particle aggregation (small clusters) still exists, until or unless $\varepsilon > \varepsilon_{max}$, such as is the case for high fluid velocity or for idealized fluidization.

Solution 2, corresponding to $f \neq 0$, stands for the heterogeneous state (two-phase) of a particle-fluid system characterized by N_{st} =min and ε =min. This solution cannot be arrived at analytically, and calls for a numerical method.

3.1.2 Numerical Solution

Model LG is a nonlinear optimization problem involving eight variables and nine constraints, the latter consisting of both equalities and inequalities, and can be solved by using the so-called GRG-2 algorithm which codes the *Generalized Reduced Gradient* method, as will be explained in the next section.

Computation of Model LG with GRG-2 shows that the solution corresponding to W_{st} =min or N_{st} =max is the same as the analytical solution for $f = 0$, whereas the solution N_{st} =min defines the heterogeneous state of two phases ($f \neq 0$), which is stable in the PFC regime, but not stable in the FD regime.

In solving Model LG by the numerical method, the transition from the PFC to the FD regime is determined by calculating W_{st} with respect to both $(N_{st})_{max}$ and $(N_{st})_{min}$ respectively, to find the point at which

$$(W_{st})_{(N_{st})_{min}} = (W_{st})_{(N_{st})_{max}}|_{\varepsilon_c=\varepsilon_{mf}}$$

which, as mentioned at the end of Chapter 2, defines the transition, and hence the saturation carrying capacity K^*. At this point, W_{st} shows an abrupt change at an undifferentiable point on its curve, corresponding to the physical phenomenon of "choking."

This is but one typical case for identifying the transition between regimes for particle-fluid two-phase flow. The relevant mechanism will be discussed in Section 3.4.

3.2 Algorithm and Computation Technique

3.2.1 Generalized Reduced Gradient Method

For solving nonlinear optimization problems with *nonlinear* constraints, the generalized reduced gradient (GRG) method as proposed by Abadie and Carpentier (1969) is an improvement of Wolfe's reduced gradient method (1963) which is applicable only to nonlinear programming prob-

lems with *linear* constraints. The GRG method of Abadie and Carpentier can be used to solve the following type of problems:

$$\begin{aligned} &\text{Minimize}: && f(\mathbf{X}) \\ &\text{subject to}: && g_i(\mathbf{X}) = 0, \quad i = 1, 2, ..., NC \\ & && lb_j \leq x_j \leq ub_j, \quad i = 1, 2, ..., NN \end{aligned}$$

where $\mathbf{X} = \{x_1, x_2, ..., x_{NN}\}$ is a vector of variables, lb_j and $ub_j (i = 1, 2, ..., NN)$ are given constants, for the lower and upper boundaries, defining the feasible region of x_j, NN is the number of variables, and NC is the number of constraints including inequalities which can be transformed into equalities by introducing nonnegative slack variables. To illustrate this procedure, assume a problem containing the constraint

$$h_i(\mathbf{X}) \geq 0$$

The slack variable s_i is introduced to force equality:

$$h_i(\mathbf{X}) - s_i = 0$$

Then set its lower and upper boundaries

$$glb_i = 0; \quad gub_i = \infty$$

in order to set up the problem in the desired form.

As in the original reduced-gradient method of Wolfe, the set of variables $\mathbf{X} = \{x_1, x_2, ..., x_{NN}\}$ is partitioned into two subsets: $\mathbf{X}_\mathrm{B}$ comprising NC basic variables (one for each constraint), and $\mathbf{X}_\mathrm{NB}$ comprising NN-NC nonbasic variables.

The basic idea of the GRG method is to eliminate $\mathbf{X}_\mathrm{B}$ (as a function of $\mathbf{X}_\mathrm{NB}$) and consider the optimization problem only in terms of $\mathbf{X}_\mathrm{NB}$. Now,

$$\mathrm{d}f(\mathbf{X}) = \nabla_{\mathbf{X}_\mathrm{NB}} f(\mathbf{X})^T \mathrm{d}\mathbf{X}_\mathrm{NB} + \nabla_{\mathbf{X}_\mathrm{B}} f(\mathbf{X})^T \mathrm{d}\mathbf{X}_\mathrm{B}$$

and

$$\frac{\mathrm{d}f(\mathbf{X})}{\mathrm{d}\mathbf{X}_{\mathrm{NB}}} = \nabla_{\mathbf{X}_{\mathrm{B}}} f(\mathbf{X}) + \nabla_{\mathbf{X}_{\mathrm{NB}}} f(\mathbf{X})^T \frac{\mathrm{d}\mathbf{X}_{\mathrm{B}}}{\mathrm{d}\mathbf{X}_{\mathrm{NB}}}$$

where

$$\nabla_{\mathbf{X}_{\mathrm{B}}} f(\mathbf{X}) = \left(\frac{\partial f(\mathbf{X})}{\partial x_{\mathrm{B}}^1}, \frac{\partial f(\mathbf{X})}{dx_{\mathrm{B}}^2}, \ldots, \frac{\partial f(\mathbf{X})}{\partial x_{\mathrm{B}}^{NC}} \right)^T$$

and

$$\nabla_{\mathbf{X}_{\mathrm{NB}}} f(\mathbf{X}) = \left(\frac{\partial f(\mathbf{X})}{\partial x_{\mathrm{NB}}^1}, \frac{\partial f(\mathbf{X})}{\partial x_{\mathrm{NB}}^2}, \ldots, \frac{\partial f(\mathbf{X})}{\partial x_{\mathrm{NB}}^{NN-NC}} \right)^T$$

Now, as

$$g_i(\mathbf{X}) = 0, \qquad i = 1, 2, \ldots, NC$$

$$\mathrm{d}g_i(\mathbf{X}) = \nabla_{\mathbf{X}_{\mathrm{NB}}} g_i(\mathbf{X})^T \mathrm{d}\mathbf{X}_{\mathrm{NB}} + \nabla_{\mathbf{X}_{\mathrm{B}}} g_i(\mathbf{X})^T \mathrm{d}\mathbf{X}_{\mathrm{B}} = 0, \quad i = 1, 2, \ldots, NC$$

we have

$$\frac{\mathrm{d}g(\mathbf{X})}{\mathrm{d}\mathbf{X}_{\mathrm{NB}}} = \frac{\partial g(\mathbf{X})}{\partial \mathbf{X}_{\mathrm{NB}}} + \left(\frac{\partial g(\mathbf{X})}{\partial \mathbf{X}_{\mathrm{B}}} \right)^T \frac{\mathrm{d}\mathbf{X}_{\mathrm{B}}}{\mathrm{d}\mathbf{X}_{\mathrm{NB}}} = 0$$

where

$$\frac{\mathrm{d}g}{\mathrm{d}\mathbf{X}_{\mathrm{NB}}} = \left(\frac{\mathrm{d}g_1}{\mathrm{d}\mathbf{X}_{\mathrm{NB}}}, \frac{\mathrm{d}g_2}{\mathrm{d}\mathbf{X}_{\mathrm{NB}}}, \ldots, \frac{\mathrm{d}g_{NC}}{\mathrm{d}\mathbf{X}_{\mathrm{NB}}} \right)^T$$

Thus

$$\frac{\mathrm{d}\mathbf{X}_{\mathrm{B}}}{\mathrm{d}\mathbf{X}_{\mathrm{NB}}} = -\left(\frac{\partial g}{\partial \mathbf{X}_{\mathrm{B}}} \right)^{-1} \frac{\partial g}{\partial \mathbf{X}_{\mathrm{NB}}}$$

On substitution, we obtain

$$\nabla_r f = \frac{\mathrm{d}f_{(\mathrm{X})}}{\mathrm{d}\mathbf{X}_{\mathrm{NB}}} = \nabla_{\mathbf{X}_{\mathrm{NB}}} f(\mathbf{X}) - \nabla_{\mathbf{X}_{\mathrm{B}}} f(\mathbf{X})^T \left(\frac{\partial g}{\partial \mathbf{X}_{\mathrm{B}}}\right)^{-1} \frac{\partial g}{\partial \mathbf{X}_{\mathrm{NB}}}$$

This last expression, called the generalized reduced gradient, permits a reduction in the dimensionality of the problem, thereby transforming the original problem into an unconstrained optimization problem.

Now, if $f(\mathbf{X})$ has a local minimum at $\mathbf{X}^*$, it is necessary that

$$\frac{\mathrm{d}f(\mathbf{X}^*)}{\mathrm{d}\mathbf{X}_{\mathrm{NB}}} = 0.$$

The search for $\mathbf{X}^*$ begins at point $\mathbf{X}_o$ and continues until

$$\frac{\mathrm{d}f(\mathbf{X})}{\mathrm{d}\mathbf{X}_{\mathrm{NB}}} = 0,$$

at which a local minimum is thus found.

3.2.2 GRG-2 Algorithm and Its Application to the EMMS Model

The EMMS Model in GRG-2 Format

The GRG-2 algorithm was developed by Lasdon and Waren (1978) on the basis of an earlier version (Lasdon *et al.*, 1978) for coding the GRG method to solve the following type of optimization problem:

minimize or maximize: $g_{NC+1}(\mathbf{X})$

subject to:
$$g_i(\mathbf{X}) = 0 \quad (i = 1, 2, ..., NE)$$
$$glb_k \leq g_k(\mathbf{X}) \leq gub_k \quad (k = NE+1, ..., NC)$$
$$lb_j \leq x_j \leq ub_j \quad (j = 1, 2, ..., NN)$$

where glb_k and gub_k $(k = NE+1, ..., NC)$ are the lower and upper boundaries for $g_k(\mathbf{X})$ respectively. According to the above requirements of the GRG-2 algorithm, the EMMS model can be converted into

$$\left.\begin{array}{ll} \text{minimize or maximize :} & N_{\mathrm{st}}(\mathbf{X}) \\ \text{subject to :} & F_i(\mathbf{X}) = 0 \quad (i = 1, 2, ..., 6) \\ & 0 \leq F_i(\mathbf{X}) \leq \infty \quad (i = 7, 8, 9) \\ & lb_j \leq x_j \leq ub_j \quad (i = 1, 2, ..., 8) \end{array}\right\} \text{Model LGa}$$

According to the physical nature of

$$\mathbf{X} = \{\varepsilon_{\mathrm{f}}, \varepsilon_{\mathrm{c}}, f, U_{\mathrm{f}}, U_{\mathrm{c}}, l, U_{\mathrm{df}}, U_{\mathrm{dc}}\}$$

its feasible region can be set with its lower boundary and upper boundary as follows:

$$\begin{array}{lllllllll} \mathbf{lb} = \{\varepsilon_{\mathrm{mf}}, & \varepsilon_{\mathrm{mf}}, & 0, & -\infty, & -\infty, & d_{\mathrm{p}}, & -\infty, & -\infty\} \\ \mathbf{ub} = \{1.0, & 1.0, & 1.0, & \infty, & \infty, & \infty, & \infty, & \infty\} \end{array}$$

If $N_{\mathrm{st}}(\mathbf{X})$ is minimized, the objective function is $N_{\mathrm{st}}(\mathbf{X})$ itself; if it is maximized, the objective function must be $-N_{\mathrm{st}}(\mathbf{X})$.

Main Program for Calling GRG-2

For calling GRG-2, a main program has to be written for IBM–PC compatible computers, and the EMMS model has to be translated into a subroutine named FNT(X, F, G), in which X represents the vector of variables, F the objective function to be optimized and G the vector of constraints, as follows:

```
MAIN PROGRAM
DIMENSION X0(NN),VARLB(NN),VARUB(NN),G(NC)
DATA VARLB/lb_j  (j = 1,2,...,NN)/
DATA VARUB/ub_j  (j = 1,2,...,NN)/
DATA NN,NC,NE,NL/...../
READ(5,*) X0
OPEN(2, file="out.dat", status="new")
CALL GRG2(X0,G,F,VARLB,VARUB,NN,NC,NE,NL)
STOP
END
```

```
C
C
      SUBROUTINE FNT(X,F,G)
      IMPLICIT REAL*8(A-H,O-Z), INTEGER*2(I-N)
      DIMENSION X(NN),G(NC)
      F = N_st(X)
      G(1) = F_1(X)
      G(2) = F_2(X)
      ......
      G(6) = F_6(X)
      G(7) = -U_sc
      G(8) = -U_sf
      G(9) = -U_si
      RETURN
      END
```

After running the program, the output results are stored in a file named "out.dat".

Kuhn-Tucker Optimality Condition

According to the optimization theory, $\mathbf{X}$ is not an optimal solution unless it satisfies the Kuhn-Tucker condition expressed as

$$\frac{\mathrm{d}(N_{\mathrm{st}}(\mathbf{X}))}{\mathrm{d}x_{\mathrm{NB}_j}} = 0 \quad lb_{\mathrm{NB}_j} \leq x_{\mathrm{NB}_j} \leq ub_{\mathrm{NB}_j}$$

$$\frac{\mathrm{d}(N_{\mathrm{st}}(\mathbf{X}))}{\mathrm{d}x_{\mathrm{NB}_j}} > 0 \quad x_{\mathrm{NB}_j} = lb_{\mathrm{NB}_j}$$

$$\frac{\mathrm{d}(N_{\mathrm{st}}(\mathbf{X}))}{\mathrm{d}x_{\mathrm{NB}_j}} < 0 \quad x_{\mathrm{NB}_j} = ub_{\mathrm{NB}_j}$$

where $\frac{\mathrm{d}(N_{\mathrm{st}}(\mathbf{X}))}{\mathrm{d}x_{\mathrm{NB}_j}}$ is the generalized reduced gradient of $N_{\mathrm{st}}(\mathbf{X})$ with respect to the non-basic variable x_{NB_j}.

All computation results in this book meet the above K-T condition. The following is an example of the output for the FCC/air system at $U_{\mathrm{g}} = 2.0$ m/s and $G_{\mathrm{s}} = 50$ kg/(m^2 · s).

```
 VELOCITY OF GAS=  2.0000 m/s
 FLOW RATE OF SOLID=  50.0000 kg/(m.m.s)

 NUMBER OF VARIABLES IS     8
 NUMBER OF FUNCTIONS IS    10
 SPACE RESERVED FOR HESSIAN HAS DIMENSION     8
 LIMIT ONBINDING CONSTRAINTS IS     9
 ACTUAL LENGTH OF Z ARRAY IS    473
 EPNEWT =   .1000E-03  EPINIT =   .1000E-03  EPSTOP =   .1000E-03
 EPPIV =   .1000E-02  PH1EPS =  .00000E+00
 NSTOP =    3  ITLIM =   10  LIMSER =     10000
 IPR =    0  PN4 =    0  PN5 =    0  PN6 =    0  PER =    0  DUMP =    0
 TANGENT VECTORS WILL BE USED FOR INITIAL ESTIMATES   BASIC
VARIABLES
 THE FINITE DIFFERENCE PARSH USING FORWARD DIFFERENCE WILL BE USED
 OBJECTIVE FUNCTION WILL BE MINIMIZED.
 LIMIT ON HESSIAN IS     0

                                OUTPUT OF INITIAL VALUES

GRG2GRG2GRG2GRG2GRG2GRG2GRG2GRG2GRG2GRG2GRG2GRG2GRG2GRG2GRG2G
RG2GRG2GRG2GRG2

 SECTION 1 -- FUNCTION
      FUNCTION                                 INITIAL          LOWER          UPPER
 NO.    NAME       STATUS   TYPE               VALUE           LIMIT          LIMIT
   1    ..  ..      ***     EQ     8.6338825E+01  0.0000000E+00  0.0000000E+00
   2    ..  ..      ***     EQ     7.3294945E+01  0.0000000E+00  0.0000000E+00
   3    ..  ..      ***     EQ    -1.2688780E-03  0.0000000E+00  0.0000000E+00
   4    ..  ..      EQ      EQ     8.0389118E-09  0.0000000E+00  0.0000000E+00
   5    ..  ..      ***     EQ    -5.4711192E+01  0.0000000E+00  0.0000000E+00
   6    ..  ..      ***     EQ     1.1244903E+02  0.0000000E+00  0.0000000E+00
   7    ..  ..      ***     RNGF   1.0000000E+02 -1.0000000E+31  0.0000000E+00
   8    ..  ..              RNGF  -7.9999955E+00 -1.0000000E+31  0.0000000E+00
   9    ..  ..              RNGF  -1.8198028E+02 -1.0000000E+31  0.0000000E+00
  10    ..  ..              OBJ    2.3017536E+01

 SECTION 2 -- VARIABLES
     VARIABLE                    INITIAL          LOWER          UPPER
 NO.    NAME       STATUS         VALUE           LIMIT          LIMIT
   1    ..  ..                 9.9000001E-01  5.0000000E-01  9.9989998E-01
   2    ..  ..      LL         5.0000000E-01  5.0000000E-01  9.9900001E-01
   3    ..  ..                 5.4711187E-01  0.0000000E+00  1.0000000E+00
   4    ..  ..                 4.3403592E+00  4.9999999E-05  2.0000000E+01
   5    ..  ..                 6.2698014E-02 -1.0000000E+00  1.0100000E+01
   6    ..  ..                 1.1670364E-01  9.9999997E-06  1.0000000E+01
   7    ..  ..                 4.3033890E-02  0.0000000E+00  1.0000000E+00
   8    ..  ..                 1.6269802E-01  0.0000000E+00  1.0000000E+00
```

```
 TERMINATION CRITERION MET.  KUHN-TUCKER CONDITIONS SATISFIED TO
 WITHIN  1.00000E-04 AT CURRENT POINT

                    FINAL RESULTS

GRG2GRG2GRG2GRG2GRG2GRG2GRG2GRG2GRG2GRG2GRG2GRG2GRG2GRG2GRG2G
RG2GRG2GRG2GRG2

 SECTION 1 -- FUNCTIONS

                                                    DISTANCE
         .          INITIAL       FINAL                FROM       LAGRANGE
 NO.    NAME         VALUE         VALUE     STATUS   NEAREST    MULTIPIER
                                                      BOUND
   1   ..   ..  8.63388E+01-4.07445E-06 EQUALITY-4.074E-06   5.60690E+00
   2   ..   ..  7.32949E+01 4.15189E-06 EQUALITY-4.152E-06  -4.19892E+00
   3   ..   .. -1.26888E-03 3.08429E-10 EQUALITY-3.084E-10   4.39056E-02
   4   ..   ..  8.03891E-09-8.32922E-06 EQUALITY-8.329E-06  -8.89042E-01
   5   ..   .. -5.47112E+01-6.35002E-05 EQUALITY-6.350E-05   1.01982E-03
   6   ..   ..  1.12449E+02-3.12085E-05 EQUALITY-3.121E-05  -3.21191E-01
   7   ..   ..  1.00000E+02-1.38272E+00  FREE     1.383E+00:U
   8   ..   .. -8.00000E+00-7.37646E+00  FREE     7.376E+00:U
   9   ..   .. -1.81980E+02-1.82144E+02  FREE     1.821E+02:U
  10   ..   ..  2.30175E+01 1.07887E+01  OBJ

 SECTION 2 -- VARIABLES

   1   ..   ..  9.90000E-01 9.99800E-01 NONBASIC  UPPERBND-5.68055E+01
   2   ..   ..  5.00000E-01 5.00000E-01 NONBASIC  LOWERBND 4.77956E+00
   3   ..   ..  5.47112E-01 4.61721E-01  BASIC    4.617E-01:L
   4   ..   ..  4.34036E+00 3.61514E+00  BASIC    3.615E+00:L
   5   ..   ..  6.26980E-02 1.17063E-01  BASIC    1.117E+00:L
   6   ..   ..  1.16704E-01 9.42359E-03  BASIC    9.414E-03:L
   7   ..   ..  4.30339E-02 7.06780E-04  BASIC    7.068E-04:L
   8   ..   ..  6.26980E-02 1.15680E-01  BASIC    1.157E-01:L

 RUN STATISTICS

GRG2GRG2GRG2GRG2GRG2GRG2GRG2GRG2GRG2GRG2GRG2GRG2GRG2GRG2GRG2G
RG2GRG2GRG2GRG2

 NUMBER OF ONE DIMENSIONAL SEARCHES =     405
 NEWTON CALLS = 1266  NEWTON ITERATIONS = 1279  AVERAGE = .10E+01
 FUNCTION CALLS = 2543  GRADIENT CALLS =   406
 ACTUAL FUNCTION CALLS (INC,FOR GRADIENT) =    5791
 NUMBER OF TIMES BASIC VARIABLE VIOLATED A BOUND =      4
 NUMBER OF TIMES NEWTON FAILED TO CONVERGE =   657
 TIMES STEPSIZE CUT BACK DUE TO NEWTON FAILURE =   608
```

3.3 Extremum Behavior and Sufficient Condition for Stability

For elucidating the stability of particle-fluid two-phase flow and understanding its general characteristics, extensive calculation was carried out to identify the extrema of different parameters, revealing the following two important aspects.

3.3.1 Extremum Behavior

Both analytical and numerical solutions show that extremum for N_{st} correspond to extremum for ε. That is, if ε is taken to be the objective function in optimization, the same results would be reached as with N_{st}, or vice versa. Therefore, in the PFC regime for which both N_{st} =min and ε =min, maximal pressure gradient is expected from the relation $\Delta P = (1-\varepsilon)\rho_p \cdot g$, and for the contrary case of the FD regime, for which ε =max, minimal pressure gradient. Figure 3-1a, calculated from Model LG (Yan *et al.*, 1993), shows the dependence of N_{st} and ε on flow structure and their relationships, indicating that N_{st} is maximized when a uniform single-phase structure at points B and B', characterized by $\varepsilon = \varepsilon_c = \varepsilon_f = \varepsilon_{max} = 0.975$, prevails in the system, but is minimized in the case of a two-phase structure at points A and A', for which $\varepsilon_c = (\varepsilon_c)_{min} = \varepsilon_{mf} = 0.5$ and $\varepsilon_f = (\varepsilon_f)_{max} \rightarrow 1.0$, leading to minimal average voidage ε_{min}, as shown in Figure 3-1b.

More extensive calculations, summarized in Figure 3-2 (Yan *et al.*, 1993; Li *et al.*, 1993), show similar extremum characteristics of the dependent parameters, and energy consumptions, N and W, for any specified operating conditions, U_g and G_s. This figure indicates that for a stable system all the parameters tend toward either minimum or maximum, depending on whether the prevailing regime is PFC or FD, except for $W_t = \frac{\rho_p - \rho_f}{\rho_p} G_s g$ and $N_T = \frac{\rho_p - \rho_f}{\rho_p} U_g g$ which depend solely on operating conditions. These extrema can be used for substituting N_{st} as the objective function in solving Model LG, as was verified by calculation (Yan, 1993). As soon as one parameter is changed, corresponding changes take place with all other parameters to reach a new extremal state. This explains why the two-phase structure can be preserved though intensive turbulent fluctuations exist in the system.

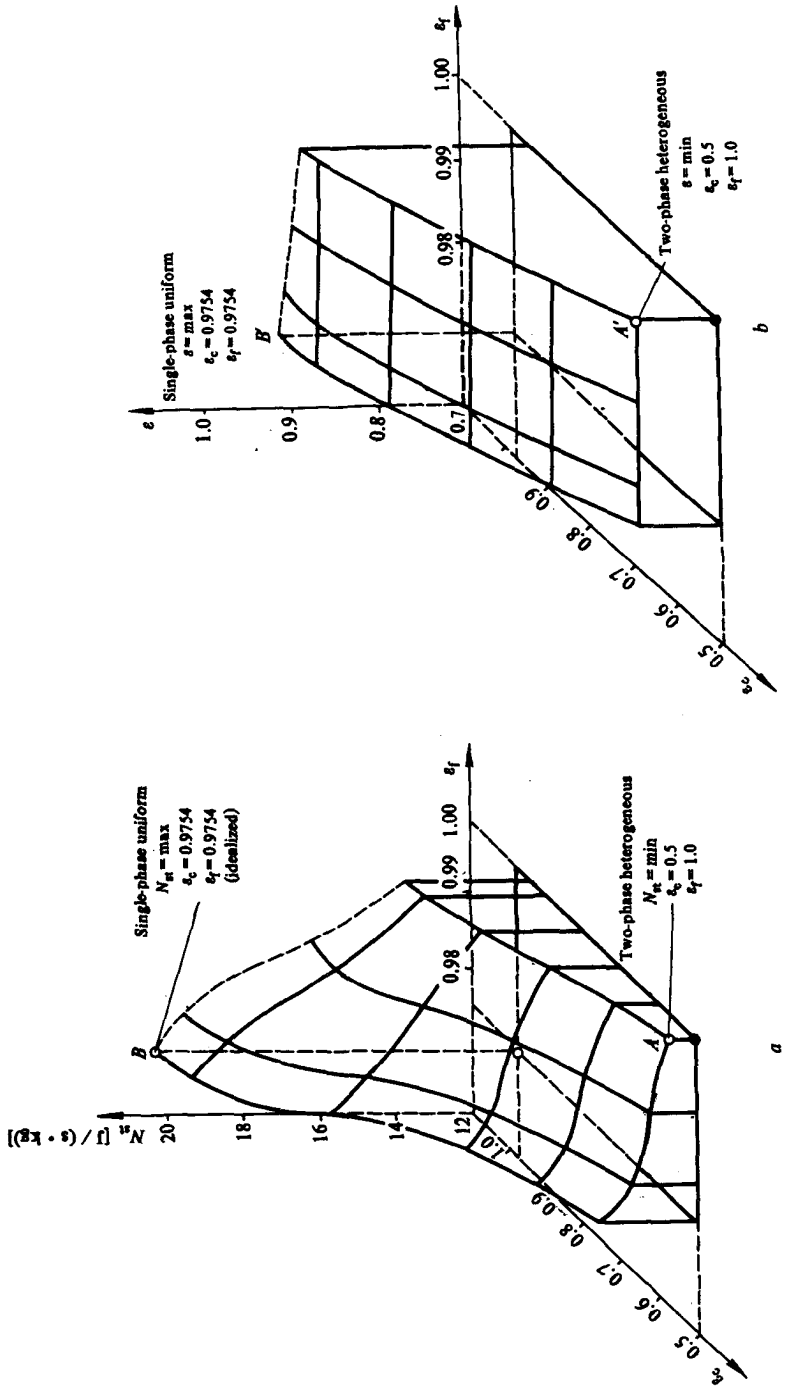

Figure 3-1 Dependence of N_{st} on Flow Structure ($U_g = 2.2$ m/s, $G_s = 50$ kg/m$^2 \cdot$ s)
a — $N_{st} \sim \varepsilon_c \sim \varepsilon_f$; b — $\varepsilon \sim \varepsilon_c \sim \varepsilon_f$

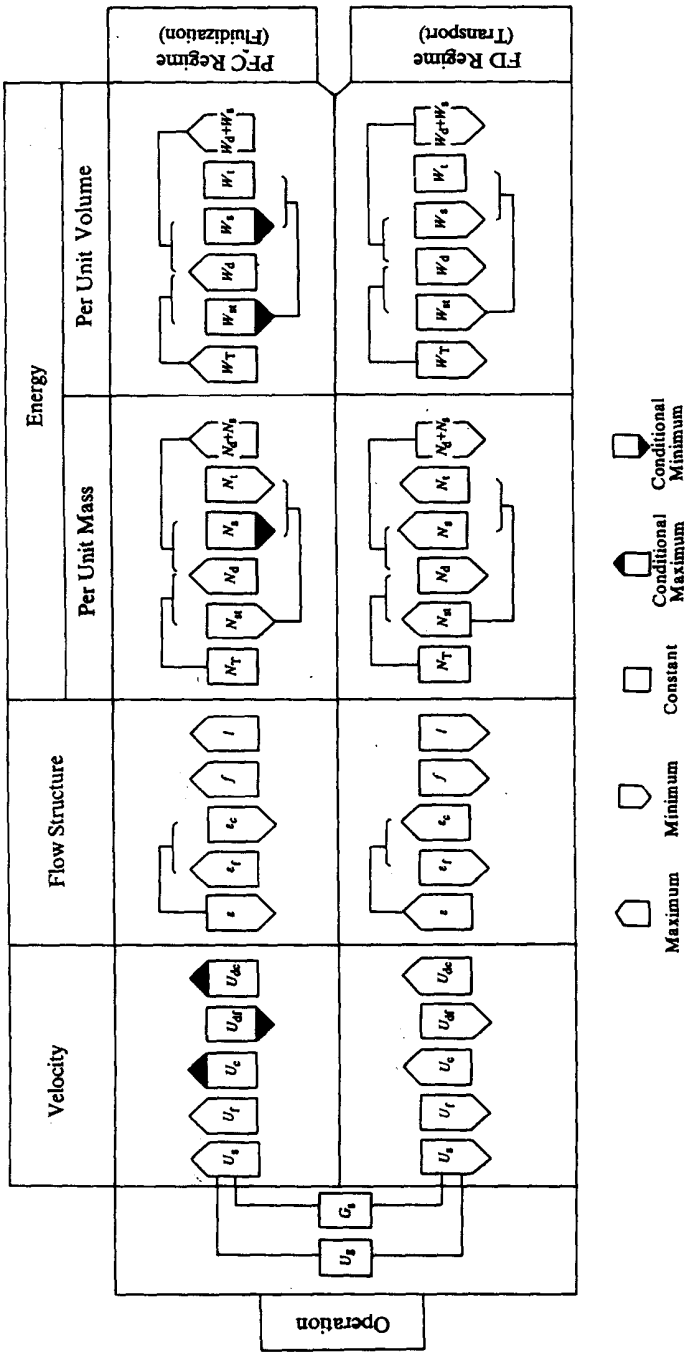

Figure 3-2 Extremum Characteristics of Flow Structure and Energy

Figure 3-2 also shows certain necessary relationships between these extremal variables. Take the PFC regime for example: since N_T =constant as long as U_g is specified, N_{st} =min, which naturally corresponds to N_d =max according to the first of the simple relations in Section 2.2:

$$N_T = N_{st} + N_d$$

$$= N_t + N_s + N_d$$

It has been shown (Yan, 1993) that when N_{st} =min, N_t =min, which, according to the second of the above relations, leads to $N_d + N_s$ =max.

Similar relationships hold with respect to W, from which the correspondence of the extrema of ε, U_s and ΔP can also be deduced.

We see, in particular, that N_{st} and N_d tend toward opposite extrema in both regimes. Thus, by resolving a heterogeneous system into the ST and ED subsystems, the non-extremal and flow-structure-independent total energy N_T is partitioned into two extremal and flow-structure-dependent components N_{st} and N_d, thus separating the analyzable energy component N_{st} from N_d which is difficult to formulate, and making the overall heterogeneous system analyzable. It should be realized that resolution of the total energy consumption N_T into the two extremal components N_t and $(N_d + N_s)$ is also feasible.

It is evident that particle-fluid two-phase flow is characterized by nonequilibrium features due to the existing dissipative processes in the system. However, the difference between the nonequilibrium behaviors for the FD and the PFC regimes has not been noted previously, which is essential in analyzing the stability and flow structure of the system.

In fact, $N_d + N_s$ is the total dissipated energy corresponding to the entropy production rate defined by Nicolis and Prigogine (1977). Therefore, from Figure 3-2, we know that the entropy production rate in the FD regime tends toward a minimum, while the PFC regime stabilizes at maximum dissipative energy ($N_d + N_s$ = max) corresponding to maximum entropy production rate, characterized by nonlinearity and nonequilibrium with an ordered two-phase dissipative structure relating

to self-organization of particles.

Therefore, we know that the theorem of minimum entropy production in thermodynamics (Prigogine, 1967; Li, 1984) might be applied to the FD regime of particle-fluid two-phase flow, as used by Gidaspow (1978) and Zhou (1985), but not to the PFC regime. The PD/PFC and the PFC/FD transitions are related to the bifurcation phenomenon in thermodynamics, and need to be explored further.

It seems that particle-fluid two-phase flow is dominated by its extremum behavior leading to the ordered structure, which is however disturbed by the inherent turbulence of the flowing fluid and the generated turbulence in particle-fluid interaction inducing the disordered change in flow structure. Therefore, future research should be focused not only on the ordered aspect but also on the disordered aspect of the system and their coupling.

3.3.2 Sufficient Conditions for Stability

Inasmuch as the PFC regime and the FD regime need to satisfy N_{st} =min and N_{st} =max respectively, Model LG alone is still not sufficient for identifying whether the PFC regime or the FD regime would prevail in a system at any specified U_g and G_s. An additional condition is needed for identifying the stable regime. At the end of Section 2.5, this sufficient condition was defined as the equality of W_{st} calculated from both these regimes, as can be elucidated further by referring to Figure 3-2. Figure 3-2 shows that in the PFC regime N_{st} is minimized with a corresponding W_{st} minimized only *conditionally* (constrained by $\varepsilon_c = \varepsilon_{mf}$), compared to W_{st} =min *unconditionally* in the FD regime, which corresponds, however, to N_{st} =max.

Figure 3-3 shows the changes of W_{st} calculated with respect to N_{st} =min for the PFC regime and to N_{st} =max for the FD regime, respectively. The two curves cross each other at point B

$$(W_{st})_{(N_{st})_{min}} = (W_{st})_{(N_{st})_{max}}|_{\varepsilon_c=\varepsilon_{mf}}$$

which defines the critical condition for breaking up the two-phase structure of dense fluidization into a uniform structure of dilute transport (Li *et al.*, 1992). Combined with this condition, Model LG can be solved for providing a comprehensive understanding of local fluid dynamics of particle-fluid two-phase flow.

In the early stage of solving the EMMS model, the dilute transport regime was assumed to be uniform and the transition from the PFC regime to the FD regime was roughly determined by the jump of $(N_{st})_{min}$

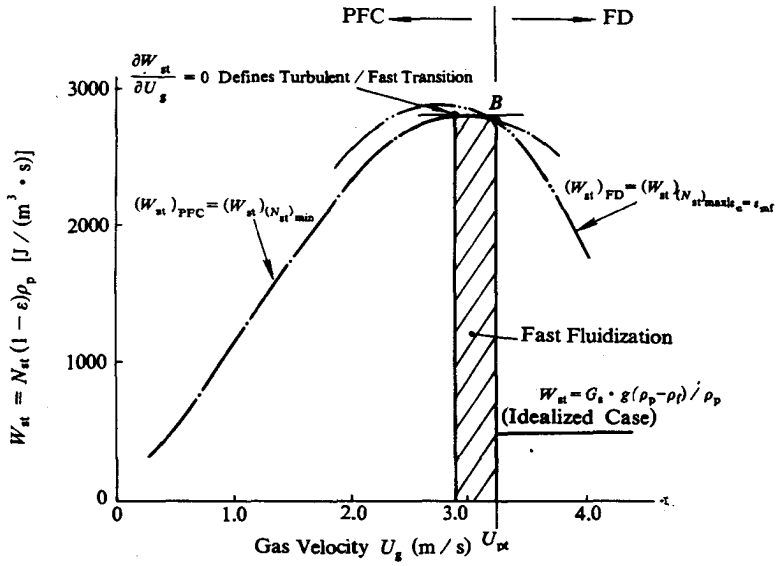

Figure 3-3 Definition of Saturation Carrying Capacity and Transition from PFC to FD Regime (system FCC/air)

from a low value for the heterogeneous structure to a high value for the uniform structure. The location of this jump on the gas velocity axis depends, to a great extent, on the convergence of computation which was often imprecise, thus leaving a range of uncertainty, as shown in Figure 3-4. Such a deficiency is now made up by considering the sufficient conditions for stability (Li *et al.*, 1992), that is, defining the intersection point B in Figure 3-3.

In fact, the PFC/FD transition is also characterized by undifferential points for $(W_{st})_{min}|_{\varepsilon_c=\varepsilon_{mf}}$, $(\frac{W_{st}}{\varepsilon\rho_f})_{min}|_{\varepsilon_c=\varepsilon_{mf}}$ and $(\frac{W_{st}}{\varepsilon\rho_f})_{max}$, as shown in Figure 3-5.

Therefore, the sufficient conditions for the PFC and the FD regimes can be summarized, according to Figure 3-3, as follows

Regime	Sufficient condition for stability
PFC	N_{st} =min; $(W_{st})_{(N_{st})_{min}} < (W_{st})_{(N_{st})_{max}|_{\varepsilon_c=\varepsilon_{mf}}}$
FD	N_{st} =max; $(W_{st})_{(N_{st})_{min}} > (W_{st})_{(N_{st})_{max}|_{\varepsilon_c=\varepsilon_{mf}}}$

Figure 3-6 provides a summary of the extrema of the different energy terms—W_{st}, N_{st} and $W_{st}/\varepsilon\rho_f$—in both the PFC and FD regimes and for the transition from the PFC to the FD regime.

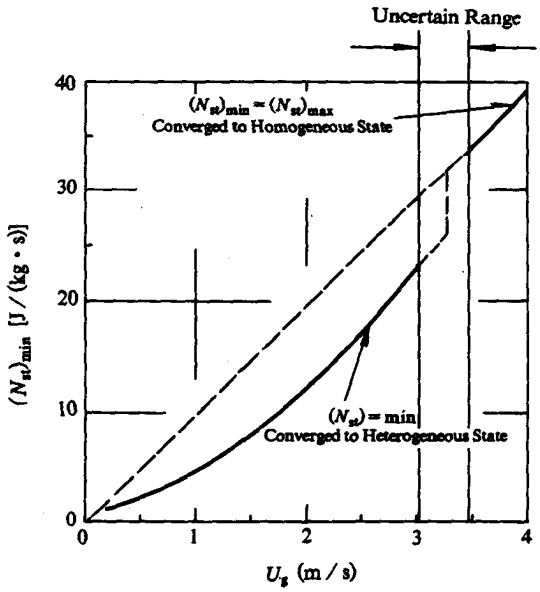

Figure 3-4 Uncertain Range of Convergence of $(N_{st})_{min}$

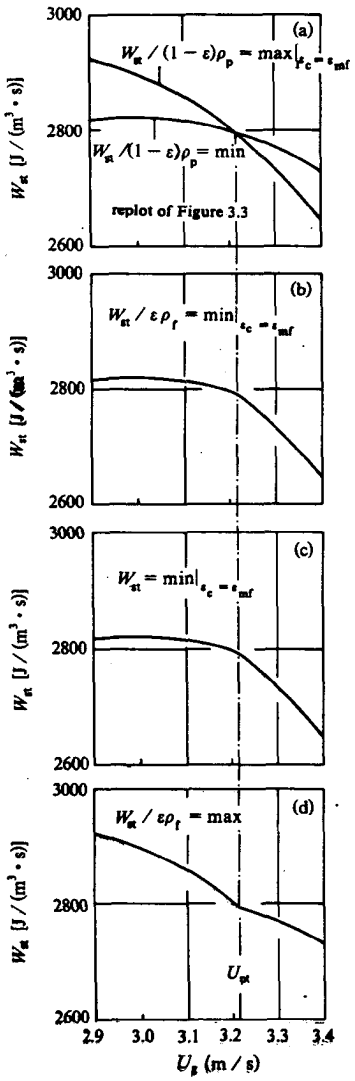

Figure 3-5 Alternative Definitions of K^* with Respect to Different Energy Terms (system FCC/air)

Energy	Characterization	PFC regime	PFC/FD Transition	FD regime	
				Nonidealized	Idealized
N_{st}	Particles	min	$(W_{st})_{(N_{st})_{min}} = (W_{st})_{(N_{st})_{max}}\|_{\varepsilon_c=\varepsilon_{mf}}$	$\max\|_{\varepsilon_c=\varepsilon_{mf}}$	min = max = $U_g g(\rho_p - \rho_f)/\rho_p$
W_{st}	Fluid	$\min\|_{\varepsilon_c=\varepsilon_{mf}}$	$(W_{st})_{min,U_{pt}^+} = (W_{st})_{min,U_{pt}^-}$ $\frac{\partial W_{st}}{\partial U_g}\|_{U_{pt}^+} \neq \frac{\partial W_{st}}{\partial U_g}\|_{U_{pt}^-}$	$\min\|_{\varepsilon_c=\varepsilon_{mf}}$	min
$\frac{W_{st}}{\varepsilon\rho_f}$	Fluid	$\min\|_{\varepsilon_c=\varepsilon_{mf}}$	$(\frac{W_{st}}{\varepsilon\rho_f})_{min,U_{pt}^+} = (\frac{W_{st}}{\varepsilon\rho_f})_{min,U_{pt}^-}$ $\frac{\partial(W_{st}/\varepsilon\rho_f)}{\partial U_g}\|_{U_{pt}^+} \neq \frac{\partial(W_{st}/\varepsilon\rho_f)}{\partial U_g}\|_{U_{pt}^-}$	$\min\|_{\varepsilon_c=\varepsilon_{mf}}$	min

Figure 3-6 Relationships between Extrema of Different Energy Terms

3.4 Local Fluid Dynamics—Phases

3.4.1 Fluid Dynamic States

With increasing fluid velocity, as shown in Figure 1-3, a particle-fluid system starts with the particle-dominated fixed bed terminating at U_{mf}, spans the particle-fluid-compromising regimes of particulate, bubbling, turbulent and fast fluidization, and finally becomes fluid-dominated at the so-called choking velocity U_{pt} with the onset of dilute transport. In actual reality, transport is yet possessed with vestigial heterogeneity which disappears however at U_{uni} while lapsing into idealized transport. Below U_{mf} and beyond U_{uni}, the particle-fluid two-phase flow is homogeneous, and therefore the traditional theories apply. In the range from U_{mf} to U_{uni}, Model LG has two solutions corresponding to (N_{st}) =min and (N_{st}) =max, of which only one, depending on conditions, is stable.

Model LG was solved by using the GRG-2 algorithm to illustrate the essential features of the local fluid dynamics of a typical particle-fluid system consisting of FCC particles (d_p = 54 μm, ρ_p = 929.5 kg/m^3) fluidized with air, in particular, the transition from the PFC to the FD regime. All computation results satisfy the Kuhn-Tucker condition.

Figure 3-7 shows the relationship between the saturation carrying capacity K^* and fluid velocity U_g, which defines the transition from the PFC regime to the FD regime, that is, from dense fluidization to dilute transport, as corroborated by the experimental points (the data at high velocities was transposed from Figure 4-31).

For instance, if the solids flow rate is specified at G_s = 50 kg/(m^2 · s), choking will takes place at U_g = 3.21 m/s for system FCC/air as indicated in the figure. Throughout the entire regime spectrum, only at this unique point (U_{pt}, K^*) both dense-phase fluidization and dilute-phase transport can coexist. At velocities higher than U_{pt}, only dilute transport can exist, shown as Mode FD in Figure 3-3; and at velocities lower than U_{pt}, only dense-phase fluidization can take place, shown as Mode PFC in Figure 3-3. The transition point at U_{pt} identifies the unique Mode PFC/FD on the curve of Figure 3-7 for the coexistence of both modes, the relative proportion of which depends on other external conditions such as the imposed pressure ΔP_{imp} as will be shown later.

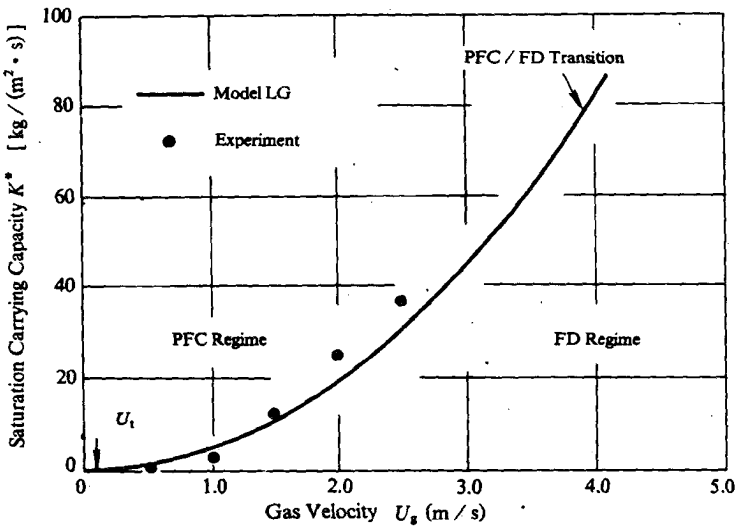

Figure 3-7 Definition of Saturation Carrying Capacity K^* and Its Change with Gas Velocity (FCC/air)

Figure 3-8 shows the flow structures of the circulating fluidized bed (CFB) for all the above three operating modes. The curves in the lower diagram give computation results of $\varepsilon_f, \varepsilon_c$ and ε, while the operating conditions and flow structures are summarized at the top.

At gas velocities below U_{pt}, the system is stabilized at N_{st} =min, since $(W_{st})_{(N_{st})_{min}} < (W_{st})_{(N_{st})_{max}|\varepsilon_c=\varepsilon_{mf}}$. Therefore, Mode PFC prevails, showing a dense region only with an average voidage of ε_a, operating in the PFC regime at $G_s > K^*$ with a two-phase structure—a dense phase with voidage ε_c, which is close to ε_{mf}, and a dilute phase with voidage ε_f, which approaches unity. These characteristic voidages are shown as optical voidage measurements at the top of the figure. For Mode PFC, the external condition $\Delta P_{imp} \geq (1 - \varepsilon_a)\rho_p g H$ must be satisfied.

With increasing gas velocity, $(W_{st})_{(N_{st})_{min}}$ approaches $(W_{st})_{(N_{st})_{max}|\varepsilon_c=\varepsilon_{mf}}$ gradually, and reaches it finally at U_{pt}, corresponding to $G_s = K^*$, that is, $(W_{st})_{(N_{st})_{min}} = (W_{st})_{(N_{st})_{max}|\varepsilon_c=\varepsilon_{mf}}$, implying that both the PFC regime and FD regime are stable, that is, Mode PFC/FD, characterized

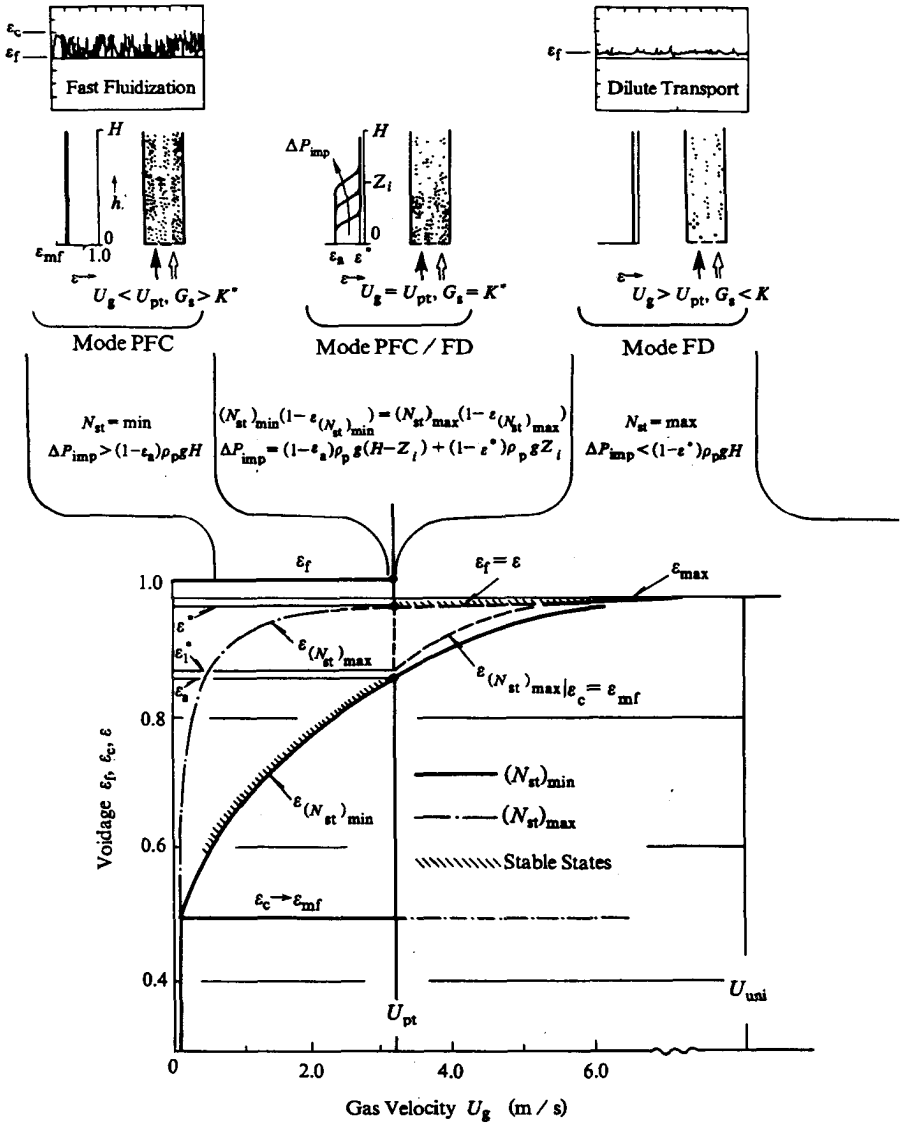

Figure 3-8 Calculation Showing Essential Aspects of Fluid Dynamics of Circulating Fluidized Beds (G_s = 50 kg/m^2 · s)

by the coexistence of these two regimes with a dense region at the bottom having average voidage ε_a and a dilute region at the top having average

voidage ε^* for the idealized case, or ε_1^* for real nonidealized cases with some degree of particle aggregation. Mode PFC/FD shows an S-shaped axial voidage profile with an inflection point Z_i, which changes with ΔP_{imp} in the range from $(1-\varepsilon^*)\rho_p g H$ to $(1-\varepsilon_a)\rho_p g H$, and is stabilized at $\Delta P_{imp} = (1-\varepsilon^*)\rho_p g(H - Z_i) + (1-\varepsilon_a)\rho_p g Z_i$. In real units, Mode PFC/FD sometimes may not appear due to limited vessel height.

Beyond U_{pt}, the FD regime replaces the PFC regime which becomes unstable at $G_s < K^*$, resulting in Mode FD, showing a dilute region only, and characterized by N_{st} =max and $\Delta P_{imp} \leq (1-\varepsilon^*)\rho_p g H$. In this mode, the dilute phase voidage ε_f deviates from values close to unity as shown by calculated results and corroborated by optical measurements shown at the top of the figure. For the idealized case, a single-phase uniform structure prevails with $\varepsilon = \varepsilon_f$; but for any real case, a certain extent of particle aggregation exists, until, with increase in gas velocity it approaches the idealized homogeneous condition. Here, only two extreme cases can be calculated and discussed due to lack of understanding of the structure of clusters existing in any real nonidealized FD regime: one is the idealized case with uniform structure as discussed above, for which average voidage at the choking point jumps from ε_a to ε^*; the other is the case with the assumption of nonideality, that is, clusters still exist with voidage $\varepsilon_c = \varepsilon_{mf}$ as in the PFC regime. For the latter, the average voidage calculated from Model LG will change as shown by the dashed line for $\varepsilon_{(N_{st})_{max}|\varepsilon_c=\varepsilon_{mf}}$, and the voidage at the choking point would jump from ε_a to ε_1^*. The structural difference of particle aggregates between Mode PFC and Mode FD (much smaller for FD) warrants further study.

For Mode PFC and Mode FD, any change in ΔP_{imp} certainly causes variation of solid flow rate G_s, and hence, local voidage in the whole unit, while in Mode PFC/FD it only affects the location of the inflection point Z_i.

As soon as gas velocity reaches U_{uni}, the corresponding bed voidage ε reaches ε_{max} at which the particle concentration is so low that clusters can no longer exist, particles are dispersed discretely and the system becomes really uniform. At this point, the two solutions characterized by $(N_{st})_{max}$ and $(N_{st})_{min}$ approach each other, and idealized transport prevails.

Figure 3-9 shows the computed results for the local fluid dynamic states

of the system FCC/air to illustrate the change of the status parameters with gas flow rate U_g for two solids rates $G_s = 50$ and 75 kg/(m^2 · s).

Figure 3-9a shows that the voidages for the dense cluster phase and the surrounding dilute phase remain essentially constant at $\varepsilon_c \rightarrow \varepsilon_{mf} = 0.5$ and $\varepsilon_f \rightarrow 1.0$, respectively, indicating that stability calls for this heterogeneity of the coexistence of the two phases, which leads to bubbling at low gas velocities and clustering at high gas velocities.

As gas velocity U_g increases, the average voidage ε in Figure 3-9a increases while the cluster fraction f in Figure 3-9c decreases, until at some gas velocity a sudden change takes place with f dropping to zero for the idealized case, denoting the disappearance of the cluster phase. At this point single-phase solids transport begins to take over the two-phase structure which has hitherto existed, with a new voidage of ε^* as Figure 3-9a shows, from which the average voidage increases gradually with further increase in gas velocity.

Figure 3-8 has already shown that only at this singular point of sudden change two regions can coexist in a reactor, a dilute transport region with voidage ε^* surmounting a dense region with voidage ε_a, such as is the case for the S-shaped voidage distribution curve in fast fluidization shown for Mode PFC/FD. The position of the point of inflection in this S-shaped curve can vary and is determined by the imposed pressure ΔP_{imp} across the fast fluidized bed, or the solids inventory of the entire circulating fluid-bed system (Weinstein *et al.*, 1983), as explained in connection with Figure 3-8. At gas velocities less than that at this singular point, only one heterogeneous region of a two-phase structure can exist, and at gas velocities greater than that at this singular point, only a single-phase region for transport can exist.

Figure 3-9b shows that before this sudden change, in the PFC regime, the slip velocity U_s between solid particles and the fluid is far greater than the terminal velocity U_t of the particles. After this sudden jump, in the FD regime, however, U_s drops to a much lower value close to U_t as one approaches the idealized case. However, for nonidealized cases, U_s in the FD regime is still somewhat higher than U_t due to residual particle aggregation, as will be shown experimentally in Figure 4-24.

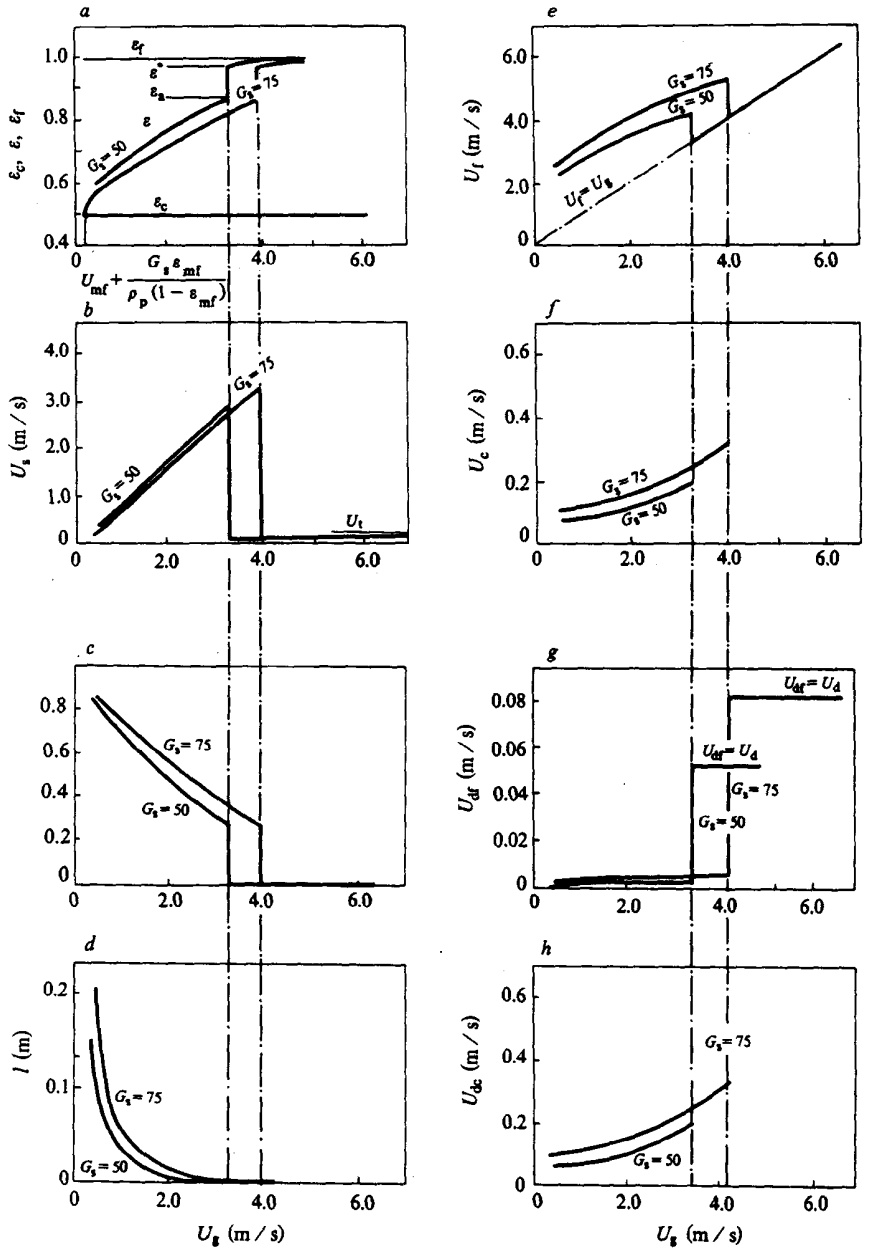

Figure 3-9 Computation Results of Changes of Parameters with Gas Velocity (system FCC/air)

Figure 3-9d shows that the dimension of clusters l is large at low gas velocities (down to dense phase continuous for bubbling fluidization), decreasing with gas velocity down to d_p at the point of this sudden change, at which clusters disappear as noted already.

Figure 3-9e shows that gas velocity in the dilute phase U_f increases with the entering gas velocity U_g until it drops at the point of sudden change when clusters disappear, to a value identical to that of U_g. Figure 3-9f shows that gas velocity in the dense cluster phase U_c, which is approximately an order of magnitude smaller than the dilute phase velocity U_f, also increases with the entering gas velocity U_g until U_c terminates with the disappearance of clusters at the point of sudden change.

Figure 3-9g shows that solids velocity U_{df} in the dilute phase is small when clusters exist, implying that major solids flow occurs through the clusters, only to jump to a high value at the point of sudden change. Figure 3-9h indicates that solids velocity U_{dc} in the dense cluster phase increases steadily with the entering gas velocity U_g, and terminates at the point when clusters stop to exist all of a sudden.

The dominant mechanism of particle aggregation is related to the stability of the system: in the PD regime, particles are held together by gravity; in the PFC regime, the fluid and the particles compromise each other to seek an energy-minimized state, resulting in the aggregation of particles to form a two-phase structure; in the FD regime, the high fluid velocity works against this tendency of particle aggregation, thus disrupting the two-phase structure, with a dramatic drop in cluster diameter l.

3.4.2 Meso-Heterogeneity

The two-phase structure in a particle-fluid system is a localized meso-scale phenomenon of heterogeneity, and has been shown to result from the tendency of the system to seek a minimal energy for suspending and transporting the particles, N_{st} =min. Figure 3-10 shows that if the particle-fluid system were uniform, N_{st} would be $\frac{\rho_p-\rho_f}{\rho_p}U_g g$, which is higher than the corresponding N_{st} for the heterogeneous structure composed of the sum of $(N_{st})_{dense}$ for the dense phase, and $(N_{st})_{dilute}$ + $(N_{st})_{inter}$ for the dilute and inter phases. The lower value of N_{st} for

the heterogeneous structure is due to the low value of the $(N_{st})_{dense}$ component as shown in the lowest curve in Figure 3-10. Section 2.2 on energy analysis already indicated that changes in ε_c and ε_f affect $(N_{st})_{dense}$ and $(N_{st})_{dilute}$, and hence N_{st} considerably. It was shown that N_{st} increases with increase in ε_c and decrease in ε_f. Therefore, in minimizing N_{st}, ε_c tends toward the minimal value of ε_{mf} and ε_f towards the maximal value of unity, as shown in Figure 3-8 for the PFC regime.

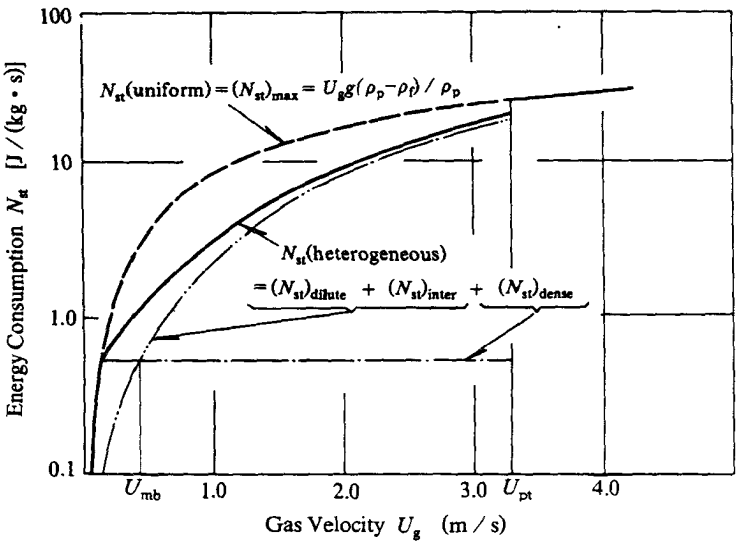

Figure 3-10 Mechanism of Local Heterogeneity in Gas/Solid Fluidization (FCC/air, G_s = 50 kg/(m^2 · s))

3.5 Effect of Operating Conditions—Regimes

Not only the phase structure for particle-fluid flow, but also the configuration of phase combination depends on operating conditions. A regime defines the range of operating conditions within which the principal features of any particular configuration of phase combination are preserved. Crossing this range, a different configuration appears and a regime transition is said to have taken place. Regime-related characteristics of particle-fluid systems are of fundamental importance to the design, operation and optimization of industrial processes.

3.5.1 Energy Transport

Regime transitions are related to energy transport in particle-fluid systems which is determined by operating conditions. Figure 3-11 shows the disbursement of energy consumptions, calculated by using Model LG of Section 2.5: N_T per unit mass of solids and W_T per unit volume of the system, versus fluid velocity U_g and solid flow rate G_s, indicating that the contributions due to suspension, N_s or W_s, and due to dissipation, N_d or W_d, are considerable except for dilute-phase transport and near minimum fluidization, while that due to transport, N_t or W_t, is minimal. The $N_{st} \sim U_g$ diagram suggests that dense-phase pneumatic transport at low gas velocities would be economic, indicating further that the efficiency of pneumatic transport could be increased by suppressing the heterogeneity in the system. In fact, the total dissipated energy should be $N_s + N_d$ or $W_s + W_d$, though N_s (or W_s) is dissipated differently from N_d (or W_d), that is, in retaining the potential energy of the particles by keeping the system expanded. In dilute transport, however, N_{st} is mainly attributable to N_t and is very close to N_T, meaning that $N_d + N_s$ is negligible due to the isolated movement of the discretely dispersed particles, for which the slip velocity between the fluid and particles is very low.

3.5.2 Regime Transition

Among the various components of energy consumption discussed above, N_{st} characterizes the stability of a particle-fluid system and governs the regime transitions PD/PFC and PFC/FD, which occur at undifferentiable points of N_{st} with respect to U_g, as shown in Figure 3-10. The term W_{st} can be used for distinguishing subregime transitions bubbling/turbulent and turbulent/fast, corresponding to extrema of W_{st} with respect to G_s as shown in Figure 3-12, and with respect to U_g as shown in Figure 3-3.

Calculated curves shown in Figure 3-12 indicate that W_{st} reaches a maximal value at $(\partial W_{st}/\partial G_s) = 0$ corresponding to a common dense phase fraction of $f = 0.5$, regardless of gas velocity and solid flow rate. At

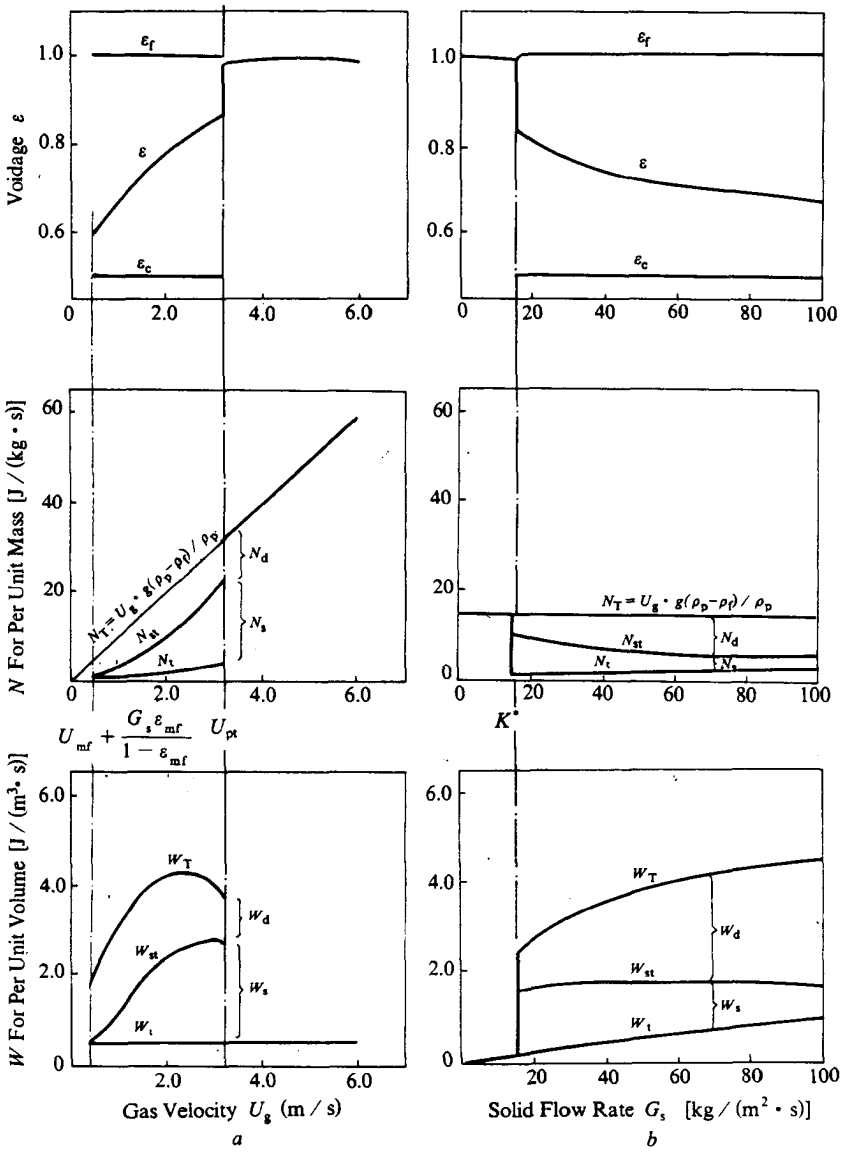

Figure 3-11 Disbursement of Energy Consumptions versus Fluid Velocity and Solids Flow Rate (FCC/air)
a — versus fluid velocity ($G_s = 50$ kg/(m^2 · s))
b — versus solids flow rate ($U_g = 1.5$ m/s)

$f = 0.5$, it is obvious that the dense phase fraction is equal to the dilute phase fraction, and it is hard to identify which phase is the continu-

ous one. In other words, a phase inversion from dense-phase continuous to dilute-phase continuous is taking place, and the system can be considered to have reached a state of maximum heterogeneity. This can be construed to mark the transition from bubbling to turbulent fluidization as suggested by Grace (1985).

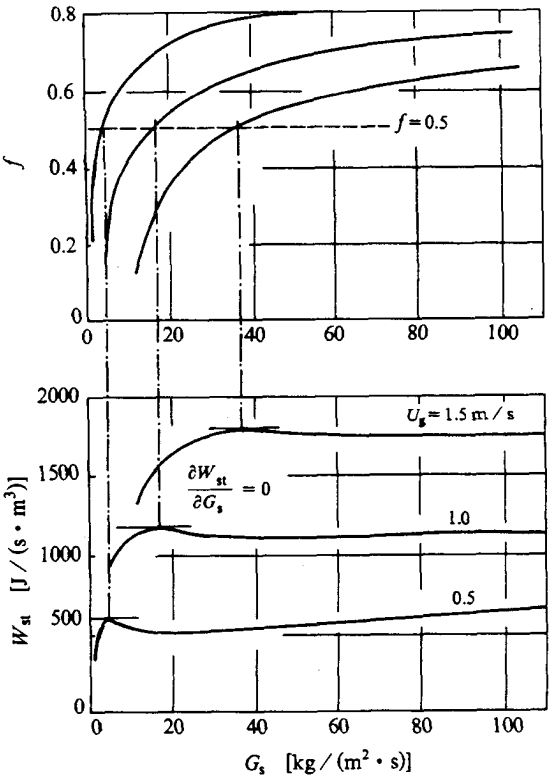

Figure 3-12 Bubbling/Turbulent Transition: Correspondence between $f = 0.5$ and $\frac{\partial W_{st}}{\partial G_s}$

As discussed in Section 3.3, local or meso-heterogeneity is attributed to any difference in value between $(N_{st})_{dense}$ and $(N_{st})_{dilute} + (N_{st})_{inter}$. Their equality, as shown by their intersection at U_{mb} in Figure 3-10, can therefore be considered to imply a transition from a uniform structure to a heterogeneous structure, that is, a regime transition from particulate to bubbling fluidization.

Particle-Dominated PD-Regime—Fixed bed

The particle-dominating PD-regime, that is the fixed bed, which is generally operated at fluid velocities ranging from zero to U_{mf} (unless the particles are externally constrained), is characterized by the dominance of particles over the movement of fluid, in which both the pressure drop generated by the flowing fluid ΔP and the energy consumption W_{st} tend toward minima as the fluid passes upward through the immobile particles in the most preferred way. With increasing fluid velocity, ΔP gradually approaches the weight of the particles, and finally at U_{mf} the particles are forced to start moving, thereby losing their dominance over the system by rearranging themselves to satisfy the requirement of the flowing fluid, that is, to reduce the resistance to fluid flow, thus resulting in the beginning of the PFC-regime.

A generally accepted criterion for this transition is

$$\Delta P = (1 - \varepsilon_{mf})(\rho_p - \rho_f)g$$

or

$$U_g = U_{mf} + \frac{G_s \varepsilon_{mf}}{(1 - \varepsilon_{mf})\rho_p}$$

The fluid dynamics of this regime is relatively simple.

Fluid-Particle-Compromising PFC-Regime—Fluidization

As soon as the particles start to surrender their immobile existence to the flowing fluid at U_{mf}, the stability of the system begins to be determined jointly by both the particles and the fluid. The particles and the fluid coordinate with each other in this new particle-fluid-compromising or PFC regime, as the latter continues to seek a path of least resistance and the former to aggregate as much as possible, to reach a state of minimal energy consumption for suspending and transporting the particles N_{st}. With increasing fluid velocity, the particle-fluid system continues to expand as it traverses the following series of subregimes.

PFC-Subregime 1: Uniform or Particulate This first subregime spans the fluid velocity range between the minimum fluidization velocity U_{mf} and the minimum bubbling velocity U_{mb}. Figure 3-10 shows that at U_{mb}, $(N_{st})_{dense} = (N_{st})_{dilute} + (N_{st})_{inter}$. At fluid velocities exceeding U_{mb}, $(N_{st})_{dense} < (N_{st})_{dilute} + (N_{st})_{inter}$, implying that segregation of some particles to form a dense phase would promote a reduction of N_{st}, thus resulting in a heterogeneous two-phase structure. As more particles aggregate, bubbles form to accommodate increased fluid flow. And therefore, formation of the two-phase structure at U_{mb} is characterized by the appearance of bubbles. Below U_{mb}, however, Figure 3-10a shows that $(N_{st})_{dense} > (N_{st})_{dilute} + (N_{st})_{inter}$, indicating that particles segregation into a separate dense phase would not lead to a decrease in N_{st}, and therefore the uniform one-phase structure would be stable. Thus, uniform expansion is possible even in the PFC regime so long as $U_{mb} > U_{mf}$.

PFC-Subregime 2: Bubbling The low-expansion PFC-regime at fluid velocities beyond U_{mb} is characterized by low-frequency bubbling (or slugging when the dimension of the retaining vessel is small) of the particle-fluid system with the coexistence of individual air-rich bubbles and a continuous particle-rich emulsion phase.

PFC-Subregime 3: Turbulent With increasing fluid velocity, bubbles grow larger with a corresponding decrease in the volume fraction of the emulsion phase f, until f goes down to $\frac{1}{2}$, at which, what may be called a phase inversion takes place as the continuous dense phase emulsion begins to break up into discrete particle clusters, which are now immersed in a newly formed continuous broth of dilute suspension of essentially discrete particles, to form a new subregime 3, called turbulent fluidization. Computation shown in Figure 3-12 indicates that this point of $f = \frac{1}{2}$ corresponds to a maximal value of W_{st} with respect to G_s, regardless of fluid velocity and solids flow rate. Therefore, the transition between PFC subregions 2 and 3, or between bubbling and turbulent fluidization can be identified quantitatively as

$$\frac{\partial W_{st}}{\partial G_s} = 0 \quad \text{or} \quad f = 0.5$$

PFC-Subregime 4: Fast With increasing fluid velocity, especially with the simultaneous withdrawal of solids at the top and their recirculation to the bottom of the particle-fluid system, W_{st} continues to increase until at higher solids dilution, it decreases, thus displaying a maximum as shown in Figure 3-3. This maximum of W_{st} with respect to fluid velocity marks the transition of the turbulent subregime into fast fluidization, and is defined by

$$\frac{\partial W_{st}}{\partial U_g} = 0.$$

The high frequency of cluster formation and dissolution in fast fluidization is reflected in high-frequency random voidage fluctuations as shown in the middle inset at the top of Figure 3-13. Such a change in two-phase behavior promotes efficient gas/solids contacting.

While the transition from turbulent to fast fluidization is mathematically definable as $\frac{\partial W_{st}}{\partial U_g} = 0$, in practice the differentiation between the two subregimes is actually hard to perceive, and, though controversial, turbulent and fast fluidization are often grouped together under the overall designation of "high-velocity fluidization" or "circulating fluid bed" (Reh, 1971).

When the upflowing fluid acquires enough momentum at U_{pt} to entrain all the particles at the saturation carrying solids flow rate of K^*, the heterogeneous two-phase structure breaks down altogether, and all of a sudden, fast fluidization is taken over by dilute-phase transport, essentially single-phase, with vestigial particles aggregation, however, for any real system. This marks the final transition of the PFC-regime into the FD-regime, as already discussed in Section 3.3.1, under the criterion

$$(W_{st})_{(N_{st})_{min}} = (W_{st})_{(N_{st})_{max}}|_{\varepsilon_c=\varepsilon_{mf}}$$

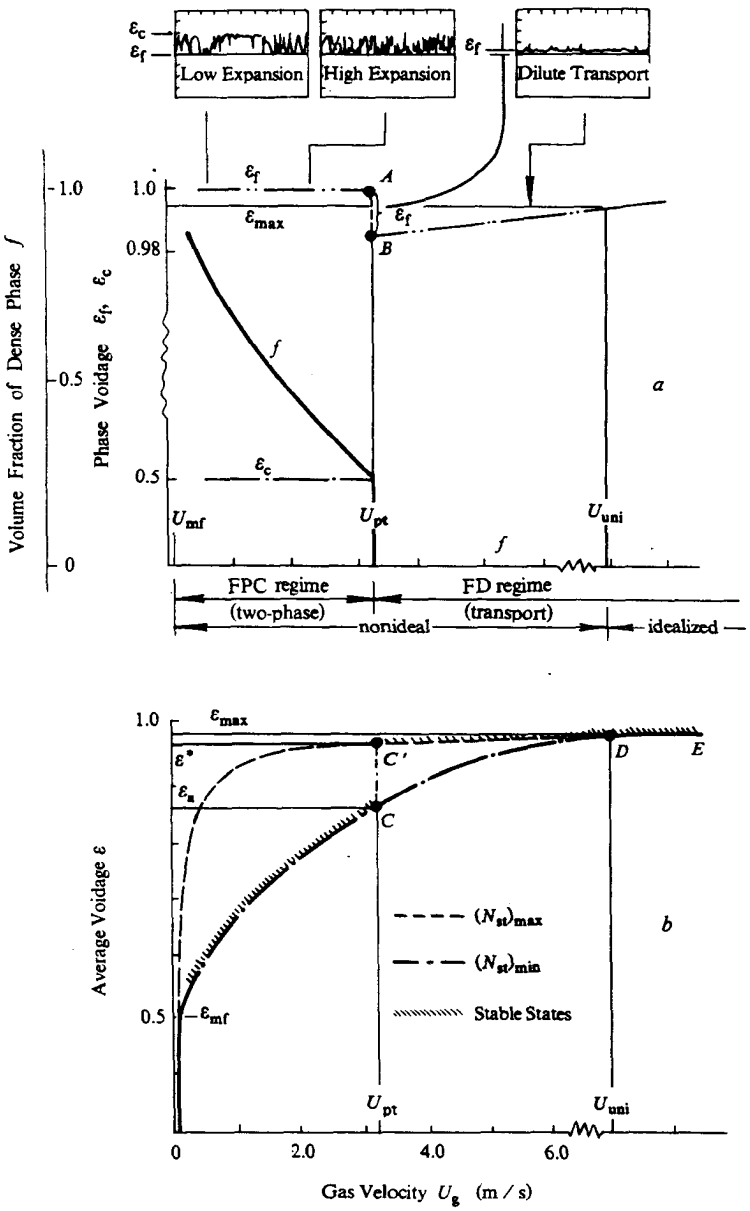

Figure 3-13 Flow Structures and State Characteristics of Gas/Solid Fluidization in Different Regimes (FCC/air, $G_s = 50\text{kg}/(\text{m}^2 \cdot \text{s})$)

Fluid-Dominated FD-Regime—Transport

The FD-regime is characterized by the dominance of the fluid over the movement of particles, as already shown in Figure 3-8. When the fluid-dominated FD-regime is first formed, the clusters of fast fluidization are disintegrated to form an essentially one-phase structure in which the particles are however not completely discretely suspended, that is, at a much higher concentration as compared to the ε_f computed for the broth before U_{pt}. This is shown by the fluctuating voidage considerably above zero, as can be seen in the upper right hand side of Figure 3-13. This essential change in ε_f is related to the dramatic change of flow structure at the choking point.

According to the degree of uniformity of the system, the fluid-dominated FD-regime can be divided into two subregimes: dilute transport for real systems and idealized dilute transport. the transition between the two subregimes occurring at the value of ε_{max} as defined in Section 2.3.

FD-Subregime 1: Actual Transport This subregime comprises the case for most actual systems right after the fluid velocity exceeds U_{pt}, in which vestigial particles aggregation is yet present, though the size of clusters is orders of magnitude smaller than those observable in fast fluidization. Therefore, meso-heterogeneity due to interparticle forces still persists until the voidage of the particle-fluid system reaches the value of ε_{max} at an even higher fluid velocity when all particles are dispersed to reach the idealized state of complete uniformity. Therefore, the termination of this subregimes can be identified by calculating ε_{max}, which will discussed in the next section.

FD-Subregime 2: Idealized Transport This regime is characterized by the complete dominance of the fluid over the particles with the total suppression of the effect of interparticle forces, thus realizing complete dispersal of solids and complete uniformity in the particle-fluid system.

The spectrum of regimes and subregimes for particle-fluid systems and their transitions as well as their principal characteristics are summarized in Figure 3-14.

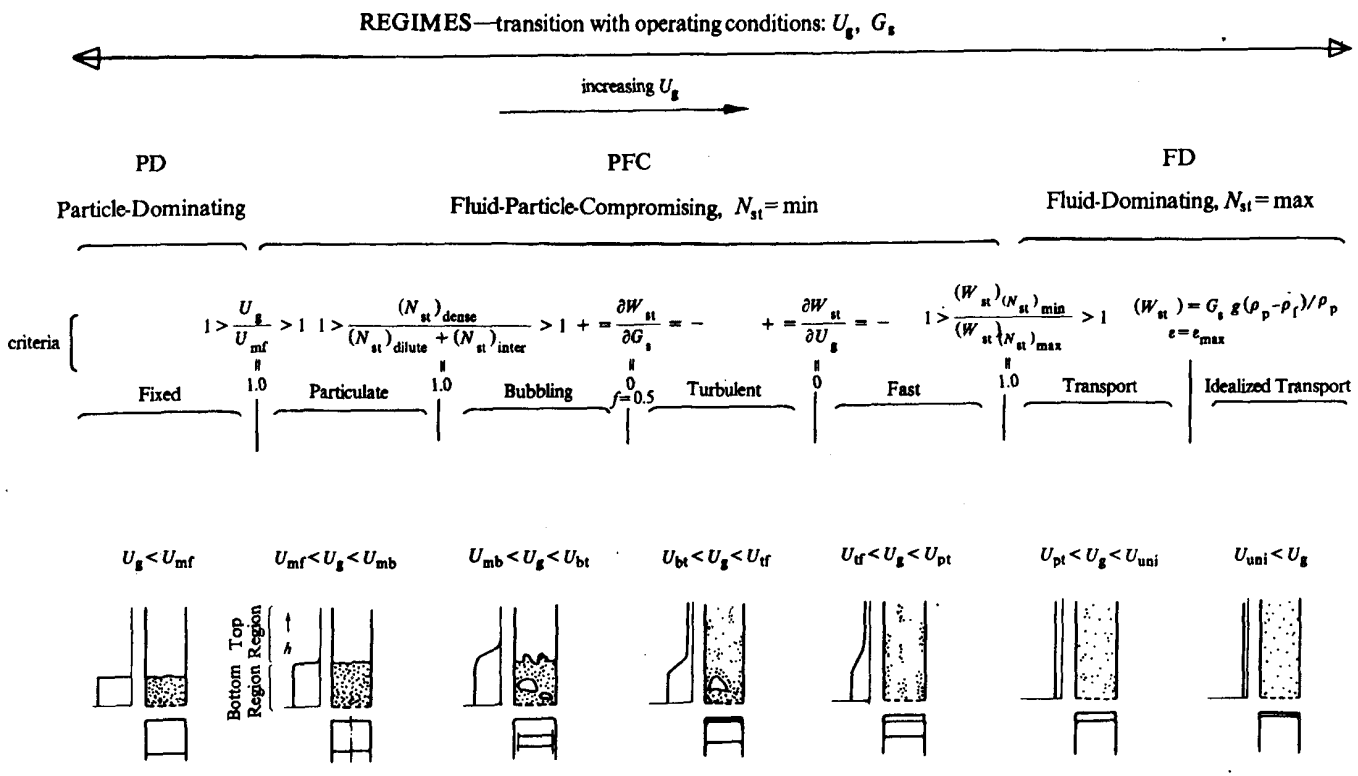

Figure 3-14 Outline of Complete Spectrum of Regime Transitions

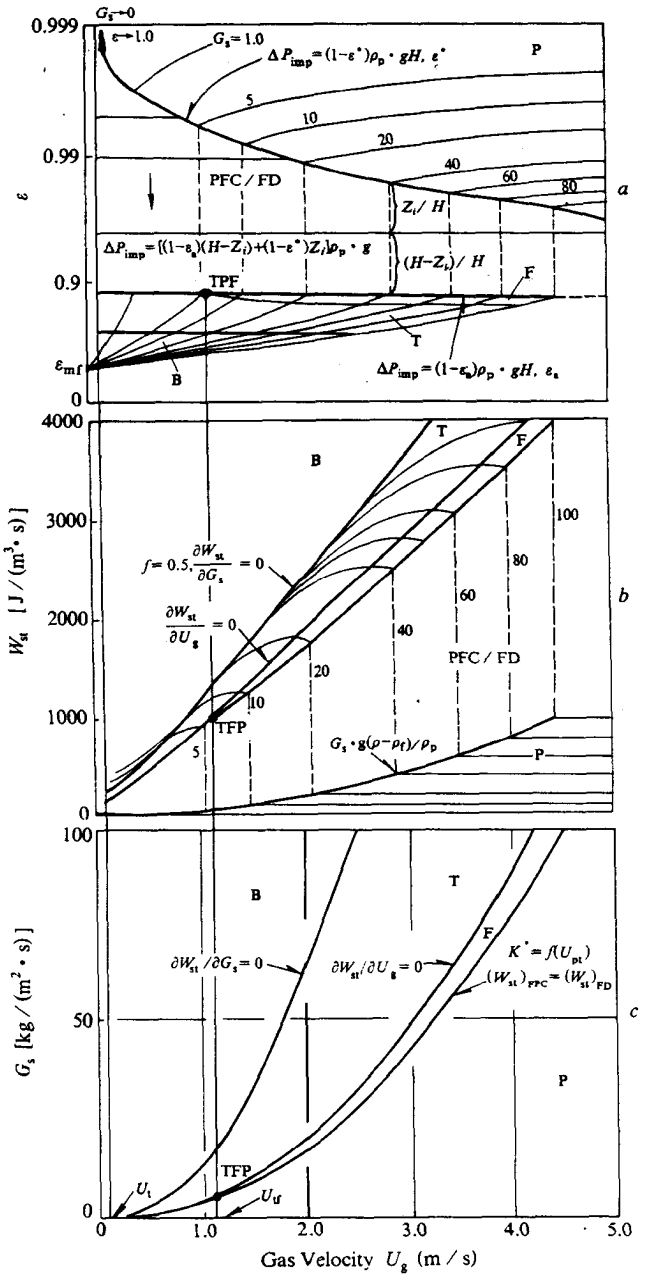

Figure 3-15 Regime Diagrams for Particle-Fluid Two-Phase Flow (FCC/air) (B — bubbling; T — turbulent; F — fast; P — transport)

Figure 3-15 shows still another version of calculated regime diagrams. Figure 3-15a is a two-dimensional $\varepsilon \sim U_g \sim G_s$ regime diagram. The partly cross-hatched, wedge-shaped region toward the top is the region for Mode PFC/FD, in which axial voidage profiles are S-shaped. The influence of imposed pressure drop ΔP_{imp} on the inflection point Z_i of an axial voidage profile is shown in this mode as a family of horizontal lines. This figure also shows relationships between other flow regimes. Figure 3-15b shows a two-dimensional $W_{st} \sim U_g \sim G_s$ regime diagram, indicating the boundary between the turbulent regime and the fast regime defined by $\frac{\partial W_{st}}{\partial U_g} = 0$, and the boundary between the bubbling regime and the turbulent regime defined by $\frac{\partial W_{st}}{\partial G_s} = 0$, as well as the jump of W_{st} from $(W_{st})_{PFC}$ to $G_s g$ at choking points. Figure 3-15c shows a two-dimensional $G_s \sim U_g$ regime diagram which represents the relations between G_s and U_g when regime transitions occur. If $U_g < U_t$, the system cannot operate in the *FD* regime, meaning that only one state can exist with a two-phase structure. Comparison between Figure 3-15a, Figure 3-15b and Figure 3-15c, shows that there is a triple point TFP below which turbulent fluidization transits directly to dilute-phase transport without passing through the fast regime.

3.6 Effect of Material Properties—Patterns

Dependence of local fluid dynamics of particle-fluid two-phase flow on material properties, e.g., density and viscosity of the fluid and density and size of the particles, results in different *patterns* of regime spectra, which are important to the design, development and operation of processes. The complete regime spectrum—*particulate-bubbling-turbulent-fast-transport*—is illustrated by the fluidization by gas of smooth, fine and well graded powders belonging to Geldart's Class A. The extreme aggregative degenerate of the regime spectrum is *bubbling-transport* for Geldart's D particles, and the extreme particulate degenerate is for relatively fine and uniform particles fluidized by a liquid—*particulate* fluidization only.

3.6.1 Particle Aggregation

The direct effect of the properties of the fluid and the particles on particle-fluid two-phase flow is the degree of particle aggregation which is reflected in the cluster diameter l. In Section 2.3, the cluster diameter l was considered to diminish to d_p when the voidage has increased to $\varepsilon_{max} = 0.9997$. This value was recommended by Matsen (1982) for the fluidization of fine particles by a gas, and can therefore be used for the FCC/air system.

In fact, ε_{max} depends not only on the properties of materials but also on operating conditions as well (Wu *et al.*, 1991; Chen *et al.*, 1994). For evaluating the variation of ε_{max} with material properties, a correlation has been developed on the basis of the following considerations: If the ratio of the frequency of particle-fluid interaction to the frequency of particle-particle interaction, f_f/f_p, is much high than unity, the particle-fluid system can be considered dilute, and the effect of particle-particle interactions can be neglected (Soo, 1984).

Wu *et al.* (1991) calculated f_p and f_f by using the following correlations developed from Soo's expressions of f_p and f_f (1984):

$$f_p = \frac{6\sqrt{2}\left\langle u_p^2\right\rangle^{\frac{1}{2}}(1-\varepsilon)}{d_p} \tag{3.1}$$

$$f_f = \frac{\rho_f}{\rho_p}\left(\frac{18\nu_f}{d_p^2} + \frac{2.7{\nu_f}^{0.313}{u_s}^{0.687}}{d_p^{1.313}}\right) \tag{3.2}$$

Therefore,

$$\frac{f_f}{f_p} = \frac{\rho_f}{\rho_p}\frac{1}{\sqrt{2}\left\langle u_p\right\rangle^{\frac{1}{2}}(1-\varepsilon)}\left(\frac{3\nu_f}{d_p} + \frac{0.45\nu_f^{0.313}u_s^{0.687}}{d_p^{0.313}}\right) \tag{3.3}$$

where the particle velocity fluctuation $\left\langle u_p^2\right\rangle^{\frac{1}{2}}$ is calculated according to Lee (1989) with the assumption of low particle concentration:

$$\left\langle u_p^2\right\rangle^{\frac{1}{2}} = \left\langle u_f^2\right\rangle^{\frac{1}{2}}\left(\frac{\beta T_{Lf}}{0.7+\beta T_{Lf}}\right)^{\frac{1}{2}}$$

where $\langle u_f^2 \rangle^{\frac{1}{2}}$ is the velocity fluctuation of the fluid, and

$$\beta = \frac{3C_{D_o}\rho_f}{4d_p\rho_p}\left(\langle u_f^2\rangle^{\frac{1}{2}} - \left\langle u_p^2\right\rangle^{\frac{1}{2}}\right)$$

$$C_{D_o} = \frac{24}{Re_B} + \frac{3.6}{Re_B^{0.313}}$$

$$Re_B = \frac{\left(\langle u_f^2\rangle^{\frac{1}{2}} - \langle u_p^2\rangle^{\frac{1}{2}}\right)d_p}{\nu_f}$$

$$T_{Lf} = \frac{0.037u^*d_B}{\langle u_f^2\rangle}$$

According to Hinze (1975),

$$\frac{\langle u_f^2\rangle^{\frac{1}{2}}}{u^*} \approx 1.1$$

$$\frac{u_f}{u^*} = 2.44ln\left(\frac{u^*d_B}{2\nu_f}\right) + 2.0$$

Thus, $\left\langle u_p^2\right\rangle^{\frac{1}{2}}$ can be evaluated. Equation 3.3 defines the relationship between ε and f_f/f_p. Then, Wu took $u_s \approx u_t$, and defined $\varepsilon(f_f/f_p = 1.0) = \varepsilon_{max}$. Chen *et al.* (1993) modified Wu's definition by analyzing the dependence of f_f/f_p on ε and deriving the expression of real slip velocity u_s. Assuming that the dissipated energy can be neglected in a dilute uniform suspension, we have

$$W_{st} = G_s \cdot g = U_g\Delta P = (\rho_p - \rho_f)(1-\varepsilon)\cdot gU_g$$

Since $G_s = U_d \cdot \rho_p$, we get

$$U_g = \frac{U_d\rho_p}{(\rho_p - \rho_f)(1-\varepsilon)}$$

Noting $u_f = U_g/\varepsilon$ and $u_p = U_d/(1-\varepsilon)$, we have

$$u_s = u_f - u_p = \frac{U_d}{(1-\varepsilon)}\left[\frac{\rho_p}{(\rho_p - \rho_f)\varepsilon} - 1\right]$$

With the above u_s and $\left\langle u_p^2\right\rangle^{\frac{1}{2}}$, the curve in Figure 3-16 can be computed from Equation 3.3, resulting in the asymptotic value of $\varepsilon_{max} = 0.9987$

as f_f/f_p tends to infinity.

Figure 3-16 for glass beads in CO_2 shows that at first f_f/f_p changes little with increasing voidage ε until ε reaches 0.9987 after which f_f/f_p increases dramatically with increasing ε, implying that particle/particle interaction is rapidly suppressed. This critical voidage ε_{max}, signifies the disappearance of particle/particle interaction, that is, particle aggregation can no longer exist.

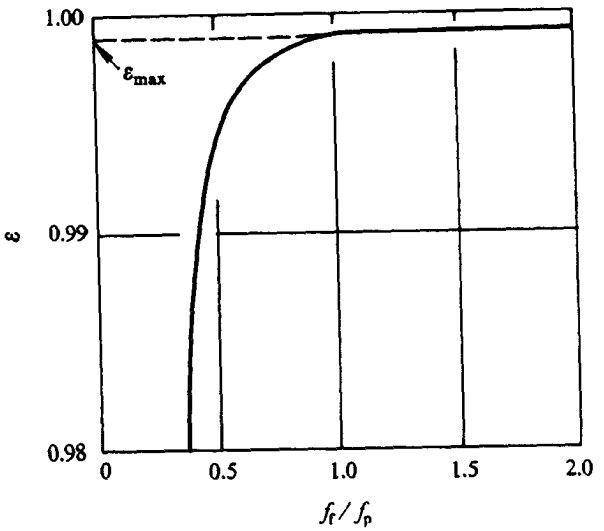

Figure 3-16 Change of f_f/f_p with Voidage and Definition of ε_{max} (system glass/CO_2: $\rho_p/\rho_f = 127.5$, $\nu_f = 10^{-6}$ m^2/s)

From the above analysis, it is evident that ε_{max} is dependent not only on density ratio as shown in Figure 3-17, but also on particle diameter as shown in Figure 3-18a, as well as on operating conditions (G_s) as shown in Figure 3-18b. Figure 3-17 shows the relationships between voidage ε and f_f/f_p for different ρ_p/ρ_f, indicating that ε_{max}, defined such as in the Figure 3-16, decreases with decreasing ρ_p/ρ_f.

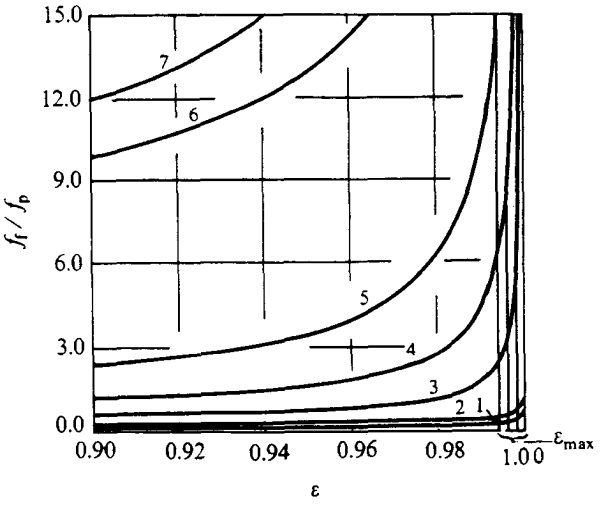

Figure 3-17 Dependence of f_f/f_p on Voidage ε and Density ratio ρ_p/ρ_f

curve	ρ_p/ρ_f	ν_f	system
1	2162	1.6×10^{-5} m^2/s	Glass/air
2	127.5	10^{-6} m^2/s	Glass/CO_2
3	12.75	9.5×10^{-8} m^2/s	Glass/CO_2
4	6.38	7.5×10^{-8} m^2/s	Glass/CO_2
5	3.64	8×10^{-8} m^2/s	Glass/CO_2
6	3.19	10^{-6} m^2/s	Glass/Ethylether
7	2.55	10^{-6} m^2/s	Glass/H_2O

With the value of ε_{max}, cluster diameter can be calculated from $F_6(\mathbf{X})$ in Chapter 3. Figure 3-19 shows the variation of calculated cluster diameters for the FCC/air system with gas velocity, indicating different mechanisms of particle aggregation in different regimes: packed in the PD regime due to the gravity, formation of emulsion and clusters in the PFC regime, and of particle aggregates due to vestigial interparticle forces in the FD regime. With the onset of dilute transport , the size of clusters is dramatically reduced because of the dwindling dominance of $(N_{st})_{min}$.

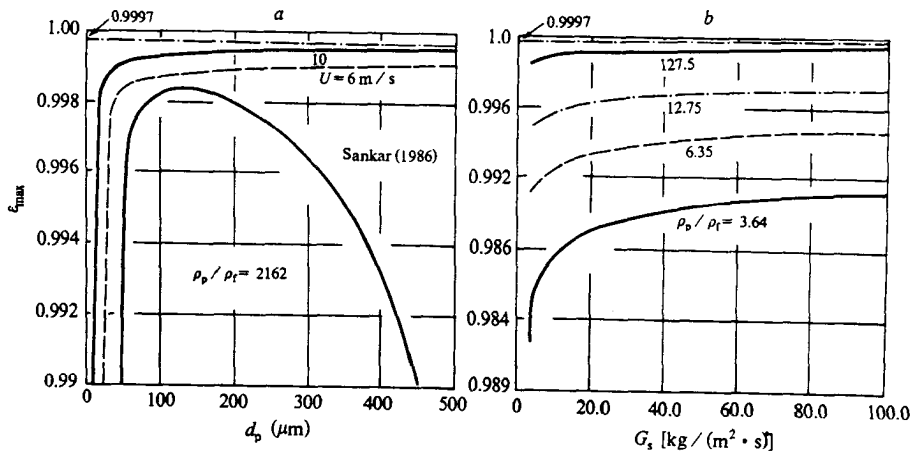

Figure 3-18 Dependence of ε_{max} on Particle Diameter and Solids Flow Rate
a — particle diameter ($\rho_p/\rho_f = 2162$);
b — solids flow rate ($U_g = 6$ m/s)

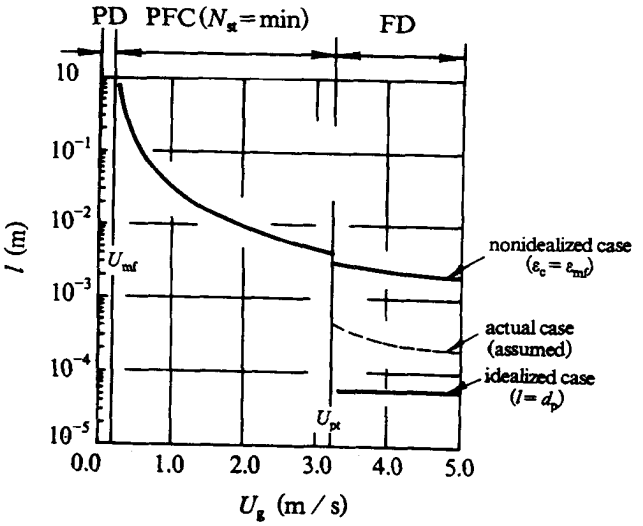

Figure 3-19 Cluster Diameter in Different Fluidization Regimes
(system FCC/air: $\rho_p/\rho_f = 788, \nu_f = 1.6 \times 10^{-5}$ m^2/s)

3.6.2 Density Ratio

Figure 3-20 compares the computed results for the FCC/air system against those for the glass/water system, to illustrate the disparate behaviors of G/S and L/S fluidization.

The first three insets on the lefthand side show the change of voidages, $\varepsilon_f, \varepsilon_c$ and ε, cluster phase fraction f and slip velocity U_s. The discontinuity at $U_g = 3.21$m/s should be noted for the sudden change corresponding to the condition of "choking," commonly recognized for G/S fluidization. In the corresponding insets for the L/S system, however, the three voidages $\varepsilon_f, \varepsilon_c$ and ε are identical, and the cluster phase fraction f is zero, indicating the absence of clusters throughout the velocity range of U_g, that is, fluidization is homogeneous. Also, the slip velocity U_s between solid particles and the surrounding liquid is always less than the terminal velocity U_t of the particles, which remains the asymptotic value for the increasing slip velocity U_s as the liquid velocity U_g increases.

The lowest two insets of Figure 3-20 compares the power for suspending and transporting the solid particles N_{st} for the G/S and L/S systems. For the FCC/air system, N_{st} is always less than the total energy $N_T = \frac{\rho_p - \rho_f}{\rho_f} U_g g$, until it jumps to the latter value at the point of sudden change of choking, while for glass/water, N_{st} is always the same as N_T in view of its homogeneous nature:

1. *no jump of parameters;*

2. *no two-phase structure, that is* $f = 0$*;*

3. U_s *is always lower than* U_t*, and close to* U_t *with increasing expansion of system;*

4. N_d *is negligible, implying that energy is mainly consumed for suspending and transporting particles;*

5. *the transition from the PFC to the FD regime takes place smoothly without choking*

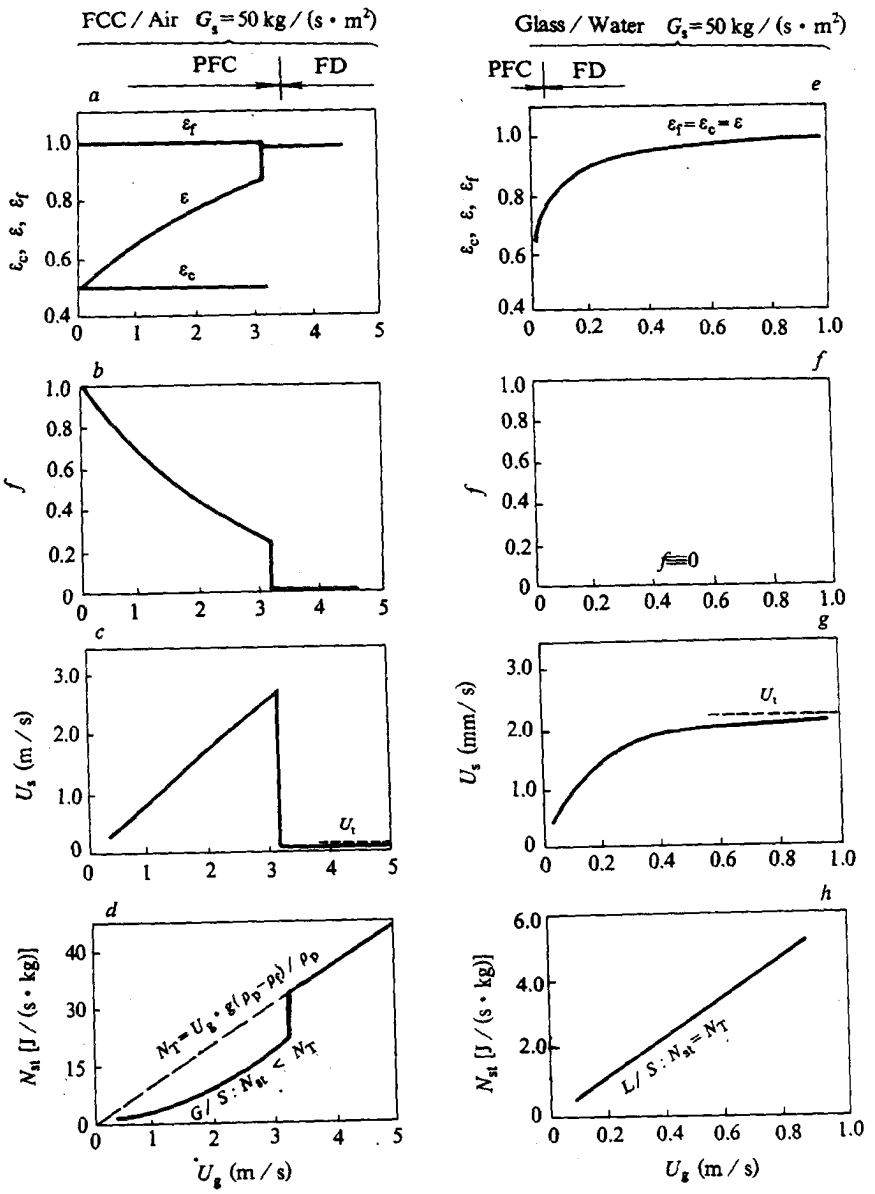

Figure 3-20 Differences between G/S and L/S Systems

Figure 3-21 shows the gradual transition of the homogeneous glass/water fluidization to the highly heterogeneous or aggregative glass/air flu-

idization, as the particle/fluid density ratio ρ_p/ρ_f increases from water through ethyl ether, and carbon dioxide under different stages of decreasing pressure from its critical condition, to atmospheric air. The appearance and gradual growth of the two-phase structure is evident in the order of the fluids listed. For instance, the curves in the top left inset show that at $\rho_p/\rho_f = 2.55$ for glass/water, $f = 0$ throughout the range of fluid velocity U_g, indicating a homogeneous particle-fluid system. When the ratio ρ_p/ρ_f has increased to 3.19 for glass/ethyl ether, however, the two-phase structure appears for fluid velocities U_g up to 0.25 m/s. This velocity range broadens through carbon dioxide under decreasing pressures near its critical point, until at $\rho_p/\rho_f = 2,162$ for glass/air, this two-phase structure has extended beyond $U_g = 2.8$ m/s.

With decreasing ρ_p/ρ_f from G/S system to L/S system, the voidage curve characterized by a sudden change at the choking point degenerates into a smooth curve, showing the gradual shift of the choking point from high velocity to low velocity. Finally, the choking point disappears, and the two states become identical in L/S system.

While Figure 3-20 demonstrates from modeling the disparate nature between G/S and L/S fluidization, Figure 3-21 shows continuity in particle-fluid behavior through properly selected intermediate fluids, thus reconciling in theory the phenomenological discrimination between aggregative and particulate fluidization.

Figure 3-22 shows $N_{st} \sim U_g$ plots corresponding to the $\varepsilon \sim U_g$ plots in Figure 3-21. Heterogeneity in particle-fluid two-phase flow is attributed, as was noted in Figure 3-10, to the difference between $(N_{st})_{dense}$ for the dense phase and $(N_{st})_{dilute} + (N_{st})_{inter}$ for the dilute phase. As soon as $(N_{st})_{dense}$ is lower than $(N_{st})_{dilute} + (N_{st})_{inter}$ two-phase structure prevails, as shown in Figure 3-22 in relation to Figure 3-21. However, the choking point shrinks gradually to the bubbling point defined by the equality of $(N_{st})_{dilute} + (N_{st})_{inter}$ and $(N_{st})_{dense}$ with decreasing ρ_p/ρ_f, and finally merges into the particulate regime, indicating that the PFC/FD transition can occurs without choking. This type of PFC/FD transition happens in most L/S systems. With increasing liquid velocity, the systems expand uniformly without entrainment of solids, until at some liquid velocity, the expanded solids begin to spill out of systems.

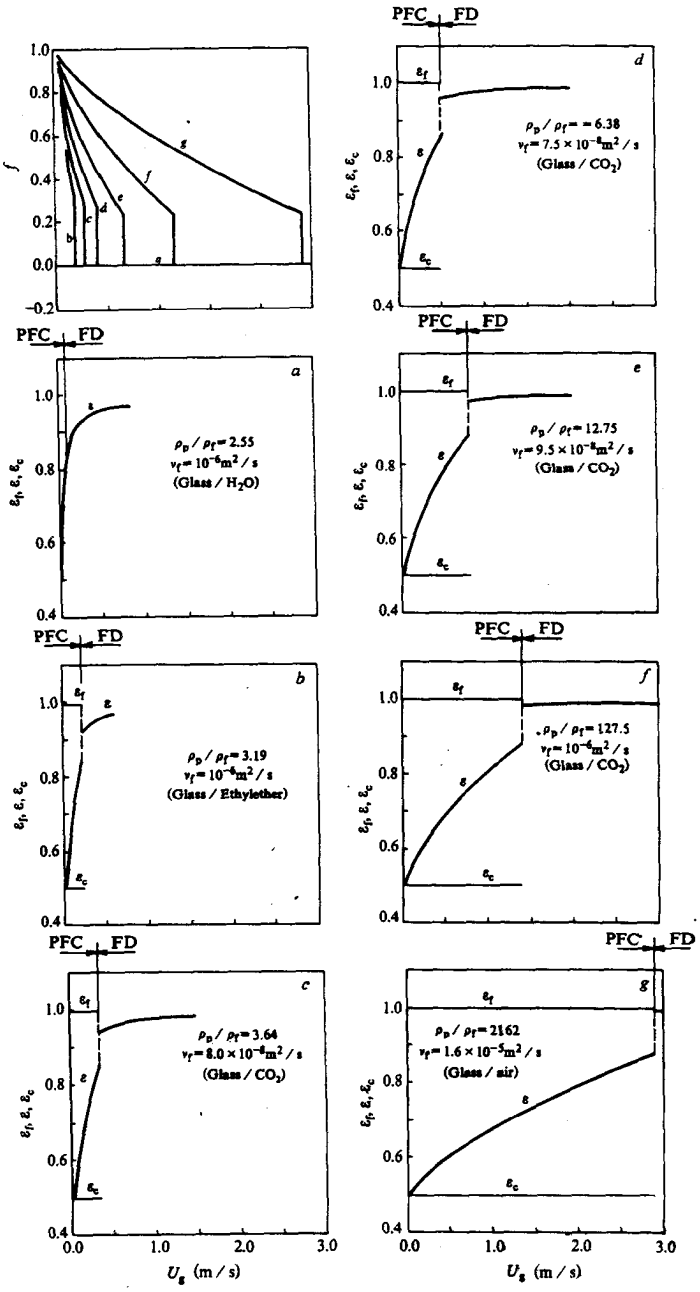

Figure 3-21 Gradual Transition from Particulate to Aggregative

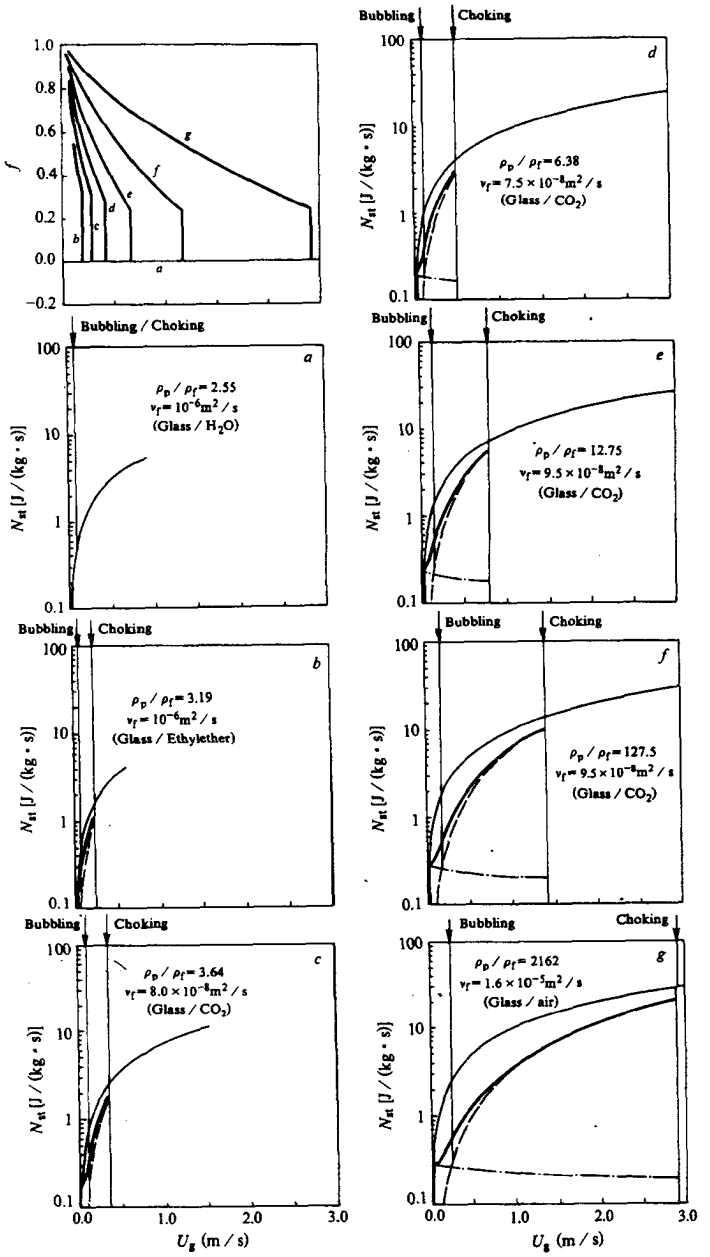

Figure 3-22 Transition from Particulate to Aggregative occurs with Merging of Choking Point into Bubbling Regimes
(———— N_{st} =max; ———— N_{st} =min;
— · — · — $(N_{st})_{dense}$; — — — $(N_{st})_{dilute} + (N_{st})_{inter}$)

At higher ρ_p/ρ_f ratios, however, heterogeneity can appear even for L/S systems, as shown in the $N_{st} \sim U_g$ plot for glass beads/ethyl ether in Figure 3-22 (corresponding to $\varepsilon \sim U_g$ in Figure 3-21), or in the $\varepsilon - U_g$ plot for copper-shot/water system (Yu, 1986) in Figure 3-23, for which $\rho_p/\rho_f = 7.8$.

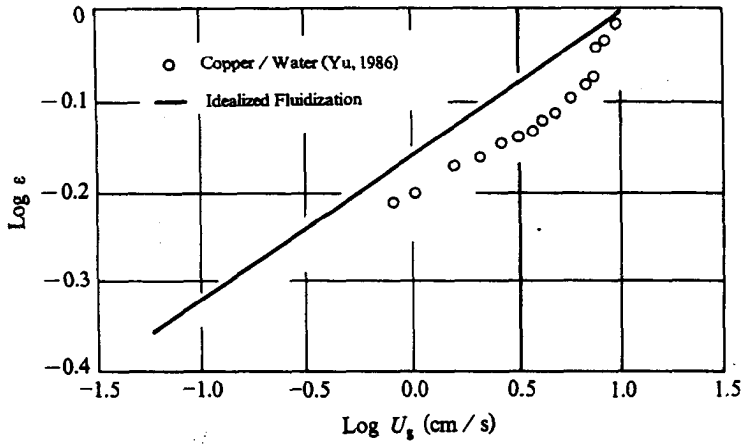

Figure 3-23 Aggregative Behavior in Copper/Water System

3.6.3 Particle Diameter

To understand the effect of particle diameter on local fluid dynamics of particle-fluid systems, it is essential to analyze constraint $F_3(\mathbf{X})$ in Model LG for comparing the structural difference between the dilute and the dense phases.

Because the pressure drop generated by fluid flow in the dilute phase is mainly due to interaction at the interface between clusters and their surrounding broth, that is, $\Delta P_{dilute} << F_{inter}/(1-f)$, $F_3(\mathbf{X})$ can be simplified to

$$\Delta P_{dense} = F_{inter}/(1-f)$$

that is

$$\frac{3}{4}C_{\mathrm{D_{oc}}}\varepsilon^{-4.7}\frac{1-\varepsilon_{\mathrm{c}}}{d_{\mathrm{p}}}\rho_{\mathrm{f}}U_{\mathrm{sc}}^2=\frac{3}{4}C_{\mathrm{D_{oi}}}(1-f)^{-4.7}\frac{f}{(1-f)l}\rho_{\mathrm{f}}U_{\mathrm{si}}^2$$

For systems with fine particles, $C_{\mathrm{D_{oc}}}$ related to d_{p} and U_{sc} is much higher than $C_{\mathrm{D_{oi}}}$ related to l and U_{si}, because of the strong dependence of drag coefficient on particle diameter and fluid velocity in the Stoke's range. To maintain the equality $\Delta P_{\mathrm{dense}}=F_{\mathrm{inter}}/(1-f)$ as required by fluid dynamics, $\varepsilon_{\mathrm{c}}^{-4.7}\frac{1-\varepsilon_{\mathrm{c}}}{d_{\mathrm{p}}}\rho_{\mathrm{f}}U_{\mathrm{sc}}^2$ representing the flow structure in the dense phase must be considerably smaller than $(1-f)^{-4.7}\frac{f}{(1-f)l}\rho_{\mathrm{f}}U_{\mathrm{si}}^2$ representing the flow structure of the inter phase.

For large particle, $C_{\mathrm{D_c}}$ is almost equal to $C_{\mathrm{D_i}}$ due to the essential constancy of the drag coefficient in the Newton's range, therefore, reducing the difference in flow structures of the two phases. It can therefore be deduced that the structural difference between the dense phase and the inter phase would become smaller and smaller with increasing particle diameter, eventually approaching the homogeneous structure. On the other hand, large particles may result in the degeneration of the regime spectrum, as has already been noted for Geldart's Class B and D particles which are impossible to fluidize in the uniform expansion regime. Size distribution of particles, which affects so much the behavior of particle-fluid two-phase flow, may well be a key to improved fluidization quality (Kwauk and Li, 1989).

3.6.4 Fluid Kinematic Viscosity

The effect of fluid kinematic viscosity ν_{f} on phase structure has not been extensively understood, and experimental results can hardly be found. However, a preliminary prediction can be made on the basis of the principle of the EMMS model.

In particle-fluid two-phase flow with low fluid kinematic viscosity, $C_{\mathrm{D_c}}$ is not very much different from $C_{\mathrm{D_i}}$ because they both correspond to high Reynolds numbers. Therefore, the phase structure in the dense phase is close to that in the dilute phase. On the contrary, Reynolds number becomes lower with increasing fluid kinematic viscosity, thus increasing the

difference between C_{D_c} and C_{D_i}, and hence, between the flow structures of the two phases. It is expected that the decrease in fluid kinematic viscosity would be beneficial to uniform flow structure.

3.7 Overall Fluid Dynamics—Regions

While local fluid dynamics of particle-fluid systems—phases, regimes and patterns—is concerned with its intrinsic stability, of direct engineering significance is its overall fluid dynamics which deals with its space-dependent characteristics subject to the boundary conditions set by the retaining vessel. For the axisymmetric equipment generally employed in engineering, overall fluid dynamics is resolved into the axial and the radial directions: top and bottom regions for the former, and core and wall regions for the latter. On this macro-scale, therefore, the principle of energy minimization has to be applied on an extended scale, in order to quantify the heterogeneous flow field.

3.7.1 Axial Fluid Dynamics

Axial Heterogeneity

Axial heterogeneity is mainly related to the coexistence of two different regions in terms of local fluid dynamics—a bottom dense region with average voidage ε_a and a top dilute region with average voidage ε^*, bridged together by a transition region, so as to form an S-shaped profile, such as was first treated by Li and Kwauk (1980) for fast fluidized beds:

$$\frac{\varepsilon(h) - \varepsilon_a}{\varepsilon^* - \varepsilon(h)} = \exp\left[-(z - Z_i)/Z_0\right]$$

in which Z_i is the location of the point of inflection in the profile, and Z_o is called the characteristic length, which governs how quickly the top and bottom regions merge into each other and is related to operating conditions and material properties (see Section 5.1.3 for its correlation).

According to the analysis of local fluid dynamics, the top dilute region operates in the FD-regime, while the bottom dense region, in the PFC-

regime. Therefore, whenever the S-shaped profile appears, the corresponding solid flow rate is bound to be equal to the saturation carrying capacity K^*. Such axial macro-heterogeneity depends not only on the local fluid dynamics given by Model LG, but also by the pressure drop imposed across the unit ΔP_{imp} which affects the position of the inflection point Z_{i}, and, as discussed in Section 3.3.1 and shown in Figure 3-8, can operate in three modes:

	Local Conditions	Overall Conditions	Voidage Regions
Mode PFC	$U_{\text{g}} < U_{\text{pt}}, G_{\text{s}} > K^*$	$\Delta P_{\text{imp}} > (1-\varepsilon_{\text{a}})\rho_{\text{p}} g H$	dense only
Mode PFC/FD	$U_{\text{g}} = U_{\text{pt}}, G_{\text{s}} = K^*$	$(1-\varepsilon^*)\rho_{\text{p}} g H < \Delta P_{\text{imp}} < (1-\varepsilon_{\text{a}})\rho_{\text{p}} g H$	dilute/dense
Mode FD	$U_{\text{g}} > U_{\text{pt}}, G_{\text{s}} < K^*$	$\Delta P_{\text{imp}} < (1-\varepsilon^*)\rho_{\text{p}} g H$	dilute only

Therefore, to realize any desired mode of operation, it is necessary to control both the local and the overall conditions.

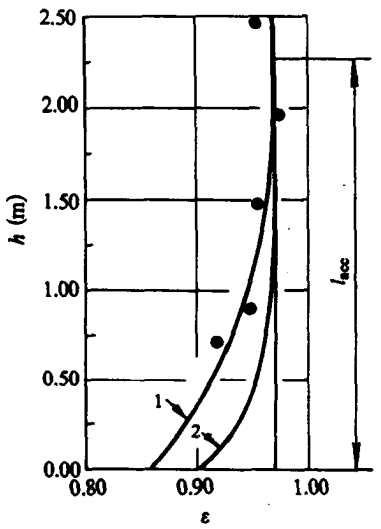

Figure 3-24 Contribution of Particle Acceleration and Hold up to Total Pressure Drop in the Acceleration Zone (see Figure 4-24 for operating conditions)
1. $\frac{\Delta P_{\text{total}}}{\rho_{\text{p}} g}$; 2. $\frac{\Delta P_{\text{holdup}}}{\rho_{\text{p}} g}$

Moreover, at the very bottom of the fluidized bed, much energy is expended in accelerating the particles with a sharp increase in bed voidage, which approaches with increasing bed height a steady state value, for instance, ε_a for Mode PFC/FD. During acceleration, the pressure drop ΔP_{acc} far exceeds that needed by the weight of the particles ΔP_{holdup}, as was shown by Weinstein and Li (1989) in Figure 3-24. In the outlet section, an increase in bed density may, too, occur, though mainly due to backmixing of particles induced by exit configuration.

Mathematical Modeling

The three modes of operation shown in Figure 3-3 are identified as follows:

Mode PFC: 1-region $\quad (W_{st})_{(N_{st})_{min}} < (W_{st})_{(N_{st})_{max}|\varepsilon_c=\varepsilon_{mf}}$

Mode PFC/FD: 2-region $\quad (W_{st})_{(N_{st})_{min}} = (W_{st})_{(N_{st})_{max}|\varepsilon_c=\varepsilon_{mf}}$

Mode FD: 1-region $\quad (W_{st})_{(N_{st})_{min}} > (W_{st})_{(N_{st})_{max}|\varepsilon_c=\varepsilon_{mf}}$

To calculate the two-regioned axial parameter profile in Mode PFC/FD, ε_a and ε^* are determined as follows:.

For the one-dimensional profile now under consideration, the fluid dynamics of the top dilute region can be described by

$$\begin{cases} (N_{st})^* = \max \\ F_i(\mathbf{X}^*) = 0 \quad (i = 1, 2, ..., 6) \\ U_{sc}^* \geq 0, U_{sf}^* \geq 0, U_{si}^* \geq 0 \end{cases}$$

Solution of this model gives $\mathbf{X}^*$ and ε^*. Of course, it is only possible to calculate the two extreme cases—the uniform case with N_{st} =max and the completely nonidealized case with $N_{st} = \max|_{\varepsilon_c=\varepsilon_{mf}}$.

And the fluid dynamics of the bottom dense region is governed by

$$\begin{cases} (N_{st})_a = \min \\ F_i(\mathbf{X}_a) = 0 \quad (i = 1, 2, ..., 6) \\ U_{sc_a} \geq 0, \ U_{sf_a} \geq 0, \ U_{si_a} \geq 0 \end{cases}$$

which gives $\mathbf{X}_a$ and ε_a.

From the values of ε_a and ε^* thus calculated, and ΔP_{imp} computed from solids inventory and the geometry of the equipment, Z_i can be deduced from pressure balance:

$$Z_i = \frac{\Delta P_{imp} - (1-\varepsilon_a)\rho_p g H}{(\varepsilon_a - \varepsilon^*)\rho_p g}$$

And then, the entire axial voidage profile can be calculated from the Li-Kwauk model mentioned earlier in the present section.

3.7.2 Radial Fluid Dynamics

Radial Heterogeneity

Radial heterogeneity, showing a dilute core region surrounded by a dense annular region next to the wall, is attributed to the role of the wall in promoting minimization of fluid-particle interaction by inducing a dense region near the wall with low N_{st}, thus resulting in the radial distributions of all parameters. Such a heterogeneous flow structure affects the performance of a chemical reactor critically, though in a positive way sometimes, but likely in a negative way, because the formation of radial distribution results in considerable decrease in fluid-particle contacting and leads to backmixing of both fluid and particles.

Mathematical Modeling

Model LG applies just as well to radial heterogeneity, though in a somewhat different functional form, to describe the fluid dynamics at any radial position r:

$$\left.\begin{array}{ll} a) & N_{st}(r) = \text{extreme (min for } G_s(r) \geq K^*; \\ & \qquad\qquad \text{max for } G_s(r) \leq K^*) \\ b) & F_i(\mathbf{X}(r)) = 0 \quad (i = 1, 2, ..., 6) \\ c) & U_{sc}(r) \geq 0, \quad U_{sf}(r) \geq 0, \quad U_{si}(r) \geq 0 \end{array}\right\} \text{Model LR}$$

This model, Model LR (Local-Radial), describes the dependence of $\mathbf{X}(r)$ on gas velocity $U_g(r)$ and particle velocity $U_d(r)$, which are however not manipulatable operating parameters, but should be correlated with the average superficial gas velocity U_g and the average superficial particle velocity U_d $(= G_s/\rho_p)$ as well as boundary conditions.

In order to calculate $U_g(r)$ and $U_d(r)$ from the specified operating parameters U_g and G_s, it is necessary to know the dominant factor defining radial heterogeneity. Extending the energy minimization method to overall fluid dynamics, a stable radial profile calls for not only Model LR for local fluid dynamics at every point, but also the minimization of the cross-sectional average $\overline{N}_{st}$ for overall stability, which is defined by

$$\overline{N}_{st} = \frac{2}{R^2(1-\bar{\varepsilon})} \int_0^R N_{st}(r)[1-\varepsilon(r)]r\mathrm{d}r \tag{3.4}$$

where the cross-sectional average bed voidage $\bar{\varepsilon}$ is defined as

$$\bar{\varepsilon} = \frac{2}{R^2} \int_0^R \varepsilon(r)r\mathrm{d}r \tag{3.5}$$

To fulfil both local and overall stability, all parameters would adjust themselves radially in such a way that not only $N_{st}(r)$ at *any radial position* is minimized for the PFC regime, or maximized for the FD regime, but also $\overline{N}_{st}$ for the *whole* cross-section is minimized, yielding radial profiles as governed by the following Overall-Radial model

a) $\overline{N}_{st}$ = extreme (min for $G_s > K^*$; max for $G_s < K^*$)
b) Model LR(r)
c) $U_g = \frac{2}{R^2}\int_0^R U_g(r)r\mathrm{d}r$
d) $U_d = G_s/\rho_p = \frac{2}{R^2}\int_0^R U_d(r)r\mathrm{d}r$
e) $\Delta P_{st}(r)$ = constant
f) boundary conditions

} Model OR

The parameter vector $\mathbf{X}(r)$, describing this twofold optimization problem, depends on both local and overall fluid dynamics. For a system without wall effects, Model OR simplifies to Model LG for local fluid dynamics.

Condition (a) in Model LR states that N_{st} may be minimal or maximal depending on radial position r:

$$\overline{N}_{st} = \frac{2}{R^2(1-\bar{\varepsilon})}\left[\int_0^{R_1}(N_{st}(r))_{max}(1-\varepsilon(r))r\mathrm{d}r + \int_{R_1}^{R}(N_{st}(r))_{min}(1-\varepsilon(r))r\mathrm{d}r\right]$$

where R_1 is the position at which regime transition from the FD regime in the core to the PFC regime near the wall occurs, which should satisfy the condition

$$(N_{st}(R_1))_{min}(1-\varepsilon(R_1)_{min}) = (N_{st}(R_1))_{max}(1-\varepsilon(R_1)_{max})|_{\varepsilon_c=\varepsilon_{mf}}$$

It is clear that in addition to the identification of operating modes, this equation has also to be used for selecting maximum or minimum N_{st} in Model LR.

If we consider the simple case in which both the core region and the wall region operate in the same regime, i.e., both FD, or both PFC, then Model OR can be applied to the top dilute region assumed to be all in Mode FD,

a) $\overline{N}_{st} = \frac{2}{R^2(1-\bar{\varepsilon})}\int_0^R (N_{st}(r))_{max}(1-\varepsilon(r))r\mathrm{d}r \rightarrow \max$
b) Model LR(r)(with $N_{st}(r) \rightarrow \max$)
c) $\Delta P_{st}(r) =$ constant
d) $U_g = \frac{2}{R^2}\int_0^R U_g(r)r\mathrm{d}r$
e) $U_d = G_s/\rho_p = \frac{2}{R^2}\int_0^R U_d(r)r\mathrm{d}r$
f) Boundary conditions

} Model OR–FD

and to the bottom dense region assumed to be all in Mode PFC,

a) $\overline{N}_{st} = \frac{2}{R^2(1-\bar{\varepsilon})}\int_0^R (N_{st}(r))_{min}(1-\varepsilon(r))r\mathrm{d}r \rightarrow \min$
b) Model LR(r)(with $N_{st}(r) \rightarrow \min$)
c) $\Delta P_{st}(r) =$ constant
d) $U_g = \frac{2}{R^2}\int_0^R U_g(r)r\mathrm{d}r$
e) $U_d = G_s/\rho_p = \frac{2}{R^2}\int_0^R U_d(r)r\mathrm{d}r$
f) Boundary conditions

} Model OR–PFC

This simplification also applies to any one-region operation, either FD or PFC.

Solution of Model OR

In theory, given the required boundary conditions, it is possible to calculate the radial profiles of all parameters with Model OR from the specified operating variables, U_g and G_s. An approximate solution to the simplest case of the PFC regime, for example, that is, $N_{st} = \min$, is possible by simplifying Model OR with experimental results, for calculating $U_d(r)$ from $U_g(r)$ and $\varepsilon(r)$.

Radial heterogeneity is assumed to be distributed in terms of a heterogeneity factor $K(r)$, defined as the ratio of the equivalent cluster diameter $l(r)$ to the particle diameter d_p, that is, $K(r) = l(r)/d_p$. When the voidage profile $\varepsilon(r)$ is known, $K(r)$ can also be expressed as $K(\varepsilon(r))$. At minimum fluidization, the cluster diameter is evidently equal to the diameter of the unit, and at infinite bed expansion, $\varepsilon = 1.0$ and $l = d_p$, that is

$$K(\varepsilon_{mf}) = d_B/d_p \quad \text{and} \quad K(\varepsilon = 1.0) = 1.0$$

At any radial position r, $U_d(r)$ can be calculated from $U_g(r)$ and $\varepsilon(r)$ by using Model LR through a triál $f(\mathbf{A},r)$ which may be approximated by polynomials or other adequate functions with the parameter vector $\mathbf{A}$, to be optimized with respect to $\overline{N}_{st}$ =min. Now, the problem becomes how to find $K(r)$, that is, how to determine $\mathbf{A}$, in order to satisfy energy minimization, force balance, continuity and the given boundary conditions. Therefore, Model OR is simplified for PFC regime as the K-Radial (KR) model:

To find $K(r) = f(\mathbf{A}, r)$

Satisfying
- *a*) $\overline{N}_{st} = \min$
- *b*) Model LR(r)
- *c*) $K(\varepsilon_{mf}) = d_B/d_p$
- *d*) $K(\varepsilon = 1.0) = 1.0$
- *e*) $U_d = \frac{2}{R^2}\int_0^R U_d(r) r\,dr$

} Model KR–PFC

For calculating the radial profiles in the FD regime, for instance, in the top dilute region, $\overline{N}_{st}$ should be maximized to form the counterpart Model KR-FD.

Model KR (PFC or FD) can also be solved by using the GRG-2 algorithm for both local and overall energy minimization. Since it is called by the main program for both local and overall optimization loops, all names of its subroutines should be changed for fitting the requirement of FORTRAN 77, resulting in a new version called GRG-21. Therefore, in solving Model KR, the local loop calls GRG-21, while the overall loop calls GRG-2. The scheme diagram for solving Model KR is shown in Figure 3-25.

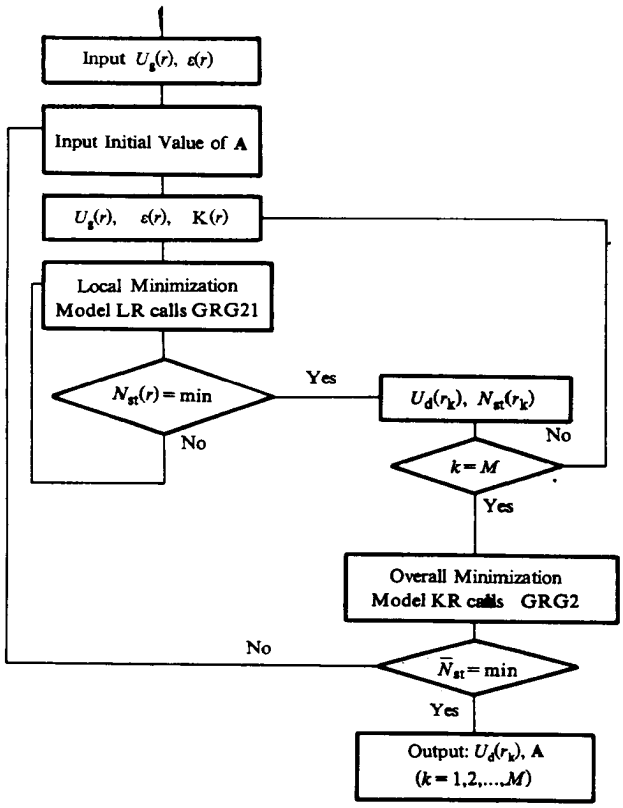

Figure 3-25 Scheme Diagram of Solving Model KR

Figure 3-26 shows the radial profiles of parameters involving the solid velocity $U_d(r)$ calculated from Model KR-PFC (Li *et al.*, 1991c) using the data provided by Bader *et al.* (1988) on radial distribution of voidage and gas throughput as shown in Figure 3-26f.

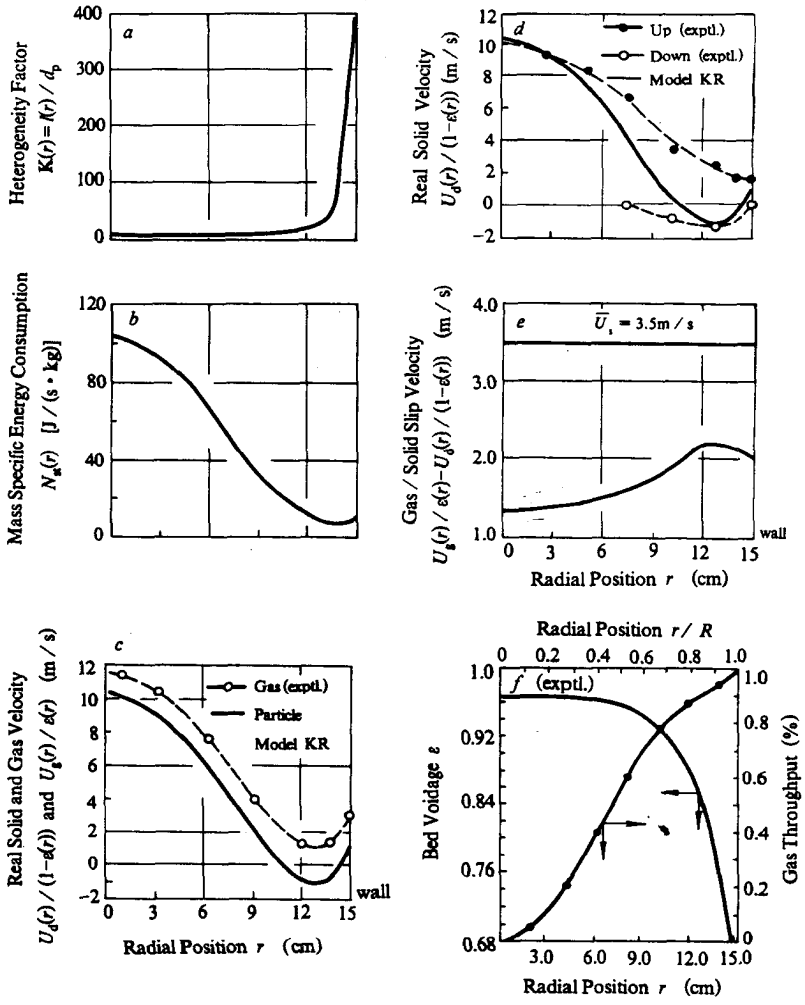

Figure 3-26 Comparison of Calculation Results of Model KR-PFC with Experimental Data of Bader *et al.* (1988)
($d_p = 76\ \mu m$, $\rho_p = 1714\ kg/m^3$, $d_B = 30.5$ cm, $U_g = 3.7$ m/s, $G_s = 98\ kg/(m^2 \cdot s)$)

Figure 3-26a shows the calculated radial distribution of the heterogeneity factor $K(r)$. In the dilute core region, the bed structure is shown to be close to homogeneous with small particle clusters. Beyond $r = 12$ cm near the wall, the heterogeneity factor increases dramatically, indicating a much more aggregated bed structure. Energy consumption $N_{st}(r)$ depends strongly on bed structure as Figure 3-26b shows—very high in the dilute core region, but extremely low in the dense wall region. Such a distribution of $N_{st}(r)$ and particle population leads to minimization of $\overline{N}_{st}$, and hence, to a stable radial profile.

The real solids velocity profile calculated from Model KR, and the real gas velocity profile deduced from Figure 3-26f, are shown in Figure 3-26c for comparison. Because of the near-homogeneous bed structure in the dilute core region, solids velocity reaches high values approaching the magnitude of the gas velocity. In the dense wall region, low and even negative solids velocity exists, which causes local solids and gas backmixing. A comparison of the calculated and the measured (Bader, 1988) solids velocity profiles, which are independent from each other because the latter was not used for simulation, is shown in Figure 3-26d. A reasonable agreement is achieved.

The calculated radial profile of slip velocity between gas and solids is shown in Figure 3-26e. The lowest slip velocity occurs in the center of the unit due to uniformity in this region, the highest not far from the wall. It is worth to note that the local slip velocity shown in this figure is lower than the cross-sectional average slip velocity $\overline{U}_s$, or $U_g/\overline{\varepsilon} - G_s/\rho_p(1-\overline{\varepsilon}) = 3.5$ m/s. This indicates that the high slip velocity for the overall circulating fluidized bed reactor should be attributed not only to overall heterogeneity—radial profile, as reported by Rhodes and Geldart (1985), but also to local heterogeneity (aggregation of particles). Therefore, the global average slip velocity is not adequate for correlating particle/fluid contacting in the system, but local slip velocity, or even more intrinsically, local fluid-particle interaction intensity, must be used as indicated by Li *et al.* (1993).

Figure 3-27 shows the respective contributions of local heterogeneity and overall heterogeneity to energy minimization, as calculated with the same conditions as for Figure 3-26. In Figure 3-27a, $N_{st}(r)$ was

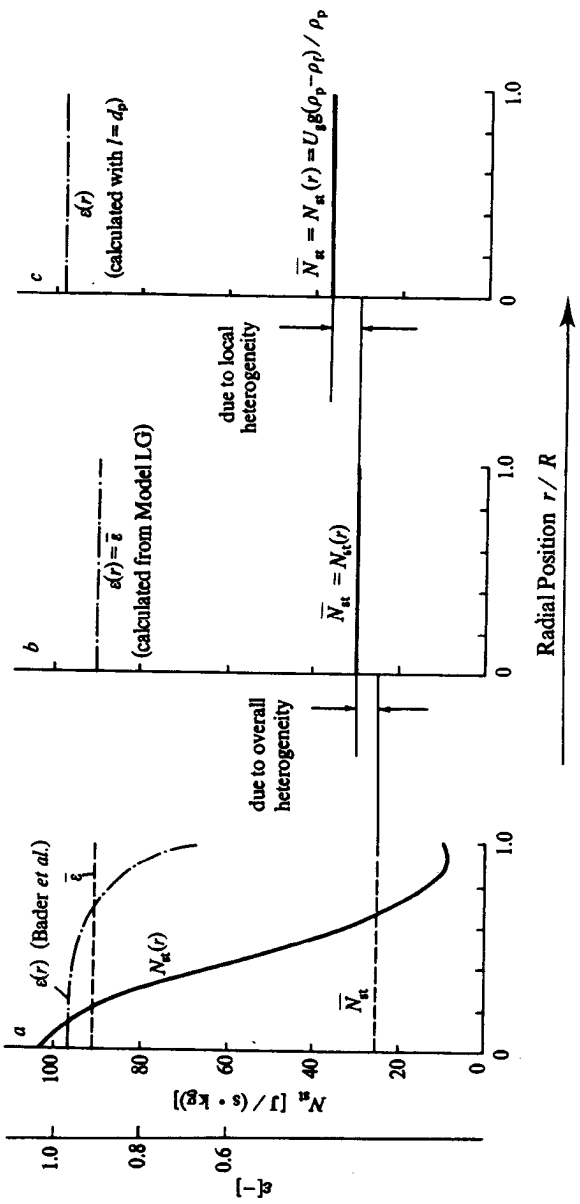

Figure 3-27 Respective Contributions of Overall and Local Heterogeneities to Minimizing of $\overline{N}_{st}$
a — with both local and overall heterogeneity (Model KR);
b — with local heterogeneity; c — without heterogeneity

calculated from Model KR with regard to both local and overall heterogeneity, and $\overline{N}_{st}$ and $\bar{\varepsilon}$ are the cross-sectional averages of $N_{st}(r)$ and $\varepsilon(r)$. Figure 3-27b was calculated from Model LG, considering only local heterogeneity (particle aggregation) and assuming that the local voidage in the cross-section is equal to the average voidage $\bar{\varepsilon}$ in Figure 3-27a. Figure 3-27c was calculated with the assumption of uniform flow structure on both local and overall scale. It is indicated that $\overline{N}_{st}$ takes to maximum if the system is uniform on both the local and overall scale. The occurrence of local heterogeneity, as shown in Figure 3-27b, reduces $\overline{N}_{st}$ considerably, as can be seen through comparison between Figure 3-27b and Figure 3-27c, while overall heterogeneity (radial profile) promotes minimization of $\overline{N}_{st}$ further, as shown by the difference between Figure 3-27b and Figure 3-27a. In fact, the wall in concurrent-up two-phase flow retards the upward movement of the particles, and plays a positive role in energy minimization, and therefore, it causes radial heterogeneity. It was indicated that radial heterogeneity could be substantially suppressed if a zigzag wall was used for hindering minimization of $\overline{N}_{st}$ (Bie *et al.*, 1992).

Radial heterogeneity not only results in the coexistence of the PFC regime and the FD regime in the radial direction, but could also affect the transition from the PFC regime to the FD regime in the axial direction, that is, saturation carrying capacity is also subject to wall effect as mentioned by Kunii and Levenspiel (1969). For dealing with this problem, the condition for this transition in a real unit may be modified as follows

$$(\overline{W}_{st})_{(\overline{N}_{st})_{min}} = (\overline{W}_{st})_{(\overline{N}_{st})_{max}|\epsilon_c=\epsilon_{mf}}$$

indicating that axial and radial profiles affect each other. In theory, the whole flow field of a particle-fluid two-phase system, including both axial and radial profiles, can be calculated with the last equation and Model OR if the operating conditions, material properties and boundary conditions are specified. However, complete solution has not yet been realized, and further effort is required.

Chapter 4

EXPERIMENTAL EVIDENCE

To verify the computed results derived from the EMMS model, experiments were conducted in a circulating fluidized bed which can be operated through the whole regime spectrum of fluid-particle two-phase flow. This chapter presents the experimental techniques employed and the experimental evidences in terms of *phase*, *regime*, *pattern* and *region*.

4.1 Experimental Techniques

4.1.1 Experimental Apparatus

A plexiglass circulating fluidized bed, as shown in Figure 4-1, was used, which consists of a riser, 10 m high and 90 mm I.D., a downcomer, 120 mm I.D., a solids-gas disengager, two cyclones and two butterfly valves. Twelve pressure taps and eleven probe ports are arranged alternately along the height of the riser for measuring the axial voidage profile and inserting signal probes into the riser.

Solids circulating rate can be adjusted by changing the opening of the butterfly valve between the riser and the downcomer, or by changing the solids inventory in the system. Gas flow rates are measured by means of

rotameters, and pressure drop by a scanning transducer-valved system which will soon be described.

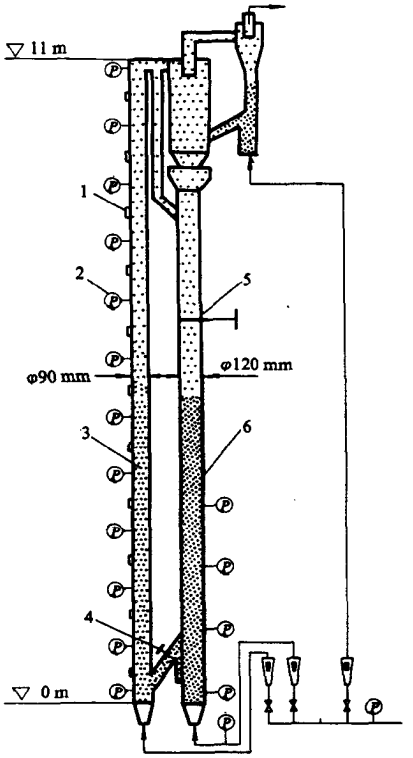

Figure 4-1 Schematic Diagram of Experimental Unit
1 — fitting; 2 — tap; 3 — riser;
4 — control valve; 5 — butterfly; 6 — downcomer

The solids used in the experiments were FCC catalyst ($\overline{d}_p = 54\ \mu m, \rho_p = 929.5\ kg/m^3$) fluidized by air.

By changing the solids inventory and gas velocity, the system can be operated in the whole regime spectrum of fluid-particle two-phase flow: particulate, bubbling, slugging, turbulent, fast and dilute transport, and with different constitutions of regions: dense only, dilute only, or dense and dilute.

4.1.2 Measurement of Axial Voidage Profile

Axial voidage profile in the CFB is derived from pressure gradient which is measured by means of a scanning transducer-valved system using only a single pressure transducer and a two-body scanning valve as shown in Figure 4-2. Each pressure tap is connected to both valves in such a way that the N^{th} tap is linked to the N^{th} channel of valve A, but to the $N+1^{th}$ channel of valve B. When these two valves are controlled by a computer to scan synchronously their channels, the pressure difference between the N^{th} and $N+1^{th}$ taps is measured in sequence.

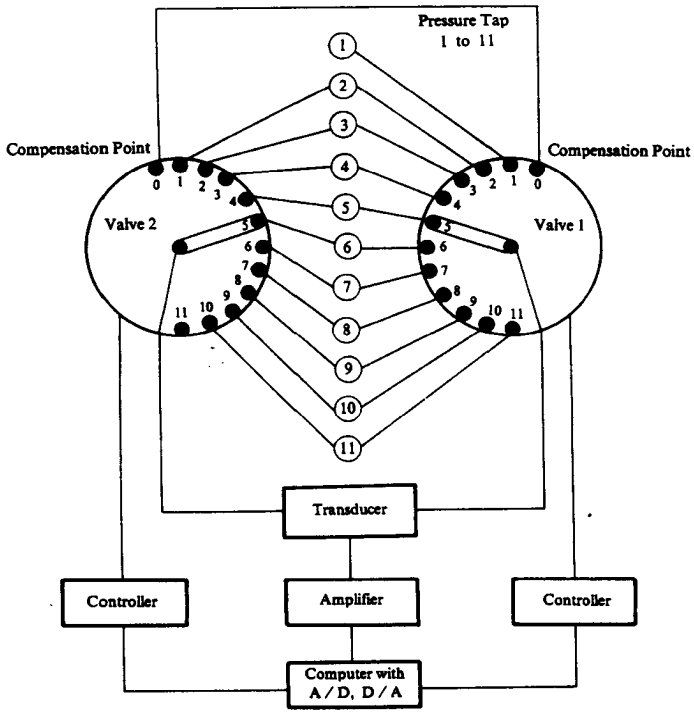

Figure 4-2 Scanning Transducer-Valved System for Pressure Drop Measurement

4.1.3 Measurement of Local Voidage

Most optical probes used in local voidage measurement (Qin and Liu, 1982; Boiarski, 1985; Hartge et al, 1986; Horio *et al.*, 1988) are based on back scattering of incident light. Both the incident light and the reflected light are transmitted by optical fibers or fiber bundles. The intensity of the back-scattered light measured by an optical detector is dependent on the concentration of particles in the system, from which local voidage is derived. According to Krohn (1986), the responses of different kinds of optical probe configurations as shown in Figure 4-3 cannot reach zero even if the reflector is far away from the probe because of their infinite measurement volumes from which the probes collect the reflection.

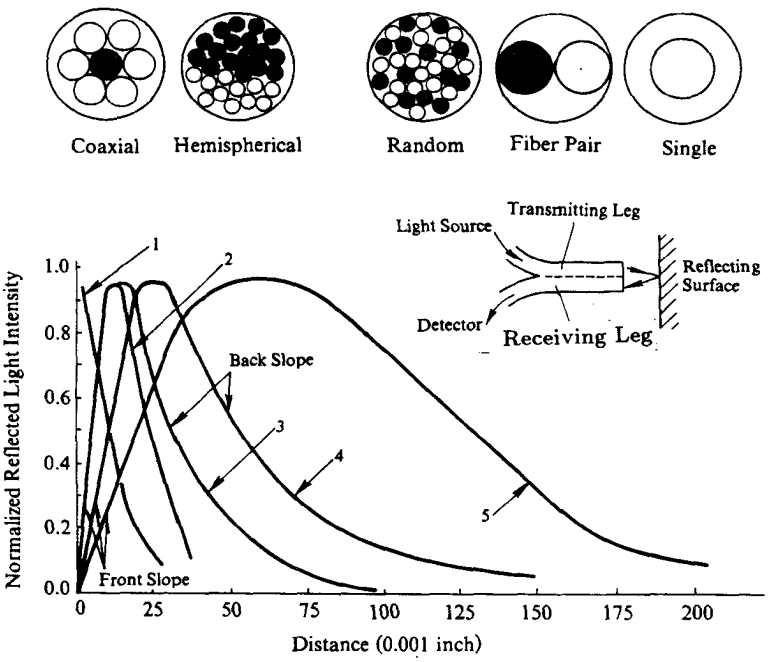

Figure 4-3 Prevailing Configurations of Reflective Optical Probes (Krohn,1986)
1 — single fiber; 2 — coaxial fiber;
3 — random; 4 — hemispherical; 5 — fiber pair

Figure 4-4 shows that the probe with an infinite measurement volume can collect the reflection from the boundary of a bubble even if the probe is located at its center, and can therefore not be used for local measurement. Figure 4-5a shows further that the measurement volume represented by the overlap region of the capture angles of two fibers is infinite, and therefore, the localizability of measurement cannot be realized. Moreover, the response of a probe to particle concentration is usually not linear, and a standard voidage for calibration is difficult to set up. For solving the above mentioned problems, the linearity and the localizability of optical voidage measurement, which mainly depends on fiber arrangement and the optical behavior of the fiber, were improved by changing the angle between the incident fiber and the receiving fiber to create a defined measurement volume as shown in Figure 4-5b (Reh and Li, 1991).

It is clear that β should be larger than θ for a defined measurement volume size of

$$l_{\max} = d_f \sin\frac{\beta}{2} + \frac{d_f \cos\beta + \frac{\delta}{2}}{\tan(\beta - \theta)}$$

For high output and small probe diameter, Reh and Li used plastic optical fibers (d_f =1 mm, numerical aperture N. A. =0.5) with very thin claddings. Figure 4-6 shows the calculated characteristic curves for both parallel ($\beta = 0°$) and crossed ($\beta = 33°$) probes, showing that the window of a crossed fiber probe should be arranged as close as possible to the fiber ends to obtain the highest output. If the windows are made of very thin glass plates (0.4 mm for this case), the characteristic curve with the window can be considered to be the same as the one without the window except for a cutaway section. This figure shows that the angle factor φ of the crossed arrangement, defined as the ratio of the received light power to the incident light power, decreases very quickly from 20 % at the plane of the window to 0.2% at X_2 = 4 mm, and then reaches zero at about X_2 = 16 mm, as contrasted with a slow decrease of the angle factor for the parallel arrangement, from 9% to 2%, in the same range, and with its infinite continuation. Of course, the design of a probe is subject to the characteristics of the fibers used (Reh and Li, 1991).

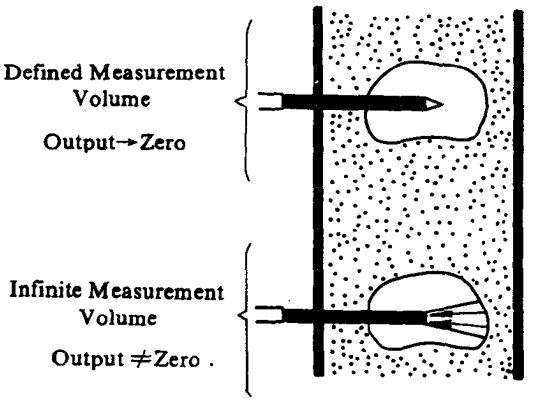

Figure 4-4 Significance of Finite Volume in Voidage Measurement by Optical Probes

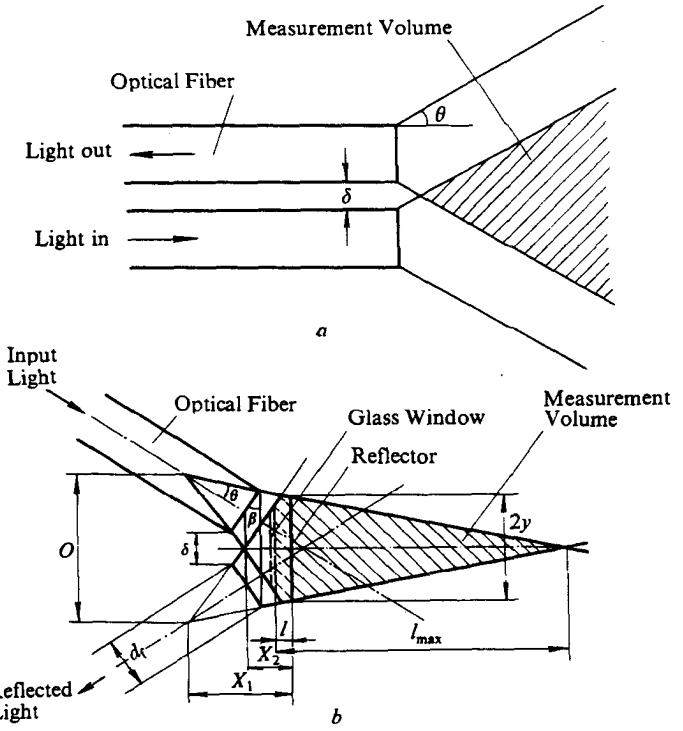

Figure 4-5 Comparison of Measurement Volumes between Parallel Probe and Crossed Probe

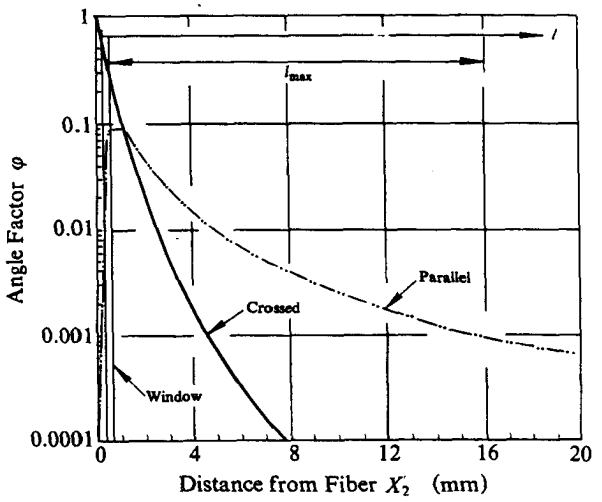

Figure 4-6 Comparison between Parallel and Crossed Fiber Arrangements ($d_f = 1.0$ mm; $d_c = 1.0$ mm; $N.A. = 0.5$; $\delta = 0.05$ mm)

According to Figure 4-6, a crossed fiber probe was designed as shown in Figure 4-7. Two end-polished fibers, one for the incident light from the light source, and the other for the reflected light from the measurement volume, are angled in a metal part at $\beta = 33°$, touching each other at their tips, and then encased in a 6.0 mm O. D. stainless steel tube. The inside of the 0.4 mm glass window is coated to avoid reflection. A parallel fiber probe was also constructed for comparison.

Experiments were performed to test the predicted characteristics of the crossed fiber probe, and to show the importance of the localizability for local voidage measurement by comparing these two different probes. Characteristic curves for both the crossed fiber probe and the parallel fiber probe, shown in Figure 4-8, were measured by setting a plane reflector in front of the probes and changing the distance between probes and the reflector, showing reasonable agreement with the calculated curves in Figure 4-6.

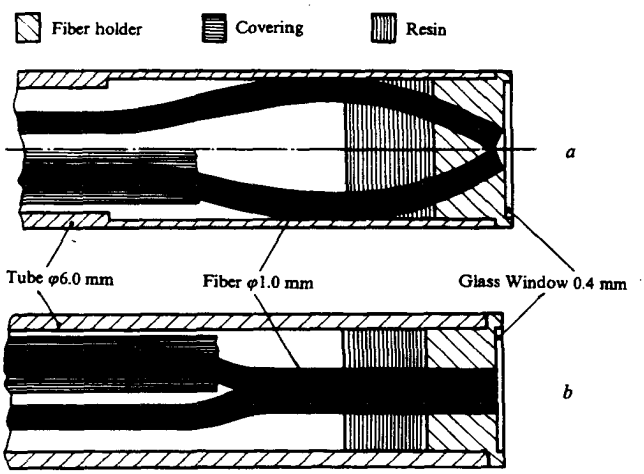

Figure 4-7 Comparison of Optical Fiber Probe Structures
a —— crossed; b —— parallel

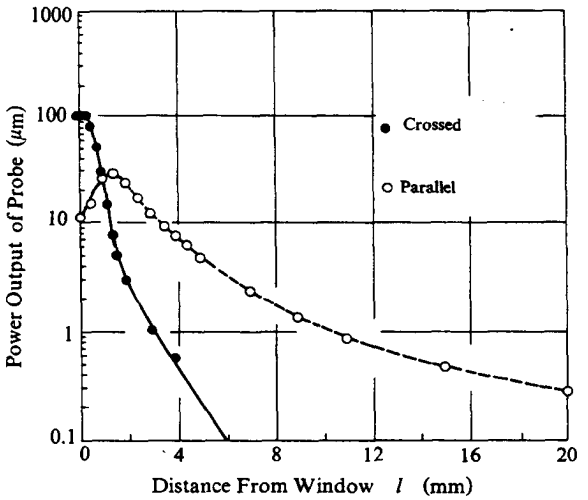

Figure 4-8 Measured Response Curves for Crossed and Parallel Probes ($d_f \doteq 1.0$ mm; $d_c = 1.0$ mm; $N.A. = 0.5$; $\delta = 0.05$ mm; calculated curves see Figure 4-5)

Both the crossed and the parallel probes were tested and calibrated in a 100 mm I.D. fluidized bed with 0~110 μm alumina particles. Signals of local voidage from these two probes are shown in Figure 4-9. It is indicated that the responses of the two probes to the same fluctuating bed structure are quite different. Bubbles, to which the responses of a probe should be zero, cannot be correctly detected by the parallel probe because the reflection from the bubble boundaries causes a certain level of output. This distortion becomes more and more marked with decreasing bubble size as shown for $\varepsilon \rightarrow \varepsilon_{mf}$ in Figure 4-9. However, the crossed fiber probe can detect bubbles without distortion, even when they are very small, due to its good localizability.

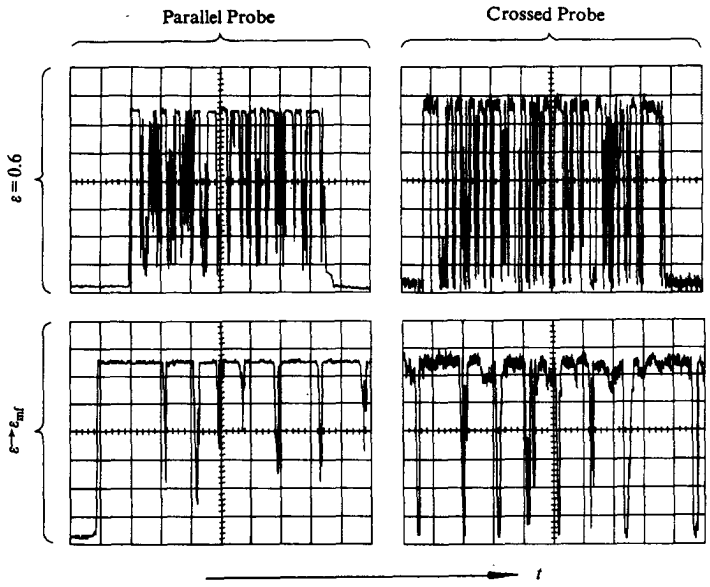

Figure 4-9 Local Voidage Signals Showing Distortion Caused by Infinite Measurement Volume
($0 \sim 110$ μm alumina in a 90 mm I.D. bed)

Reh and Li (1991) concluded from their optical voidage measurements, that if the measurement volume of a probe is reasonably small, its response to the bed density would approach linear. Calibration curves shown in Figure 4-10a illustrate such characteristics of these two different probes.

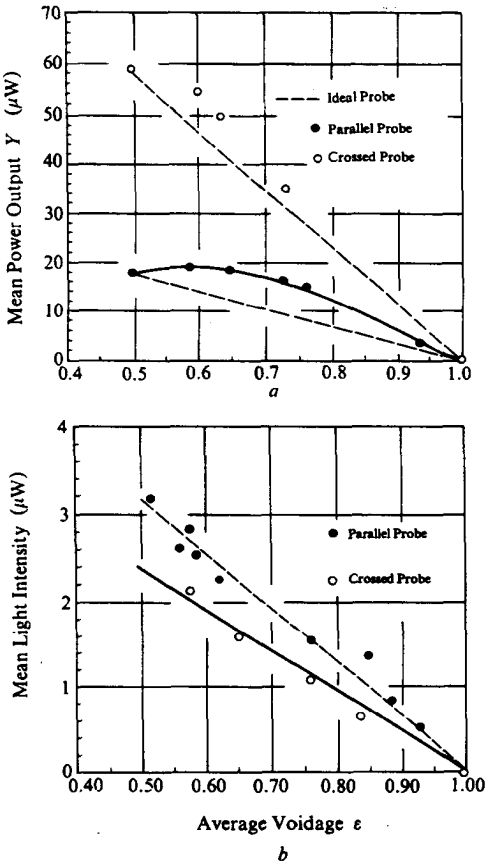

Figure 4-10 Calibration Curves for Parallel and Crossed Probes
a — air/alumina: $d_p = 0 \sim 110$ μm
b — water/glass beads: $d_p = 150 \sim 250$ μm

While the relationship between the average voidage and the output of the crossed probe is close to linear, it is highly non-linear for the parallel fiber probe. Particularly in dense-phase fluidization, the output of the parallel probe changes only slightly over a wide voidage range (e.g., 0.46 $\sim$ 0.7), or even has the same value for two different voidages, indicating poor sensitivity. This is because the parallel probe can not correctly respond to bubbles, and is not response-maximized at the window plane as shown in Figure 4-8. For the crossed probe, the near-linear response curve is attributed to its good localizability.

These two probes were also calibrated in a liquid/solid fluidization system, showing linearity for both probes, as can be seen in Figure 4-10b. Compared with Figure 4-10a, it is obvious that the behavior of optical probes in liquid/solid and gas/solid systems are quite different. Calibration from a liquid/solid system can therefore not be used directly for measurement in a gas/solid system.

In using optical probes for measuring local voidage of fluid-particle suspensions, it is also essential to know the size distribution of the particles since the output of probes are considerably dependent on the size of particles as shown in Figure 4-11. This feature is useful in detecting the change of particle size distribution.

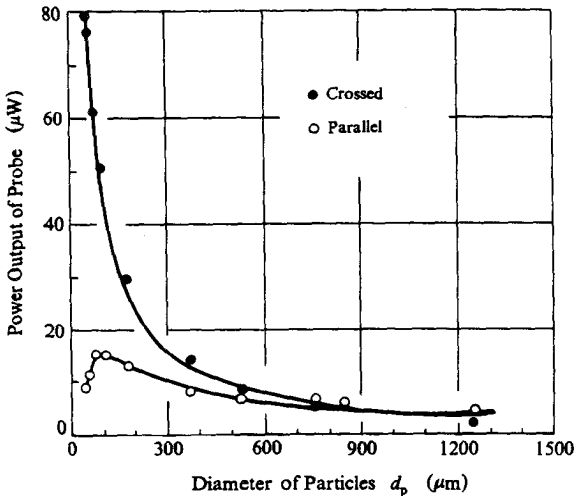

Figure 4-11 Effect of Particle Diameter d_p on Probe Output for Fixed Beds of Uniform Glass Beads

4.1.4 Measurement of Phase Structures

As mentioned in previous chapters, fluid-particle two-phase flow is characterized by a two-phase structure consisting of a particle-rich dense

phase (emulsion or cluster) and a fluid-rich dilute phase (bubble or broth). For understanding such a heterogeneous structure, several parameters, such as voidage in the dilute phase ε_f, voidage in the dense phase ε_c, the volume fraction of the dense phase f and the dimension of the dense phase l, should be evaluated.

Voidages ε_f, ε_c and dense phase fraction f can be determined approximately by using the above mentioned optical fiber probe. Figure 4-12a shows the instantaneous response of a crossed optical probe to bed density in a fluidized bed and the corresponding probability density distribution $p(\varepsilon)$ with its integral $\int_1^\varepsilon p(\varepsilon)\mathrm{d}\varepsilon$ called probability distribution. There are clearly two peak values and a valley value on the $p(\varepsilon)$ curves. These two peaks corresponds to ε_f and ε_c respectively, and the valley can be considered to represent the boundary between the two phases, and therefore, the value of the probability distribution $\int_1^\varepsilon p(\varepsilon)\mathrm{d}\varepsilon$ corresponding to the valley defines the volume fraction of the dilute phase $(1-f)$.

Figure 4-12b shows by comparison the measurement results by a parallel optical fiber probe, and recapitulates the distortion shown in Figure 4-8, for which ε_f cannot reach unity since the localizability of voidage measurement by the parallel optical probe cannot be guaranteed.

The phase dimension is difficult to measure, that is, the diameter of bubbles when the dense phase is continuous, and the size of clusters when the dense phase becomes discontinuous. Much has been reported concerning the measurements of bubble diameter and cluster diameter. For measuring cluster diameter, the cross correlation method was used, which gave however only the dimension of a cluster in the vertical direction. For direct observation of clusters, Qin and Li (1991) designed an optical fiber micrograph probe connected to a videocamera. The signals from videocamera were collected on an image processing plate, and then displayed on a TV monitor. Figure 4-13 shows the observation of clusters of Li *et al.* (1991) in a fast fluidized bed at different radial positions and under different operating conditions. The existence of clusters is obvious even in the core region of the bed.

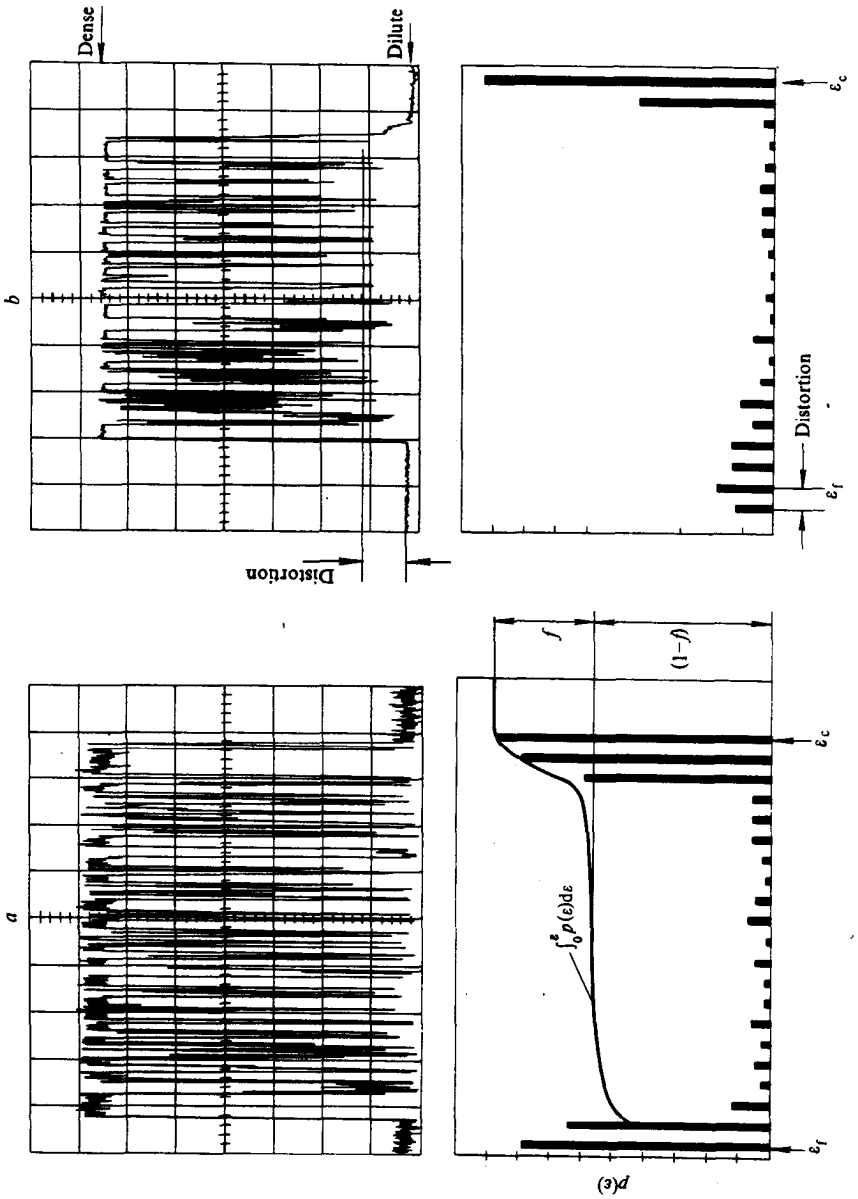

Figure 4-12 Determination of ε_f, ε_c and f by Using Optical Probe
a — crossed probe; b — parallel probe

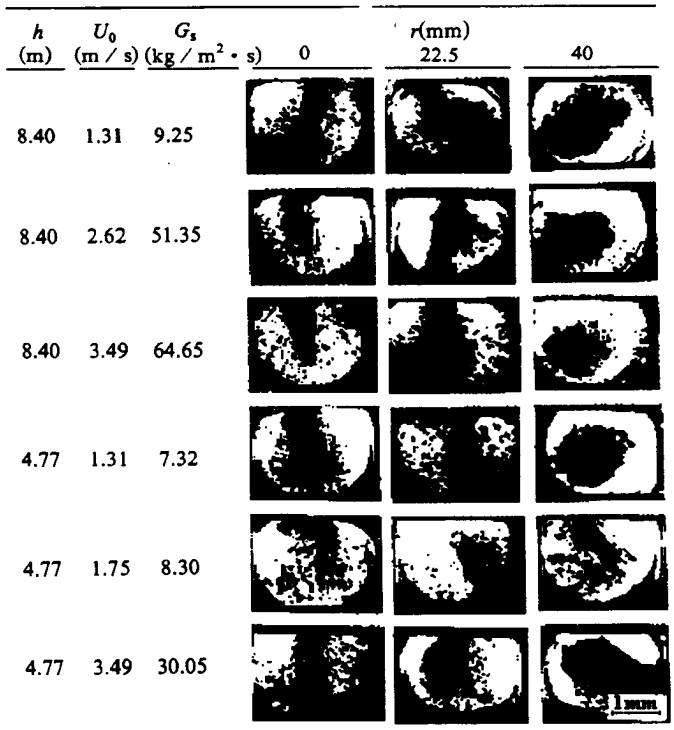

Figure 4-13 Variation of Cluster Structure with Operating Conditions, Radial and Axial Positions (Li *et al.*, 1991)

In fact, the dimension of bubbles or clusters is not so critical to fluid-particle contacting, as the exchange between the two phases, such as results from the alternate dissolution and reformation of clusters. This appears to be a key factor for future studies.

4.1.5 Measurement of Particle and Fluid Velocities

Global Average Fluid and Solids Velocity Global average velocities of both fluid and solids are independent parameters belonging to operating conditions. The measurement of average fluid velocity is more

or less standardized, using rotameter, orifice, etc. The measurement of average solids velocity can be conducted by inserting a screen-type butterfly valve into the loop. The average velocity which is correlated with solids circulating rate can be deduced from the rate of increasing pressure drop above the valve after it is closed. A simple method for such measurement was proposed by Wu *et al.* (1993), in which one strain gauge is mounted directly on the butterfly valve and another on the inside wall of the unit (to eliminate the effect of gas flow), as shown in Figure 4-14. When the butterfly valve is closed, the output of the Wheatstone bridge, consisting of the two strain gauges and two standard resistances, increases linearly with time, as shown in Figure 4-15. The slope of the output curve corresponds to the solids flow rate. Solids flow rate can also be measured by by-passing the particles into a collector for weighing. However, the operating conditions are thereby disrupted.

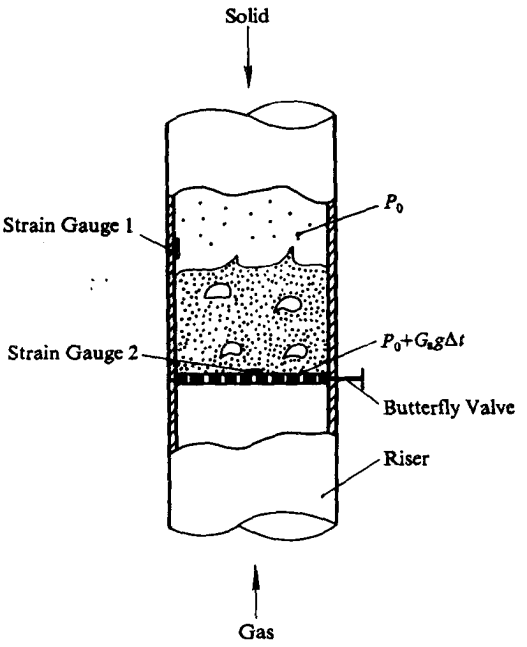

Figure 4-14 Measurement System for Solids Flow Rate

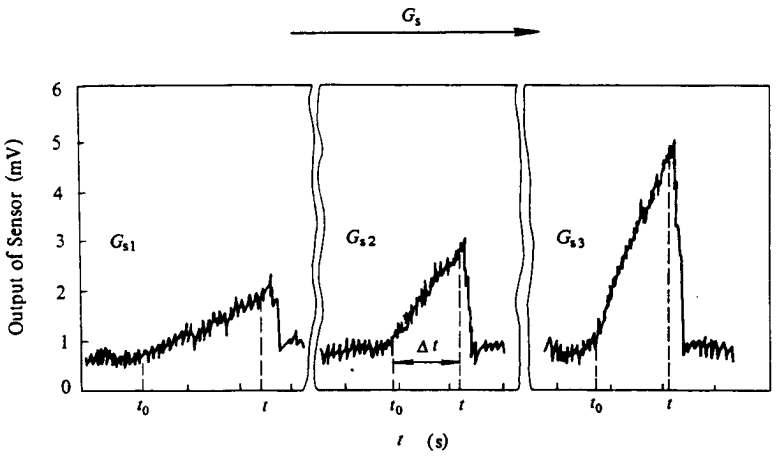

Figure 4-15 Increasing Wheatstone Bridge Output During Solids Flow Rate Measurement

Local Particle Velocity The local fluid dynamic state in CFB is characterized by the time dependence of not only particle concentration but also particle velocity. Nevertheless, neither the directly time-averaged value nor the arithmetic expectation value of particle velocity at different time is a true representation of the average particle velocity. The reason resides in the definition of

$$u_p = \frac{G_s}{\rho_p(1-\varepsilon)} \tag{4.1}$$

where $(1-\varepsilon)$ is the time-averaged particle concentration, G_s is the time-averaged solids flux, defined respectively as

$$\varepsilon = \frac{1}{T}\int_0^T \varepsilon(t)\mathrm{d}t \tag{4.2}$$

and

$$G_s = \frac{1}{T}\int_0^T G_s(t)\mathrm{d}t = \frac{\rho_p}{T}\int_0^T u_p(t)[1-\varepsilon(t)]\mathrm{d}t \tag{4.3}$$

Substituting G_s into Equation 4.1, we have

$$u_p = \frac{1}{T(1-\varepsilon)} \int_0^T u_p(t)[1-\varepsilon(t)]dt \neq \frac{1}{T} \int_0^T u_p(t)dt \qquad (4.4)$$

The above equation implies that time averaging of the instantaneous particle velocity has to be weighted with respect to *particle concentration* at the same time, though the average superficial velocity can be averaged directly over time, that is,

$$U_d = u_p(1-\varepsilon) = \frac{1}{T} \int_0^T U_d(t)dt \qquad (4.5)$$

Therefore, local average particle velocity can be obtained by either of the following two ways:

1. *Measuring real velocity and bed structure simultaneously, and then calculating the particle-concentration-weighted average of the real velocity;*
2. *Measuring superficial velocity or flux, and then averaging directly over time.*

The cross-correlation method, correlating the signals from two different points located a specified distance apart, supplies approximately the real particle velocity which should not, however, be time-averaged directly. Bed structure has to be considered for getting the average particle velocity. For the momentum method, the signal is related to the momentum of the particles, that is, $U_d \rho_p u_p$, which is a mixed term consisting of both real and superficial velocities, and too, cannot be averaged over time.

According to the above analysis, an integral voidage/momentum probe, shown in Figure 4-16a, was designed by Qian and Li (1993). It consists of an optical fiber voidage probe having near linear response characteristics to bed density (Reh and Li, 1991), mounted very close to a pair of strain gauges. Strain gauge 1, which is very close to the measurement volume of the optical probe, responds not only to upflowing but also to downflowing particles, while strain gauge 2, which is parallel to the direction of flow, is used for temperature compensation. These two strain gauges are connected with two standard resistances to form a

Wheatstone bridge to respond to the instantaneous dynamic pressure of particles. The simultaneous voidage and dynamic pressure signals were sent to a computer for data acquisition and processing. The instantaneous dynamic pressure of particle-fluid two-phase flow is attributed to both particle and gas, represented as

$$P(t) = \frac{1}{2}\{\rho_f \varepsilon(t) u_f^2(t) + \rho_p[1 - \varepsilon(t)] u_p^2(t)\} \tag{4.6}$$

For the case of high particle concentration, the dynamic pressure of gas can be neglected, and the instantaneous particle velocity can be obtained from the corresponding instantaneous voidage $\varepsilon(t)$ and dynamic pressure $P(t)$ as follows:

$$u_p(t) = \sqrt{\frac{2P(t)}{\rho_p[1 - \varepsilon(t)]}} \tag{4.7}$$

For very dilute suspensions, $u_p(t) \approx u_f(t)$, the contribution of the gas to $P(t)$ should be taken into account, and $u_p(t)$ can be expressed as

$$u_p(t) = \sqrt{\frac{2P(t)}{\rho_p[1 - \varepsilon(t)] + \rho_f \varepsilon(t)}} \tag{4.8}$$

By assuming that the strain gauge responds to the impact of particles as gas with the same dynamic pressure, the momentum sensor could be calibrated against the dynamic pressure of air flow measured by a pitot tube, as shown by the curve in Figure 4-16b. The optical probe was calibrated by correlating the probe output at minimum fluidization and that in pure air by assuming a linear relation. By programming the computer with the above correlations and calibrations, the instantaneous values of voidage, particle dynamic pressure, real particle velocity and superficial particle velocity can be obtained on line, thus yielding the average particle velocity as defined by Equation 4.4. The probe was tested in a CFB of 75 mm I.D. and 10 m high with FCC ($d_p = 54$ μm, $\rho_p = 930$ kg/m^3) fluidized by air.

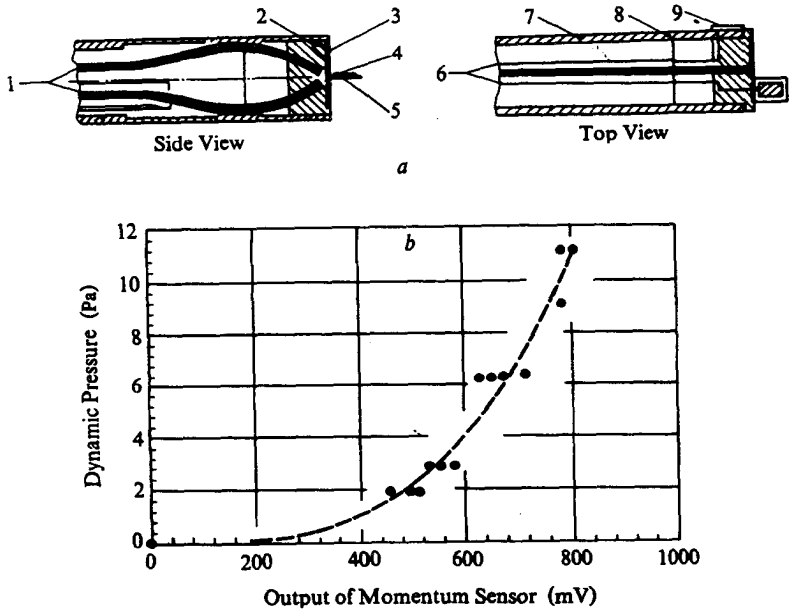

Figure 4-16 The Integral Voidage/Momentum Probe
a — probe configuration (1 — optic fiber;
2 — fiber fixing; 3 — optical glass;
4 — strain gauge 1; 5 — strain beam;
6 — wires; 7 — sheath;
8 — resin; 9 — strain gauge 2)
b — calibration

Figure 4-17a shows the output signals of the optical fiber sensor and the strain gauge Wheatstone bridge ($H = 6.5$ m, $r/R = 0.8$). The voidage signal shows the alternate change of dense phase and dilute phase in CFB, while the dynamic pressure signal is subject not only to voidage but also to particle velocity, therefore showing another pattern of change.

Figure 4-17b shows the instantaneous particle real velocity and the corresponding superficial velocity deduced from Figure 4-17a according to Equation 4.7 and 4.8. Compared to Figure 4-17a, Figure 4-17b also indicates the two-phase flow structure—high superficial velocity and low real velocity in the dense phase, but the opposite in the dilute phase. The time-series of real particle velocity in Figure 4-17b was averaged

directly over time, resulting in an average value of 0.79 m/s. However, a value of 0.53 m/s was obtained when the time average was weighted with respect to bed density as shown in Figure 4-17a.

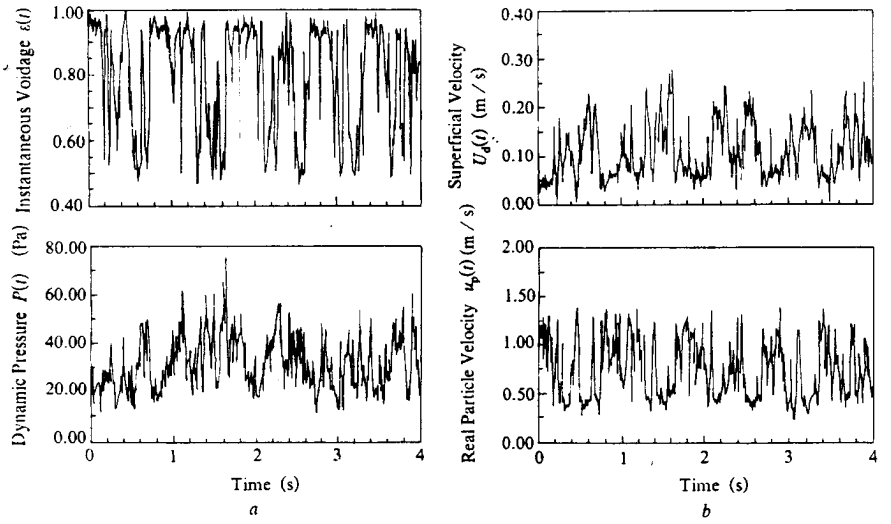

Figure 4-17 Probe Outputs and the Deduced Velocities
a — probe outputs; b — deduced velocities

4.1.6 Measurement of Gas Backmixing

Particle downflow causes gas backmixing in vertical concurrent two-phase flow, which affects the performance of a chemical reactor. Some understanding on flow patterns could be gained from gas backmixing (Stephens *et al.*, 1967; Nguyen *et al.*, 1981; van Deemter, 1980; 1985; Cankurt and Yerushalmi, 1978; Brereton et al., 1989; Jin *et al.*, 1992) to supplement, or in the absence of, local fluid and particle velocity measurement. Though the backmixing method does not give a true description of flow pattern, it provides some evaluation of reactor performance.

Two methods are available for measuring gas backmixing in fluidized beds: upstream pulse injection of a tracer gas for measuring residence

time distribution of the gas, from which the axial gas dispersion coefficient is deduced, and downstream continuous injection of a tracer gas for measuring upstream tracer concentration profile, from which the axial gas dispersion coefficient can also be obtained. Figure 4-18 compares these two methods. Downstream injection insures a steady tracer concentration profile for accurate measurement, but tracer consumption is high. Though upstream pulse injection saves tracer gas, it calls for dynamic measurement and is therefore complicated. Selection of the measurement method depends on the characteristics of the system studied. If backmixing is slight and the system rather homogeneous, the pulse injection is generally used. Otherwise, the steady injection is preferred.

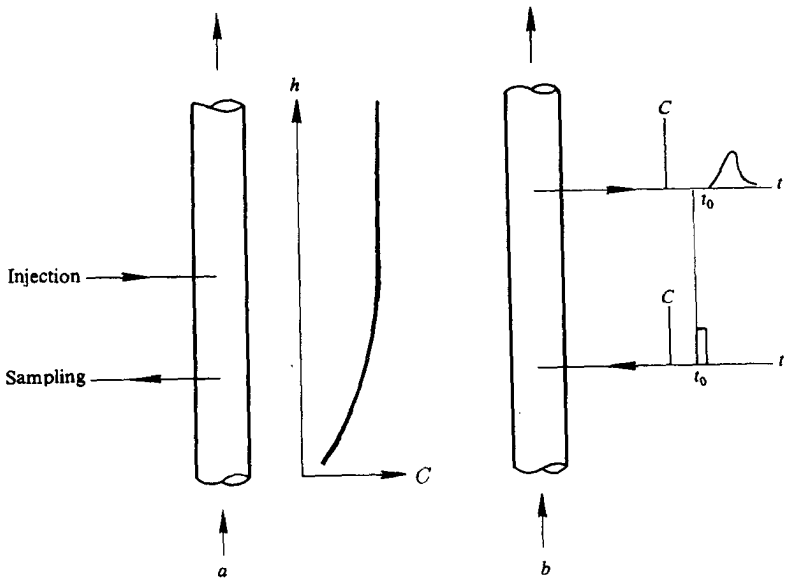

Figure 4-18 Tracer Injection Methods for Studying Gas Backmixing
a — downstream steady injection;
b — upstream pulse injection

Li and Weinstein (1989) selected the steady injection method for comparing gas backmixing characteristics in different fluidization regimes,

in a high-velocity fluidization facility, 0.152 m in diameter by 8 m tall, using helium as the tracer gas in order to eliminate gas adsorption by the bed material they used, Engelhard craking catalyst FFZ-33 (ρ_p = 1450 kg/m^3, d_p = 59 μm). A steady stream of tracer gas was injected at a single point by a traversing probe which could be located at seven different radial positions, as shown in Figure 4-19. Tracer gas was injected consecutively at all these seven points to give seven different samples for four fixed radial sampling locations of each sampling probe. By changing the solids inventory or the solids rate, it was possible to have the injector located in the top dilute, the middle transition or the bottom dense region, even though its elevation was fixed. Sample probes were located at three elevations below the injector. The inlets of the probes were covered by cylinders of porous sintered metal. The combination of the sampling probe position number and the injector location letter shows the condition of sampling and injection. For example, A1 means sampling gas with the first probe when the injector is located at both positions A.

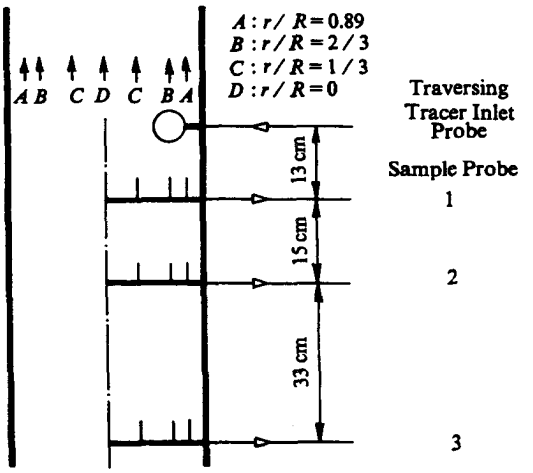

Figure 4-19 Positions for Downstream Injection and Upstream Sampling in Experiments of Li and Weinstein (1989)

The sample gas and the reference gas from the bottom of the bed were drawn into an on-line GOWMAC thermal conductivity analyzer connected to a computer-based data acquisition system. For each run, the axial voidage profile was observed and adjusted in order to locate the injection probe in the desired region. Data used to obtain the axial voidage profile were taken simultaneously with the backmixing data in order to correlate the mixing measurements with the bed structure.

The effects of the completely mixed helium injection concentration, C_o, on gas backmixing was investigated first to determine the optimal value of the injection concentration with respect to linearity and detectability for each flow regime. The response of the helium concentration at several points to changing injection concentration is shown in Figure 4-20 for the dense region of fast fluidization. The variation of C with C_o is linear only at the lower values of C_o, particularly for probe position A1. Therefore, the injection concentration was limited to a maximum of about 0.7 % in this regime. For all other regimes appropriate limits were set by testing. In general, the lowest C_o possible was used considering the detectability of helium with the analyzer.

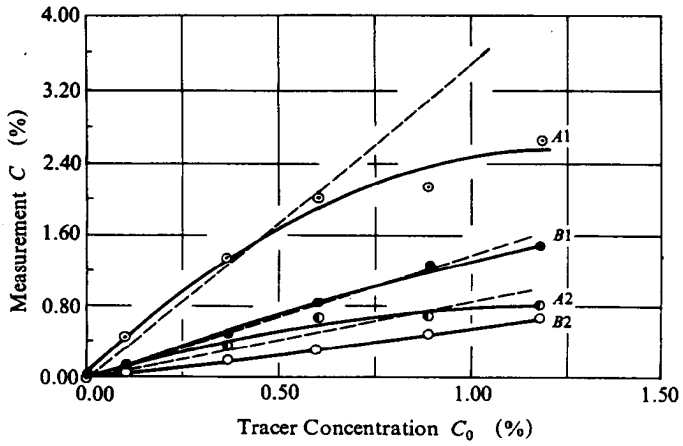

Figure 4-20 Dependence of Backmixed Tracer Concentration on Average Injection Concentration (fast fluidization regime: $r/R = 0.922$, $U_g = 2.8$ m/s, $G_s = 200$ kg/(s · m^2), $I = 2.5$ m)

4.2 Experimental Results

4.2.1 Phase Structure

Figure 4-21 shows the time series of local bed voidage taken with a reflection-based optical fiber probe designed by Qin and Liu (1982) which was located at the center of the bed. High voltage value represents high bed density, and zero voltage corresponds to bubbles or the dilute phase. In the bubbling and slugging regimes, the local voidage changes periodically at a low frequency. With increasing expansion, the fraction of the dense phase decreases, demonstrated by a decrease in the high voltage component. No essential difference exists between the bubbling and slugging regimes except that local turbulent behavior can be noted only occasionally in the slugging regime. When slugging is succeeded by turbulent fluidization as velocity increases, high-frequency random changes replace the periodic low-frequency changes. The waveform of the signal in the fast regime is almost the same as that in the turbulent regime. In the above-mentioned regimes, the peak-to-valley ratio of the signals remains constant, implying that both the dense-phase voidage and the dilute phase voidage remain more or less constant, and change in overall bed voidage can therefore be attributed merely to change of the volume ratio of the two phases. When the dilute transport regime starts. such a situation is totally changed—the voltage for the dilute-phase increases, and the dense-phase almost disappears. This results in a more or less uniform structure demonstrated by the rise of the base line of the signal above zero. Such a jump change in bed structure is consistent with the prediction in Figure 3-13.

Figure 4-22 shows the values of ε_f, ε_c, and f in a two dimensional fluidized bed of FCC catalyst, determined by using the method described in Section 4.1.4, also showing the constancy of both ε_f, and ε_c and a steady decrease of f with increasing gas velocity, and verifying the calculated results in Figure 3-4.

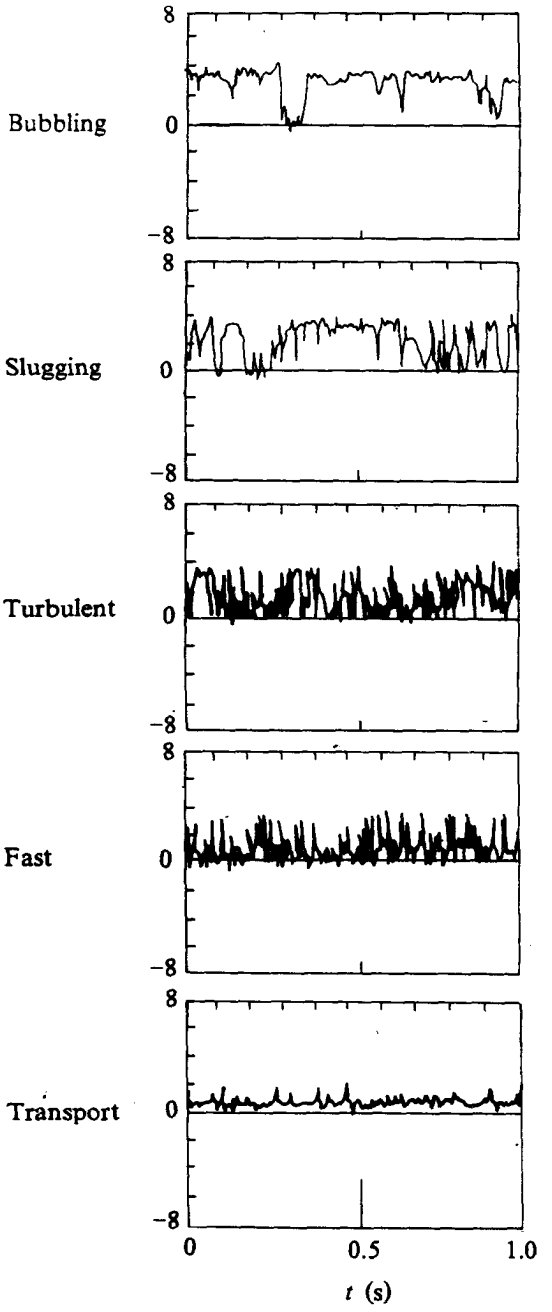

Figure 4-21 Measured Instantaneous Voidage in Different Regimes (FCC/air)

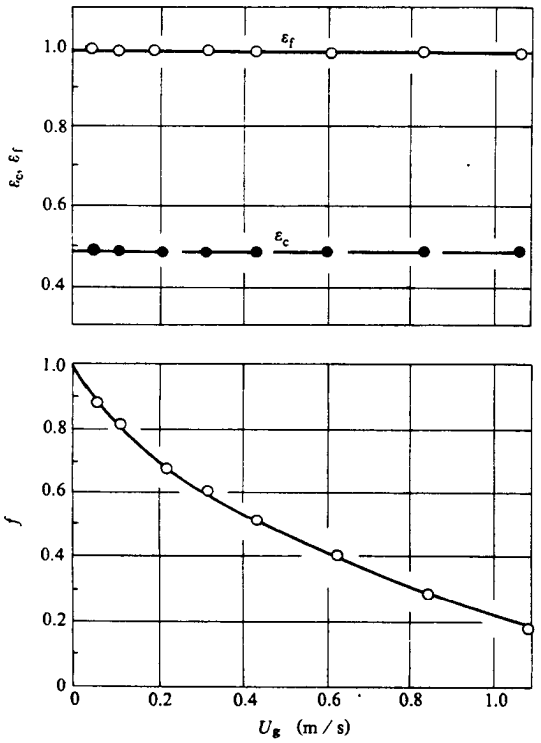

Figure 4-22 Experimental Evaluation of $\varepsilon_f, \varepsilon_c$ and f by Using Optical Fiber Probes

4.2.2 Regime Transition

Bed Structure

Figure 4-21 shows three types of flow structures which often exist in fluidization of fine particles: Low-frequency-periodic in bubbling and slugging fluidization, high-frequency-random in turbulent and fast fluidization and near-uniform in dilute transport. Comparison of these experimental phenomena with the theoretical analysis in Chapter 3, yields the following indications:

1. *In low velocity fluidization, as analyzed in Section 3.4, where the fluid and the particles compromise with each other, the particles still retain some dominance, and the fluid compromises more actively with the less mobile particles in the emulsion phase, as demonstrated by a low-frequency periodic structure of the particle-fluid system.*

2. *With increasing velocity and momentum of the fluid, the particles continue to lose their dominance, as the continuous dense phase begins to be broken up, until at* $f = 0.5$, *discrete clusters are formed which can compromise flexibly with the fluid. At this stage, both the fluid and the particles are equally active in compromising with each other, resulting in the formation of a high-frequency random structure. With further increase in the velocity and momentum of the fluid, the fluid begins to take over the particles in dominating the system.*

3. *As soon as the fluid fully dominates the particles, in the transport regime, the system becomes nearly uniform.*

Auto-Correlation Coefficient (time-dependent)

Figure 4-23a was obtained by analyzing the data in Figure 4-21 statistically with a spectrum analyzer in terms of the auto-correlation coefficient defined as

$$R_X(\tau) = \lim_{T\to\infty} \frac{1}{T} \int_0^T X(t)X(t+\tau)\mathrm{d}t$$

which represents the linear dependence between two states of *the same process at two different time transients*, that is, *time-dependence* of flow structure. In Figure 4-23a, R_{xx} is the normalized $R_X(\tau)$, R_{xx} being equal to unity at $\tau = 0$. For random signals, R_{xx} should tend toward a constant when $\tau \to \infty$, implying that the two states of this process at two different time transients are not dependent of each other. On the contrary, for the periodic process, R_{xx} will also be periodic with the same frequency as the original signal. From the change of the auto-correlation coefficient, we can deduce the time-dependent behavior of the local states in fluidization systems. Corresponding to the changes of bed structures, three types of time-dependent behavior are therefore

seen to exist in the whole spectrum of fluidization regimes: periodically strong dependence in the low expansion regime for bubbling and slugging, random weak dependence in the high expansion regime for turbulent and fast, and high constancy in the dilute transport regime with near-uniform structure.

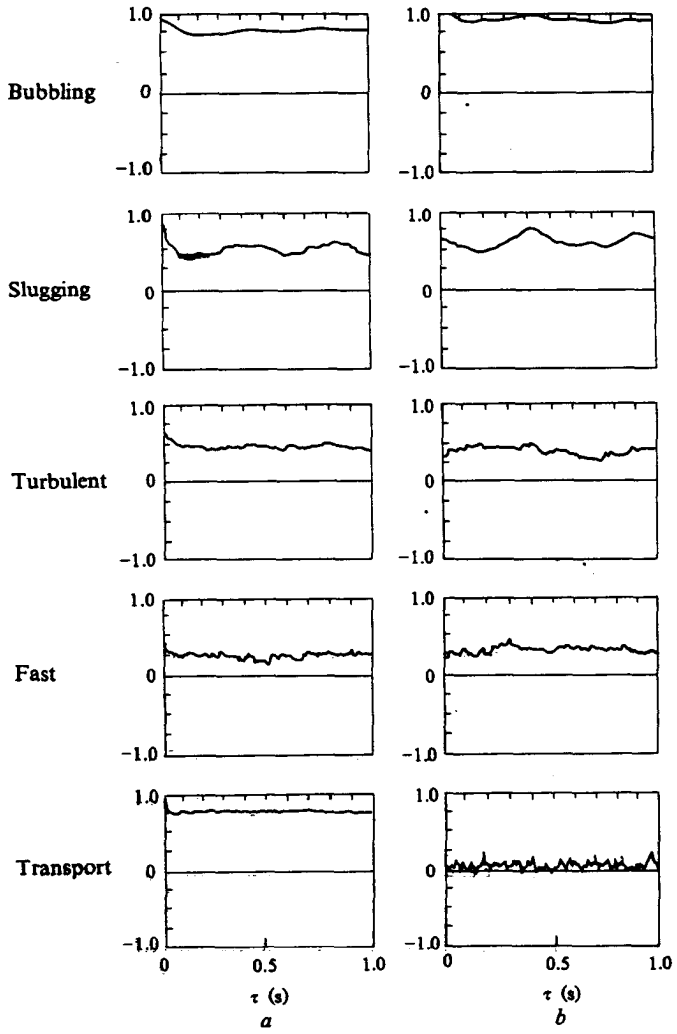

Figure 4-23 Correlation Coefficients in Different Regimes (FCC/air)
a — auto-correlation R_{xx}; b — cross correlation R_{xy}

Such changes of flow structure verify the predicted characteristics of the PFC and the FD operations.

Cross-Correlation Coefficient (space-dependent)

Figure 4-23b shows the cross-correlation coefficient of voidage signals for two different points at a distance of 0.5 m apart, defined as

$$R_{xy}(\tau) = \lim_{T\to\infty} \frac{1}{T} \int_0^T X(t)Y(t+\tau)dt$$

which represents the linear dependence between *two signals from two different locations*. R_{xy} is the normalized $R_{xy}(\tau)$. Compared with the auto-correlation coefficient reflecting time dependence of the process, the cross-correlation coefficient stands for *space-dependence*. By evaluating both auto-correlation and cross-correlation coefficient, it is possible to identify the change in structure for fluidization systems. It can be seen from Figures 4-23a and 4-23b that the cross-correlation coefficient displays a similar change as the auto-correlation coefficient except for a sudden decrease in the dilute transport regime which indicates independence in behavior of the two points in space.

Slip Velocity

Figure 4-24 shows the change of slip velocity averaged over the cross-sectional area, defined as

$$\overline{U}_s = U_g - \frac{G_s\overline{\varepsilon}}{(1-\overline{\varepsilon})\rho_p}$$

where $\overline{\varepsilon}$ is an average bed voidage determined from the axial voidage profiles, to be shown later in Figure 4-31 and Figure 4-33, averaging being carried out separately for the bottom dense region and the top dilute region. No significant change can be found in the range of turbulent and fast fluidization. With the onset of dilute transport, however, $\overline{U}_s$ drops suddenly to a relatively low value toward the terminal velocity U_t of the particles. It is worthwhile to note that in the saddle area below the dashed line two states co-exist for Mode PFC/FD of Figure 3-4, a dense

PFC region at the bottom of the bed, and a dilute FD region at the top, joined together to form an S-shaped axial average voidage profile. The saddle area contains a family of tie lines, each terminating into the PFC region at the left and the FD region at the right. The change of slip velocity demonstrated in Figure 4-24 is consistent with that shown in Figure 3-9b except for the difference in approach to U_t in the FD regime, which is attributed to the assumption of ideality in Figure 3-9b.

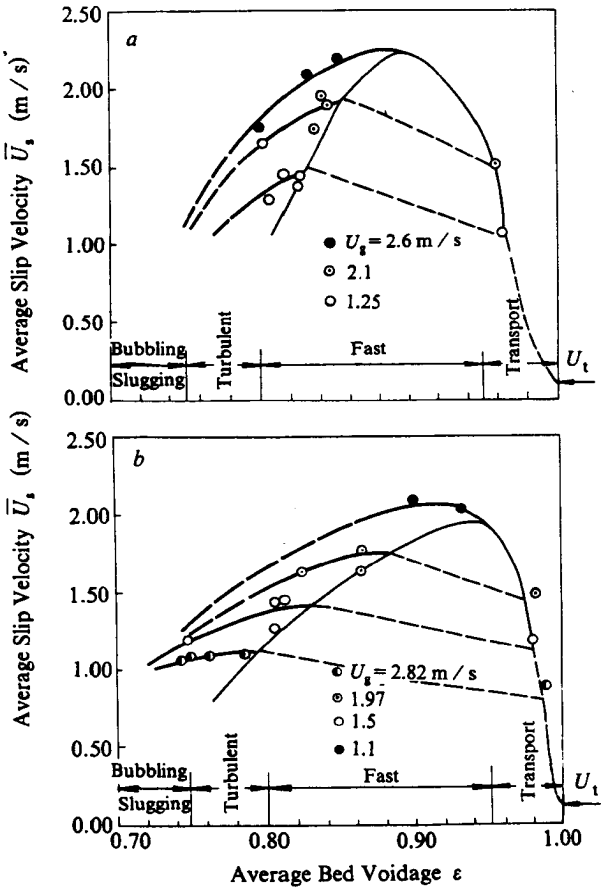

Figure 4-24 Sudden Drop of Slip Velocity at Fast/Transport Transition
a — FCC/air (ρ_p = 930 kg/m^3, d_p = 54 μm);
b — hollow glass beads/air (ρ_p = 609 kg/m^3, d_p = 75 μm)

Radial Voidage Profile

Figure 4-25 was developed from data obtained in the same experimental unit operating under the same conditions as for Figure 4-21 and with the same optical probe which was calibrated by the method developed by Tung *et al.* (1988). For the bubbling and the slugging regimes, because of insufficiently developed particle downflow, the non-uniform profiles were mainly caused by the centripetal movement of bubbles. Although a certain degree of radial heterogeneity is caused by the wall, the PFC regime could be preserved in the center, and therefore, the radial profiles of local voidage are consequently rather flat. With the onset of turbulent fluidization, discrete bubbles no longer exist in the system, and gas flows mostly through the center of the unit. Such a gas flow pattern causes the disparity of flow structure between the core and the wall regions, that is, fluid-dominating (FD) in the core and particle-fluid-compromising (PFC) in the wall region, and enhances the circulation of particles—up in the center and down near the wall, therefore, creating remarkably steep voidage profiles. With the development of the

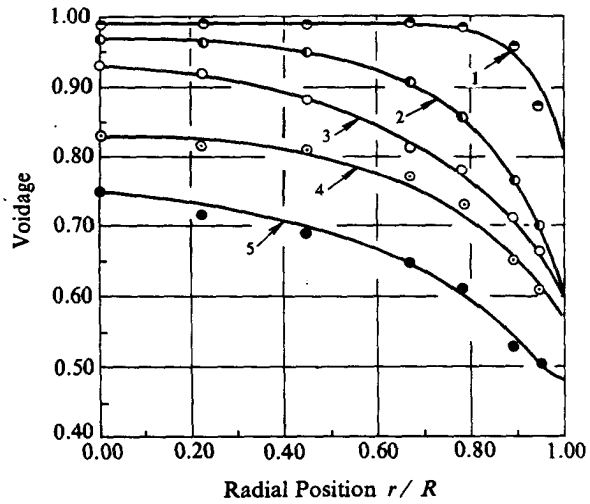

Figure 4-25 Radial Profiles of Average Voidage in Different Regimes (FCC/air)
1 — transport; 2 — fast; 3 — turbulent;
4 — slugging; 5 — bubbling

highly expanded regime from turbulent to fast, particle downflow becomes more and more extensive and the core FD region is extended to

the wall until a nearly flat voidage profile appears suddenly at the onset of dilute transport when the FD regime prevails essentially in the whole cross-section.

Gas Backmixing

Figure 4-26 also confirms the prediction of different flow structures in different regimes. Figures 4-26a and Figure 4-26b show the measurement results of gas backmixing in the bubbling and slugging regimes respectively, which are often referred to as low velocity or low expansion fluidization regimes. Comparing these regimes, no significant differences in the concentration profiles are found between wall injection, A, and centerline injection, D, except for the response of the first probe quite near the injection point. In these two regimes, the radial profiles of concentration are essentially flat and the injection position does not exert much significant effect on gas backmixing, and the dimensionless concentration C/C_o is almost independent of gas velocity (Li and Weinstein, 1989).

With the transition from the slugging regime to the turbulent regime, high velocity fluidization begins, and different gas flow patterns are evident. These are caused by and/or are the result of spatially distributed heterogeneity. The righthand side of Figure 4-26c shows results in the turbulent dense-phase regime. Different from the slugging regime, sharp radial concentration profiles exist, and the injection position has a great effect on the measured gas backmixing. For position C, the detected concentration is very low, and it is too low to detect for position D. Gas backmixing mainly results from the downflow of solid particles near the wall. The tracer gas concentration in the dilute core region is mainly due to exchange between the core region and the annular wall region. Gas backmixing in the transition or bed surface region of a turbulent bed is shown on the lefthand side of the figure. Although the injection point is located in a relatively dilute region, the extent of gas backmixing is not much less than in the turbulent dense region. Therefore, particle downflow in this transition region must be extensive.

In the fast fluidization regime at even higher gas velocities, the dilute core region extends further toward the wall, and the particle downflow

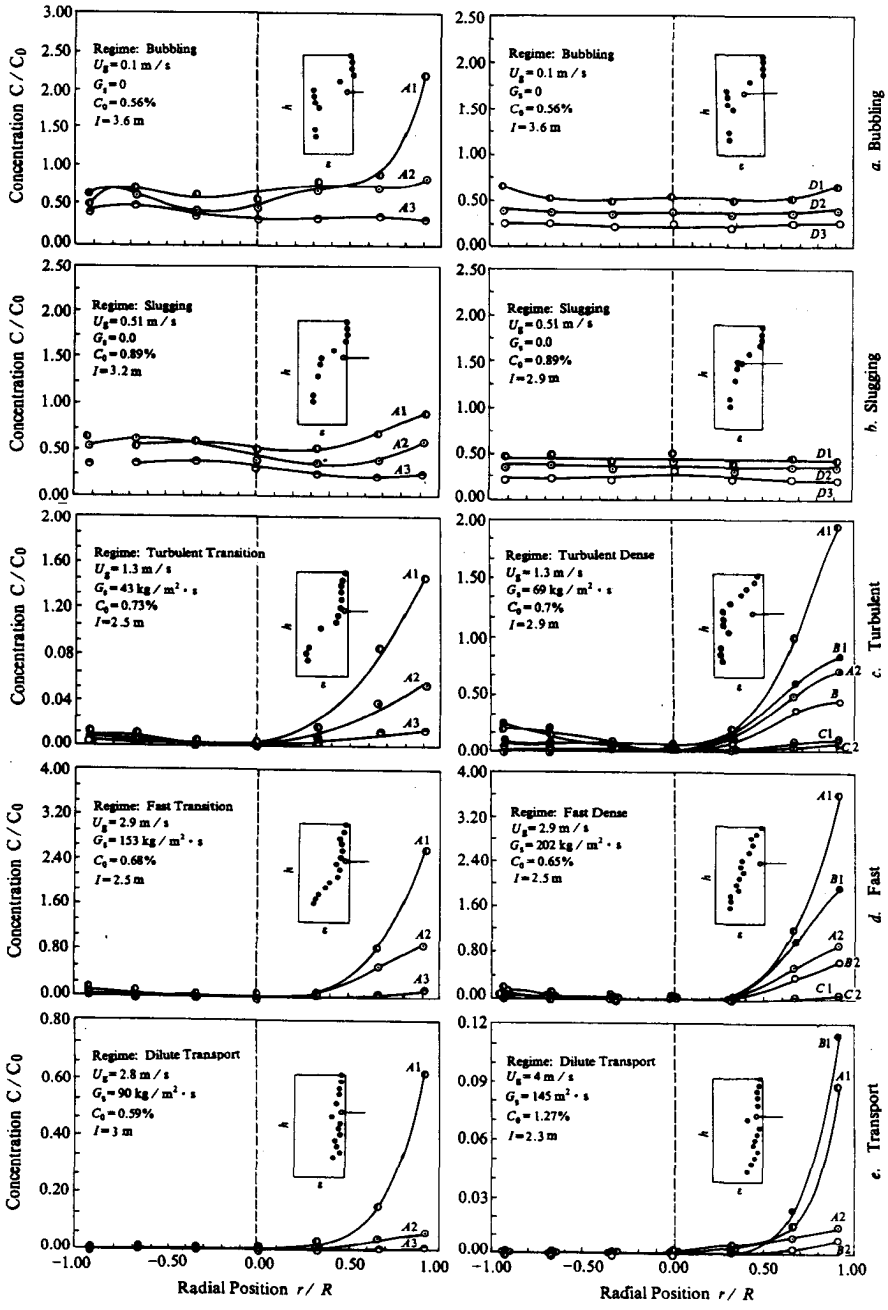

Figure 4-26 Experimental Results on Gas Backmixing in Different Fluidization Regimes

near the wall becomes even greater. These changes affect the concentration profiles as shown on the righthand side of Figure 4-26d. It can be seen that tracer concentration near the wall is much higher than that in the turbulent regime, but the concentration in the dilute core region is much lower. Injection in the core region produces a very low level of backmixed tracer concentration, even undetectable for the center injection. In this regime, the injection position has an even more critical effect on the concentration profile than in the turbulent regime. Therefore, the assumption of gas plug flow in the fast regime is not appropriate for the whole bed but only for the core. Note that circumferential mixing in the annular region is still measurable. The lefthand side of Figure 4-26d shows backmixing in the transition region, indicating that extensive backmixing prevails in the annular wall region.

Results for the dilute transport regime are shown in Figure 4-26e, demonstrating that there still exists an annular region near the wall in which gas backmixing due to solid downflow is considerable. The concentration of backmixed tracer gas is still detectable at probe position 2, 28 cm ($L/D = 2$) below the injection point. The dependence of backmixing on velocity is, however, strong in this regime with maximum C/C_o readings down by a factor of 6 with an increase in gas velocity from 2.8 to 4.0 m/s. In this regime, the difference between injection, A, and injection, B, becomes slight compared with the fast fluidization regime.

Figures 4-27 compares gas backmixing between different regimes, indicating the different mechanisms of gas backmixing in different fluidization regimes shown by quite different radial profiles of C/C_o at both probe position 1 and position 2: almost flat in the low velocity fluidization regimes, bubbling and slugging, very sharp in the high velocity fluidization regimes of turbulent and fast fluidization, and again flat in the dilute transport regimes, thus verifying the regime classifications in Section 3.4 and corresponding to the three types of bed structure noted at the beginning of Section 4.2.2.

Li and Weinstein(1989) calculated values of D_a as shown in Figure 4-28. In the low-velocity regimes, D_a is nearly proportional to gas velocity. These values agree well with those of van Deemter (1985) and Latham

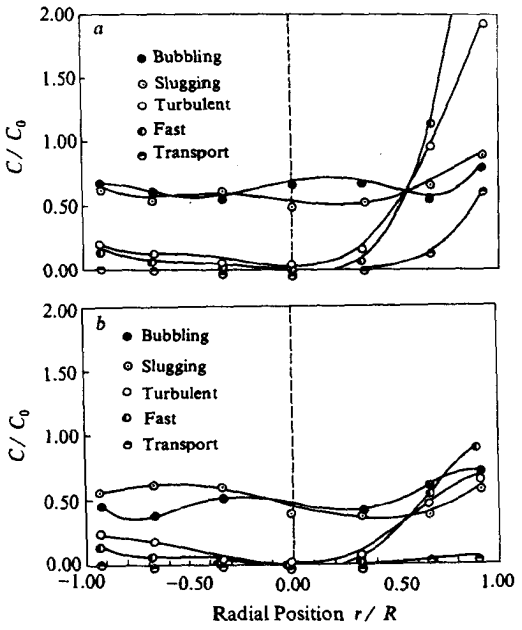

Figure 4-27 Comparison of Backmixing Intensities in Different Regimes at Two Probe Positions (Li and Weinstein, 1989)
a — probe position 1; b — probe position 2

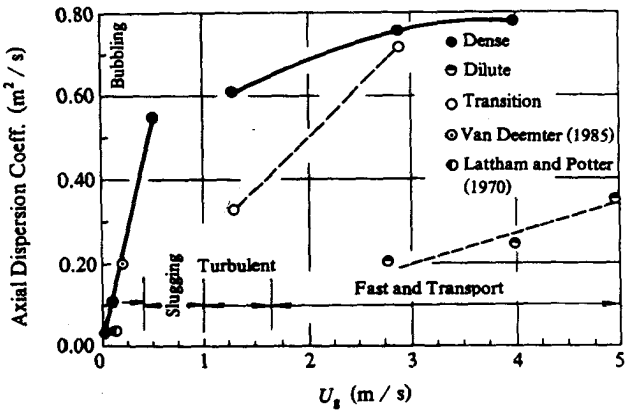

Figure 4-28 Axial Dispersion Coefficient as a Function of Gas Velocity over the Regime Spectrum

and Potter (1970), also shown in the figure. In the dense high-velocity regimes, the dependence of D_a on gas velocity becomes much less pronounced, and it appears that in the dilute transport regime D_a drops to

rather low values.

The two data points for the transition region between the top dilute and the bottom dense regions indicate a strong dependence on gas velocity, but the evidence is insufficient to make such a conclusion. The real significance of these values is that they indicate that backmixing in the transition region is almost as strong as in the dense region itself.

The three data points in the dilute transport regime show that backmixing in this regime is small but not negligible. These values are the least reliable of the set of D_a values because the corresponding measured concentrations were the lowest. However, their magnitudes can be considered to be correct.

4.2.3 Pattern Change

Experiments indicated that liquid/solid fluidization can also be aggregative under certain conditions, for instance, the appearance of liquid voids or particle clusters (Wilhelm and Kwauk, 1948). Yu (1986) compared the fluidization behavior of different liquid/solid systems consisting of water and the following particles:

particles	d_p (μm)	ρ_p (kg/m^3)
Sand	250 $\sim$ 440	2620
Magnetite	160 $\sim$ 183	4900
Iron	107 $\sim$ 142	7800
Copper	150 $\sim$ 160	8900

In Figure 4-29 his experimental results were rearranged according to increasing particle density: (a) shows the uniform or particulate flow structure with sand particles, (b) shows initial change of flow behavior from particulate to aggregative pattern, demonstrated by the deviation of experimental points from the linear log-log relationship between voidage and fluid velocity due to increase of particle density, (c) and (d) show obvious aggregative behavior in fluidized beds with high density particles characterized by a sudden and dramatic increase in voidage at

some critical fluid velocities. It can be concluded that L/S fluidization systems transit gradually from *particulate to aggregative* with increasing ρ_p/ρ_f as predicted by Kwauk (1957) and in Figure 3-21.

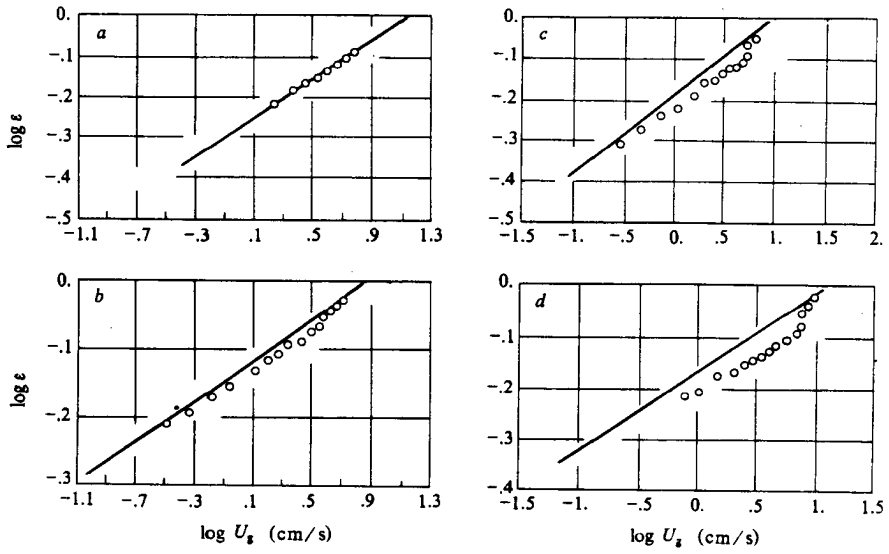

Figure 4-29 Increasing Aggregative Behavior of L/S Systems with Increasing ρ_p/ρ_f (Yu, 1986)
a — sand/water ($d_p = 250 \sim 440$ μm, $\rho_p = 2620$ kg/m^3);
b — magnetite/water ($d_p = 160 \sim 183$ μm, $\rho_p = 4900$ kg/m^3);
c — iron/water ($d_p = 102 \sim 142$ μm, $\rho_p = 7800$ kg/m^3);
d — copper/water ($d_p = 150 \sim 160$ μm, $\rho_p = 8900$ kg/m^3)

Pattern change can also take place with change of fluid viscosity as reported by Harrison (1961) and with change of pressure which affects the value of ρ_p/ρ_f, as demonstrated in pressurized fluidized beds. Recently, Knowlton (1992) reviewed the effect of pressure, temperature and viscosity on fluidization systems, and pointed out that fluidization becomes smoother when beds are operated at high pressures. The information on the effect of temperature on bubble size is somewhat inconsistent, as Knowlton mentioned, being the mixed effect of gas density and viscosity which are both affected by temperature.

4.2.4 Region Distribution

A typical fluid-particle two-phase flow system, such as the circulating fluidized bed, is characterized not only by local heterogeneous flow structure but also by overall distribution of bed density in both the axial and the radial direction.

Axial Direction

Li and Kwauk (1980) noted two regions in the S-shaped axial voidage profile in fast fluidization: a dilute-region at the top with an asymptotic voidage ε^* and a dense region at the bottom with another asymptotic ε_a. Between these two regions, there exists a transition zone in which the inflection point of voidage Z_i is located. Depending on material properties and operating conditions, the length of this transition zone is characterized by a so-called characteristic length Z_0 which can be correlated to $(\varepsilon^* - \varepsilon_a)$ empirically as follows (Li *et al.*, 1982):

$$Z_0 = 500 \exp\left[-69(\varepsilon^* - \varepsilon_a)\right]$$

Then, the axial voidage profile can be represented by

$$\frac{\varepsilon - \varepsilon_a}{\varepsilon^* - \varepsilon} = \exp[-(z - Z_i)/Z_0]$$

Weinstein *et al.* (1983) reported that axial voidage profile is also dependent on the imposed pressure drop across the bed ΔP_{imp}, that is, the position of the inflection point Z_i is affected by the solid inventory in the system. From pressure balance, Z_i can be expressed as

$$Z_i = \frac{H\rho_p g(1 - \varepsilon_a) - \Delta P_{imp}}{(\varepsilon^* - \varepsilon_a)\rho_p g}$$

It is clear that the axial voidage profile can be calculated if ε^* and ε_a are known, for which Li and Kwauk recommended the following correlations:

$$\varepsilon^* = 0.924 \left[\frac{18Re_p^* + 2.7Re_p^{*1.687}}{Ar}\right]^{0.0286}$$

where

$$Re_{\mathrm{p}}^{*} = \frac{d_{\mathrm{p}}\rho_{\mathrm{f}}}{\mu_{\mathrm{f}}}\left[U_{\mathrm{g}} - U_{\mathrm{d}}\left(\frac{\varepsilon^{*}}{1-\varepsilon^{*}}\right)\right]$$

$$Ar = \frac{d_{\mathrm{p}}^{3}\rho_{\mathrm{f}} \cdot g(\rho_{\mathrm{p}} - \rho_{\mathrm{f}})}{\mu_{\mathrm{f}}^{2}}$$

and

$$\varepsilon_{\mathrm{a}} = 0.756\left[\frac{18Re_{\mathrm{pa}} + 2.7Re_{\mathrm{pa}}^{1.678}}{Ar}\right]^{0.0741}$$

where

$$Re_{\mathrm{pa}} = \frac{d_{\mathrm{p}}\rho_{\mathrm{f}}}{\mu_{\mathrm{f}}}\left[U_{\mathrm{g}} - U_{\mathrm{d}}\left(\frac{\varepsilon_{\mathrm{a}}}{1-\varepsilon_{\mathrm{a}}}\right)\right]$$

Li *et al.* (1988) studied the dependence of axial voidage profile on $G_{\mathrm{s}}, U_{\mathrm{g}}$ and ΔP_{imp} in a circulating fluidized bed of 90 mm I.D. by using the scanning transducer-valved system. The imposed pressure drop ΔP_{imp} was altered by changing the solids inventory I, or by manipulating the solid rate-control valve.

Figure 4-30 shows the dependence of axial voidage profiles on gas velocity. If the gas velocity increases without changing the solid inventory, the difference between the bottom dense region and the top dilute region will reduce, accompanied by an increase of solids flow rate, until the difference disappears. It is evident that solids flow rate is dependent on gas velocity.

Figure 4-31 verifies the prediction in Figure 3-4, showing the dependence of axial voidage profiles on solids inventory for FCC ($\rho_{\mathrm{p}} = 929.5$ kg/m^3, $d_{\mathrm{p}} = 54$ μm). Two kinds of voidage profile curves are shown. The curves for $I = 15,\ 20$ kg in Figure 4-31a and $I = 15,\ 20,\ 22$ kg in Figure 4-31b

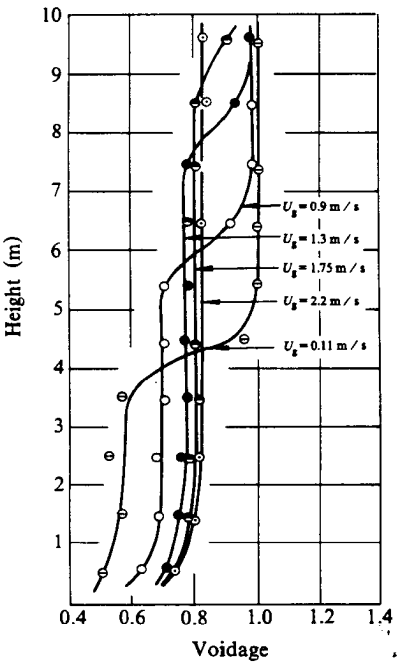

Figure 4-30 Dependence of Axial Voidage Profiles on Gas Velocity at a Constant Solids Inventory (FCC/air: I = 40 kg; G_s = max)

are S-shaped, with the co-existence of two regions, and transition occurring inside the unit, while solid can be fed at the bottom of the bed at saturation flow rates. Variation of solids inventory I does not result in any change of G_s, ε^* and ε_a, but only displaces the position of the inflection point Z_i . Solids rate G_s is always equal to the saturation carrying capacity at the corresponding gas velocity (K^* = 14.3 kg/(m^2 · s) for U_g = 1.52 m/s; K^* = 24.1 kg/(m^2 · s) for U_g = 2.1 m/s). Asymptotic voidages for the dilute and dense phases, ε^* and ε_a respectively, are only functions of U_g and relevant material properties.

At $G_s = K^*$, any change in the opening of the solid-rate control valve can only upset the initial equilibrium temporarily. For instance, if the opening is decreased, the input solid rate becomes smaller than K^* temporarily. However, the output solid rate still remains at K^*, thus,

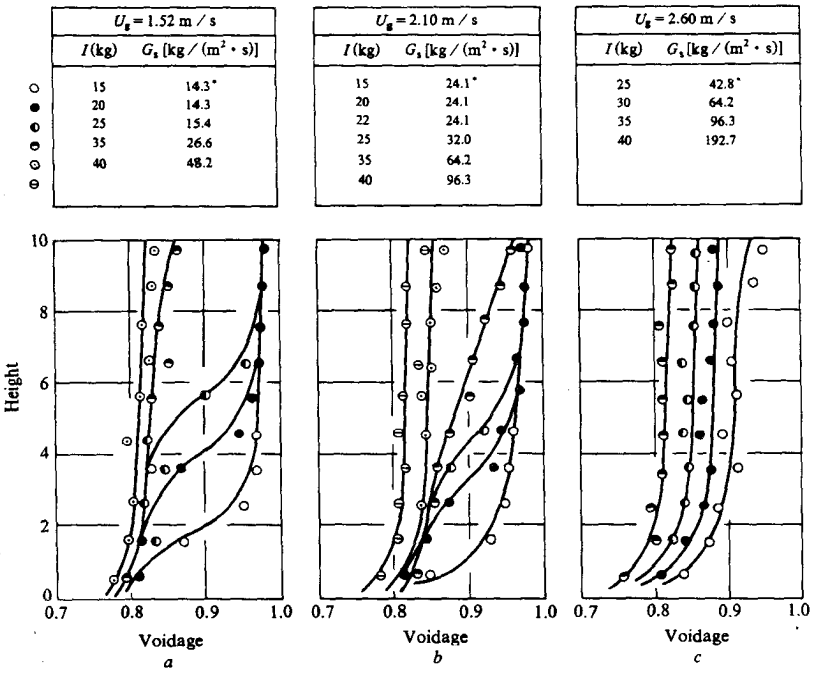

Figure 4-31 Axial Voidage Profiles for System FCC/air
(* data used in Figure 3-7)

depleting the fast bed of solids. Meanwhile the voidage of the dilute region at the top ε^* also remains constant. As a result, the dilute-phase region extends toward the bottom of the bed. The excess solids which have thus far been removed from the fast bed have accumulated in the slow bed, thus increasing the imposed pressure at the bottom, forcing more solids flow into the fast bed. This dynamic process continues until G_s equals K^* again, but at a new equilibrium position of the point of inflection Z_i, which is lower than before.

On increasing I, the inflection point in the axial voidage profile will move upward until it passes beyond the top of the bed. In the latter case, $G_s > K^*$, and a new operating region is reached, in which the axial voidage profiles are no longer S-shaped, as shown by all the curves in

Figure 4-31c and by the curves for I = 25, 35, 40 kg in Figure 4-31a and 4-31b. On the other hand, decreasing I will make the inflection point Z_i move downward until it passes beyond the bottom of the bed, with $G_s < K^*$. In this operating region, the flow pattern becomes dilute transport , and neither is the voidage profile S-shaped. In the two operating regions for $G_s < K^*$ and $G_s > K^*$, G_s is independent of U_g and can be changed independently. Therefore, the bed voidage would be related to both U_g and G_s; axial voidage profiles are not S-shaped; and any change in I would result in a corresponding change in G_s.

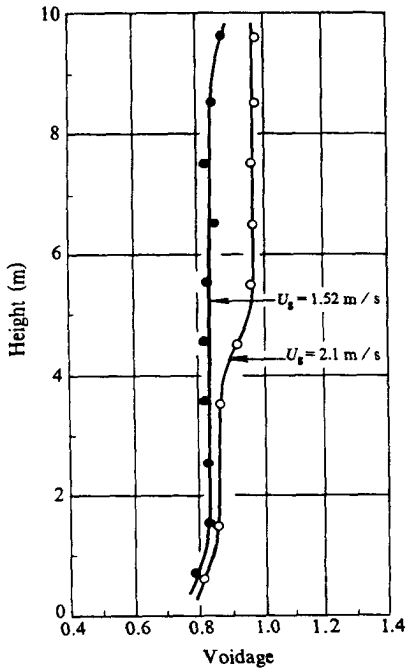

Figure 4-32 Variation of Axial Voidage Profile with Gas Velocity at Constant Solids Flow Rate (FCC/air: I = 30 kg; G_s = 25 kg/(m^2 · s))

If the solid-control valve is fully closed at the state of an S-shaped profile, the local states of both regions will not change, however the top dilute region will extend toward the bottom with a constant solid flow rate K^* until the dense region disappears, the whole bed becomes dilute, and the particles in the bed start to be blown out, and finally the bed becomes empty.

Figure 4-32 shows the dependence of axial voidage profile on gas velocity at a fixed solids flow rate. If we reduce the gas velocity of the state with an S-shaped axial voidage profile, the inflection point will immediately disappear, showing the unique relation between U_g and K^*. Figure 4-33 gives experimental results with hollow glass beads, showing changes similar to Figure 4-31 for FCC particles.

Figure 4-34 outlines the characteristics of axial voidage profiles, according to which, the operation of fast fluidized beds was classified as three operating modes (see Section 3.3 and Figure 3-8) on the basis of the three variables, U_g and G_s and ΔP_{imp}. Zone PFC/FD in the saddle area of Figure 4-34a is that for the co-existence of two flow regions with $G_s = K^*$, for which the constant-U_g curves are horizontal lines. Zone PFC toward the right is that for the single dense region with $G_s > K^*$, and zone FD toward the left, for the single dilute region with $G_s < K^*$. Point I_{min} represents the minimum solids inventory for the development of two flow regions. Point D is the critical point for S-shaped axial voidage profiles. If U_g is larger than the gas velocity corresponding to this point, the S-shaped axial voidage profile lapses into single dilute region flow. On the other hand, if G_s is larger than the solid flow rate corresponding to point D, the S-shaped axial voidage profile is replaced by single dense region flow.

It is easy to see that zone PFC/FD in Figure 4-34a corresponds to operation at choking, that is, $U_g = U_{pt}$ and $G_s = K^*$, and the righthand side, or zone PFC, corresponds to the operation of $U_g < U_{pt}$ and $G_s > K^*$ in the PFC regime, and the lefthand side, or zone FD, the operation of $U_g > U_{pt}$ and $G_s < K^*$ in FD regime.

Experiments also indicated that at any constant gas velocity, S-shaped profiles can exist only within certain limits of I, as represented by the saddle-shaped boundary of zone PFC/FD in Figure 4-34a. Thus to realize a given mode of operation, the necessary global conditions need to be satisfied in addition to intrinsic fluid dynamics. Bed height can also affect axial voidage profiles, as already noted above. The smaller the bed height is ($H < H'$), the shorter the horizontal section of $G_s = f(U_g, I)$ is in Figure 4-34a, and more difficult it is to develop the S-shaped profile.

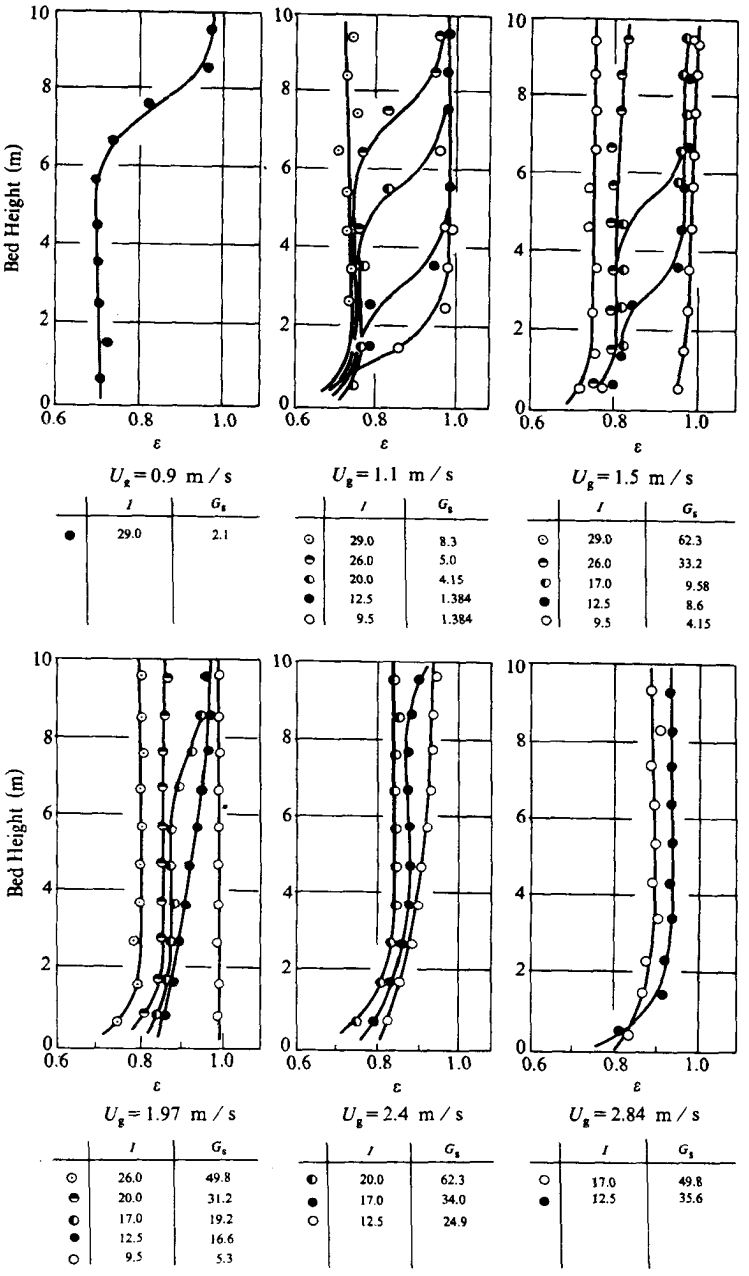

U_g = 0.9 m / s		
	I	G_s
●	29.0	2.1

U_g = 1.1 m / s		
	I	G_s
⊙	29.0	8.3
◓	26.0	5.0
◐	20.0	4.15
●	12.5	1.384
○	9.5	1.384

U_g = 1.5 m / s		
	I	G_s
⊙	29.0	62.3
◓	26.0	33.2
◐	17.0	9.58
●	12.5	8.6
○	9.5	4.15

U_g = 1.97 m / s		
	I	G_s
⊙	26.0	49.8
◓	20.0	31.2
◐	17.0	19.2
●	12.5	16.6
○	9.5	5.3

U_g = 2.4 m / s		
	I	G_s
◐	20.0	62.3
●	17.0	34.0
○	12.5	24.9

U_g = 2.84 m / s		
	I	G_s
○	17.0	49.8
●	12.5	35.6

Figure 4-33 Axial Voidage Profiles for System Glass/air

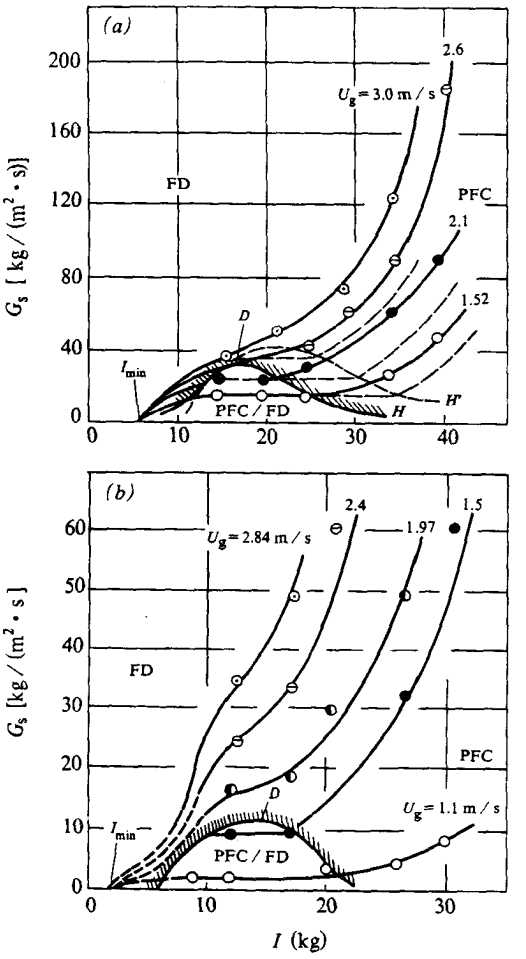

Figure 4-34 Relationships between U_g, G_s and ΔP_{imp} for Different Operating Modes
a — FCC/air; b — HGB/air

Additional data in Figure 4-34b for hollow glass beads further identify the three operating modes just enumerated above and discussed in Section 3.3.

The importance of the parameter K^* is evident. It is not only the basis for differentiating operating modes, but also the necessary condition for the existence of S-shaped axial voidage profiles, and defines, also, the critical value of solid rate for the transition between dense fluidization

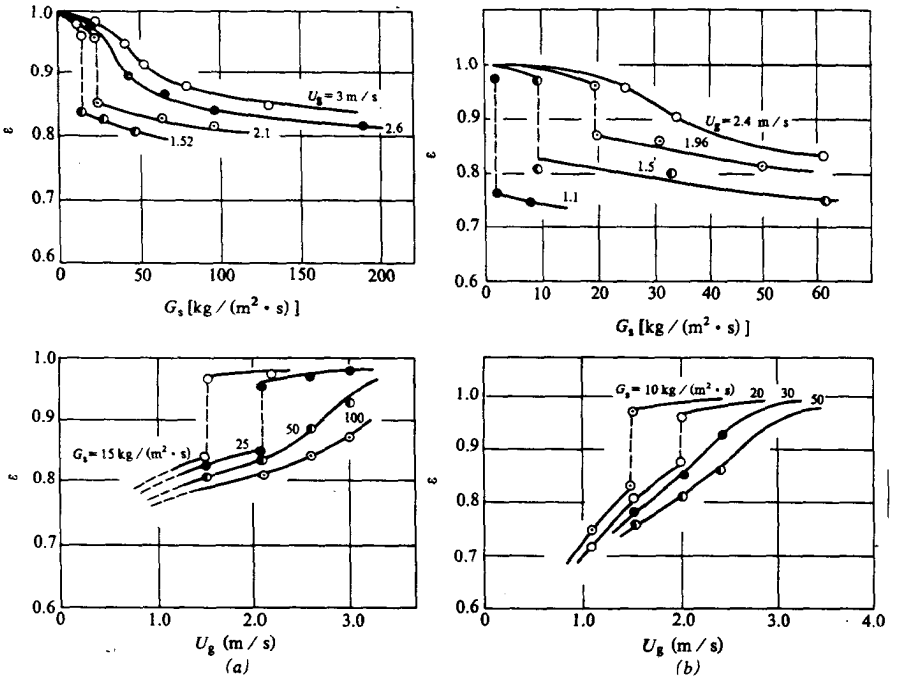

Figure 4-35 Cross Plots of $\varepsilon \sim U_g \sim G_s$ Relation to Show Choking
a — FCC/air; b — hollow glass beads/air

and dilute transport. In fact, the S-shaped axial voidage profile represents the critical state for this transition. Therefore, this transition can be determined conveniently through experiments yielding S-shaped voidage profiles. The relationships between U_g, ε and G_s in Figure 4-31 and Figure 4-33 can be replotted into $U_g \sim \varepsilon$ and $G_s \sim \varepsilon$ regime diagrams in Figure 4-35 for FCC/air system and hollow glass beads/air system to further accentuate the choking phenomenon.

Radial Direction

Radial heterogeneity promotes backmixing of both fluid and particles, and plays an unfavorable role in fluid-particle contacting. It therefore gives rise to wide attention (Monceaux *et al.*, 1986; Weinstein *et al.*, 1986; Hartge *et al.*, 1986; Bai *et al.*, 1988; Tung, *et al.*, 1988; and Horio *et al.*, 1988).

Figure 4-25 already showed typical radial voidage profiles in different fluidization regimes, indicating significant difference of bed density between the wall region and the core region. Figure 4-36 shows the spatial distribution of flow structure by illustrating the probability density distribution at different radial locations, indicating that the volume fraction of the dense phase increases from the core to the wall, and showing once again that the core region and the wall region operate in different regimes.

It was considered that the shape of the radial voidage profile curve depend on the cross sectional average voidage $\bar{\varepsilon}$, and can be represented by the following correlations for FCC catalyst (Tung *et al.*, 1988) :

$$\varepsilon(r/R) = \bar{\varepsilon}^{(\phi^2+0.191)} \qquad \phi = r/R \leq 0.75$$

$$\varepsilon(r/R) = \varepsilon^{(3.62\phi^{6.47}+0.191)} \qquad \phi = r/R \geq 0.75$$

Of course, the above correlations apply only to the case with symmetrical radial voidage distributions. For large units, the radial distribution is often asymmetrical, and may display even a multi-peak configurations (Squires *et al.*, 1985). Further work is needed for characterizing such distribution.

Figure 4-37 shows the measured radial profiles of voidage, particle dynamic pressure and particle velocity. Both the time-average particle velocity and the concentration-weighted time-average particle velocity were included in Figure 4-37b, to show the difference between the two. However, in the wall region, these two average values approach each other due to high particle concentration, for which the contribution of the dilute phase to the average particle velocity is negligible. From the radial profiles of average voidage and particle velocity shown in Figure 4-37, a cross-sectional average solids flow rate of 70 kg/(s · m^2) was obtained, which is in good agreement with the operation condition of $\overline{G}_s = 62$ kg/(s · m^2).

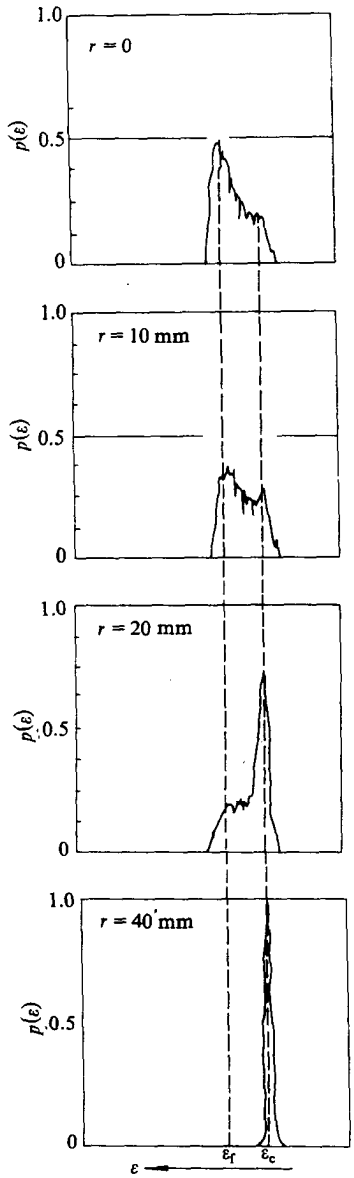

Figure 4-36 Probability Density Distribution of Local Voidage at Different Radial Positions

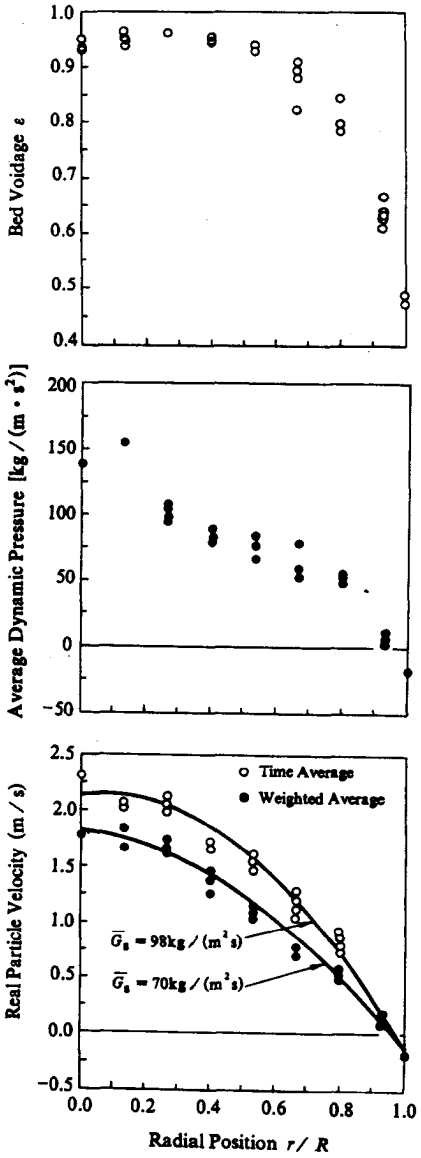

Figure 4-37 Radial Distributions of Voidage, Dynamic Pressure and Velocity of Particles (Qian and Li, 1993)

Chapter 5

APPLICATION OF THE EMMS MODEL

Application of the EMMS model includes two aspects: computation of flow field and evaluation of fluid-particle contacting in a particle-fluid two-phase system by using the formulations of the model, and conceptual design of reactors by using the basic understanding of particle-fluid two-phase flow revealed by the model. The merit of the EMMS model lies in providing quantified analysis of the local meso-scale heterogeneity and of the global macro-scale heterogeneity of a particle-fluid two-phase system, thus making possible the specification, selection or realization of the phase, regime, pattern and region desired.

Due to the recency of the EMMS model, however, its engineering potential remains yet to be explored, and the present chapter will quote only a limited number of examples in application.

5.1 Reactor Design

To use the EMMS model in reactor design calls for, first of all, the specification of the independent parameters and then the provision of a general guideline for the design procedure.

5.1.1 Reactor Specification

The independent parameters which need to be specified at the beginning involve:

1. *Material properties, such as particle diameter, particle density, fluid density, fluid viscosity, etc.*
2. *Operating conditions, such as gas velocity, solids flow rate, etc.*
3. *Boundary conditions, such as dimension and configuration of the unit, maximum pressure drop ΔP_{max} to be allowed, etc.*

5.1.2 Design Procedure

With the above specifications, the flow field of the reactor can be determined by solving the EMMS model. In principle, radial profiles of all parameters in both the top dilute region and the bottom dense region can be computed from Model OR with the identification of the Modes of operation, FD, PFC/FD and PFC. The general procedure is the following:

1. Determination of the Possible Operating Modes. From the reactor specifications, compute from Model OR, $(\overline{W}_{st})_{PFC}$ and $(\overline{W}_{st})_{FD}$, to identify the possible operating mode in the axial direction according to the following criteria (see Section 3.6):

$$\begin{aligned} &\text{Mode FD} && (\overline{W}_{st})_{FD} < (\overline{W}_{st})_{PFC} \\ &\text{Mode PFC/FD} && (\overline{W}_{st})_{FD} = (\overline{W}_{st})_{PFC} \\ &\text{Mode PFC} && (\overline{W}_{st})_{FD} > (\overline{W}_{st})_{PFC} \end{aligned}$$

2. Radial Profiles of Parameters. While calculating $(\overline{W}_{st})_{PFC}$ and $(\overline{W}_{st})_{FD}$ in the above first step, radial profiles of all parameters should also be determined with respect to all possible operating modes.

3. Justification of the Mode Chosen with Respect to ΔP_{max}. From Model OR, also compute the average voidages for Mode FD and Mode

PFC, $\bar{\varepsilon}_{FD}$ and $\bar{\varepsilon}_{PFC}$, to determine the respective pressure drops in the axial direction, which should balance the imposed pressures:

$$(\Delta P_{imp})_{FD} = (1 - \bar{\varepsilon}_{FD})\rho_p g H$$

$$(\Delta P_{imp})_{PFC} = (1 - \bar{\varepsilon}_{PFC})\rho_p g H$$

The value of $\bar{\varepsilon}_{FD}$ is subject to the structure of clusters in the FD regime, which, as discussed in Section 3.3, has not yet been fully understood. Its two extreme values can be determined with the assumption of either disappearance of clusters for ideal transport or ε_c approaching ε_{mf} for nonideal transport.

Modes FD and PFC are possible provided $\Delta P_{max} > (\Delta P_{imp})_{FD}$ and $\Delta P_{max} > (\Delta P_{imp})_{PFC}$ respectively. Mode PFC/FD is possible provided

$$(\Delta P_{imp})_{FD} < \Delta P_{max} < (\Delta P_{imp})_{PFC}$$

that is,

$$(1 - \varepsilon^*)\rho_p g H < \Delta P_{max} < (1 - \varepsilon_a)\rho_p g H$$

In short, the sufficient conditions for the three possible modes in the axial direction are

Mode FD	$(\overline{W}_{st})_{FD} < (\overline{W}_{st})_{PFC}$	$\Delta P_{max} > (\Delta P_{imp})_{FD}$
Mode PFC/FD	$(\overline{W}_{st})_{FD} = (\overline{W}_{st})_{PFC}$	$(\Delta P_{imp})_{FD} < \Delta P_{max} < (\Delta P_{imp})_{PFC}$
Mode PFC	$(\overline{W}_{st})_{FD} > (\overline{W}_{st})_{PFC}$	$\Delta P_{max} > (\Delta P_{imp})_{PFC}$

4. Determination of Inflection Point Z_i. For Mode PFC/FD, the inflection point Z_i, as shown in Figure 5-1, has to be determined for evaluating the space fractions of the dilute and the dense regions, and then the solids inventory in the system could be calculated. Subject to the specified ΔP_{max} and the characteristic curve of the compressor, Z_i and

the inventory of solids are correlated with each other through the component resistances in the circulating loop, as shown in Figure 5-1, which gives

$$\rho_p g(1-\varepsilon_a)(H-Z_i)+(1-\varepsilon^*)Z_i$$

$$=\frac{I-[(1-\varepsilon_a)(H-Z_i)+(1-\varepsilon^*)Z_i]\rho_p a}{A}\cdot g-\Delta P_c$$

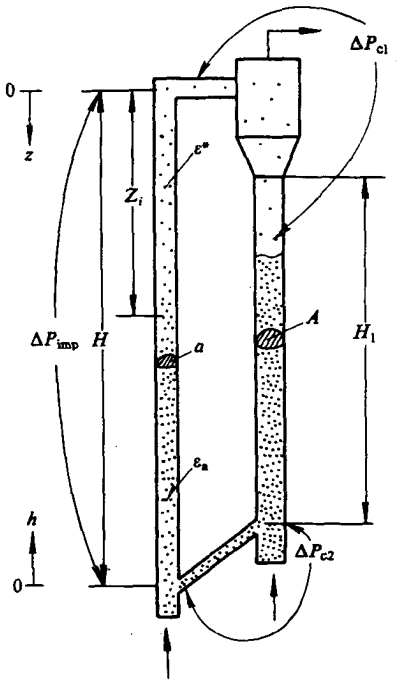

Figure 5-1 Pressure Balance in a CFB Unit

In addition, operational flexibility should be taken into account in determining Z_i or I to allow a range of operation, especially, the adjustment through $\Delta P_c = \Delta P_{c1} + \Delta P_{c2}$ which is mainly affected by the opening of the solids flow control value and solid flow rate.

The design procedure discussed above is contingent upon the solution of Model OR which has not yet been achieved at the present stage.

Another deficiency in the above procedure is the calculation of the transition zone between the dilute region at the top and the dense region at the bottom. Special attention is being paid to these two important aspects in order to make the complete design procedure possible. However, a simplified approach can be deduced from the above procedure to determine the flow field of a reactor, as shown in the following section.

5.1.3 Example of Computation of Flow Field

Reactor specifications are (see Figure 5-1)

Material Properties:	particle density	$\rho_p = 930$ kg/m^3
	particle diameter	$d_\rho = 54$ μm
	gas density	$\rho_f = 1179$ kg/m^3
	gas viscosity	$\nu_f = 1.6 \times 10^{-5}$ m^2/s
Operating conditions:	gas velocity	2.0 m/s, 4.0 m/s, U_{pt} (to be determined)
	particle flow rate	$G_s = 50$ kg/m$^2 \cdot$ s
Boundary conditions:	pressure drop	$\Delta P_{max} = 15000$ kg/(m $\cdot$ s^2)
	unit dimensions	$H = 10$ m, $H_1 = 7$ m
		$a = 7.85 \times 10^{-3}$ m^2
		$A = 1.327 \times 10^{-2}$ m^2

where ΔP_{max} is the maximum pressure drop across the unit, which is dependent on the characteristic curve of the compressor, the maximum solids inventory in the system, and $\Delta P_c = \Delta P_{c1} + \Delta P_{c2}$, defined in Figure 5-1, at the specified solids flow rate.

1. Determination of Operating Modes. Without considering radial heterogeneity by using Model OR, this section will consider Model LG instead. From Model LG, changes, with changing gas velocity, of $(W_{st})_{PFC}$, and $(W_{st})_{FD}$ and of the corresponding ε_{PFC} and ε_{FD} can be calculated. Figure 5-2 shows the computation results, in particular, the the choking velocity $U_g = 3.21$ m/s for $G_s = 50$ kg/(m$^2 \cdot$ s) at which

$$(W_{st})_{PFC} = (W_{st})_{FD}$$

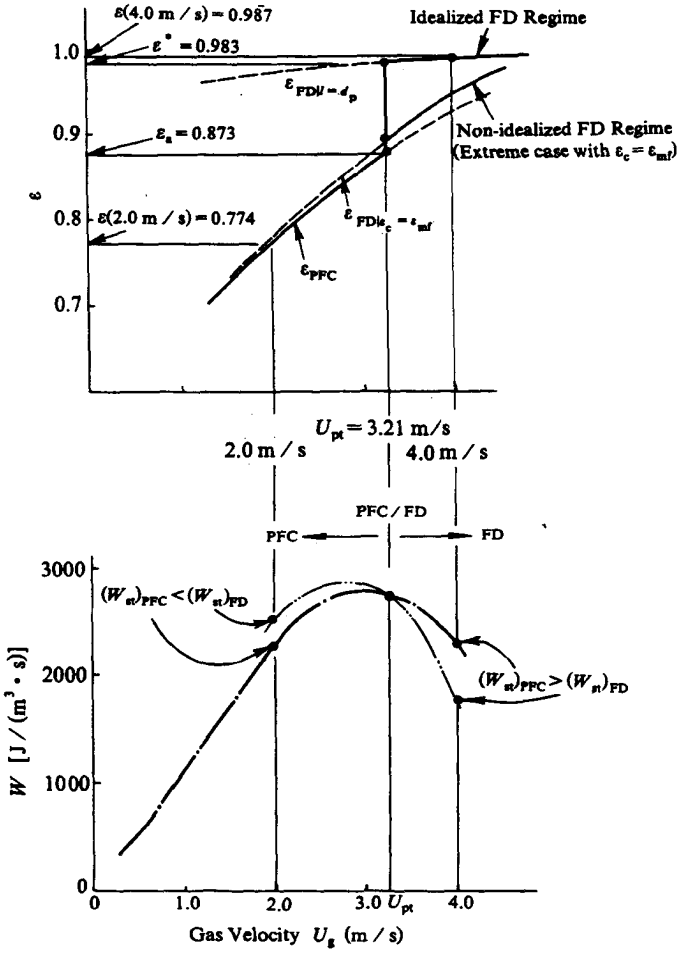

Figure 5-2 Determination of Operating Modes and Corresponding ε

The calculated parameters for U_g = 2.0 m/s, 3.21 m/s and 4.0 m/s, are listed below:

U_g, m/s	$(W_{st})_{PFC}$	$(W_{st})_{FD}$	ε_{PFC}	ε_{FD}	ε_{ideal}	ε_a	ε^*
2.0	2322	2588	0.769	0.774	0.973	–	–
3.21	2810	2810	0.873	0.883	0.983	0.873	0.983
4.0	2317	1785	0.926	0.948	0.987	–	–

where ε_{FD} is the voidage in the FD regime for nonideal transport for

which particles still aggregate with $\varepsilon_c = \varepsilon_{mf}$, and ε_{ideal} is the voidage in the FD regime for ideal transport for which particles are discretely dispersed. Without a full understanding of the flow structure in the FD regime, the designer has nevertheless to make a choice between ε_{FD} and ε_{ideal}. According to the values shown above, the relevant operating modes are identified as follows

velocity, m/s	criteria, $J/(m^3 \cdot s)$	mode
2.0	$(W_{st})_{PFC} = 2322 < (W_{st})_{FD} = 2588$	PFC (dense only)
3.21	$(W_{st})_{PFC} = 2810 = (W_{st})_{FD} = 2810$	PFC/FD (dense and dilute)
4.0	$(W_{st})_{PFC} = 2317 > (W_{st})_{FD} = 1785$	FD (dilute only)

Suppose the designer chose ideal transport for the FD regime, then the corresponding bed voidages (see top of Figure 5-2) for the above three cases would be:

velocity, (m/s)	voidage for dense region	voidage for dilute region
2.0	0.769	–
3.21	$0.873(\varepsilon_a)$	$0.983(\varepsilon^*)$
4.0	–	0.987

The corresponding pressure drops across the unit for these three cases are

velocity, m/s	ΔP_{imp}, $kg/(m \cdot s^2)$
2.0	$= (1-\varepsilon)\rho_p \cdot gH = (1-0.769) \times 930 \times 9.8 \times 10 = 21042$
3.21	$> (1-\varepsilon^*)\rho_p \cdot gH = (1-0.983) \times 930 \times 9.8 \times 10 = 1549$
	$< (1-\varepsilon_a)\rho_p \cdot gH = (1-0.873) \times 930 \times 9.8 \times 10 = 11568$
4.0	$= (1-\varepsilon)\rho_p \cdot gH = (1-0.987) \times 930 \times 9.8 \times 10 = 1184$

Because of the constraint $\Delta P_{imp} < \Delta P_{max} = 15000$ kg/(m · s^2), the operation for $U_g = 2.0$ m/s and $G_s = 50$ kg/(m^2 · s) can not be realized.

To satisfy $\Delta P_{imp} < \Delta P_{max}$, the system can therefore be operated for both $U_g = 3.21$ m/s and 4.0 m/s. To cover the operational range from 3.21 to 4.0 m/s, the adjustment range of ΔP_c (see Figure 5-1) must be so wide that it can compensate the difference between ΔP_{max} and ΔP_{imp}. The position of inflection point Z_i floats on the value of ΔP_c.

2. Evaluation of Solids Inventory. Assuming the downcomer (see Figure 5-1) operates in bubbling fluidization with $\varepsilon = 0.6$, the maximum solids inventory I_{max} at $U_g = 3.21$ m/s corresponding to the maximum height of the point of inflection $Z_i = 0$, can be evaluated:

$$\begin{aligned} I_{max} = & (1-\varepsilon_a)\rho_p \cdot H \cdot a + (1-0.6)\rho_p \cdot H_1 \cdot A \\ = & (1-0.769) \times 930 \times 10 \times 7.85 \times 10^{-3} + (1-0.6) \times 930 \\ & \times 7.0 \times 1.327 \times 10^{-2} = 51.42 \text{ kg} \end{aligned}$$

The corresponding range of ΔP_c at I_{max} should be from

$$\begin{aligned} (\Delta P_c)_{min} = & -(1-\varepsilon_a)\rho_p \cdot gH + (1-0.6)\rho_p \cdot gH_1 \\ = & -(1-0.873) \times 930 \times 9.8 \times 10 + (1-0.6) \times 930 \\ & \times 9.8 \times 7.0 = 13945 \text{ kg/(m} \cdot \text{s}^2) \end{aligned}$$

to

$$\begin{aligned} (\Delta P_c)_{max} = & -(1-\varepsilon^*)\rho_p \cdot gH + (1-0.6)\rho_p \cdot gH_1 \\ = & -(1-0.983) \times 930 \times 9.8 \times 10 + (1-0.6) \times 930 \\ & \times 9.8 \times 7.0 = 23956 \text{ kg/(m} \cdot \text{s}^2) \end{aligned}$$

The minimum solids inventory I_{min} occurs at $\Delta P_c = 0$:

$$\begin{aligned} I_{min} = & (1-\varepsilon^*)\rho_p \cdot Ha + [(1-\varepsilon^*)\rho_p \cdot H + \Delta P_c/g]A \\ = & (1-\varepsilon^*)\rho_p \cdot H(a+A) \\ = & (1-0.983) \times 930 \times 10 \times (7.85 \times 10^{-3} + 1.327 \times 10^{-2}) = 3.34 \text{ kg} \end{aligned}$$

The solids inventory increases from this minimal value toward the maximum of 51.42 kg, as the resistance of flow ΔP_c increases.

For $U_g = 4.0$ m/s, the same procedure can be adopted for evaluating I_{max}, I_{min}, ΔP_{max} and ΔP_{min}. This will not be duplicated.

3. Axial Voidage Profile. Axial voidage profile exists only in Mode PFC/FD operating at $U_g = 3.21$ m/s, and it can be evaluated by using Li and Kwauk's (1980) model with the above values of ε_a and ε^*, according to which

$$\frac{\bar{\varepsilon} - \varepsilon_a}{\varepsilon^* - \bar{\varepsilon}} = \exp[-(z - Z_i)/Z_0]$$

In consideration of the definition of z, h and Z_i in Figure 5-1, the equation becomes

$$\frac{\bar{\varepsilon}(h) - \varepsilon_a}{\varepsilon^* - \bar{\varepsilon}(h)} = \exp[-(H - h - Z_i)/Z_0] \tag{5.1}$$

where Z_0 can be calculated from ε^* and ε_a (Li and Kwauk, 1980), and Z_i from pressure balance:

$$Z_0 = 500\exp[-69(\varepsilon^* - \varepsilon_a)] = 500\exp[-69(0.983 - 0.873)] = 0.253 \text{ m}$$

$$Z_i = \frac{H\rho_p \cdot g(1 - \varepsilon_a) - \Delta P_{imp}}{\rho_p \cdot g(\varepsilon^* - \varepsilon_a)}$$

If the opening of the solid flow control valve is so adjusted as to give $\Delta P_{imp} = 6500$ kg/(m $\cdot$ s^2), calculation yields $Z_i = 5.0$ m. Substitution of $\varepsilon_a, \varepsilon^*$, Z_0 and Z_i into Equation 5-1 gives the axial voidage profile at $U_g = 3.21$ m/s as shown in Figure 5-3a.

4. Radial Voidage Profile. Radial voidage profile can be evaluated from $\bar{\varepsilon}(h)$, calculated from Eq. (5.1), by using Tung's model:

$$\varepsilon(h, r/R) = \bar{\varepsilon}(h)^{[(r/R)^2 + 0.191]} \qquad r/R \leq 0.75$$

$$\varepsilon(h, r/R) = \bar{\varepsilon}(h)^{[3.62(r/R)^{6.47} + 0.191]} \qquad r/R \geq 0.75$$

These two correlations define the spatial distribution of particle concentration in the whole unit.

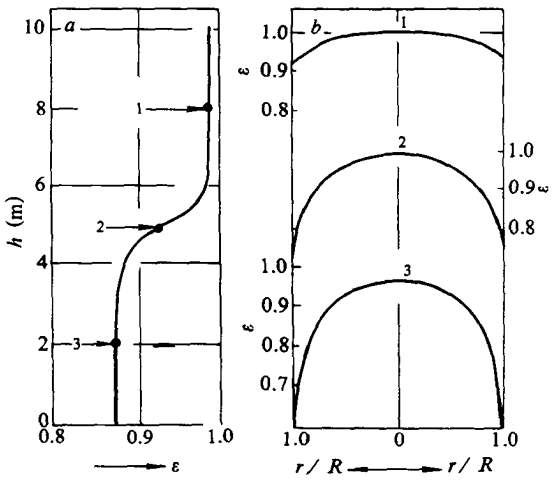

Figure 5-3 Calculated Voidage Distribution for System FCC/air at $G_s = 50$ kg/(m^2 · s), and $U_g = 3.21$ m/s
a — axial; b — radial (1. top dilute region; 2. transition region; 3. dense region)

Figure 5-3b shows the calculated radial voidage profiles for $U_g = 3.21$ m/s at three typical positions: the top dilute region, the transition region and the bottom dense region. For $U_g = 4$ m/s, radial voidage profiles at any cross-section can be expressed as

$$\varepsilon(r/R) = 0.987^{[(r/R)^2+0.191]} \qquad r/R \leq 0.75$$

$$\varepsilon(r/R) = 0.987^{[3.62(r/R)^{6.47}+0.191]} \qquad r/R \geq 0.75$$

Further efforts are needed to develop a mathematical model for the transition section to replace the empirical correlations used in the above calculation, and to understand the flow structure in the dilute transport regime for considering the real nonidealized case.

5.2 Evaluation of Particle-Fluid Contacting

The multi-scale aspect of the EMMS model makes possible the approximate evaluation of particle-fluid contacting in particle-fluid flow.

5.2.1 Drag Coefficient and Slip Velocity

The eight variables in Model LG are correlated with the average voidage ε, gas velocity U_g and solids flow rate G_s:

$$\varepsilon = \varepsilon_f(1-f) + \varepsilon_c f$$

$$U_g = U_f(1-f) + U_c f$$

$$G_s/\rho_p = U_{df}(1-f) + U_{dc} f$$

For an average particle, we have

$$\frac{\pi d_p^3}{6} \cdot \rho_p \cdot g = \overline{C}_D \frac{\pi d_p^2}{4} \cdot \frac{\rho_f U_s^2}{2}$$

that is,

$$\overline{C}_D = \frac{4 d_p \rho_p g}{3\rho_f (U_g - \frac{G_s \varepsilon}{\rho_p(1-\varepsilon)})^2}$$

However, such a global correlation is not sufficient for evaluating G/S interaction in the system due to structural difference between the two phases. It is necessary to analyze particle-fluid interaction at a micro scale in both phases and the interaction between the two phases. From Section 2.1, drag coefficients in the three different phases are

$$\text{dense phase}: \quad C_{Dc} = \frac{8 F_{\text{dense}}}{\pi d_p^2 \rho_f (U_c - \frac{U_{dc}\varepsilon_c}{1-\varepsilon_c})^2}$$

$$\text{dilute phase}: \quad C_{\mathrm{Df}} = \frac{8F_{\mathrm{dilute}}}{\pi d_{\mathrm{p}}^2 \rho_{\mathrm{f}} (U_{\mathrm{f}} - \frac{U_{\mathrm{df}}\varepsilon_{\mathrm{f}}}{1-\varepsilon_{\mathrm{f}}})^2}$$

$$\text{inter phase}: \quad C_{\mathrm{Di}} = \frac{8F_{\mathrm{inter}}}{\pi l^2 \rho_{\mathrm{f}} (U_{\mathrm{f}} - \frac{U_{\mathrm{dc}}\varepsilon_{\mathrm{f}}}{1-\varepsilon_{\mathrm{c}}})^2 (1-f)^2}$$

By using the EMMS model, all the parameters involved in the above correlations can thus be calculated.

Figure 5-4 supplements Figure 3-9 by comparing various slip velocities and drag coefficients in the different phases for system FCC/air ($d_{\mathrm{p}} = 54\ \mu\mathrm{m}, \rho_{\mathrm{p}} = 930\ \mathrm{kg/m^3}$) at $G_{\mathrm{s}} = 50\ \mathrm{kg/(m^2 \cdot s)}$ calculated from Model LG, showing dramatic difference between the dense phase and the dilute phase not only for slip velocity but also for drag coefficient.

At minimum fluidization, all drag coefficients are high because of the low slip velocity $(U_{\mathrm{s}})_{\mathrm{mf}}$ at this state. Drag coefficient C_{Dc} in the dense phase becomes even higher with increasing U_{g} due to decreasing slip velocity U_{sc} in this phase. However, slip velocity between the two phases U_{si} is much higher than U_{sc}, and increases with increasing U_{g}, leading to low drag efficient C_{Di}. Both slip velocity and drag coefficient in the dilute phase are constant in the fluidization regime, but make jump changes at U_{pt} corresponding to choking, and then gradually approach U_{t} and C_{Do} respectively for the single particle with increasing U_{g}. The global average drag coefficient and slip velocity change differently from all other phase-related terms, and are, therefore, not sufficient for characterizing particle-fluid contacting in the system. In fact, we see that the global average drag coefficient $\overline{C}_{\mathrm{D}}$ reaches quite low values, even lower than 0.1 at high fluid velocity U_{g}, which is therefore not reasonable.

From the above analysis, we know that multi-scale analysis is essential for evaluating particle-fluid contacting in heterogeneous particle-fluid systems, while the analysis based on the global average is usually insufficient. Heterogeneity not only on local scale but also on overall scale should be the main research focus in this field.

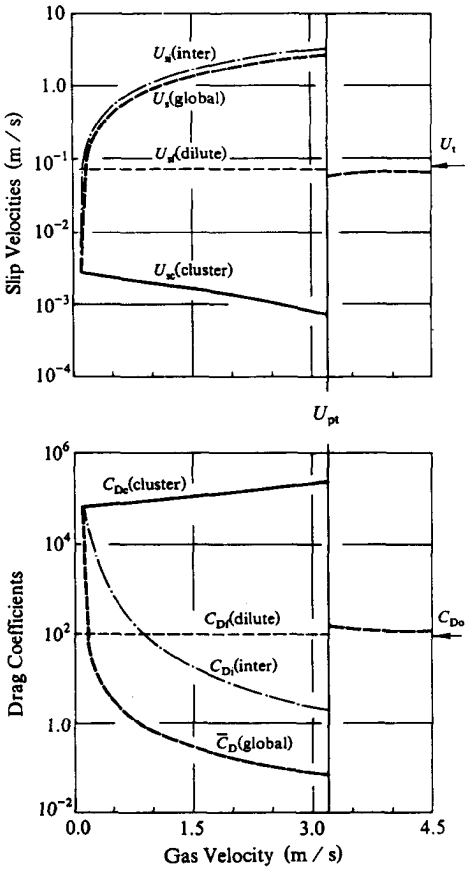

Figure 5-4 Dependencies of Slip Velocities and Drag Coefficients on Gas Velocity in Different Phases

5.2.2 Contacting Intensity

Mass-Specific Intensity

To elucidate further the mechanism of local heterogeneity as evidenced by the division of particle-fluid flow into the two phases, a term called

mass-specific intensity of particle-fluid interaction I_m is proposed as follows:

$$I_m = \frac{N_{st}}{U_g \rho_f}$$

where N_{st} represents particle-fluid contacting per unit mass of particles, and $U_g \rho_f$ represents the mass flow rate of the fluid. The quantity I_m, therefore, provides a criterion for evaluating particle-fluid contacting between unit mass of fluid and unit mass of particles in a unit cross-sectional area of the system.

For the dense and the dilute phases, the corresponding mass-specific intensities of particle-fluid interaction are

$$(I_m)_{dense} = \frac{(N_{st})_{dense}}{U_c f \rho_f}$$

$$(I_m)_{dilute} = \frac{(N_{st})_{dilute} + (N_{st})_{inter}}{U_f (1-f) \rho_f}$$

Figure 5-5a shows that $(I_m)_{dense}$ is much higher than $(I_m)_{dilute}$, implying that a great part of the total weight of the solid particles $(1-\varepsilon)\rho_p g$ is born mainly by a small portion of the upflowing fluid in the dense phase $U_c f / U_g$, shown as $\Delta P_{dense} f / (1-\varepsilon)\rho_p g$ in Figure 5-5b, while the major portion of the fluid flows through the dilute phase with hardly any interaction with particles in the dense phase. In uniform suspension, from definition $N_{st} \approx N_T = U_g g(\rho_p - \rho_f)/\rho_p$, I_m reaches the maximum value of $\frac{\rho_p - \rho_f}{\rho_p} \frac{g}{\rho_f}$. From Figure 5-5a, we can see that the formation of the two-phase heterogeneous structure leads to a dramatic decrease of the mass-specific intensity of particle-fluid interaction. Although its value in the dense phase is close to that in the uniform suspension, its contribution to the average intensity is not much due to the small fluid flow, $U_c f / U_g$, in the dense phase, as can be seen in 5-5b. Figure 5-5a shows that the local average mass-specific intensity of particle-fluid interaction I_m is critically dependent on flow regimes. Starting from incipient fluidizing, I_m drops sharply with bubbling, then increases with U_g, until at the choking velocity U_{pt}, it jumps to its maximum of $\frac{\rho_p - \rho_f}{\rho_p} \frac{g}{\rho_f}$, meaning that maximal mass-specific interaction between the fluid and particles

occurs in the state of uniform structure.

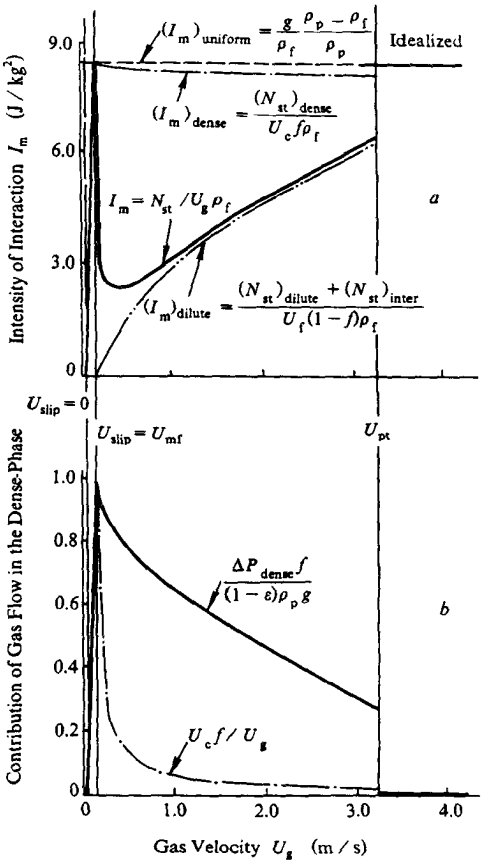

Figure 5-5 Mass-Specific Intensity of G/S Interaction in Different Phases (FCC/air: $G_s = 50$ kg/(m^2 · s))

Therefore, we define relative contacting intensity

$$I'_m = \frac{I_m}{(I_m)_{max}} = \frac{\rho_p}{\rho_p - \rho_f}\frac{\rho_f}{g} \cdot I_m$$

to evaluate the role of heterogeneity in reducing particle-fluid contacting intensity. The value of I'_m changes from zero to a maximum of unity in

the state of uniform structure.

In considering particle-fluid contacting for any global systems the local values of $I'_{\mathrm{m}}(h,r)$ need to be averaged:

$$\overline{I'_{\mathrm{m}}} = \frac{1}{\int_0^H \int_0^R [1-\varepsilon(h,r)]\rho_{\mathrm{p}} U_{\mathrm{g}}(h,r)\rho_{\mathrm{f}} \cdot r\mathrm{d}r\mathrm{d}h} \cdot$$

$$\int_0^H \int_0^R I'_{\mathrm{m}}(h,r)[1-\varepsilon(h,r)].\rho_{\mathrm{p}} U_{\mathrm{g}}(h,r)\rho_{\mathrm{f}} \cdot r\mathrm{d}r\mathrm{d}h$$

For the CFB system shown in Figure 5-6a, such average could be approximated by

$$\overline{I'_{\mathrm{m}}} = \frac{(1-\varepsilon^*)Z_{\mathrm{i}}(I'_{\mathrm{m}})^* + (1-\varepsilon_{\mathrm{a}})(H-Z_{\mathrm{i}})(I'_{\mathrm{m}})_{\mathrm{a}}}{(1-\varepsilon^*)Z_{\mathrm{i}} + (1-\varepsilon_{\mathrm{a}})(H-Z_{\mathrm{i}})}$$

In principle, $\overline{I'_{\mathrm{m}}}$ can be optimized with respect to operating conditions, both radially and axially, as shown in Figure 5-6.

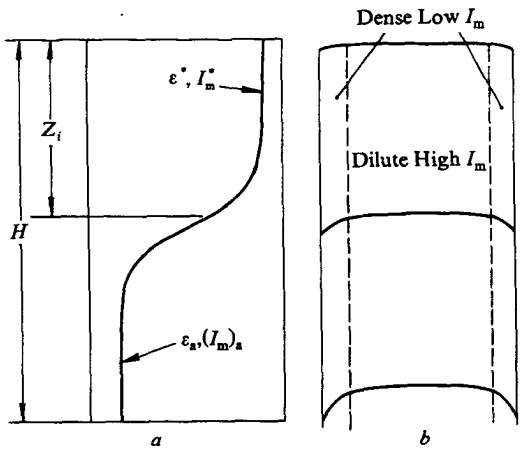

Figure 5-6 Distribution of Interaction Intensity in a Circulating Fluidized Bed
a —— axial; b —— radial

Volume-Specific Intensity

In addition to mass-specific intensity of particle-fluid interaction, volume-specific intensity I_v is an alternate criterion for evaluating particle-fluid contacting. From Section 2.2, W_{st} is itself a measure of volume-specific intensity of particle-fluid interaction, that is,

$$I_v = N_{st}(1-\varepsilon)\rho_p = W_{st}$$

Figure 5-7 maps the variation of this volume-specific intensity with gas velocity U_g and solids flow rate G_s. The subfigure at the top shows the shadowed cross-section for $G_s = 80$ kg/(m^2 · s). Maximal W_{st} corresponds to the most efficient particle-fluid contacting per unit volume, and W_{st} should be integrated volumetrically to yield the global effectiveness of particle-fluid contacting in a reactor.

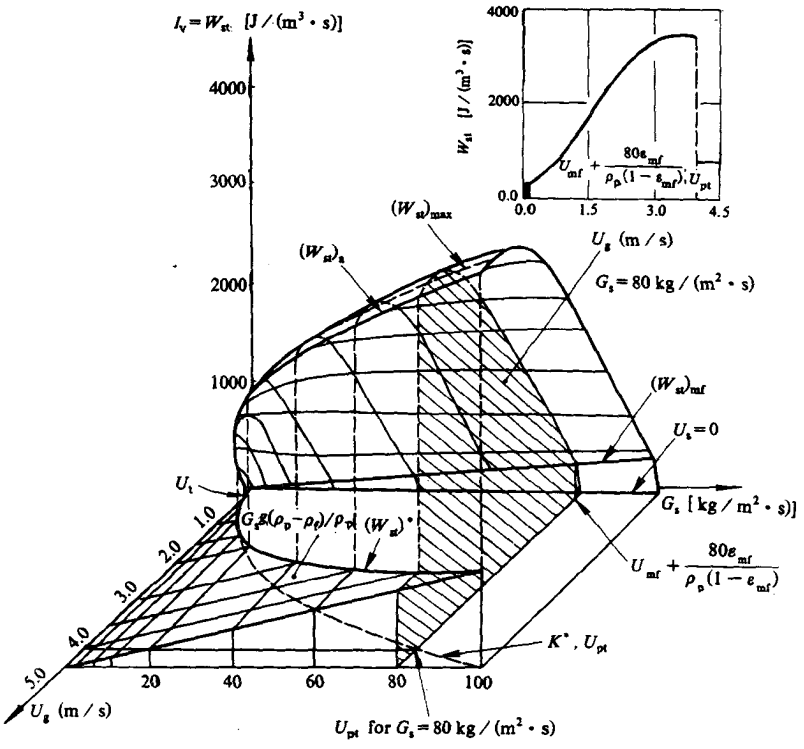

Figure 5-7 Dependence of Volumetric Intensity of Particle-Fluid Interaction on Operating Conditions (FCC/air)

The above considerations seem to imply that for efficient particle-fluid contacting in a reactor of a limited volume, high I_v should be chosen, while if the amount of particles in a reactor is limited, the system should be operated at as high a value of I_m as possible.

Mass or heat transfer between fluid and particles is related not only to particle-fluid contacting, but also to the exchange between the dense and the dilute phases. Therefore, further efforts are needed to unravel how the latter effect, which is characterized by repeated dissolution and reformation of particle aggregates, should be incorporated in order to evaluate the overall mass or heat transfer process.

Figure 5-8 shows a comparison between I_v, I_m and U_s/ε, to give some insight into G/S contacting. Slip velocity with which I_v and I_m change differently does not appear to be a well-suited parameter for characterizing G/S contacting. In theory, it appears that the best G/S contacting prevails only when both I_v and I_m reach maxima simultaneously, that is, in a *uniform dense* state. Therefore, G/S contacting should be optimized by balancing I_v and I_m according to the characteristics of the process.

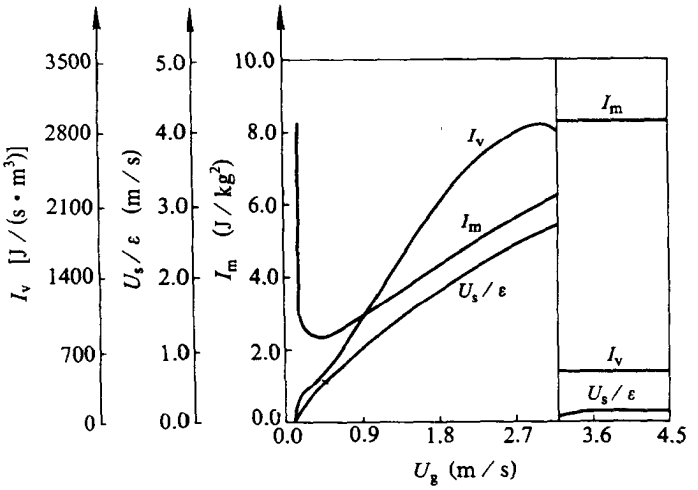

Figure 5-8 Dependence of I_v, I_m and U_s/ε on Gas Velocity (FCC/air: $G_s = 50$ kg/(m^2 · s))

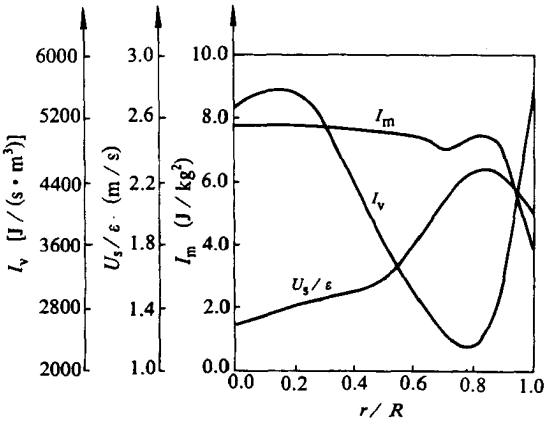

Figure 5-9 Radial Distributions of I_v, I_m and U_s/ε Calculated from Experimental Data of Bader *et al.* (1988)

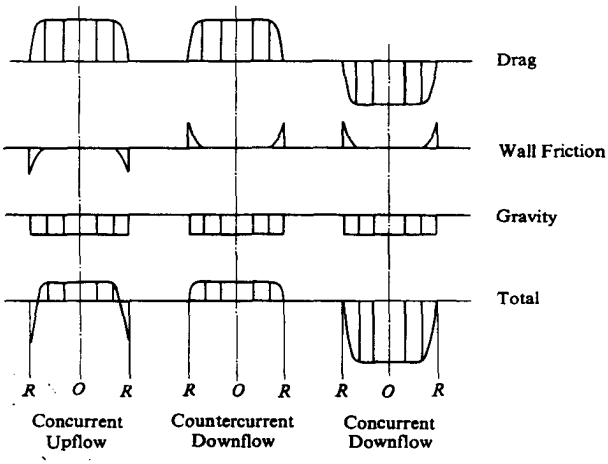

Figure 5-10 Comparison of Radial Heterogeneity in Different Types of Flow (Yan, 1993)

With the above discussion, we are now in a position to re-examine the radial heterogeneity shown in Figure 3-26. Figure 5-9 compares radial distributions of I_m, I_v and U_s/ε, showing that maximum slip velocity does not correspond to maxima for I_m and I_v, and that the most efficient G/S contacting, prevailing in the core region for this case, does not correspond to the highest slip velocity. The small peak in I_m near the wall region is attributed to local countercurrent flow.

Figure 5-10 (Yan, 1993) shows a qualitative comparison of drag force, wall friction and gravity between different types of flow under the assumption of discretely dispersed particles in the fluid. For countercurrent downflow, wall friction counteracts drag force, resulting in relatively uniform radial distribution of the total force, and hence, relatively uniform distribution of particles, while for both concurrent upflow and downflow wall friction reinforces drag force, therefore, intensifying radial heterogeneity.

5.3 Reactor Conceptualization

5.3.1 Voidage Redistribution

As analyzed in Chapter 3 and demonstrated in Chapter 4, the S-shaped axial voidage profile is typical of CFB, which consists of a top dilute region with few particles, and a bottom dense region with extensive backmixing of both particles and gas. Such characteristics often cannot satisfy the demand of some processes, for example, fluid catalyst cracking, which require both high concentration of particles and low backmixing of gas for high yield and good selectivity.

To reduce backmixing in the dense region, baffles were used for arresting the downflow of particles in the wall region (Zheng and Tung, 1990). This, however, led to decrease in solids concentration, which is by no means desirable, and the operation with both high concentration of particles and low backmixing is still difficult to realize. On the basis of the EMMS model, the analysis of the axial fluid dynamics of CFB has resulted in the concept of axial redistribution of voidage profile by ring internals (Zheng *et al.*, 1991) to solve the above problem.

An S-shaped voidage profile satisfies the approximate static pressure balance:

$$(1-\varepsilon^*)\rho_p \cdot gZ_i + (1-\varepsilon_a)\rho_p g(H - Z_i) = \Delta P_{imp}$$

that is

$$Z_i = \frac{H\rho_p \cdot g(1-\varepsilon_a) - \Delta P_{imp}}{(\varepsilon^* - \varepsilon_a)\rho_p g}$$

The ring internal was so designed that in its influence region, the length of which is ΔZ, the voidage is perceptibly raised from ε_a to ε_{in} as shown in Figure 5-11a. Keeping the imposed pressure drop ΔP_{imp} constant, the creation of this high voidage zone ΔZ results in a rise of the inflection point Z_i upward to Z_i^* expressed as

$$Z_i^* = \frac{[H\rho_p \cdot g(1-\varepsilon_a) - \Delta P_{imp}] - \Delta Z\rho_p \cdot g(\varepsilon_{in} - \varepsilon_a)}{(\varepsilon^* - \varepsilon_a)\rho_p \cdot g}$$

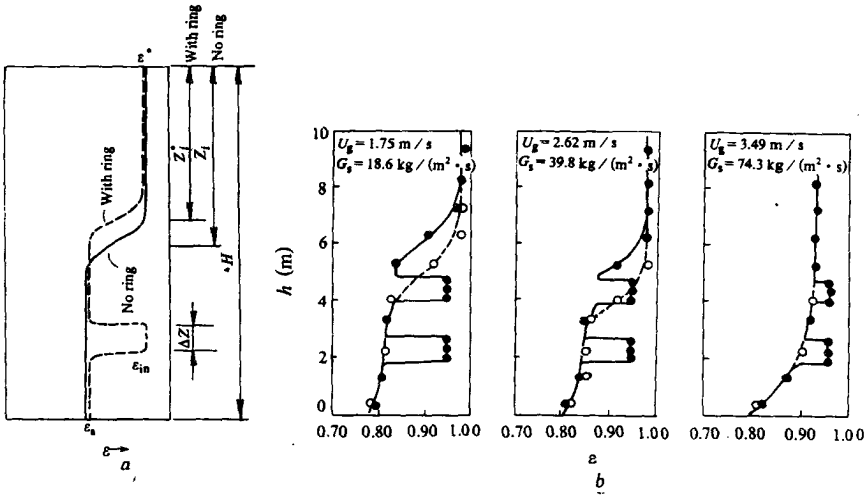

Figure 5-11 Effect of Ring Internals on Axial Voidage Profiles in Fast Fluidization (Zheng *et al.*, 1991)
a — conceptual analysis;
b — experiments with two rings

that is, the ring internal diverts a part of the dilute phase space at the

top to the influence zone within the dense phase region, while the total inventory of solids remains the same, as verified by experiments in Figure 5-11b for two such rings. Obviously, for suppressing gas backmixing in the dense region without changing the solids inventory in the system, a series of internals can be inserted into the bed for apportioning the dilute region at the top to their influence zones between dense layers to form a multi-layer structure with alternating dense and dilute zones. Such a solids redistribution is characterized by high concentration of particles and low gas backmixing in the whole system, without much affecting, however, local mixing. For this solids redistribution, the minimal number of internals without mutual overlapping is

$$N = Z_i/(Z_i - Z_i^*)$$

On the basis of the above analysis, Zheng *et al.*, (1992) conducted experiments in a fluidized bed of 90mm I.D. to measure both axial and radial voidage profiles with different number of internals as shown in Figure 5-11b and Figure 5-12, and to evaluate the backmixing of particles in the system by using tracer particles as shown in Figure 5-13. Their results indicate a considerable suppression of backmixing by segmenting the solids inventory in the axial direction.

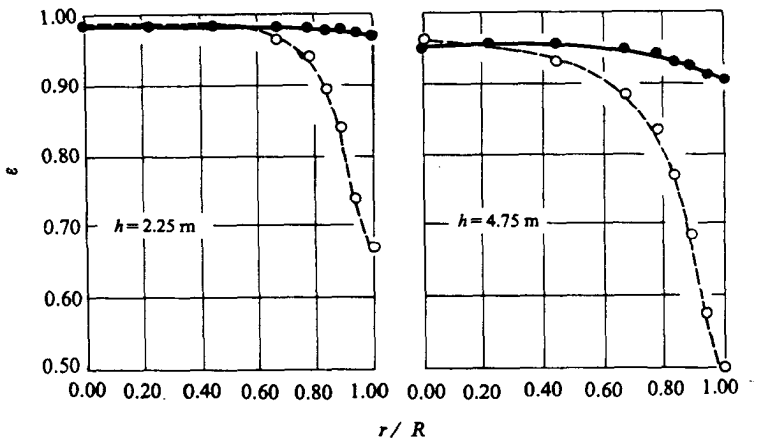

Figure 5-12 Effect of Ring Internals on Radial Voidage Profiles in Fast Fluidized Beds

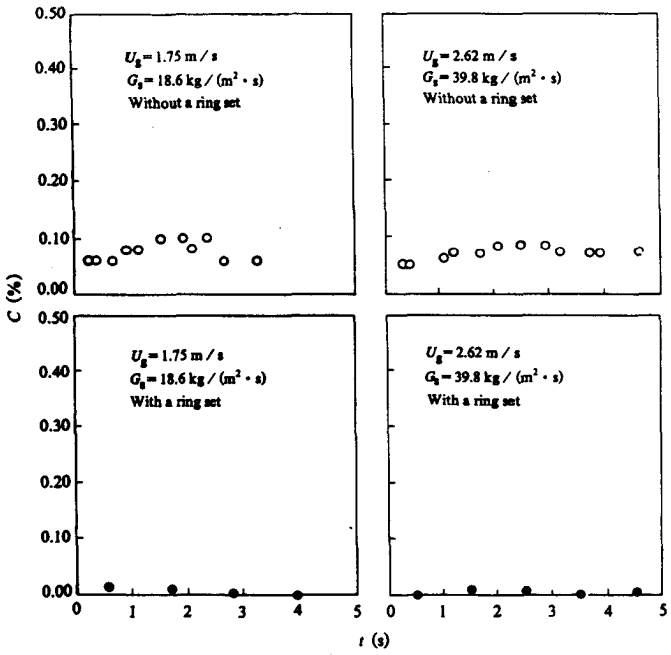

Figure 5-13 Ring Internal Suppresses Solids Backmixing

5.3.2 Wall Reconfiguration

The EMMS model suggests that the heterogeneous structure in particle fluid two-phase flow, which is attributed to minimization of energy consumption for suspending and transporting unit mass of particles, might be suppressed by hindering such energy minimization. With such a consideration, Bie *et al.* (1991) designed a CFB riser consisting of alternately contracting and expanding sections, for flattening the radial distribution of particles.

The wall of a traditional CFB unit plays the role of minimizing $\overline{N}_{st}$ by forming a dense annular region of low N_{st}, thus causing radial heterogeneity. Such a wall effect could be suppressed by alternately enlarging and shrinking the cross-section of the unit, as shown in Figure 5-14a (Bie *et al.*, 1992).

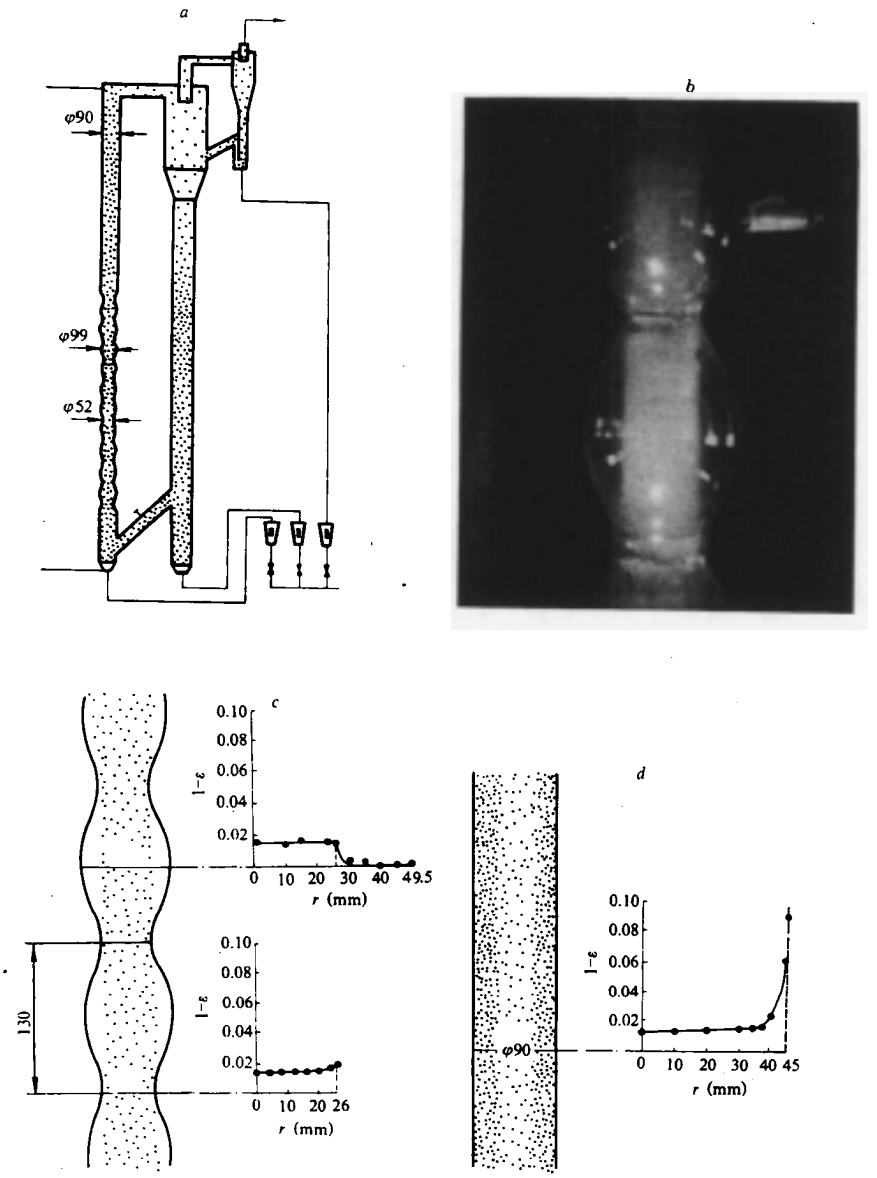

Figure 5-14 Wall-Reconfigured Riser (Bie *et al.*, 1991)
a — experimental unit;
b — reconfigured riser in operation;
c — radial profiles of the reconfigured riser;
d — radial profiles of the straight-wall riser

In the contracting sections, the wall forces the fluid and particles to move inward and against their inherent tendencies, thus, preventing the formation of the dense annular region. The expanding sections serve to

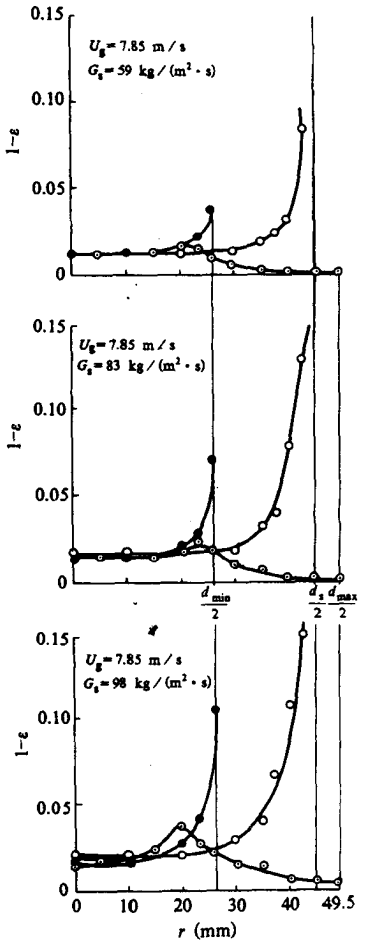

Figure 5-15 Changes of Radial Voidage Profiles in Different Cross-Sections with Solids Flow Rate
(• ϕ52 mm and ⊙ ϕ99 mm for multiple contracting-expanding tube; ○ ϕ90 mm for straight tube)

detach the wall from the fluid and the particles, thus preventing radial heterogeneity. The alternate changes in cross-section prove to be

quite effective in maintaining a more uniform structure along the height of the unit. At an expansion the particles can not follow the increasing cross-section due to their inertia, and move straight upward. Before they lose their inertia and diffuse toward the wall, they meet the next contracting section and are centralized once again by the wall. Therefore, a periodic gas layer forms between the G/S suspension and the wall, as shown in Figure 5-14b. For comparison with the traditional straight tube riser, experiments were conducted with FCC particles (ρ_p = 925.9 kg/m^3, $\bar{d}_p$ = 54 μm) in a riser consisting of two sections, a top section with a straight tube of 90 mm ID. and a bottom section with multiple-contracting-expanding subsections with a pitch of 130 mm, minimum diameter of 52 mm and maximum diameter of 99 mm, as shown in Figure 5-14a.

An optical fiber probe was used for measuring radial particle concentration profiles in these two sections, the results of which are shown in Figure 5-14c for the bottom multiple-contracting-expanding section and Figure 5-14d for the top straight-tube section. It can be seen that the radial heterogeneity is considerably suppressed in the multiple-contracting-expanding section, with hardly any particles between the wall and the G/S suspension in the expanding section.

Figure 5-15 shows the change of radial particle concentration profile with increasing solid flow rate for both the traditional straight tube and the proposed multiple contracting-expanding tube, illustrating further the role of alternate contraction and expansion.

5.4 Further Development

The EMMS model contributes toward a comprehensive understanding of particle-fluid two-phase flow though its application in engineering yet awaits further exploration. A few remarks seem to be in order as to what is needed and what is possible.

5.4.1 Pragmatization of the EMMS Model

Complete Solution of Model OR

In Section 3.6, Model OR was solved by simplifying it to Model KR which calculates radial profiles but only with relevant experimental data. For a complete solution, it is highly desirable to transform the two-fold optimization problem of Model OR into a common single-fold optimization problem. Also, in Model OR, local fluid dynamics is described by a submodel, Model LR(r). To resolve the complexity of Model OR involving local optimization and overall optimization, Xu (1993) simplified the model by introducing two innovations:

1. *Instead of solving Model OR directly, Model LR(r) is replaced by a set of equations consisting of* $\partial N_{st}/\partial x_i (i = 1, 2, ...8)$ *and the original nine constraints as in Model LR, and the two-fold optimization problem is thus converted into a single-fold problem.*

2. *Proper forms of initial radial profiles of both gas and solids velocity are assumed at the beginning of an iterative process with adjustable parameters represented by vectors* **A** *and* **B** *respectively.*

Model OR is thereby reduced to a common optimization problem with respect to **A** and **B** , and can thus be solved in the same way as Model LG.

Combination of the EMMS Model with the Pseudo-Fluid Model

Since the pseudo-fluid models do not take into account the heterogeneous structure consisting of a dense phase and a dilute phase, differences of particle-fluid interactions in the two phases can not be discerned. Therefore, it is difficult to analyze local heterogeneous structure and regime transition though the appearance of bubbles or clusters in fluidized bed can be predicted (Ding and Gidaspow, 1990). However, the pseudo-fluid models are rigorously formulated, and can be easily resolved to describe the time- and space-dependent behaviors of particle-fluid systems. On the contrary, the EMMS model resolves a global system into two interdependent subsystems, the dense phase and the dilute phase, and

multi-scale analysis and energy minimization serve to quantify such a heterogeneous structure. However, the simplifications adopted in this model have precluded its use from time-dependent behavior. Therefore, combination of the EMMS model and the pseudo-fluid model may yield a comprehensive understanding of both the heterogeneous structure and the time-dependent behavior of particle-fluid two-phase flow.

According to such a consideration, Xu *et al.*(1993) proposed a integrated model in which the pseudo-fluid model was used for formulating the fluid dynamics of both the dilute and the dense phase, while the EMMS model for determining inter-phase parameters involved in the interaction between the two phases. The solution of their model also indicated the coexistence of a dilute phase with voidage $\varepsilon_f = 1.0$ and a dense phase with voidage $\varepsilon_c \rightarrow \varepsilon_{mf}$. Such an approach seems to be promising though further efforts are still needed.

Particle Aggregation in Dilute Transport Regime

Between the two extreme cases of cluster structure in the FD regime—ideal transport with uniform and discrete particles dispersion and non-ideal transport with "small" clusters—an adequate correlation is needed for particle aggregation on the basis of interparticle forces, particle-fluid interaction and the effect of turbulence. Computer-aided experiment is now under way (Chen and Ge, 1993) for studying particle aggregation in the FD regime by means of graphical simulation.

Consideration of Dynamic Behavior

The global particle-fluid two-phase flow involves both ordered and disordered processes. The EMMS model is mainly devoted to the ordered aspects of the system, and needs to be supplemented by exploring an approach with respect to the alternate dissolution and reformation of particle clusters, which account for the greater part of the dissipated energy N_d.

5.4.2 Application of EMMS Modeling in Other Processes

The methodology of the EMMS model is characterized by resolution of a global heterogeneous system into particulate subsystems and partition of the total non-extremal energy into two extremal components. Such a methodology is considered to be effective for analyzing other heterogeneous systems.

Heat Transfer in Heterogeneous Media

Heat transfer in heterogeneous materials is very similar to particle-fluid two-phase flow with equivalence of pressure to temperature, fluid velocity to heat flux, and particle-fluid interaction to heat resistance. As suggested by Ozisik (1989) during his discussion with one of the authors on the EMMS model, if a material consists of two different components, with one distributed in the other in the form of discrete particles, the discrete material can be considered to correspond to clusters in particle-fluid systems. Figure 5-16a shows a mixed material consisting of two components having different heat transfer coefficients λ_1 and λ_2. If $\lambda_1 \neq \lambda_2$, the distribution of heat flux in this material is qualitatively shown in Figure 5-16a. Such a process is expected to satisfy the minimum heat resistance or the maximum heat flux with constraints governed by heat transfer. In this system, if λ_1 and/or λ_2 is subject to a temperature change, a phenomenon similar to "choking" in fluid-particle systems may occur. For example, if the inversion from $\lambda_1 < \lambda_2$ to $\lambda_1 > \lambda_2$ takes place in the prevailing temperature range, the distribution of heat flux will change from the pattern of Figure 5-16a to that shown in Figure 5-16b. A detailed analysis of this system is of engineering significance.

Three Phase Fluidization

Three phase fluidization can be referred to as a compound fluidization system consisting of a liquid/solid subsystem in which the liquid fluidizes the particles, a gas subsystem in which gas flows in the form of bubbles, and an inter phase in which gas flows through the L/S mixture, as shown in Figure 5-17. It appears that each of these three phases

could be analyzed individually with the proposed EMMS model. What is needed to be further analyzed is how to integrate these three separate phases into a global model.

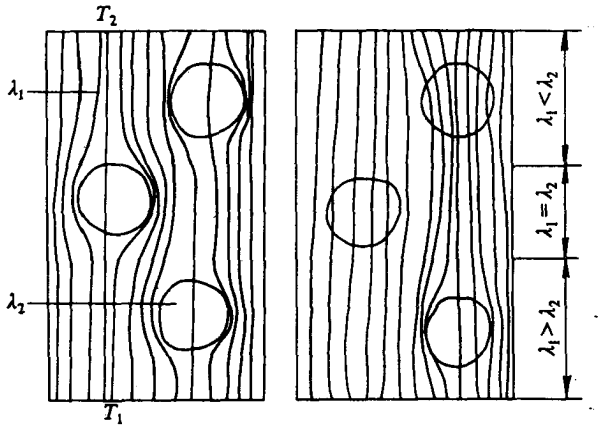

Figure 5-16 Showing Heat Transfer in Heterogeneous Materials
a — λ = constant, $\lambda_1 > \lambda_2$;
b — $\lambda = f(T)$

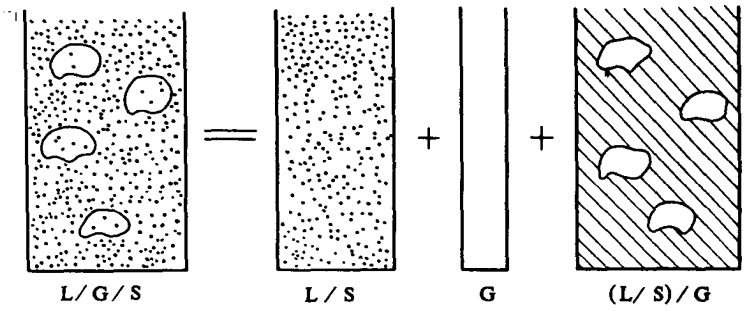

Figure 5-17 Resolution of L/G/S Three Phase Fluidization

ACRONYM

FD	fluid-dominating
PD	particle-dominating
PFC	particle-fluid-compromising
LG	local general
LR	local radial
OR	overall radial
KR	K-radial

NOTATION

$\mathbf{A}$	parameter vector to be optimized
A	cross-sectional area of downcomer, [m^2]
a	cross-sectional area of riser, [m^2]
C	tracer concentration [%]
C_o	C at injection point [%]
C_D	drag coefficient of a single particle in suspension
C_{D_o}	drag coefficient of a single particle
$\overline{C}_D^D$	average C_D with respect to $\overline{d}$
$\overline{d}$	hydrodynamic mean particle diameter, [m]
$\overline{d}_s$	volume to surface mean diameter, [m]
d_B	unit diameter, [m]
d_p	particle diameter, [m]
d_f	optical fiber diameter, [m]
d_c	fiber cladding diameter, [m]
D_a	axial diffusion coefficient, [m^2/s]
D_r	radial diffusion coefficient, [m^2/s]
f	volume fraction of dense phase
$f(\mathbf{X})$	objective function in general
$F_i(\mathbf{X})$	equations for mass and momentum conservation
F	force acting on each particle or cluster, [$(kg \cdot m)/s^2$] or objective function in GRG-2
f_f	fluid-particle interaction frequency, [s^{-1}]
f_p	particle-particle interaction frequency, [s^{-1}]

g	gravity acceleration, [m/s^2]
$g_i(\mathbf{X})$	constraint function
G_s	solids flow rate, [kg/(m^2.s)]
H	riser height, [m]
H_1	downcomer height, [m]
h	height coordinate, [m]
I	solids inventory in a unit, [kg]
I_m	mass-specific intensity of particle-fluid interaction, [J/kg^2]
I'_m	dimensionless mass-specific intensity of particle-fluid interaction
I_v	volume-specific intensity of particle-fluid interaction, [J/(s $\cdot$ m^3)]
K	factor
K^*	saturation carrying capacity, [kg/(m^2 $\cdot$ s)]
K(r)	radial heterogeneity factor
lb	variable vector for upper limit of **X**
$L(X)$	Lagrange's function
l	equivalent diameter of particle clusters, [m]
	or distance between optical probe tip and reflector, [m]
m	particle or cluster number in unit volume
N	energy consumption with respect to unit mass, [J/(s.kg)]
	or Total number of particle fractions
NC	total number of constraints
NE	number of equality constraints
NL	number of linear inequality constraints
NN	number of variables
n_i	particle number for fraction i
ΔP	pressure gradient or total force in unit volume, [kg/(m^2 $\cdot$ s^2)]
ΔP_{imp}	imposed pressure drop across a unit, [kg/(m $\cdot$ s^2)]
ΔP_{max}	maximum of ΔP_{imp}, [kg/(m $\cdot$ s^2)]
ΔP_c	pressure drop $\Delta P_{c1} + \Delta P_{c2}$ defined as Figure 5-1, [kg/(m $\cdot$ s^2)]
R	radius of unit [m]
Re	Reynolds number
Re_B	Reynolds number corresponding to velocity fluctuation
R_{xx}	auto-correlation coefficient
R_{xy}	cross-correlation coefficient
r	radial coordinate, [m]
s_i	slack variable
T	time interval, [s]; or temperature, [K]
t	time, [s]
T_{Lf}	Lagrange's time constant, [s]

ub	variable vector for upper limit of **X**
U_c	superficial gas velocity in dense phase, [m/s]
U_d	superficial solid velocity, [m/s]
U_f	superficial gas velocity in dilute phase, [m/s]
U_g	superficial gas velocity, [m/s]
U_s	slip velocity, [m/s]
U_t	terminal velocity of particles, [m/s]
U_{uni}	minimum U_g for uniform suspension, [m/s]
u_p	real solid velocity, [m/s]
$\overline{u}_p$	average solid velocity, [m/s]
u_f	real fluid velocity
u_s	real slip velocity
$\langle u_f^2 \rangle^{\frac{1}{2}}$	fluctuation of fluid velocity, [m/s]
$\langle u_p^2 \rangle^{\frac{1}{2}}$	fluctuation of solid velocity, [m/s]
u^*	friction velocity at the wall, [m/s]
W	energy consumption with respect to unit volume, [J/(m^3 · s)]
X	variable vector
$\mathbf{X}_B$	basic variable vector
$\mathbf{X}_{NB}$	nonbasic variable vector
x_i	mass fraction of particle fraction i
X_1, X_2	see definition in Figure 4-5
Y	average output of optical probe
z	see definition in Figure 5-1, [m]
Z_i	inflection point of axial voidage profile, [m]
Z_i^*	Z_i after inserting one ring internal, [m]
ΔZ	height of affecting zone by a single ring, [m]

Subscript

a	bottom dense region
c or dense	dense phase
d	dissipation, particle
f or dilute	dilute phase, fluid
i or inter	inter phase
min	minimum
mf	minimum fluidization

mb	minimum bubbling
max	maximum
pt	value for choking point
p	particles
s	suspension
st	suspension and transport
t	transport
T	total
FD	fluid-dominating regime
PFC	particle-fluid-compromising regime
*	top dilute region
′	dimensionless parameter

Greek letters

β	crossed angle between the incident fiber and the receiving fiber
δ	distance between two fibers, [m]
ε	local average voidage
ε_1^*	average voidage in the dilute region at the top in real case with the assumption of the existence of clusters.
ε_{max}	maximum voidage for occurrence of clusters
θ	maximum incident angle of optical fiber
ρ	density, [kg/m^3]
λ_i	Lagrange's multiplier
λ	thermal conductivity, [W/m.K]
ν	kinematic viscosity, [m^2/s]
μ	viscosity, [kg/(m · s)]
φ	angle factor of incident fiber to receiving fiber
ϕ_s	shape factor of particles

Overline

–	time average or cross-sectional average
=	global average over the whole unit

REFERENCES

Azbel, D. and Liapis, A. I. (1983), Chapter 16: Hydrodynamics of Gas Solids Flow, in Handbook of Fluids in Motion, Cheremisinoff, N. P. (ed), Ramesh Gupta, p. 427

Abadie, J. and Carpentier, J. (1969), Generalization of the Wolfe Reduced Gradient Method to the Case of Non Linear Constraints, In OPTIMIZATION, R. Fletcher(ed), Academic Press, London, p. 37

Arastoopour, H. and Gidaspow, D. (1979), Analysis of IGT Pneumatic Conveying Data and Fast Fluidization Using a Thermohydrodynamic Model, Powder Technology, Vol. 22, p. 77

Abrahamsen, A. R. and Geldart, D. (1980), Behavior of Gas-Fluidized Beds of Fine Powders, Part I. Homogeneous Expansion, Powder Technology, Vol. 26, p. 35

Bader, R., Findlay, J. and Knowlton, T. M. (1988), Gas/Solid Flow Patterns in a 30.5cm Diameter Circulating Fluidized Bed, in Circulating Fluidized Bed Technology II, P. Basu and J. F. Large (eds), Pergamon Press, p. 123

Batchelor, G. K. (1988), A New Theory of the Instability of a Uniform Fluidized Bed, J. Fluid Mech., Vol. 193, p. 75

Bai, D., Jin, Y., Yu, Z. (1991), In Fluidization '91 — Science and Technology, Acceleration of Particles and Momentum Exchange Between Gas and Solids in Fast Fluidized Beds, Kwauk, M. and Hasatani, M. (eds), Science Press, Beijing, p. 46

Bai, D., Jin, Y., Yu, Z. and Gan, N. (1991), Radial Profiles of Local Solid Concentration and Velocity in a Concurrent Downflow Fast Fluidized Bed, in Circulating Fluidized Bed, Technology III, P. Basu, M. Horio and M. Hasatani (eds), Pergamon Press, p. 157

Bai, D., Jin, Y. and Yu, Z. (1992), Residence Time Distributions of Gas and Solids in a CFB, in Fluidization VII, O. E. Potter and D. J. Nicklin (eds), Eng. Found., New York, p. 195

Bai, D., Jin, Y. and Yu, Z. (1988), The Two-channel Model for Fast Fluidization, In Fluidization '88 — Science and Technology, Kwauk, M. and Hasatani, M. (eds), Science Press, Beijing, p. 155

Bai, D., Yi, J., Jin, Y. and Yu, Z. (1992), Residence Time Distributions of Gas and Solids in a Circulating Fluidized Bed, in Fluidization VII, O. E. Potter and D. J. Nicklin (eds), Eng. Found., New York, p. 195

Baker, W. E. and Westine, P. S. (1973), Similarity Methods on Engineering Dynamics, Hayden Book Company, INC., Rochelle Park, New Jersey

Berruti, F. and Kalogerakis, N. (1989), Can. J. of Chem. Eng. Vol. 67, p. 1010

Bie, R., Chen, A., Li, J. and Yang, L. (1992), A Circulating Fluidized Bed without Radial Heterogeneity, Selected Papers of Eng. Chem. & Metallurgy, Science Press, p. 177

Boiarski, A. A. (1985), Fiber Optic particle Concentration Sensor, SPIE, Vol. 566, p. 122

Briens, C. L. and Bergougnou, M. A. (1986), New Model to Calculate the Choking Velocity of Monosize and Multisize Solids in Vertical Pneumatic Transport Lines, Can. J. of Chem. Eng. Vol. 64, p. 196

Brereton, C. M. H., Grace, J. R. and Yu, J. (1988), Axial Gas Mixing in a Circulating Fluidized Bed, in Circulating Fluidized Bed Technology II, P. Basu and J. F. Large (eds), Pergamon Press, p. 57

Cankurt, N. T. and Yerushalmi, J. (1978), Gas Backmixing in High Velocity Fluidized Beds. In Fluidization (Edited by J. F. Davidson and D. L. Keairns), Cambridge University Press. Cambridge, p. 387

Chavan, V. V. (1984), Physical Principles in Suspension and Emulsion Processing, in Advances in Transport Processes, A. S. Mujumdar and R. A. Mashelkar (eds), John Wiley & Sons, New York, p. 1

Chen, A., Wu, W., Li, J. and Kwauk, M.(1994), Particle Aggregation in Particle-fluid Two-Phase Flow, in Fluidization '94 — Science and Technology, (Organizing Committee of CJF-5, ed.), Chemical Industry Press, Beijing, p. 254

Chen, A. (1993), personal communication

Couderc, J. -P. (1985), Incipient Fluidization and Particulate Systems, in Fluidization, J. F. Davidson, R. Clift and D. Harrison (eds), Academic Press, London, p. 1

Davidson, J. F.(1961), Discussion, Trans. Inst. Chem. Eng. Vol. 39 p. 230

Ding, J. and Gidaspow, D. (1990), A Bubbling Fluidization Model Using Theories of Granular Flow, AIChE J., Vol. 36, p. 523

Ding, J., Lyczkowski, R. W., Sha, W. T., Altobelli, S. A. and Fukushima, E. (1992), Analysis of Liquid-Solids Suspension Velocities and Concentrations Obtained by NMR Imaging, NSF/DOE Workshop on Flow of Particles and Fluids, Sep. 17~18, Gaithersburg, Maryland

Flemmer, R. L. C. and Banks, C. L. (1986), On the Drag Coefficient of a Sphere, Powder Technology, Vol. 48, p. 217

Gage, D. H., Schiffer, M., Kline, S. J. and Reynolds, W.C. (1966), the Non-Existence of a General Thermodynamic Variational Principle, in Non-Equilibrium Thermodynamics Variational Techniques and Stability, R. J. Donnelly, R. Herman and I. Prigogine (eds.), the University of Chicago Press, Chicago, p. 283

Gan, N., Jiang, D., Bai,D., Jin, Y. and Yu, Z.(1990), Concentration Profiles in Fast Fluidized Bed with Bluff-Body, J. of Chem. Eng. of Chinese Universities, Vol.4, p. 273

Gidaspow, D.(1978), Two-phase Transport and Reactor Safety, Proceedings of the Two-phase Flow and Heat Transfer Symposium Workshop, Hemisphere Publishing Corp., Vol. 1, p. 283

Gidaspow, D.(1986), Hydrodynamics of Fluidization and Heat Transfer: Supercomputer Modeling, Appl. Mech. Rev., Vol. 39, p. 1

Gidaspow, D., Tsuo, Y. P. and Luo, K. M.(1989), Computed and Experimental Cluster Formation and Velocity Profiles in Circulating Fluidized Beds, In Fluidization VI, Grace, J. R., Shemilt, L. W. and Bergougnou, M. A. (eds), Engineering Foundation, New York, p. 81

Grace, J. R. and Clift, R.(1974), On the Two-Phase Theory of Fluidization, Chem. Eng. Sci., Vol. 29, p. 327

Grace, J. R. and Tuot, J.(1979), A Theory for Cluster Formation in Vertically Conveyed Suspensions of Intermediate Density, Trans. IChemE., Vol. 57, p. 49

Grace, J. R.(1985), personal communication

Hancock, R. T.(1937), The Law of Motion of Particles in a Fluid, Trans. Instn. Min. Engrs. (London), Vol. 94, p. 114

Harrison, D., Davidson, J. F. and Dekock, J. W. (1961), On the Nature of Aggregative and Particulate Fluidization, Trans. Instn. Chem. Engrs., Vol. 39, p. 202

Hartge, E. U., Li, Y. and Werther, J. (1986), Flow Structures in Fast Fluidized Beds, in Fluidization V, ϕstergaard, K. and Srensen. A. (eds), Eng. Found., New York, p. 345

Hartge, E. U., Rensner, D. and Werther, J. (1988), Solids Concentration and Velocity Patterns in Circulating Fluidized Beds, in Circulating Fluidized Bed Technology II, P. Basu and J. F. Large (eds.), Pergamon Press, p. 165

Hinze, J. O. (1975), Turbulence, McGraw-Hill, p. 700

Horio, M., Morishita, K., Tachibana and Murata, N. (1988), Solid Distribution and Movement in Circulating Fluidized Beds, in Circulating Fluidized Bed Technology II, P. Basu and J. F. Large (eds), Pergamon Press, p. 147

Ishii, H., Nakajima, T. and Horio, M. (1989), The Annular Flow Model of Circulating Fluidized Beds, J. of Chem. Eng. of Japan, Vol. 22, p. 484

Jackson, R. (1963), The Mechanics of Fluidized Beds, I. the stability of the state of uniform fluidization, Trans. Inst. Chem. Engrs., Vol.44, p. 13

Keohe, P. W. K. and Davidson, J. F. (1971), Continuously Slugging Fluidized Beds, Inst. Chem. Eng. Symp. Ser., Vol. 33, p. 97

Knowlton, T. M. and Bachovchin, D. M. (1975), The Determination of Gas- Solids Pressure Drop and Choking Velocity as a Function of Gas Density in a Vertical Pneumatic Conveying Line, International Conference on Fluidization, Pacific Grove, June 15-20, p. 253

Knowlton, T. M. (1992), Pressure and Temperature Effects in Fluid-Particle Systems, in Fluidization VII, O. E. Potter and D. J. Nicklin (eds), Eng. Found., New York, p. 27

Krohn, D. A. (1986), Intensity Modulated Fiber Optic Sensors.Overview, SPIE, Vol. 718, Fiber Optic and Laser Sensors IV, p. 2

Kunii, D. and Levenspiel, O. (1969), Fluidization Engineering, Wiley, New York

Kwauk, M. (1957), Intermediate Zone Fluidization, MK-1-10-57

Kwauk, M. (1973), Particulate Fluidization in Chemical Metallurgy, Science in China, Vol. 22, p. 298

Kwauk, M.(1980), Towards a Unified Hypothesis for Fluidized Systems, CHEMECA '80, 8th Australian Chemical Engineering Conference, Melbourne, Aug. 24-27, Proceedings, p. 98

Kwauk, M. (1990), Fluidization Regimes, MK-30-10-90

Kwauk, M. and Li, H. (1989), Particularization of G/S Fluidization, research proposal, Institute of Chemical Metallurgy, Academia Sinica

Lamb, H. (1945), Hydrodynamics, Dover, New York, p. 617

Ladson, L. S. and Waren, A. D. (1978), Generalized Reduced Gradient Software for Linearly and Nonlinearly Constrained Problems, in Design and Implementation of Optimization Software, H. Greenberg (ed), Sijthoff and Noordhoff, p. 363

Lasdon, L. S., Waren, A. D., Jain, A. and Ratner, M. (1978), Design and Testing of a GRG code for Nonlinear Optimization, in ACM Transactions on Mathematical Software, Vol. 4, No. 1, p. 34

Latham, R. and Potter, O. E. (1970), Backmixing of Gas in a 6*in* Diameter Fluidized Bed, Chem. Eng. J., Vol. 1, p. 152

Lanneau, K. P. (1960), Gas Solid Contacting in Fluidized Beds, Trans. Inst. Chem. Engrs., Vol. 38, p. 125

Lee, M. M., Hanratty, T. J. and Adrian, R. J. (1989), The Interpretation of Droplet Deposition Measurement with a Diffusion Model, Int. J. Multiphase Flow, Vol. 15, p. 459

Li, H., Xia, Y., Tung, Y. and Kwauk, M. (1991). Micro-Visualization of Two-Phase Structure in a Fast Fluidized Bed, in Circulating Fluidized Bed Technology III, P. Basu, M. Horio and M. Hasatani (eds), Pergamon Press, p. 183

Li, J. (1987), Multi-Scale Modeling and Method of Energy Minimization for Particle-Fluid Two-Phase Flow, Ph. D. thesis, Institute of Chemical Metallurgy, Academia Sinica, Beijing

Li, J., Tung, Y. and Kwauk, M. (1988a), Axial Voidage Profiles in Fast Fluidized Beds, in Circulating Fluidized Bed Technology II, P. Basu and J. F. Large (eds), Pergamon Press, p. 193

Li, J., Tung, Y. and Kwauk, M. (1988b), Energy Transport and Regime Transition of Particle-Fluid Two-Phase Flow, in Circulating Fluidized Bed Technology II, P. Basu and J. F. Large (eds), Pergamon Press, p. 75

Li, J., Tung, Y. and Kwauk, M. (1988c), Multi-Scale Modeling and Method of Energy Minimization in Particle-Fluid Two-Phase Flow, in Circulating Fluidized Bed Technology II, P. Basu and J. F. Large (eds), Pergamon Press, p. 89

Li, J. and Weinstein, H. (1989), An Experimental Comparison of Gas Backmixing in Fluidized Beds across the Regime Spectrum, Chem. Eng. Sci., Vol. 44, p. 1697

Li, J., Tung, Y. and Kwauk, M. (1990), Mathematical Modeling of Particle- Fluid Two-Phase Flow, Science in China, Series B, Vol. 33, p. 524

Li, J., Bie, R., Kwauk, M., Wu, W. and Yang, L. (1991a), A Circulating Fluidized Bed without Radial Heterogeneity, Chinese Patent: 91216163.9

Li, J., Li, Z., Yang, L. and Liu, W. (1991b), Hydrodynamic Mean Diameter of Multisized Particles, in Proceeding of China-Japan Chemical Engineering Conference, Tianjin University Press, p. 754

Li, Jinghai, Reh, Lothar and Kwauk, Mooson (1991c), Application of Energy Minimization Principle to Hydrodynamics of Circulating Fluidized Beds, in Circulating Fluidized Bed Technology III, P. Basu, M. Horio and M. Hasatani (eds), Pergamon, Press, p. 163

Li, J., Reh, Li, Tung, Y. and Kwauk, M. (1991d), Multi-Aspect Behavior of Fluidization in Different Regimes, in FLUIDIZATION '91 — Science and Technology, M. Kwauk and M. Hasatani (eds), Science Press, Beijing, p. 11

Li, J., Kwauk, M. and Reh, L. (1992), Role of Energy Minimization in Gas/ Solid Fluidization, in Fluidization VII, O. E. Potter and D. J. Nicklin (eds), Engineering Foundation, New York, p. 83

Li, J., Chen, A., Yan, Z., Xu, G. and Zhang, X. (1993), Particle-Fluid Contacting in Circulating Fluidized Beds, the 4th International Conference on Circulating Fluidized Beds, Aug. 1~5, Hidden Valley

Li, R. (1986), Nonequilibrium Thermodynamics and Dissipative Structure, Tsinghua University Press, Beijing (Chinese)

Li, Y. and Kwauk, M. (1980). Hydrodynamics of Fast Fluidization, in Fluidization, J. R. Grace (ed), Plenum Press, p. 537

Li, Y., Chen, B., Wang, F. and Wang, Y. (1982), Hydrodynamic Correlations for Fast Fluidization, 1st China-Japan Symp. Fluidization, Hangzhou, China, p. 124

Matsen, J. M. (1982), Mechanisms of Choking and Entrainment, Powder Technology, Vol. 32, p. 21

Militzer, J. (1986), Numerical Prediction of the Fully Developed Two-Phase (air-solids) Flow in a Pipe, in Circulating Fluidized Bed Technology, P. Basu(ed), Pergamon Press, p. 173

Molerus, O. (1967), The Hydrodynamic Stability of the Fluidized Bed, in Proceeding of the International Symposium on Fluidization, June 6~9, Eindhoven, p. 134

Monceaux, L., Azzi, M., Molodtsof, Y. and Large, J. F. (1986), Particle Mass Flux Profiles and Flow Regime Characterization in a Pilot-Scale Fast Fluidized Bed Unit, 5th Intern. Conf. Fluidization, Elsinore, p. 377

Nakamura, K. and Capes, C. E. (1973), Vertical Pneumatic Conveying: A Theoretical Study of Uniform and Annular Particle Flow Models, Can. J. of Chem. Eng., Vol. 51, p. 39

Nguyen, H. V., Potter, O. E., Dent, D. C. and Whitehead, A. B. (1981). Gas Backmixing in Large Fluidized Beds Containing Tube Assemblies, AIChE. J., Vol. 27, p. 509

Nicolis, G. and Prigogine, I. (1977), Self-Organization in Nonequilibrium Systems, for dissipative structures to order through fluctuations, John Wiley & Sons, New York

Oziski, M. N. (1989), personal communication

Prigogine, I. (1967), Introduction to Thermodynamics of Irreversible Processes, 3rd edition, Interscience Publication, New York

Qian, G. and Li, J. (1993), Particle Velocity Measurement in CFB with a Integrated Probe, Engineering Chemistry & Metallurgy, Vol. 14, p. 72

Qin, S. and Liu, G. (1982), Application of Optical Fibers to Measurement and Display of Fluidized Systems, in Fluidization '82 — Science and Technology, M. kwauk and M. Kunii (eds), Science Press, Beijing, p. 258

Qin, S. and Li, G. (1990), An Image Analysis System for Moving Particle, the 5th National Fluidization Conference, Apr. 9~13, Beijing

Reh, L. (1971), Fluidized Bed Processing, Chem Eng. Prog. Vol. 67(2), p. 58

Reh, L. and Li, J. (1991), Measurement of Voidage in Fluidized Beds by Optical Probe, in Circulating Fluidized Beds Technology III, P. Basu, M. Horio and M. Hasatani (eds), Pergamon Press, p. 105

Rhodes, M. J. and Geldart, D. (1986), From Minimum Fluidization to Pneumatic Transport — a Critical Review of the Hydrodynamics, in Circulating Fluidized bed Technology, P. Basu (ed), Pergamon Press, p. 21

Richardson, J. F. and Zaki, W. N. (1954), Sedimentation and Fluidization, Trans. Instn. Chem. Engrs., Vol. 32, p. 35

Romero, J. B. and Johanson, L. N. (1962), Factors Affecting Fluidized Bed Quality, Chem. Eng. Prog. Symp. Ser., Vol. 58, p. 28

Sankar, S. R. and Smith, T. N. (1986), Slip Velocities in Pneumatic Transport, Part I, Powder Technology, Vol. 47, p. 167

Satija, S., Young, J. B. and Fan, L. S. (1985), Pressure Fluctuation and Choking Criterion for Vertical Pneumatic Conveying of Fine Particles, Powder Technology, V. 43, p. 257

Schouten, J. C., van der Stappen, M. L. M. and Van der Bleek, C. M. (1992), Deterministic Chaos Analysis of Gas-Solid Fluidization, in Fluidization VII, O. E. Potter and D. J. Nicklin (eds), Eng. Found., New York, p. 103

Soo, S. L. (1967), Fluid Dynamics of Multiphase Systems, Blaisdell, Waltham MA

Soo, S. L. (1989), Particulates and Continuum: Multiphase Fluid Dynamics, Hemisphere, New York

Squires, A. M., Kwauk, M. and Avidan, A. A. (1985), Fluid Beds: At Last, Challenging Two Entrenched Practices, Science, Vol. 230, p. 1329

Stephens, G. K., Sinclair, R. L. and Potter, O. E. (1967), Gas Exchange between Bubbles and Dense Phase in a Fluidized Bed, Powder Technology, Vol. 1, p. 157

Soo, S. L. (1982), Chapter 3: Gas-Solid Systems, in Handbook of Multiphase Systems, G. Hetsroni (ed), Hemisphere Publishing Corporation, New York, p. 3-1

Subbarao, D. (1986), Cluster and Lean-phase Behavior, Powder Technology, Vol. 46, p. 101

Tung, Y., Li, J. and Kwauk, M. (1988), Radial Voidage Profiles in a Fast Fluidized Bed, in Fluidization '88 — Science and Technology, M. Kwauk and D. Kunii (eds), Science Press, Beijing, p. 35

Toomey, R. D. and Johnstone, H. F. (1952), Gaseous Fluidization of Solid Particles, Chem. Eng. Prog., Vol. 48, p. 220

van Deemter, J. J. (1980), Mixing Patterns in Large-Scale Fluidized Beds, In Fluidization (Edited by J. R. Grace and J. M. Matsen), Plenum Press. New York, p. 69

van Deemter, J. J. (1985), Chapter 9: Mixing, in Fluidization, J. F. Davidson, R. Clift and D. Harrison (eds), Academic Press, New York, p. 331

Wallis, G. B. (1969), One-Dimensional Two-Phase Flow, McGraw-Hill, New York, p. 182

Weinstein, H., Graff, R. A., Meller, M. and Shao, M. (1983), The Influence of the Imposed Pressure Drop across a Fast Fluidized Bed, Proc. 4th Intern. Conf. Fluidization, Kashikojima, Japan, p. 299

Weinstein, H., Shao, M., Schnitzlein, M. and Graff, R. A. (1986), Radial Variation in Void Fraction in a Fast Fluidized Bed, the 5th Intern. Conf. Fluidization, Elsinore, p. 329

Weinstein. H. and Li, J. (1989), An Evaluation of the Actual Density in the Acceleration Section of Vertical Risers, Powder Technology, Vol. 57, p. 57

Weinstein, H., Li, J., Bandlamudi, E.,Feindt, H. J. and Graff, R. A. (1989), Gas Backmixing of Fluidized Beds in Different Regimes and Different Regions. In Fluidization (Edited by J. R. Grace, L. W. Shemilt and M. A. Bergougnou), Engineering Foundation, New York, p. 57

Wilhelm, R. H. and Kwauk, M. (1948), Fluidization of Solid Particles, Chem. Eng. Prog., Vol. 44, p. 201

Wolfe. P. (1963), Method of Nonlinear Programming, in Recent Advances in Mathematical Programming, R. L. Graves and P. Wolfe (eds), McGraw-Hill Book Company

Wu, W., Li, J., Yang, L. and Kwauk, M. (1992), Critical Condition for Particle Aggregation in Particle-Fluid Two-Phase Flow, Journal of Engineering Thermophysics, Vol. 13, p. 324

Wu, W., Qian, G., Chen, A. and Yang. L. (1993). Measurement of Particle Flow Rate in CFB with a Stress-Strain Sensor, Engineering Chemistry & Metallurgy, Vol. 14, p. 68

Xu, G. (1993), personal communication

Yang, W. C. (1983), Criteria for Choking in Vertical Pneumatic Conveying Lines, Powder Technology, Vol. 35, p. 143

Yang, W. C. (1988), A Model for the Dynamics of a Circulating Fluidized Bed Loop, in Circulating Fluidized Bed Technology II, Basu, P. and Large, J. F.(eds), Pergamon Press, p. 181

Yang, Y., Jin, Y., Yu, Z. and Wang, Z. (1990), Changes of Cross-Sectional Average Particle Velocity in Circulating Fluidized Beds with Low Density, Chem. Reac. Eng. & Tech., in Chinese, Vol. 6, p. 30

Yan, Z. (1993), Extreme Behavior and Countercurrent Operation of Vertical Particle-Fluid Two-Phase Flow, Master Thesis, Harbin Institute of Technology, Harbin

Yan, Z., Chen, A. and Li, J. (1993), Extreme Behavior of Particle-Fluid Two-Phase Flow, the 6th National Fluidization Conference, Wuhan, Oct. 14~15

Yang, Y., Jin, Y., Yu, Z., Wang, Z. and Bai, D. (1991), The Radial Distribution of Local Particle Velocity in a Dilute Circulating Fluidized Bed, in Circulating Fluidized Bed Technology III, P. Basu, M. Horio and M. Hasatani(eds), Pergamon Press, p. 201

Yang, Y. (1992), Study of Concurrent Up- and Down-Flow in Circulating Fluidized beds, Ph. D. Thesis, Tsinghua University, Beijing

Yerushalmi, J., Turner, D. H. and Squires, A. M. (1976), The Fast Fluidized Bed, Ind. Eng. Chem. Process Des. Dev., Vol. 15, p. 47

Yerushalmi, J. R., Cankurt, N. T., Geldart, D. and Liss, B. (1978), Flow Regimes in Gas-Solids Contact Systems, AIChE Symp. Ser., Vol.76, p. 1

Yerushalmi, J. and Cankurt, N. J. (1979), Further Studies of the Regimes of Fluidization, Powder Technology, Vol. 24, p. 187

Yu, Y. (1986). Segregation and Mixing of Solid Particles in Generalized Fluidization, Master Thesis, Institute of Chemical Metallurgy, Academia Sinica, Beijing

Zhang, H., Xie, Y. S., Chen, Y. and M. Hasatani (1990), Mathematical Modeling for Longitudinal Voidage Distribution of Fast Fluidized Beds, in Circulating Fluidized Bed Technology III, P. Basu, M. Horio and M. Hasatani (eds) Pergamon Press, p. 151

Zhang, H., Xie, Y. S. and Hasatani, M. (1991), A New Two Dimensional Correlation for Voidage Distribution of Fast Fluidized Beds, in Fluidization '91 — Science and Technology, M. Kwauk and M. Hasatani (eds), Science Press, Beijing, p. 21

Zheng, C., Tung, Y., Xia, Y., Hua, B. and Kwauk, M. (1991), Voidage Redistribution by Ring Internals in Fast Fluidization, in Fluidization '91 — Science and Technology, Kwauk, M. and M. Hasatani (eds), Science Press, Beijing, p. 168

Zheng, C. and Tung, Y. (1990), Effects of Internals on Radial Distribution of Particles in CFB, Eng. Chem. & Metallurgy, Vol. 11, p. 294

Zheng, C., Tung, Y., Li, H. and Kwauk, M. (1992), Characteristics of Fast Fluidized Beds with Internals, in Fluidization VII, O. E. Potter and D. J. Nicklin (eds), Eng.Found., New York, p. 256

Zhou, S.(1985), Irreversible Thermodynamics as an Approach to Studying Mixing in Fluidized Bed, in Fluidization '85 — Science and Technology, M. Kwauk and D. Kunii (eds), Science Press, Beijing, p. 158

Zhou, L. (1991), Numerical Simulation of Turbulent Two-phase Flow and Combustion, Tsinghua University Press, Beijing (in Chinese)

Liu, D. (1993), Fluid Dynamics of Two-phase Systems, Hight Education Press, Beijing (in Chinese)

INDEX

PARTICLE-FLUID TWO-PHASE FLOW

The Energy-Minimization Multi-Scale Method

By **Jinghai LI** and **Mooson KWAUK**

CAPSULE SUMMARY: This book is devoted to particle-fluid two-phase flow which forms the basis of, among others, fluidization. Main attention is focused on the underlying mechanisms of the phenomena and their interrelationships with a view to formulating an integrated theory to guide the intelligent design and operation of two-phase equipment: chemical reactors, heat and mass transfer apparatus, pipelines for transporting or moving granular materials. This book propounds two essential concepts—**multi-scale** analysis and the method of **energy-minimization**. These concepts are applied to various possible structures of two-phase flow designated under four categories—**phase, regime, pattern** and **region**—to describe both local and overall hydrodynamics.

DESCRIPTION OF CHAPTERS: This book consists of five chapters. The **first chapter** introduces the essential characteristics of particle-fluid two-phase flow, and proposes the primary framework of system designation. **Chapter 2** formulates the Energy-Minimization Multi-Scale, or EMMS model, on the basis of the two essential concepts. **Chapter 3** gives the solution of the model and presents the results of computation dealing, in succession, with local hydrodynamics (phases), dependency of local hydrodynamics on operating conditions (regimes), and on material properties (patterns), and, lastly, overall hydrodynamics, or spatial distribution of regimes (regions). **Chapter 4** outlines significant experimental evidence for the EMMS model and other phenomena relevant to particle-fluid two-phase flow. **Chapter 5** presents an example of simulating a typical two-phase flow system—the circulating fluidized bed, to demonstrate how to calculate its whole flow field and how to evaluate gas/solid contacting in the system, and presents several new types of reactors designed according to the EMMS model. This last chapter concludes the book with multi-aspect prospects for further application of the EMMS model in other fields.

ABOUT AUTHORS: Prof. Jinghai Li earned both his B.S. and M.S. degree from the Harbin Institute of Technology in North China, and studied particle-fluid two-phase flow by using the EMMS concept in his doctoral research under Prof. Mooson Kwauk at the Institute of Chemical Metallurgy (ICM), Academia Sinica. He continued his research in the United States and Switzerland, until he returned to Beijing in 1990, and is now a deputy director of the Multi-Phase Reaction Laboratory of ICM. Prof. Kwauk studied chemistry at the University of Shanghai and did graduate research in fluidization at Princeton University during the forties, and has continued working in this field both in USA and China up to the present. At the moment he is professor and emeritus director of ICM. He is Member of Academia Sinica and heads the Chinese Society of Particuology.

READERSHIP: Researchers and engineers in fluidization and other fields dealing with particle-fluid flow; graduate students on chemical engineering.

ISBN 7-5024-1572-6

9 787502 415723 >

ISBN 7-5024-1572-6/TQ.67